Rapid 3D Whole Brain Molecular MRI at 7T

Dissertation
zur
Erlangung des Doktorgrades (Dr. rer. nat.)
der
Mathematisch-Naturwissenschaftlichen Fakultät
der
Rheinischen Friedrich-Wilhelms-Universität Bonn

von
Suzan Akbey
aus
Andernach

Bonn, 2024

Angefertigt mit Genehmigung der Mathematisch-Naturwissenschaftlichen Fakultät der Rheinischen Friedrich-Wilhelms-Universität Bonn

Gutachter / Betreuer:	Prof. Dr. Tony Stöcker
Gutachter:	Prof. Dr. Klaus Desch
Tag der Promotion:	03.12.2024
Erscheinungsjahr:	2024

Abstract

Magnetic resonance imaging (MRI) has emerged as a leading, non-ionizing diagnostic tool in medical practice over the last decades. Beyond, MRI has evolved into an expansive field of research, yielding a multitude of novel advancements in technical innovations and a variety of new contrasts. The MR signal provides information not only regarding the tissue composition, but also concerning the magnetic, chemical, and physical interactions of the spin system. Here, chemical exchange saturation transfer (CEST) imaging utilizes the chemical exchange of protons and its associated magnetization transfer to provide insights into biochemistry with unprecedented resolution. The CEST technique represents a promising in-vivo approach to studying mobile proteins non-invasively. It has the potential to facilitate new insights into the pathogenesis of neurodegenerative diseases (NDs), given that many forms are associated with the accumulation of misfolded proteins.

Aim of this thesis was the development of a robust and rapid technique for whole-brain CEST imaging at 7 T, as the method benefits significantly from ultra-high field (UHF) strength in particular from the increased spectral resolution. Hence, a saturation scheme containing a train of Gaussian-shaped RF pulses was designed with the objective of maximizing the amide contrast resulting from the peptide bond in the backbone of mobile proteins while minimizing the required time. By employing a snapshot approach with centric-reordered 3D-EPI readout, a whole-brain field of view (FOV) is acquired after a single saturation block. One challenge associated with whole-brain imaging at UHF is the wide range of B_1 variations, which significantly affects the CEST signal. To that end, it was necessary to implement an effective B_1 correction method.

The proposed approach enables the robust acquisition of artifact-free wholebrain CEST maps at 7 T within a total scan time of less than 15 min. In the snapshot 3D-EPI CEST sequence, the saturation block lasts for 3.6 s, while the readout time ranges from 734 ms to 1.1 s, resulting in an isotropic resolution of 2 mm and 1.61 mm respectively. Consequently, the total duration of the sequence is less than 4 min including 43 frequency offsets and two unsaturated images. The acquisition of two supplementary repetitions with varying B_1 allows for the correction of the deviations in B_1 within the cerebrum. The transfer of the sequence to a parallel transmission excitation (pTx) allows for the reduction of required repetitions. Furthermore, the so-called PUSHUP approach enables the quantification of CEST effects within the cerebellum.

The snapshot 3D-EPI CEST approach is well-suited for large-scale and multi-modality studies given its manageable time effort and high degree of flexibility.

Contents

CHAPTER 1

Introduction

1.1 Motivation

Magnetic resonance imaging (MRI) has emerged as a leading diagnostic tool since its initial application in medical practice in the early 1980s. In addition to the remarkable soft tissue contrast, it is distinguished by its non-invasive nature. Unlike computed tomography (CT) or positron emission tomography (PET), MRI is a non-ionizing imaging technique that obtains information about the tissue by manipulating nuclear spins. Following the initial reports of nuclear magnetic resonance (NMR) experiments by Felix Bloch [1] and Edward Purcell [2] in 1946, Paul Lauterbur was the first to identify a method for imaging in 1973 [3], through the utilization of field gradients. Over the past five decades, MRI has evolved into an expansive field of research, yielding a multitude of novel advancements. These include not only technical innovations (such as higher field strengths, enhanced hardware, advanced computing and data processing capabilities) but also the introduction of a diverse array of contrasts. In addition to the various morphological representations with different weighting, such as T_1- or T_2- weighting, the visualization of processes in the brain is also possible, such as brain activation using bold oxygenation level dependent contrast, brain perfusion using aterial spin labeling, or diffusion.

A comparatively new approach to accomplish endogenous in-vivo image contrast is the so-called chemical exchange saturation transfer (CEST). The concept was first introduced by Sture Forsén and Ragnar A. Hoffman in the 1960s [4] and subsequently transferred to imaging by Kathleen Ward, Anthony Aletras, and Robert S. Balaban in 2000 [5]. Protons of low-concentrate molecules, such as metabolites or proteins, are indirectly observed via their chemical exchange with water. During a prolonged saturation period, the selective radiofrequency irradiation of the solute proton pool results in the saturation of its signal, which is continuously transferred to the water proton pool through the exchange of magnetization. This process results in a cumulative water signal attenuation. By repeating the measurement at different presaturation frequencies arranged around the tissue water resonance, a voxel-wise spectrum, designated as Z-spectrum, can be obtained. Through the analysis of this spectrum, it is possible to extract different image contrasts that are dependent on molecular functional groups, such as amides (-NH), amines (-NH2) or hydroxyl (-OH). In order to achieve the most accurate detection of the metabolites of interest, it is necessary to adjust the saturation scheme depending on exchange rates and frequency offsets. The most prominent in-vivo CEST effect is the one of amides in peptides or in the peptide bond in the backbone of mobile proteins [6]. Proteins also exhibit an effect in the frequency range of aliphatic protons, originating from a phenomenon known as relayed nuclear Overhauser effect (rNOE) [7]. Moreover, other metabolites including creatine [8], glutamate [9], and glucose [10–14] have been demonstrated to be detectable with CEST at 7 T.

Such knowledge of the molecular microenvironment may facilitate new insights into the pathogenesis of neurodegenerative disorders. Neurodegenerative diseases (NDs) are a significant cause of disability and premature death among older people worldwide [15]. There is a great diversity of clinical phenotypes, and there are currently no disease-modifying therapies. An additional tool to understand the pathological pathways is therefore required. Many forms of neurodegenerative diseases are associated with the accumulation of misfolded proteins, which spread throughout the brain with the progression of the disease. CEST is a promising in-vivo approach to study mobile proteins non-invasively. Its potential has been demonstrated in numerous preclinical studies of the human brain [16], with the broadest field being tumor research [17–21]. However, findings in the field of stroke research [22–24] have also been demonstrated, as have first studies in the field of neurodegenerative diseases [25, 26].

A variety of fast acquisition techniques have been developed with the objective of acquiring the CEST-prepared magnetization in vivo. While turbo spin echo (TSE) [6] and gradient and spin echo (GRASE) [27] approaches were previously used at 3 T, gradient echo (GRE) [28–30] and segmented echo planar imaging (EPI) [17, 31–33] readouts were also recently applied at 7 T and 9.4 T MRI systems.

In particular, EPI is noteworthy for its high signal to noise ratio (SNR) efficiency as a result of its high ratio of signal acquisition time to total acquisition time and its high average k-space velocity. In comparison to other highly efficient techniques, such as TSE and GRASE, EPI is less constrained by specific absorption rate (SAR) limitations at ultra-high fields (UHF). In contrast to interleaved 2D multi-slice acquisitions, 3D-EPI approaches are distinguished by an SNR advantage associated with volumetric acquisitions [34, 35] , a slice-independent CEST contrast and particularly low SAR. Furthermore, the 3D acquisition enables the implementation of high parallel imaging acceleration through the utilization of undersampling techniques along both phase-encoding directions, thereby reducing the overall acquisition time.

CEST experiments have a special benefit from higher field strengths, as the greater spectral dispersion enables more accurate separation of the CEST effects of dilute molecules. In addition, the higher sensitivity and prolonged T_1 relaxation of water observed at UHF improve the reliability and precision of the measurements [36]. However, CEST measurements at UHF must also address the issue of stronger field inhomogeneities and a higher RF power deposition. In order to remain within SAR limits, prolonged scan times are often required.

The objective of this work was to develop a robust and rapid technique for whole-brain CEST imaging, with a particular focus on the amide contrast, that addresses the aforementioned challenges and leverages the high SNR and spectral resolution at UHF. A considerable challenge is the time-consuming saturation process, which is compounded by the alteration of the preparation state during the readout. Consequently, in order to achieve a larger volume coverage, it is typically necessary to apply repeated saturation imaging blocks, which consequently results in a longer scan time. The proposed snapshot 3D-EPI approach effectively addresses this issue, as the fast volume acquisition is following a single CEST preparation block. The previously reported 3D-EPI-based CEST methodologies, in contrast, necessitated the use of multiple preparation blocks at each specific saturation frequency [17, 31–33]. In contrast to the snapshot GRE approach proposed by Zaiss et al. [30], 3D-EPI enables whole-brain imaging rather than a much smaller volume due to its more time-efficient readout scheme.

Another challenge associated with whole-brain CEST at 7 T is the wide range of B_1 variations (up to 50 %), which significantly affects the CEST signal. Previous whole-brain approaches [17, 31] have demonstrated that correction for B_1 inhomogeneities is essential when B_1 varies by more than 10-20 %. This prolongs the total experiment duration due to the necessity of repeating the measurement at each saturation frequency with varying B_1 amplitude [37]. Parallel transmission (pTx) approaches have been proposed as a further possible solution to these challenges [38–40]. Thus, another objective of this study was to identify an appropriate B_1 correction method for the snapshot 3D-EPI CEST approach.

1.2 Thesis outline

The content of this thesis is divided in six main parts, starting with a brief review of the theoretical background (Chapters 2 and 3), followed by the methods (Chapter 4) and results (Chapter 5) of the rapid 3D whole-brain molecular imaging approach which was developed during this thesis. After a discussion part (Chapter 6), a conclusion is presented that summarizes the outcomes and offers a brief outlook (Chapter 7).

The theoretical background in Chapter 2 covers fundamental principles of MR imaging, from the theoretical foundations, spatial encoding and k-space formalism to parallel imaging and parallel transmission. In a second part, the basics of the EPI sequence are covered, including the extension to 3D-EPI, as well as an outline of the EPI-typical challenges at UHF. Finally, the principle of field mapping is described.

In the following Chapter 3, the physical and experimental background of CEST is explained. Beyond the theoretical aspects, practical issues of in-vivo experiments are summarized. These include the functional exchange groups in the human brain, concomitant effects such as rNOE and MT, and the basics of the Z-spectrum analysis. Lastly, the potential of CEST imaging in the context of neurodegenerative diseases is reviewed.

The experimental setups used to develop the snapshot 3D-EPI CEST sequence are described within Chapter 4. The sequence combines a 3D-EPI readout with a Gaussian pulse train for saturation, both of which had to be adapted for parallel transmission at a later stage of this thesis. Apart from the sequence details, the image processing required to compute the CEST contrast maps and to compensate for artifacts such as motion, distortion, or field variations is described. Following simulations and phantom experiments, Chapter 4 includes the multiple in-vivo experiments performed during development together with a brief statistical survey using the final sequence.

Chapter 5 is divided into three categories. First, the optimization results of the saturation scheme are presented. Second, the feasibility of whole-brain CEST is demonstrated, including the adaptation of the 3D-EPI readout to the requirements of CEST imaging and the optimization of a B_1 correction for whole-brain CEST at 7 T. Third, CEST quantification is demonstrated in test-retest experiments and in a group analysis. The findings have been partially published in two MRM papers [41, 42]. Subsequently, in Chapter 6, the results are subjected to interpretation and evaluation. This is followed by a summary of all relevant insights in Chapter 7, which also provides a brief outlook.

1.3 Publications

The following works have been published as part of the work on this thesis:

Journal Papers

- Völzke Y, **Akbey S**, Löwen D, Pracht, ED, Stirnberg R, Gras V, Boulant N, Zaiss M, & Stöcker T, 2024. PUSHUP-CEST: Calibration free whole-brain ultra-high field CEST imaging using parallel transmit. Magnetic Resonance in Medicine *(under review)*
- Müller S, Stirnberg R, **Akbey S**, Ehses P, Scheffler K, Stöcker T & Zaiss M, 2020. Whole brain snapshot CEST at 3T using 3D-EPI: Aiming for speed, volume, and homogeneity. Magnetic Resonance in Medicine, 84(5), 2469-2483. `https://doi.org/10.1002/mrm.28298`
- **Akbey S**, Ehses P, Stirnberg R, Zaiss M, & Stöcker T, 2019. Whole-brain snapshot CEST imaging at 7 T using 3D-EPI. Magnetic Resonance in Medicine, 82(5), 1741-1752. `https://doi.org/10.1002/mrm.27866`

Conference Contributions

- **Akbey S**, Stöcker T, 2020. CEST Simulations with JEMRIS. Proceedings of the 37th Scientific Meeting of the European Society for Magnetic Resonance in Medicine and Biology, p. 156-157. `https://doi.org/10.1007/s10334-020-00876-y`
- Müller S, Stirnberg R, **Akbey S**, Ehses P, Scheffler K, Stöcker T & Zaiss M, 2020. Snapshot whole brain CEST MRI at 3T with 3D-EPI. Proceedings of the 28th Scientific Meeting of the International Society for Magnetic Resonance in Medicine, #3096, `https://cds.ismrm.org/protected/20MProceedings/PDFfiles/3096.html`.
- **Akbey S**, Ehses P, Stirnberg R, Zaiss M, & Stöcker T, 2019. Optimized B1/B0 correction for whole-brain CEST imaging using 3D-EPI at 7T. Proceedings of the 27th Scientific Meeting of the International Society for Magnetic Resonance in Medicine, #4019, `https://cds.ismrm.org/protected/19MProceedings/PDFfiles/4019.html`.
- **Akbey S**, Ehses P, Stirnberg R, Zaiss M, & Stöcker T, 2018. Single-shot whole-brain CEST imaging using centric-reordered 3D-EPI. Proceedings of the 26th Scientific Meeting of the International Society for Magnetic Resonance in Medicine, #2231, `https://cds.ismrm.org/protected/18MProceedings/PDFfiles/2231.html`.

CHAPTER 2

Basics of magnetic resonance imaging

This chapter provides a concise introduction to the basic principles of nuclear magnetic resonance (NMR) and an overview of the techniques employed in magnetic resonance imaging MRI, focusing on relevant topics for this thesis. For a more complete review, it is recommended to consult the textbooks by Haacke et al. [43] and Liang and Lauterbur [44].

2.1 Nuclear magnetic resonance

Nuclear magnetic resonance can be observed when a nucleus with a nuclear spin that is not equal to zero is placed in an external magnetic field. Although the NMR phenomenon can only be fully described by quantum mechanics, some of its basic principles can be explained by a classical description. The NMR effect was first published independently by Felix Bloch [1] and Edward Purcell [2] in 1946.

These nuclei possess a non-zero spin angular momentum $\vec{J}$ resulting in a nuclear magnetic dipole moment:

$$\vec{\mu} = \gamma \cdot \vec{J}, \tag{2.1}$$

where γ is a nucleus-dependent physical constant, the so-called gyromagnetic ratio. For hydrogen, the most commonly used nucleus for MRI applications, the gyromagnetic ratio has been experimentally identified to be $\gamma = 2.675 \cdot 10^8$ rad/s/T, respectively $\frac{\gamma}{2\pi} = 42.58$ MHz/T. Because of the single proton of hydrogen, the terms spin, proton and nucleus are often used synonymously in the MRI literature.

When placed in an external magnetic field B_0, the spin experiences a torque and precesses around the applied field (by definition pointing in the z direction) at the so-called Larmor frequency ω_0:

$$\omega_0 = \gamma \cdot B_0. \tag{2.2}$$

This angular precession frequency varies when nuclei in a spin system are bound to different molecules. The orbital electrons surrounding the molecule produce their own weak magnetic fields, which vary according to the position of the electron within the molecule. The slightly shifted precession frequency is then given by:

$$\hat{\omega}_0 = \omega_0(1 - \delta) = \gamma \cdot B_0(1 - \delta). \tag{2.3}$$

The parameter δ, which is also referred to as the chemical shift, is a shielding constant. Usually, it is within the range of several parts per million (ppm). In NMR spectroscopy, the frequency spectrum is used to gain insights into the chemical composition and structure of a sample.

The bulk magnetization of a collective spin system can be expressed as the sum of the individual microscopic magnetic moments:

$$\vec{M} = \sum_{n=1}^{N_\mathrm{s}} \vec{\mu}_n. \tag{2.4}$$

In this context, N_s represents the total number of spins within the object, while $\vec{\mu}_n$ denotes the magnetic moment of the n-th nuclear spin. For spin-$\frac{1}{2}$ systems such as ^{1}H, ^{13}C, ^{19}F, ^{31}P, the spins are oriented either parallel (spin up) or anti-parallel (spin down) with respect to B_0. This results in two distinct energy levels. This effect is called Zeeman splitting. The difference in energy between the two states can be expressed as

$$\Delta E = E_\uparrow - E_\downarrow = \gamma\hbar B_0 \quad \text{with} \quad \hbar = \frac{h}{2\pi}. \tag{2.5}$$

$E_\uparrow$ and $E_\downarrow$ designate the energy levels associated with the spin up and spin down states, while h is the Planck's constant.

In the thermodynamic equilibrium state, the Boltzmann distribution determines the distribution of spins into the two energy levels:

$$\frac{N_\uparrow}{N_\downarrow} = \exp\left(\frac{\Delta E}{k_\mathrm{B} T}\right) = \exp\left(\frac{\gamma\hbar B_0}{k_\mathrm{B} T}\right). \tag{2.6}$$

$N_\downarrow$ and $N_\uparrow$ express the population of the two spin states. $k_\mathrm{B} = 1.38 \cdot 10^{-23}\,\mathrm{J/K}$ is the Boltzmann constant and T corresponds to the temperature of the spin system. The population discrepancy between these states is typically very small. For instance, in a magnetic field of $B_0 = 7\,\mathrm{T}$ and at room temperature, the population difference can be estimated to be on the order of 0.005 %.

2.2 Bloch equation

Classically, the macroscopic magnetization $\vec{M}$ is parallel to the static magnetic field B_0 precessing around the applied field at the Larmor frequency. The transverse magnetization is zero at equilibrium. To measure magnetization, the sample is excited by an oscillating radio-frequency (RF) field B_1 perpendicular to B_0 and resonate at the Larmor frequency.

The time evolution of the macroscopic magnetization vector is described by the Bloch equation [1]:

$$\frac{\mathrm{d}\vec{M}}{\mathrm{d}t} = \gamma\left(\vec{M} \times \vec{B}\right) + \frac{M_\mathrm{x}\vec{e}_\mathrm{x} + M_\mathrm{y}\vec{e}_\mathrm{y}}{T_2} - \frac{(M_\mathrm{z} - M_0)\vec{e}_\mathrm{z}}{T_1}. \tag{2.7}$$

Here, M_0 denotes the equilibrium magnetization and $\vec{B} = \vec{B}_0 + \vec{B}_1(t)$ is the effective magnetic field . T_1 and T_2 are the tissue dependent time constants of longitudinal and transverse relaxation, respectively.

Induced by spin-lattice interactions, the longitudinal relaxation describes the slow return of the longitudinal magnetization M_z to thermal equilibrium. The transverse relaxation denotes the decay of the transverse magnetization M_{xy} caused by spin-spin interactions leading to the loss of phase coherence. In addition, static and time-independent field inhomogeneities can lead to further dephasing of the spins. The effective transverse relaxation time T_2^* is therefore defined as:

$$\frac{1}{T_2^*} = \frac{1}{T_2} + \frac{1}{T_2'}, \tag{2.8}$$

where T_2' denotes the static relaxation due to the field inhomogeneities.

The excitation angle for tilting the magnetization from equilibrium to the transverse plane is given by:

$$\alpha = \int_0^\tau \omega_1(t)\mathrm{d}t = \int_0^\tau \gamma B_1(t)\mathrm{d}t, \tag{2.9}$$

where τ is the duration and B_1 is the amplitude of the applied RF-pulse. The resulting signal, which can be quantified, is referred to as the free induction decay (FID).

The phenomena of NMR are usually described in a rotating frame of reference

$$(x' = x \cdot \cos(\omega_{\mathrm{RF}} \cdot t), y' = y \cdot \sin(\omega_{\mathrm{RF}} \cdot t), z' = z). \tag{2.10}$$

In the case of on-resonant excitation, the reference frame is rotating at the Larmor frequency $\omega_{\mathrm{RF}} = \omega_0$ with the result that B_1 and B_0 are static and $\vec{B}_1$ is aligned in x' direction. Moreover, the magnetization is typically divided into the longitudinal component, parallel to B_0, and the transverse component, which is usually expressed as a complex quantity:

$$M_{xy} = M_x + iM_y. \tag{2.11}$$

In the event of off-resonant excitation, the effective field is given by:

$$\vec{B}_{\mathrm{eff}} = \begin{pmatrix} B_1 \\ 0 \\ B_0 - \omega_{\mathrm{RF}}/\gamma \end{pmatrix}. \tag{2.12}$$

The magnetization precesses around the B_{eff} at the specific frequency $\omega_{\mathrm{eff}} = \sqrt{\omega_1^2 - \Delta\omega^2}$, where the frequency difference $\Delta\omega$ is defined as $\Delta\omega = \omega_0 - \omega_{\mathrm{RF}}$. The effective field is tilted away from the z-axis by the angle

$$\theta = \arctan\left(\frac{\omega_1}{\Delta\omega}\right). \tag{2.13}$$

2.3 MR imaging

As described so far, the NMR signal includes information from the entire measurement sample. To enable the spatial encoding of three-dimensional objects, magnetic field gradients need to be applied. MRI scanners provide three orthogonal coil gradients in x-, y-, and z-direction, whose shapes can be set independently of each other. The timing of RF pulses and gradients is referred to as sequence. It allows great flexibility to optimize the overall measurement time and produce a variety of image contrasts.

2.3.1 Spatial encoding

First proposed in 1973 [3], spatial encoding is realized by superimposing the static magnetic field with spatially varying magnetic field gradients. These field changes cause each spin to precess at a different frequency, depending on its position, according to Equation 2.2. In the most commonly used case of linear gradients, the Larmor frequency is subsequently defined as:

$$\omega(\vec{r}) = \gamma(B_0 + \vec{G}(\vec{r}) \cdot \vec{r}) = \omega_0 + \gamma\vec{G}(\vec{r}) \cdot \vec{r}, \tag{2.14}$$

where $\vec{r}$ denotes the spin position.

Slice selection

By applying a linear gradient $\vec{G} = G_S\vec{z}$ during the excitation period, for instance in z-direction, the frequency selective RF pulse will only excite spins within its bandwidth. The central frequency of the RF pulse determines the position of the selected slice, while the slice thickness is given by:

$$\Delta z = \frac{2\pi\Delta f}{\gamma G_S}, \tag{2.15}$$

depending on the pulse bandwidth Δf and the gradient amplitude G_S.

Frequency encoding

The frequency dependence of the spins is used during the acquisition of the signal for one dimensional encoding. The application of a linear gradient during the signal readout results in the measured MR signal containing a spectrum of frequencies that correspond to the spin position along the readout gradient G_{RO}. For a correct reconstruction of the spin position, it is required that the Nyquist sampling theorem is fulfilled:

$$f_s = \frac{1}{\Delta t} \geq 2f_{max}, \tag{2.16}$$

where f_s is the Nyquist frequency, Δt is the sampling interval and f_{max} denotes the largest frequency of the sample.

Phase encoding

A second dimension can be encoded by the use of a third gradient field for a brief period of time T_{PE} between excitation and signal acquisition. The spins precess with different frequencies depending on their position, while the gradient field is active. As soon as the gradient field is switched off, the spins precess with ω_0 again, but an initial phase angle is induced:

$$\Phi(\vec{r}) = -\gamma T_{\mathrm{PE}} \vec{G}_{\mathrm{PE}} \cdot \vec{r}, \tag{2.17}$$

where G_{PE} is the amplitude of the phase encoding gradient. In contrast to frequency encoding, a single phase shift can be achieved per acquisition. In order to achieve the complete information about the second dimension, the experiment must be repeated with varying phase modulations, leading to the long scan times associated with MR imaging.

Two-dimensional phase encoding

Compared MR experiments with slice-selective excitation, the entire volume can be excited for two-dimensional phase encoding. The third dimension is then encoded by an additional phase encoding (PE) loop of varying phase modulations along the z-direction.

2.3.2 Signal equation and k-space formalism

The MR signal of the entire sample can be expressed as the integral over the transverse magnetization $M_{\mathrm{xy}}(\vec{r})$:

$$s(t) = \int\limits_{\text{volume}} M_{\mathrm{xy}}(\vec{r}) \cdot \mathrm{e}^{-t/T_2^*} \cdot \mathrm{e}^{-i\omega_0 t} \mathrm{d}^3\vec{r}, \tag{2.18}$$

where e^{-t/T_2^*} is the spin-spin relaxation term, which is typically neglected, and $\mathrm{e}^{-i\omega_0 t}$ describes the precession of the spins, what is omitted when using the rotating frame formalism. Considering these aspects and by applying gradient fields to spatially encode the MR signal, the signal equation changes to:

$$s(\vec{k}) = \int\limits_{\text{volume}} M_{\mathrm{xy}}(\vec{r}) \cdot \mathrm{e}^{-i2\pi\vec{k}\cdot\vec{r}} \mathrm{d}^3\vec{r} \propto \mathcal{FT}\left[M_{\mathrm{x,y}}(\vec{r})\right]. \tag{2.19}$$

$\vec{r}$ is the position vector in image space and $\vec{k}$ is the spatial frequency variable, the so-called k-space vector, defined as:

$$\vec{k} = \frac{\gamma}{2\pi} \int_0^t \vec{G}(\tau) d\tau. \tag{2.20}$$

The relationship between the received signal $s(\vec{k})$ and the Fourier transform of the transverse magnetization is demonstrated in the signal equation 2.19. Hence, the spatial distribution of spin density, visualized as MR image, can be obtained by the inverse Fourier transform of the acquired signal.

Only discrete points in k-space are sampled, since $s(\vec{k})$ cannot be sampled at an infinite number of points. The spacing Δk between these points determines the field of view (FOV) according to the Nyquist criterion:

$$FOV_{\mathrm{i}} = \frac{1}{\Delta k_{\mathrm{i}}}; \quad i \in \{x, y, z\}. \tag{2.21}$$

The spatial resolution of the MR image, which is given by the size of the FOV and the number of pixels N corresponds to the highest sampled spatial frequency $k^{\max}$ and is given by:

$$\Delta i = \frac{FOV_\mathrm{i}}{N_\mathrm{i}} = \frac{1}{2k_\mathrm{i}^{\max}}\,; \quad i \in \{x, y, z\}. \tag{2.22}$$

Once all the requisite spatial frequencies have been acquired, the k-space data can be utilized to reconstruct an image of the object. The k-space property of Hermitian symmetry

$$s(-k) = s^*(k) \tag{2.23}$$

allows for partial sampling of the k-space, resulting in a reduction of the total scan time. The omitted information can then be reconstructed according to equation 2.23, conventionally called partial Fourier. Theoretically, only half of the k-space needs to be acquired, but due to phase errors, e. g. from B_0 inhomogeneity or susceptibility effects, usually only up to 25% of the frequencies are skipped.

2.3.3 Fundamental MRI pulse sequence

There is a large number of sequences, most of which fall into two categories: Gradient echo (GRE) sequences and spin echo (SE) sequences. A third category of echoes, stimulated echoes (STE), that occur if three RF pulses are applied in relatively rapid succession, are rarely used for imaging. The sequence used in this work is based on a GRE, so the principle is explained below. An overview of the variety of possible MR sequences can be found in [45].

Figure 2.1 depicts a schematic sequence diagram representing the shortest possible timing of a 2D GRE sequence. The magnetization of a slice, selected by the slice selection gradient G_S, is excited by the flip angle (FA), which is typically very small. A rewinder gradient nulls the accumulated phase induced by the slice selection gradient. To spatially encode the transverse magnetization, a

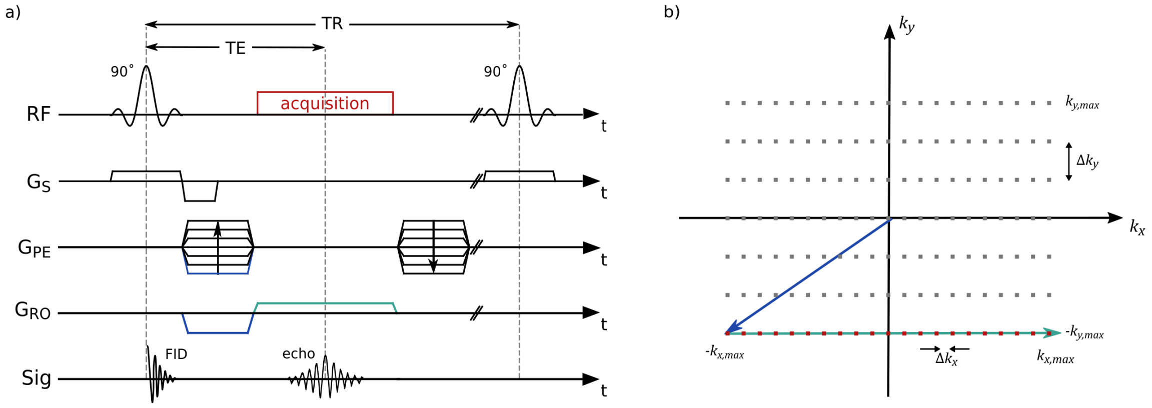

Figure 2.1: a) Schematic sequence diagram of a basic 2D GRE sequence, including slice selection as well as phase and frequency encoding gradients. The acquisition takes place in time with the readout gradient.
b) k-space trajectory associated with one phase encoding step. While phase encoding gradient and read dephasing gradient are employed to facilitate the movement of the k-space vector to the beginning of a k-space line, the readout gradient is responsible for the trajectory being moved through the current k-space line during the signal acquisition process.

phase encoding gradient G_{PE} and a readout gradient G_{RO} are played out successively after excitation, whereby slice rewinder, phase gradient and readout prephaser can be applied simultaneously. With the help of the prephasing gradient, the magnetization will be refocused in the middle of the acquisition period and a so-called gradient echo can be measured. The time of the echo is called echo time (*TE*). During the readout, one line in k-space is acquired. To fully sample the k-space, the depicted sequence has to be repeated with varying phase encoding gradient. The time interval between subsequent excitations is called repetition time (*TR*). To reduce image artifacts, the phase encoding gradient is rewound after readout. Typically, strong spoiler gradients are used at the end of *TR* to destroy the remaining transversal magnetization (not depicted in Figure 2.1) .

2.3.4 Signal-to-noise ratio

Because of the low sensitivity of NMR experiments, the signal of a voxel can be strongly affected from noise, mainly from random thermal noise. An important parameter to evaluate the image quality is the signal-to-noise ratio (SNR), which is given by the fraction of the mean signal intensity within a region of interest (ROI) and the standard deviation of the background ROI signal:

$$\mathrm{SNR} = \frac{\text{mean signal}}{\text{standard deviation of background noise}}. \tag{2.24}$$

The choice of sequence parameters directly influences the SNR of the MR image, for instance the SNR in a voxel is proportional to its volume. A common method to improve the SNR is signal averaging, whereby the SNR is proportional to the square root of the number of repetitions.

2.3.5 Specific absorption rate

Furthermore, an important point, especially in human imaging, is that the applied RF power is deposited as heat in the MR sample during excitation. In order to guarantee the protection of the subject, strict limits are set for the specific absorption rate (SAR) of RF power by the body. The guide value is here that the heating of the body should not exceed 1° C per hour. Next to tissue conductivity and body size, the amount of SAR per measurement is also proportional B_0^2, B_1^2 and the duty cycle (DC) of a sequence. SAR estimation is integrated in the scanner software by default and needs to be considered in the pulse sequence design and the choice of measurement parameters.

2.3.6 Parallel imaging

The main disadvantage of MRI is the long measurement time, so image acceleration is an important part of sequence development. The use of a receive coil array instead of a single coil allows the reduction of the number of phase encoding steps by replacing parts of the k-space data with additional RF coil data. Thus, the k-space can be subsampled by measuring only every R-th k-space line, reducing the number of phase encoding steps by factor R (the so-called acceleration factor). For 3D imaging, it is then possible to accelerate in both phase encoding directions.

According to Equation 2.21, increasing Δk by R leads to a decrease of the FOV. In case the imaged object is larger than the FOV, this leads to fold-in/aliasing artifacts due to the violated Nyquist theorem. Therefore, advanced reconstruction algorithms were developed, which can be divided in image based and k-space based correction methods. For a good overview, the reader is referred to [46].

For this work, only the k-space based method GRAPPA (GeneRalized Autocalibrating Partially Parallel Acquisitions) [47] was used. While each R-th k-space line is omitted when acquiring the k-space data, a fully-sampled region in the k-space center of all coils, the so-called autocalibration signal (ACS), serves as base for reconstructing the missing information. The ACS data can be achieved either by integrating a fully sampled k-space center within the accelerated measurement or by using a separate calibration scan. Based on the ACS, weighting factors are determined, which fit one k-space line of an individual coil by means of a combination of the recorded neighboring k-space lines from multiple coils. A sliding block reconstruction enables the 3D kernel to traverse the k-space, multiplying the kernel source points by the weights to ascertain the missing target points. After the k-space data has been fully reconstructed, the data of the individual coils is transferred to the image space via Fourier transformation. At last, the individual coil images are combined to the final magnitude image, e.g. using the sum of squares algorithm.

Combined with GRAPPA, a method called the controlled aliasing in parallel imaging results in higher acceleration (CAIPIRINHA, short: CAIPIRINHA) [48] can be used to acquire and reconstruct k-space data across multiple lines instead of skipping whole k-space lines. This is realized by shifting every n-th k-space point to the neighboring line.

2.3.7 Parallel transmit

Especially for high and ultra-high field (> 7 T) experiments, the homogeneity of both the transmit and the receive RF field (B_1^+ and B_1^-) is hampered by wave propagation effects, since the electromagnetic wavelength in tissue is similar to that of the imaging object, e.g. $\lambda = 13\,\mathrm{cm}$ at 7 T (300 MHz) [49–51]. The subject dependent inhomogeneity of the transmit field, B_1^+, impairs image signal and contrast due to varying flip angles, what is particularly problematic for quantitative imaging methods. One way to counteract the non-uniformity of the B_1^+ field is to use a coil-array with multiple channels for parallel transmission (pTx) [52] instead of a single transmit (sTx) coil. While the principle of parallel transmission is only briefly explained below, a more detailed overview can be found in the reviews of Katscher [53], Padormo [51] and Webb [50].

The main advantage of transmit coil arrays is the individual control of magnitude and phase of the current channels to create spatially varying RF field patterns. The net B_1^+ field is then derived by the superposition of the fields from the distinct channels, $B_{1,i}(\vec{r},t)$ [51]:

$$B_1^+(\vec{r},t) = \sum_{i=1}^{N_T} B_{1,i}^+(\vec{r},t) \quad \text{with} \quad B_{1,i}^+(\vec{r},t) = p_i(t) S_i(\vec{r}). \tag{2.25}$$

Here, N_T is the number of transmit channels and the $B_{1,i}^+$ field can be divided into the time dependent RF pulse $p_i(t)$ and the spatial component $S_i(\vec{r})$ corresponding to the transmit sensitivity of the i-th coil. All pTx methods require prior knowledge of $S_i(\vec{r})$, which is usually gained through B_1 mapping (see following Section 2.5.2).

The most basic form of parallel transmit is called B_1-shimming. Here, each coil transmits a RF pulse of the same waveform, $p(t)$, scaled with a coil-specific complex weight, w_i:

$$B_1^+(\vec{r},t) = p(t) \sum_{i=1}^{N_T} w_i S_i(\vec{r}). \tag{2.26}$$

Typically, the best weights to fulfill the B_1 target goal are determined by iterative minimization of a cost function, including the homogeneity of the B_1^+ distribution within a defined ROI as well as SAR restrictions and hardware limits.

While static B_1 shimming is limited by the number of transmit channels, the individual modulation of the RF pulses for each coil element could significantly improve the homogeneity of the B_1^+ field. Dynamic RF shimming addresses the flip angle target distribution using channel-specific tailored RF pulses. While the different RF waveforms are played out on each channel, gradient pulses G are used to cover a predetermined trajectory in excitation k-space. Assuming the small tip angle (STA) approximation, the excitation pattern of the coil array in the spatial domain is given by a superposition of the Fourier integral of the excitation k-space trajectory, spatially weighted by the complex transmit sensitivity $S_r(x)$ [54, 55]:

$$m(x) = i\gamma \sum_{r=1}^{R} S_r(x) \int B_{1,r}(t) \mathrm{e}^{ix\vec{k}(t)} \mathrm{d}t \quad \text{with} \quad \vec{k}(t) = -\gamma \int_t^T G(\tau) \mathrm{d}\tau, \tag{2.27}$$

where R is the number of transmit channels and T is the duration of the excitation pulse. The large number of excitation k-space trajectories developed in recent years can be roughly divided into two categories: while e.g. 'spokes' [56] belong to the slice-selective excitation trajectories, 'k_T-points' [57] allow the excitation of non-selective patterns. Like the weights in static B_1 shimming, the optimal excitation k-space trajectory can be determined by iteratively solving the minimization problem.

2.4 Echo planar imaging

Another option to speed up the acquisition time is to collect multiple gradient echos and therefore multiple k-space lines after a single excitation. The sequence, which contains a readout train after a single excitation, is called Echo Planar Imaging (EPI).

2.4.1 2D imaging

The idea to acquire all spatial frequencies necessary to reconstruct a 2D image following a single excitation pulse was already published in 1977 from Sir Peter Mansfield [58]. The original form of the GRE single-shot EPI, contains a oscillating readout gradient and a simultaneously applied constant small phase encoding gradient, leading to a "zig-zag" trajectory in k-space. The replacement of the constant phase encoding gradient by short blips between two differently poled readout gradients [59] was the biggest change from the original idea to today's typical implementation. A schematic sequence diagram of a typical 2D EPI and it's related k-space trajectory is shown in Figure 2.2.

The slice selective excitation is followed by pre-dephasing gradients in phase and readout direction (k_y and k_x, respectively) with the objective of moving the k-space vector to the outer corner of the

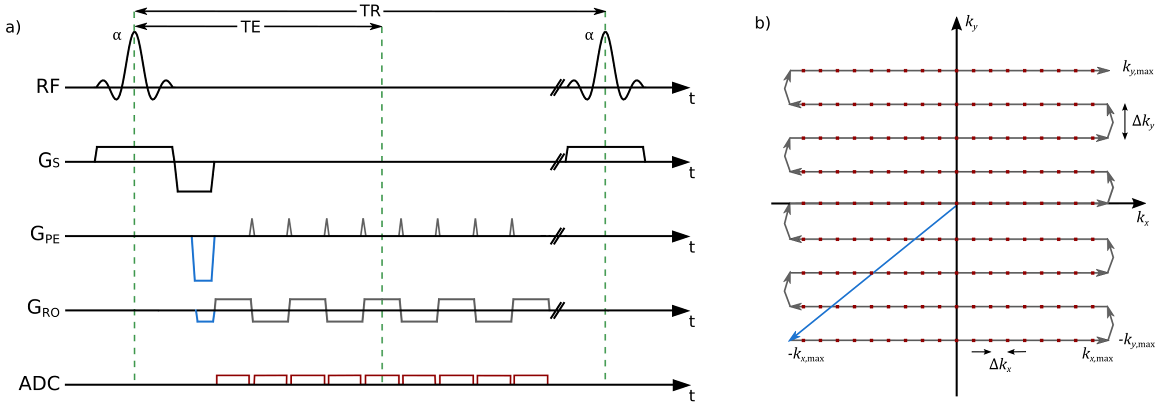

Figure 2.2: Schematic sequence diagram of a basic 2D EPI sequence (a) and the associated k-space trajectory (b). Readout gradients and phase encoding blips are played out alternately. The phase encoding blips correspond to the shift of the k-space trajectory in the k_y direction while data is acquired during the read gradient in k_x direction (indicated by the red dots).

k-space. The acquisition of the signal occurs during the flat top time of the readout gradients while no phase gradient is active (depicted by small dots on the trajectory). The phase encoding blips provide the stepwise increasing along the k_y axis. Since the echos are sampled with alternating gradients, every second k-space line has to be flipped to fill the data matrix in the correct order. The number of acquired k-space lines is called the EPI factor. However, it is common practice to collect data also during ramp times, which necessitates regridding of these data.

In EPI each k-space line is acquired at different echo times resulting in a variant T_2^* weighting along the PE direction which can be observed as T_2^* blurring in the images. The amplitude of the corresponding gradient echo decay is given by:

$$S(n) = S_0 \exp\left(-TE(n)/T_2^*\right), \tag{2.28}$$

where S_0 is the signal at $t = 0$ and n is the index of the echo within the echo train. Since the image contrast is mainly determined by the echo time of the central k-space lines, the effective echo time is defined as $TE_{\text{eff}} = TE(k_y = 0)$. To counteract strong signal decay at very long readout trains, parallel imaging in phase encoding direction is typically used. Another way to shorten the echo train length (ETL), especially in high resolution imaging, is to split the acquisition of the k-space data into several excitations. The segmentation scheme of the k-space data can vary between block wise acquisition of k-space lines, possibly with small overlap or enlarged Δk_y and interleaved k-space filling. The segmentation factor N_{shot} is then the number of excitations needed to acquire all phase encoding steps. In the case of interleaved segmentation, the bandwidth in phase encoding direction is defined as:

$$\Delta\nu_{\text{PE}} = \frac{N_{\text{shot}}}{t_{\text{esp}}}, \tag{2.29}$$

where $N_{\text{shot}} = 1$ in the case of single shot EPI and t_{esp} is the echo spacing, which represents the time between the k_y sample points at $k_x = 0$.

2.4.2 3D-EPI

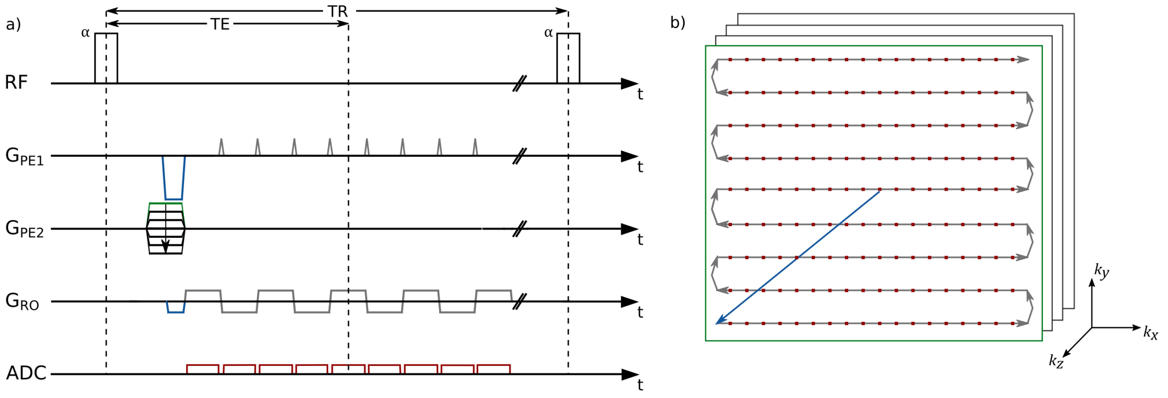

Figure 2.3: Schematic sequence diagram of a 3D-EPI sequence (a) and the corresponding schematic illustration of the three dimensional k-space (b). After the non-selective excitation pulse, the k-partition is determined by the varying second phase encoding gradient, which is filled using the typical EPI pattern. The zig-zag trajectory in k-space is obtained partition by partition through alternating phase-encoding blips and readout gradients.

One method to obtain a 3D volume is to stepwise acquire imaging slices by repeating the sequence with different slice selection gradients. Another way is the acquisition of a 3D k-space and then reconstruct the image using a 3D Fourier Transform (see Chapter 2.3.1).

Echo volume imaging (EVI) [60, 61], which implies the acquisition of the complete 3D k-space after a single excitation, is rarely used due to its very low spatial resolution. More prominent are hybrid 3D-EPI sequences which requires several excitations to fill the k-space.

A schematic sequence diagram of a 3D-EPI sequence is depicted in Figure 2.3. The volume of interest is non-selectively excited multiple times and then the varying second phase encoding (PE_2) gradient is applied to define the k_z-increment. Afterwards, the typical zig-zag k-space trajectory is obtained with first phase encoding (PE_1) blips and alternating readout gradients in turns to fill a 2D plane in k-space, a so-called partition.

The non-selective excitation significantly shortens the time between two successive excitations of the same tissue which leads to reduced steady state magnetization [35]:

$$M = \frac{M_0 \sin\alpha \left(1 - \exp\left(\frac{-TR_{\text{slice}}}{T_1}\right)\right)}{1 - \cos\alpha \cdot \exp\left(\frac{-TR_{\text{slice}}}{T_1}\right)}, \tag{2.30}$$

which is maximized with the Ernst angle defined by :

$$\alpha_{\text{E}} = \arccos\left(\exp\left(-\frac{TR}{T_1}\right)\right). \tag{2.31}$$

In contrast to the reduced steady state magnetization, 3D excitation brings the benefit that the signal of N_{slices} more data points contribute to each data point of the 3D Fourier transformation, resulting in a SNR advantage of $\sqrt{N_{\text{slices}}}$. Another profit of 3D sequences is the possibility to accelerate not only in one but in two phase encoding directions by means of parallel imaging. In addition, image artifacts caused by parallel imaging are also reduced when using 3D-EPI. Since the GRAPPA coil weights, needed for the reconstruction algorithm, have to be calculated only once for the entire volume, slice dependence, which is mainly determined by SNR differences between slices, can be prevented. Beside the gain in acquisition time, the usage of a second phase encoding direction avoids slice selection artifacts due to an imperfect slice profile. In addition, high-resolution measurements are less limited by the gradient amplitude boundaries, which are necessary to avoid nerve stimulations.

2.4.3 Challenges

Echo planar imaging provides an excellent opportunity to acquire a large ROI in a very short time. However, EPI acquisitions also have to deal with some challenges.

N/2 ghosting

A prominent artifact in EPI is Nyquist ghosting originating from phase differences between even and odd lines. The artifact appears as a weak duplicate of the image shifted by half the FOV in phase encoding direction, why it is also called N/2 ghosting. The signal amplitude of the ghost image is modulated by a sinusoidal profile in readout direction and reduces the image intensity of the object.

An overview of phase correction (PC) methods can be found in [62]. Within the scope of this work, a widely used calibration method is utilized, which leads to a reasonable reduction of the N/2 ghost. To correct the spatially constant phase difference in the EPI acquisition, a short echo train of three alternating readout gradients without phase encoding is measured directly after excitation. The complex phase of the second echo is then compared to the averaged phase of the first and the third echo. A linear approximation of the phase is then used for correction.

Susceptibility-induced artifacts

Typically, the objects to be imaged contain adjacent regions of different tissues. Since different tissue types have different magnetic properties, this leads to small susceptibility-induced gradients. These local gradients overlay with the static magnetic field B_0 and influences the precession frequency of the spins which may disrupt the spatial encoding. In case of EPI, the phase encoding bandwidth is typically very small and the susceptibility-induced field inhomogeneities lead to misplaced image intensity which becomes noticeable as geometric distortions in the reconstructed image. A reduction of the echo train length, e.g. by using segmentation, counteracts the distortions. Moreover, the susceptibility-induced field inhomogeneities lead especially in GRE EPI to enhanced spin dephasing during the echo train. This leads to a strong decrease of T_2^* relaxation time, which may cause significant signal dropouts due to the long echo time in EPI.

Chemical shift artifact

In consequence of the low phase encoding bandwidth, EPI has also to deal with chemical shift artifacts. The distinct electrical shielding of different molecules leads to variations of the resonance frequency and thus, to a spatial misregistration of these signal. The spatial shift depends on the chemical shift Δf_{cs} (in Hz), the phase encoding bandwidth $\Delta \nu_{PE}$ and the FOV in the phase encoding direction (here,

$\mathrm{FOV_y}$):

$$\Delta y_{\mathrm{cs}} = \frac{\Delta f_{\mathrm{cs}}}{\Delta \nu_{\mathrm{PE}}} \mathrm{FOV}_y. \tag{2.32}$$

As a prominent example, the chemical shift of lipids (on average at -3.5 ppm relative to free water) can lead to substantial artifacts due to the low phase encoding bandwidth in the order of 1 kHz. Therefore, almost all EPI sequences use lipid suppression methods.

2.5 Field mapping

Magnetic resonance imaging systems are designed to provide magnetic fields as homogeneously as technically possible. In reality, a variety of factors interfere with the homogeneity of the magnetic fields. However, advanced MR imaging methods rely on homogeneity from both the static magnetic field B_0 and the radio-frequency field B_1. Accurate field mapping is a crucial step to correctly interpret MR images and reducing errors that may occur due to the field inhomogeneities.

2.5.1 B_0 mapping

The introduction of the object to be imaged, e.g. the human body, into the MRI bore causes deviations from the static magnetic field due to local susceptibility differences. The inhomogeneity of B_0 can be specified as superposition of spherical harmonics. To counteract those inhomogeneities, dedicated shim coils are used to generate a specific field based on a measured B_0 map. In addition, the B_0 maps are also used in some MRI data processing pipeline to correct for remaining field inhomogeneities.

B_0 mapping is based on the dependence of the spin phase to the local field shift $\Delta B_0(\vec{x})$ and the time while the spins are precessing in the M_{xy}-plane. A common method to calculate the B_0 field map is to use a double-echo gradient echo sequence with distinct echo times [63, 64]. Using the phase map Φ from each image, the local field shift can be determined by:

$$\Delta B_0(\vec{x}) = \frac{\Delta\Phi\left(\vec{x}\right)}{2\pi\gamma\Delta TE} = \frac{\Phi_{TE_2}\left(\vec{x}\right) - \Phi_{TE_1}\left(\vec{x}\right)}{2\pi\gamma\left(TE_2 - TE_1\right)}. \tag{2.33}$$

Since the dynamic range of the phase maps is given by 1/TE, additive 2π components can occur in regions with strong inhomogeneities. These phase wraps can be solved by unwrapping techniques. More detailed information about the method used in this work can be found in [65].

2.5.2 B_1 mapping

Knowledge of the actual B_1-field is an indispensable prerequisite for a variety of approaches, especially for quantitative methods or pTx applications, in order to counteract the effects resulting from the B_1-field inhomogeneity and also for retrospective correction methods. A multitude of methods for rapid and robust B_1 mapping have been developed. However, in the scope of this work, a method called 3DREAM [66] was used and is briefly explained below.

The 3DREAM sequence is based on the 2D method dual refocusing echo acquisition mode (DREAM) [67], which combines a stimulated echo preparation with a single-shot low-angle gradient-echo readout. By quasi-simultaneous refocusing of the stimulated echo and the free induction decay, the signal ratio of the gradient-recalled echoes yields an expression of the actual flip angle of the preparation pulse:

$$\alpha = \arctan \sqrt{\frac{2S_0^{\mathrm{STE}}}{S_0^{\mathrm{FID}}}} \tag{2.34}$$

because the signals of the STE and the FID are given by

$$S_0^{\mathrm{STE}} = \frac{1}{2} \sin\beta \sin^2\alpha \cdot M_0 \tag{2.35}$$

and

$$S_0^{\mathrm{FID}} = \frac{1}{2} \sin\beta \cos^2\alpha \cdot M_0. \tag{2.36}$$

β is the first imaging angle and M_0 the magnetization at $t = 0$. In case of on-resonant STE preparation with a block RF pulse, the spatial distribution of the transmit field can be calculated as:

$$B_1 = \frac{\alpha}{\gamma\tau}, \tag{2.37}$$

where τ is the duration of the STE preparation pulse.

The 3D version 3DREAM [66] uses short non-selective STE preparation and imaging pulses. In contrast to the original method [67], the readout module is based on a 2D spiral center-out phase encoding order, which enables early acquisition of the desired image contrast. The prolonged readout train of the 3D acquisition comes together with a signal evolution of S^{STE} and S^{FID}, leading to image blurring. A blurring kernel, which can be estimated from the experiment itself, can be used to account for the different blurring in STE and FID images. Since a deconvolution of the STE image increases the noise level, the FID image is filtered to match the blurring of the STE image.

By enlarging the echo time difference between STE and FID image, the 3DREAM sequence can also be used to acquire a B_0 map additionally to the flip angle map.

CHAPTER 3

Chemical exchange saturation transfer imaging

The MR signal contains information not only about the local distribution of water protons in the body but also about magnetic, chemical and physical interactions. Effects such as diffusion, flow or the exchange of protons change the relaxation properties of the water protons, which in turn affects the MR signal. During all these interactions, also magnetization can be transferred, which further complicates the interpretation of MR images. Yet, it offers new opportunities to study the tissue physiology. Over the last decades, many new contrast mechanism were developed and established besides conventional MRI methods.

This chapter provides an overview of chemical exchange saturation transfer imaging (CEST) and explains the underlying theory as well as substantial aspects for practical application. The reader is referred to a number of excellent reviews [68–73], summarizing the CEST literature and additionally to two dissertations for further insight in quantitative CEST MRI [74, 75].

3.1 Magnetization transfer processes

The contrast of MR images is almost exclusively generated by the contribution of mobile water protons, which, however, interact with the bound protons in their vicinity. These interactions can lead to a transfer of magnetization between the so-called proton pools and influence the measured MR signal. A proton pool is a magnetic environment, which is defined by its identical physical properties, e.g. same chemical shift δ_i, equal relaxation properties and an uniform exchange rate k_{ij} to other pools. In the case of in-vivo imaging, the water pool w is the main pool, while the solute pools s are less common.

The transfer of magnetization between spin systems is based on various processes such as the exchange of protons or dipolar coupling effects. These effects are always mixed and cannot be considered separately. Three different processes, chemical exchange, nuclear Overhauser effect (NOE) and semisolid magnetization transfer (ssMT), play a special role for CEST imaging and will be briefly explained in the following.

3.1.1 Chemical exchange

In general, chemical exchange (CE) refers to chemical or conformational kinetic processes in which nuclear spins are stochastically transferred between proton pools [76]. Although the protons are physically exchanged, they do not change their quantum state, leading to a transfer of properties between the pools.

The exchange rate k depends on the type of exchange as well as on the environment. The hydrogen exchange rates of interest for MRI studies can be described in aqueous solution as follows [68]:

$$\begin{aligned} k_{sw} &= k_a[\mathrm{H}^+] + k_b[\mathrm{OH}^-] + k_0 \\ &= k_a \cdot 10^{-\mathrm{pH}} + k_b \cdot 10^{\mathrm{pH}-\mathrm{p}K_w} + k_0 \end{aligned} \tag{3.1}$$

in which k_a, k_b and k_0 designate the rate constants for acid based exchange, base catalyses exchange and other possible contributions, respectively. pK_w is the temperature dependent dissociation constant of water. The temperature dependency of the rate constant is given by the Arrhenius Equation [77, 78]:

$$k_{rc}(T) = k_{rc}(298.15K) \cdot \exp\left(-\frac{E_a}{R}\left(\frac{1}{T} - \frac{1}{298.15K}\right)\right), \tag{3.2}$$

E_a refers to the activation energy, and R represents the universal gas constant, which has a value of $8.314\,\mathrm{J\,mol^{-1}\,K^{-1}}$.

3.1.2 Nuclear Overhauser effect

Besides proton exchange, magnetization can also be transferred if neighboring spins have sufficient through-space dipolar coupling [72, 73]. Compared to normal MR conditions, as explained in Chapter 2.2, the spins no longer relax only with T_1 but also with a much faster cross-relaxation rate. The dipolar coupling depends on the distance between spins, gyromagnetic ratios and their relative orientation.

In a two-spin system, in which the spins w and s are dipolar coupled, the stationary spin states will be a linear combination of the spin functions representing the uncoupled spins [79]. The proton spins of $I = \frac{1}{2}$ can couple to four distinct spin states of a coupled system, depicted in Figure 3.1. The transition probability W is dependent on both the correlation time c and the distance r. The correlation time is the time period over which a molecule rotates about a specified axis, typically arbitrary. In cross relaxation pathways, magnetization is transferred due to zero- W_0 and double-quantum transitions W_2.

The transfer of magnetization between two spin pools via cross-relaxation pathways due to dipolar-coupling is called the nuclear Overhauser effect [80]. With sufficiently slow molecular motion, NOEs can be passed through the backbone of macromolecules and large proteins due to the high proton density, which is then referred to as spin diffusion.

Exchange-relayed NOE

With respect to CEST imaging, the indirect exchange of magnetization between macromolecules and water is of particular interest. Via spin diffusion, the magnetization can be transferred to the exchangeable protons within the macromolecule and subsequently transferred to water via chemical exchange [73]. This indirect process is designated as exchange-relayed NOE (rNOE). It is a more

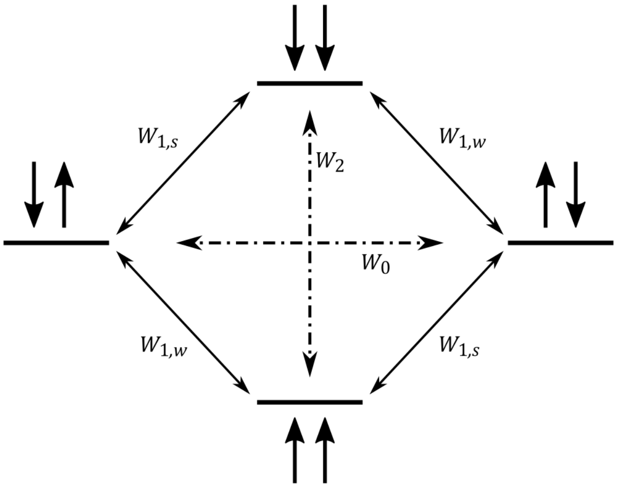

Figure 3.1: Energy levels of a dipolar coupled two-spin system and the transition probability W between the spin states in a static magnetic field. The magnetization is transferred via the relaxation paths W_0 and W_2.

efficacious process than direct dipolar coupling, and thus, it represents the dominant pathway for dipolar-based magnetization exchange between macromolecules and water [69].

3.1.3 Semisolid macromolecular magnetization transfer

The magnetization transfer (MT) between free water and large macromolecules with very short T_2 relaxation e.g. cell membranes or the cytoskeleton, is called the semi-solid MT [81]. The protons of macromolecules are strongly coupled to each other resulting in a homogeneously broadened lineshape in the NMR spectrum. A special feature here is that both pools have approximately the identical central resonance frequency.

In addition to the mobile bulk water, the free pool also contains water protons that bind to the macromolecular surface for a short time. This surface layer interacts with the protons bound in the macromolecules due to cross-relaxation, while the magnetization is transferred between the surface layer and free water by diffusion. Exchange-relayed NOEs also contribute to the ssMT in addition to this intermolecular NOE. [69]. The imaging contrast, which is based on the semi-solid magnetization transfer, is referred to as MTC [81, 82].

3.2 Principles of the CEST mechanism

Chemical exchange saturation transfer (CEST) is a technique for studying proton groups at different resonance frequencies that transfer magnetization to water via proton exchange. Instead of detecting the proton groups directly, as MR spectroscopy (MRS) does, CEST measures the change in the water signal by saturating exchangeable protons of metabolites and contrast agents that resonate at a frequency different from water protons. In the field of NMR, saturation is a phenomenon whereby the polarization of a spin pool, which is induced by the static magnetic field, is annihilated. At complete saturation, the spin pool has a magnetization of zero due to the perfectly balanced population of both energy levels.

CEST can already detect proton groups of concentrations in the range of millimoles. However, the increased sensitivity of CEST is accompanied by lower specificity compared to MRS because the resonances of exchangeable protons are generally broader than those of aliphatic protons and furthermore the linewidth is proportional to B_1.

While the principle was first demonstrated in 1963 by Forsen and Hoffmann [4], it was not until the work of Ward and Balaban in 2000 [5], that CEST gained prominence in MRI research.

3.2.1 CEST experiment

The CEST experiment comprises two distinct components: a saturation period, during which frequency-selective RF irradiation is employed, and a readout period, during which the signal of the water protons is acquired and spatially encoded, if applicable.

The saturation is gained by RF irradiation on-resonant to the Larmor frequency ω_s of the solute pool s, and thus, off-resonant to the water pool w over a time interval t_{sat}. Due to the exchange of the saturated protons, the saturation is transferred to the water pool, slightly attenuating the water signal

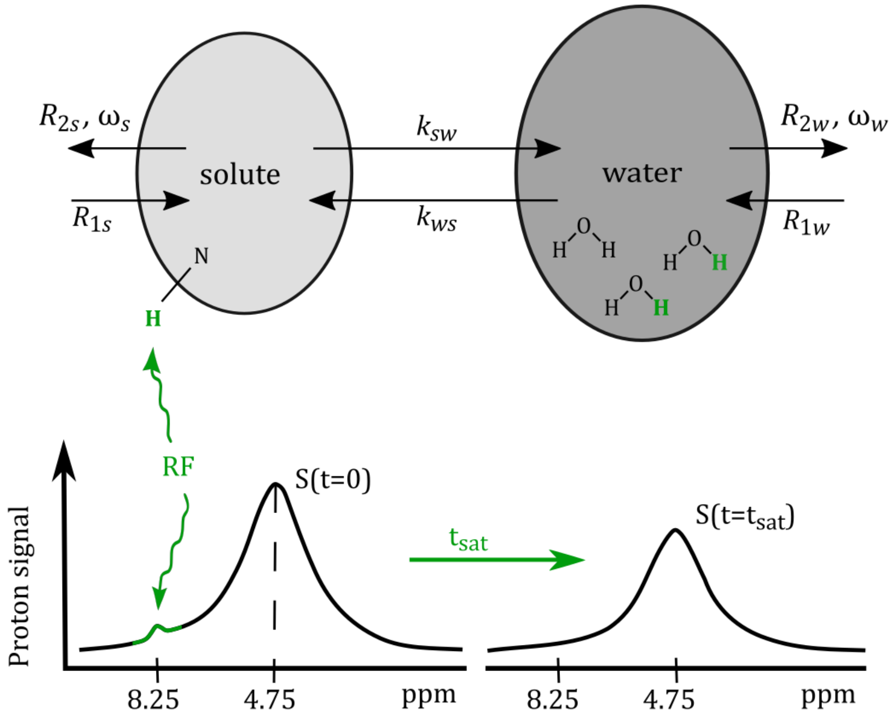

Figure 3.2: Schematic illustration of the CEST experiment for a two-pool model. The pools are defined by their relaxation rates R_1 and R_2, their resonance frequency ω, and by the exchange rate k between the pools. The protons of the smaller solute pool are saturated at their specific resonance frequency, with an example being 8.25 ppm for amide protons. The saturation is transferred to water (4.75 ppm) through the physical exchange of protons between the pools, with the exchange rate k_{sw}. This results in the non-saturated protons (black) replacing the saturated protons (green). The process repeats itself and after a period (t_{sat}), the effect is noticeable on the water signal. Adapted from reference [69].

in the order of the concentration of the solute protons, which is shown schematically in Figure 3.2. A single exchange of saturated protons does not produce a sufficient signal difference due to the low concentration of the solute pool (μM to mM range) compared to the high concentration of bulk water ($\approx 110\,\mathrm{M}$). During the long saturation period t_{sat}, the unsaturated protons from bulk water, which replaced the saturated solute protons, are also saturated by the RF irradiation. The more often these exchange events are repeated, the more the signal loss of water increases until a state of equilibrium is reached. The main condition to achieve a measurable signal enhancement is, that

$$t_{\mathrm{sat}} \gg \frac{1}{k_{sw}}. \tag{3.3}$$

A favorable condition is that the relaxation time constant of the saturated water protons T_{1w} is large enough to allow the saturation to remain until the steady-state is reached. Moreover, to ensure sufficient selectivity of the CEST experiment, it is necessary that the frequency difference $\Delta\omega_{sw}$ to water is large enough to separate the signal contributions from the solute pool and bulk water. This is usually given in the exchange regime of the slow to intermediate range, i. e. :

$$\Delta\omega_{sw} \geq k_{sw}. \tag{3.4}$$

Therefore, the main advantage of higher B_0 fields in CEST experiments is, besides a slight increased CEST effect due to longer T_{1w}, that the frequency difference $\Delta\omega$ enlarges with increasing B_0, so that the slow-exchange condition is easier to fulfil.

Assuming slow exchange, no direct perturbation from RF irradiation to the water protons and no back exchange of saturated protons, a simplified analytical expression of the proton transfer ratio (PTR) can be given for the CEST effect of a two pool model [71, 83, 84]:

$$\mathrm{PTR} = f_s \cdot \alpha \cdot k_{\mathrm{sw}} \cdot T_{1\mathrm{w}} \cdot \left(1 - e^{-t_{\mathrm{sat}}/T_{1\mathrm{w}}}\right), \tag{3.5}$$

where f_s is the relative population fraction, k_{sw} is the exchange rate and t_{sat} is the time of the saturation period. T_{1w} is the T_1 relaxation time constant of water, which is measured without saturation, avoiding the influence of saturation effects to the relaxation rate. α is the saturation efficiency for mobile protons.

In the most basic scenario, the RF irradiation of the saturation block comprised of a prolonged and uninterrupted continuous wave (cw) pulse spanning a range of approximately one hundred milliseconds to several seconds. This is illustrated in Figure 3.3 a). Since a long continuous wave irradiation leads to high SAR exposure, so-called pulsed saturation schemes have been developed as an alternative, e. g. consisting of a train of Gaussian shaped RF pulses with same amplitude, duration and center frequency (Fig. 3.3 c)). The pulse bandwidth BW, which is a measure of the frequency selectivity, can be expressed in terms of the reciprocal of the pulse duration t_{p}, $BW \approx 1/t_{\mathrm{p}}$. The relationship of pulse duration and interpulse delay t_{d} is called duty cycle and given by:

$$DC = \frac{t_{\mathrm{p}}}{t_{\mathrm{p}} + t_{\mathrm{d}}}. \tag{3.6}$$

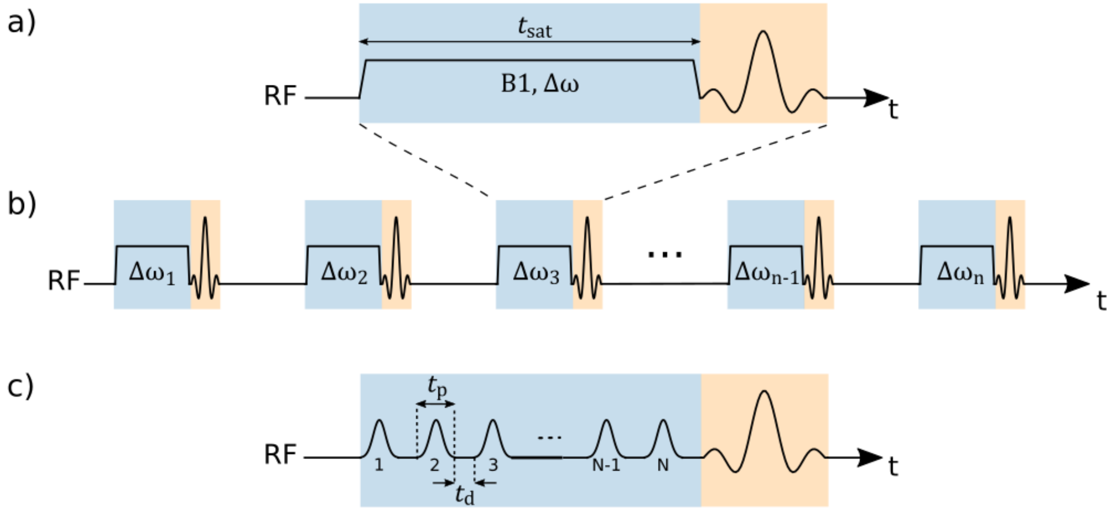

Figure 3.3: The CEST pulse sequence includes two distinct parts: a saturation part (blue) and a water signal acquisition part (orange) (a). The saturation block compromises a long continuous wave (cw) pulse with the saturation amplitude B_1 and frequency offset of $\Delta\omega$. This scheme is repeated for a number n of different frequency offsets $\Delta\omega$ to acquire the Z-spectrum (b). A pulsed CEST sequence (c) uses a train of N RF pulses (e.g. Gaussian-shaped) instead of a continuous wave saturation, characterized by the pulse duration t_p and the interpulse delay t_d. Here, B_1 is referred to as mean saturation amplitude.

3.2.2 Z-spectrum

The acquisition of a complete CEST spectrum can be achieved by repeating the sequence of saturation and signal acquisition for a number of saturation frequency offsets $\Delta\omega$, as depicted in Figure 3.3 b). When $\Delta\omega$ is in close proximity with that of the water proton pool w, or when the RF irradiation is directly resonant with it, the magnetization of the water protons is saturated directly. This effect is designated as direct saturation (DS) and hampers the interpretation of the Z-spectrum for proton pools with a resonance frequency near the Larmor frequency of water.

The Z-spectrum is achieved by plotting the water magnetization M_{zw}, normalized by the unsaturated water magnetization M_{z0}, as a function of the saturation frequency offset $\Delta\omega$:

$$Z(\Delta\omega) = \frac{M_{zw}(\Delta\omega)}{M_{z0}}. \tag{3.7}$$

Due to the normalization, the Z-spectrum is largely independent of system parameters such as the readout parameters and their associated contrast. Figure 3.4 shows an example Z-spectrum of a two pool model. In contrast to MRS, the frequency axis is shifted by 4.75 ppm, since all considerations in CEST imaging are in direct relation to the water frequency. Therefore, the water frequency is represented at 0 ppm. If CEST is combined with an imaging part, the Z-spectrum is calculated for each voxel.

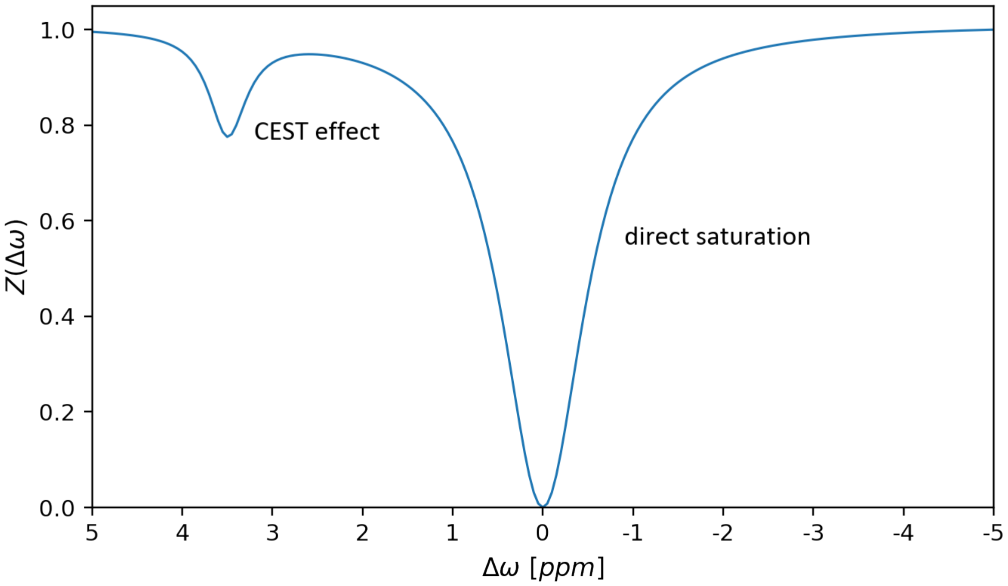

Figure 3.4: Simulated Z-spectrum with a CEST effect at $\delta\omega_s = 3.5$ ppm. The normalized water magnetization is depicted as function of the saturation frequency offset $\Delta\omega$. Symmetrically around 0 ppm, the effect of direct saturation can be seen. In the field of CEST, it is a standard convention to plot the axis of a frequency shift from a positive to a negative value range. JEMRIS simulation parameters were: $t_{\text{sat}} = 5$ s, $T_{2w} = 80$ ms, $T_{1w} = 1220$ ms, $T_{2s} = 15$ ms, $T_{1s} = T_{1w}$, $k_{sw} = 0.5$ kHz and $f_s = 0.5$ %, $B_1 = 0.8\,\mu$T and $B_0 = 7$ T.

3.2.3 Functional exchanging groups in human brain

The interpretation of an in-vivo Z-spectrum is much more complicated as not only the effects of chemical exchange of different molecules overlap, but also magnetization transfer processes based on NOE and MT influence the CEST spectrum [71, 73]. Although the chemical shift varies for different functional groups, it is generally not always possible to unambiguously assign CEST peaks to metabolites. However, information of the contributors in studied tissues and their chemical shifts, exchange rates as well as relaxation parameters often enables a correlation between observed effects and metabolites.

A number of CEST phenomena in natural tissue components, so-called endogenous contrast agents, and their properties have been reported from in-vivo studies. An overview of functional exchanging groups, which are present in human brain tissue is given in Table 3.1.

A prominent CEST effect is the amide proton transfer (APT). Amide protons origin in the peptide bond of proteins and peptides and resonate in the downfield at $\delta\omega_s = 3.5$ ppm. Their exchange rate range (10 - 300 s^{-1}) satisfies the slow exchange condition, see Equation 3.3, allowing good selective irradiation under physiological conditions [18]. In contrast, the group of amine protons from protein and peptide side chains or free amino acids belongs to the range of rapid exchange with water, resulting in the need for ultra-high field MRI examinations [85–87]. Another endogenous contrast agent is glutamate (Glu), a major neurotransmitter in the brain. The CEST peak of the glutamate amine protons is observed at 3.0 ppm downfield from water, but it should be noted that even at ultra-high fields there is an overlap of coalescent resonances with GABA, glutamine and taurine [73]. Also the hydroxyl protons on Myo-Inositol (mIns), which is an abundant substrate in human brain tissue, located mainly in glial cells and acting as an osmolyte, cause a measurable CEST effect [88]. Because the resonance frequency of Myo-Inositol ($\delta\omega_s$=0.6 ppm) is so close to the resonance frequency of water, superposition with direct water saturation is ubiquitous.

Besides the magnetization transfer due to chemical exchange, also NOE is present in an in-vivo Z-Spectrum of the brain. While the effect of aliphatic protons is reported upfield from water, there are also reports of aromatic NOEs in the downfield at 1 to 4 ppm [89]. In addition to endogenous molecules, there are exogenous contrast agents that can be used for CEST imaging, e.g., the CT contrast agent iopamidop or various paramagnetic agents [71].

Functional group		$\delta\omega_s$ [ppm]	k_{sw} [Hz]
Amides	-NH	3.5	$28.6^1, 30^2, 280^3$
Amines	$-NH_2$	2.0	$700 - 10000^4$
Glutamate	-CH, $-CH_2$	3.0	$2000^5, 4500^6$
Myo-Inositol	-OH	0.6	600^7
Aliphatic		-5 to -1(2)	$5 - 30^{2,3,8}$

Table 3.1: Overview of functional exchanging groups present in human brain. The magnetization transfer of amides, amines and hydroxyl groups occurs through chemical exchange while aliphatic groups transfer magnetization via NOE. Reported values from: 1. Zhou et al. [18] 2. Xu et al. [86] 3. Liu et al. [90] 4. Liepinsh and Otting [91] 5. Cai et al. [9] 6. Jin et al. [87] 7. Haris et al. [88] 8. Friedman et al. [92]

3.3 Bloch-McConnell equations

To describe the evolution of macroscopic magnetization in the presence of magnetization transfer, the Bloch equations (see Sec. 2.2) must be extended. This results in a set of coupled differential equations, the Bloch-McConnell (BMC) equations [93]. Assuming a two-pool model, the dynamics of the magnetization in the rotating frame during RF irradiation is given by:

$$\frac{\mathrm{d}}{\mathrm{d}t}\vec{M} = \mathbf{A} \cdot \vec{M} + \vec{C} \tag{3.8}$$

with the six-dimensional magnetization vector

$$\vec{M} = \begin{pmatrix} M_{xw}, & M_{yw}, & M_{zw}, & M_{xs}, & M_{ys}, & M_{zs} \end{pmatrix}^{\mathrm{T}}, \tag{3.9}$$

the block matrix $\mathbf{A}$

$$\mathbf{A} = \begin{bmatrix} \mathbf{L}_w - \mathbf{K}_w & \mathbf{K}_s \\ \mathbf{K}_w & \mathbf{L}_s - \mathbf{K}_s \end{bmatrix} \tag{3.10}$$

and the constant vector $\vec{C}$

$$\vec{C} = \begin{pmatrix} 0, & 0, & R_{1w}M_{0w}, & 0, & 0, & R_{1s}M_{0s} \end{pmatrix}^{\mathrm{T}}. \tag{3.11}$$

In the static magnetic field $\vec{B}_0 = (0, 0, B_0)$, the equilibrium magnetization of the water proton pool, w, and the solute proton pool, s, is given by M_{0w} and M_{0s}, respectively. $R_{1i} = 1/T_{1i}$ and $R_{2i} = 1/T_{2i}$ are the relaxation rates of the corresponding pools.

The matrix $\mathbf{A}$ includes two types of 3×3 submatrices, where ($i \in \{w, s\}$:

$$L_i = \begin{pmatrix} -R_{2i} & -\Delta\omega_i & 0 \\ \Delta\omega_i & -R_{2i} & \omega_1 \\ 0 & -\omega_1 & -R_{1i} \end{pmatrix}, \quad K_i = \begin{pmatrix} k_i & 0 & 0 \\ 0 & k_i & 0 \\ 0 & 0 & k_i \end{pmatrix}. \tag{3.12}$$

$\omega_1 = \gamma B_1$ is the precession frequency of the magnetization around the x-axis induced by the RF irradiation field $\vec{B}_1 = (B_1, 0, 0)$. $\Delta\omega_i = \Delta\omega - \delta_i$ is the frequency offset of pool i, with its chemical shift δ_i, relative to the frequency $\Delta\omega$ of the RF irradiation. $k_s = k_{sw}$ and $k_w = k_{ws}$ are the exchange rates of the forward proton exchange from solutes to water ($s \to w$) and of the back transfer ($w \to s$), respectively. The equilibrium condition for the exchange of protons is defined as:

$$k_{sw} \cdot M_{0s} = k_{ws} \cdot M_{0w} \tag{3.13}$$

In consideration of the relative population fraction $f_s = M_{0s}/M_{0w}$, the backward exchange rate is also given by

$$k_{ws} = f_s \cdot k_{sw}. \tag{3.14}$$

Since in most CEST experiments the population fraction is less than 1%, k_{ws} is much smaller than k_{sw}. The Bloch-McConnell equations shown here for two pools can be easily expanded for any number of solute pools that exchange with water.

3.3.1 Numerical solution

To analyze a CEST experiment in more detail, and therefore to simulate it, it is necessary to solve the Bloch-McConnell equation. The BMC equation are first-order ordinary differential equations (ODEs) (see. Eq. 3.8). Its formal solution for cw-saturation with saturation time t_{sat} is given by [71, 94]:

$$\vec{M} = (\vec{M}_0 = \mathbf{A}^{-1}\vec{C}) \cdot \exp(\mathbf{A} \cdot t_{\text{sat}}) - \mathbf{A}^{-1}\vec{C} \tag{3.15}$$

and often used to derive a numerical solution of the BMC equations. Various ways have been established for this purpose. The most direct way to solve an ODE system is numerical integration, which might be time-consuming. Highly optimized libraries for numerical solutions of differential equations, e.g. the CVODE library, improve the required computational power and speed, as used in the MRI simulator JEMRIS (`https://www.jemris.org`) [95].

In contrast to this, the MRI simulator MRiLab (`https://mrilab.sourceforge.net/`) [96] abandons ODE solver libraries and uses exponential scaling and rotation matrices at each time point during a predefined pulse sequence to solve the Bloch-McConnell equations by means of discrete time solutions.

Moreover, the set of coupled equations can be solved for constant matrix $\mathbf{A}$ by performing matrix inversion and exponentiation numerically [97], which is used by the simulation platform cest-sources (`https://www.cest-sources.org`). Piecewise simulation of the constant solutions can also achieve a full time-dependent solution [98, 99], which is necessary for pulsed saturation schemes.

3.3.2 Analytical solution

In contrast to numerical solutions of the BMC equation, analytical solutions provide closer insight into the structure of the Z-spectra and also enable analytical optimization approaches for the design of CEST experiments. A way to solve the first-order linear differential BMC-equation analytically is the eigenspace approach, where **A** is transformed into a diagonal matrix [7, 71, 100]:

$$\vec{M}(t) = \sum_{n=1}^{6} e^{\lambda_n \cdot t} \vec{v}_n + \vec{M}^{\mathrm{ss}} \tag{3.16}$$

$\vec{M}(t)$ is the two-pool magnetization vector (see Eq. 3.9) and λ_n is the n-th eigenvalue with the corresponding eigenvector $\vec{v}_n$ of matrix **A**. $\vec{M}^{\mathrm{ss}}$ is the stationary solution. For off-resonant irradiation with $\omega_{\mathrm{eff}} \gg 1/T_2$ and sufficient long saturation $t_{\mathrm{sat}} \gg T_2$, the smallest eigenvalue λ_1 provides the only significant contribution to the residual magnetization of the water pool. The corresponding eigenvector $\vec{v}_1$ is colinear in a good approximation with the effective field $\vec{B}_{\mathrm{eff}}$, which was introduced in Equation 2.12). This eigenvalue λ_1 is equivalent to the negative longitudinal relaxation rate constant in the rotating frame [7, 100]:

$$\lambda_1 = -R_{1,\rho}. \tag{3.17}$$

In a two-pool model comprising a water and solute pool with exchangeable protons, the longitudinal relaxation rate constant can be calculated as the sum of the water proton relaxation rate in the rotating frame, $R_{1\rho,w}$, and the exchange-dependent relaxation rate in the rotating frame, R_{ex}:

$$R_{1\rho}(\Delta\omega) = R_{1\rho,w}(\Delta\omega) + R_{\mathrm{ex}}(\Delta\omega). \tag{3.18}$$

The water proton relaxation rate in the rotating frame can be approximated by:

$$R_{1\rho,w}(\Delta\omega) = R_{1w}\cos^2\theta + R_{2w}\sin^2\theta = R_{1w} + (R_{2w} - R_{1w}) \cdot \frac{\omega_1^2}{\omega_1^2 + \Delta\omega^2} \tag{3.19}$$

where θ is the angle between $\vec{B}_{\mathrm{eff}}$ and $\vec{B}_0$ for off-resonant irradiation, which was introduced in Equation 2.13.

The parameters of the exchanging pool are contained entirely in the exchange-dependent relaxation term R_{ex}. Assuming the large shift limit (LS) $|\delta\omega_s| \gg \omega_1$, R_{ex} turns out to a Lorentzian-shaped function centered at the resonance frequency of the exchanging pool $\delta\omega_s$ [7]:

$$R_{\mathrm{ex}}(\Delta\omega) \approx f_s k_{sw} \frac{\omega_1^2}{k_{sw}(k_{sw} + R_{2s}) + \omega_1^2} \cdot \frac{\Gamma^2/4}{\Gamma^2/4 + (\Delta\omega - \delta\omega_s)^2} \tag{3.20}$$

with the full width at half-maximum:

$$\Gamma = 2\sqrt{(R_{2s} + k_{sw})^2 + \frac{R_{2s} + k_{sw}}{k_{sw}}\omega_1^2}. \tag{3.21}$$

The maximum value is given at $\Delta\omega = \delta\omega_s$:

$$R_{\text{ex}}^{\text{max}} = f_s k_{sw} \frac{\omega_1^2}{k_{sw}\left(k_{sw} + R_{2s}\right) + \omega_1^2}. \tag{3.22}$$

Due to the low abundance of the solute pool ($M_{0w} \gg M_{0,s}$), the back exchange k_{ws} was neglected and moreover, $R_{2s} \gg R_{1s}$ and $k_{sw} \gg R_{1s}$ was assumed [71].

In the full saturation limit (strong B_1 and small k_{sw} and R_{2s}), $R_{\text{ex}}^{\text{max}}$ simplifies to:

$$R_{\text{ex,FS}}^{\text{max}} = f_s \cdot k_{sw} = k_{ws}. \tag{3.23}$$

Under the conditions of large chemical shifts and full saturation, the exchange-dependent relaxation rate R_{ex} equals the back exchange rate k_{ws} and represents the ideal CEST effect.

This results in a dynamic solution for the Z-spectrum, which can be described by the monoexponential decay of the Z-magnetization at the rate $R_{1\rho}$:

$$Z\left(\Delta\omega, t\right) = \left(\cos^2\theta \cdot Z_{\text{ini}} - Z^{\text{ss}}\right) \mathrm{e}^{-R_{1\rho} \cdot t} + Z^{\text{ss}} \tag{3.24}$$

with the initial Z-magnetization $Z_{\text{ini}} = |M_{\text{ini}}|/M_0$, which decays to steady-state Z^{ss} given by :

$$Z^{\text{ss}}\left(\Delta\omega\right) = \cos^2\theta \frac{R_{1w}}{R_{1\rho}\left(\Delta\omega\right)}, \tag{3.25}$$

which is further simplified if $\cos\theta$ becomes 1 in the case of a small angle θ.

The direct water saturation in the steady-state Z-Spectrum can be described by choosing $R_{\text{ex}} = 0$:

$$Z_{\text{DS}}^{\text{ss}}(\Delta\omega) = \cos^2\theta \frac{R_{1w}}{R_{1\rho,w}(\Delta\omega)}, \tag{3.26}$$

which can also be transformed into a Lorentzian function:

$$Z_{\text{DS}}^{\text{ss}}(\Delta\omega) = 1 - \frac{\Gamma_w^2/4}{\Gamma_w^2/4 + \Delta\omega^2} o \tag{3.27}$$

with the full width half maximum (FWHM):

$$\Gamma_w = 2\omega_1 \sqrt{R_{2w}/R_{1w}}. \tag{3.28}$$

Pulsed saturation

However, the major disadvantage of the analytical solution of the Bloch-McConnell equations is that it is only valid for cw saturation schemes. Simulations of pulsed-CEST approaches need to be performed numerically. Nevertheless, the considerations of the analytical solution for cw-saturation can be used conditionally also for pulsed sequences [101]. For this purpose, it is necessary to simplify the consideration by the assumption that a train of shaped pulses with pulse duration t_{p} and interpulse delay t_{d} can be approximated by a cw-saturation with the same average power [98, 99]. The root-mean-squared B_1 level, given by:

$$B_{1\text{rms}} = \sqrt{\frac{1}{t_\text{p} + t_\text{d}} \cdot \int_0^{t_\text{p}+t_\text{d}} B_1^2(t)\text{d}t} \tag{3.29}$$

is a dominant pulse sequence factor affecting the amount of macromolecular and direct water saturation.

Assuming a train of shaped pulses, the time-dependent relaxation rate in the rotating frame $R_{1\rho}(\Delta\omega,\omega_1(t))$ can be averaged to [102]:

$$\overline{R_{1\rho}}(\Delta\omega) = \overline{R_{1\rho,w}} + \overline{R_{\text{ex},s}^{\text{max}}}. \tag{3.30}$$

Provided that the LS conditions are fulfilled and both $R_{1w}t_\text{d} \gg 1$ and $R_{1\rho}t_\text{p} \gg 1$ are valid, the steady-state solution for pulsed saturation can be calculated as:

$$Z_{\text{pulsed}}^{\text{ss}}(\Delta\omega) = \frac{R_{1w}}{DC \cdot \overline{R_{1\rho}}(\Delta\omega) + (1 - DC) \cdot R_{1w}} \tag{3.31}$$

where DC is the duty-cycle, as introduced in Equation 3.6.

3.4 In-vivo CEST imaging

To ensure a reliable interpretation of the CEST data, it is necessary to distinguish the CEST effect from the direct water saturation effect and other contributing metabolites. Beyond multi-pool considerations, the influence of the various experimental factors on the CEST contrast must also be addressed.

3.4.1 Z-spectrum analysis

Various methods for analyzing the Z-spectrum have been established in recent years. Assuming the two-pool model, many of these metrics can be described in more detail using the analytical solution.

For this purpose, the Z-value on-resonant on the pool of interest is defined as label scan Z_lab. Assuming cw-saturation and a steady-state solution in the LS limit, Z_lab is given by [71]:

$$Z_\text{lab} = Z(\Delta\omega = \delta\omega_s) = \frac{R_{1w}}{R_{1\rho,w}(\delta\omega_s) + R_{\text{ex}^\text{max}}}. \tag{3.32}$$

The magnetization transfer rate (MTR)

$$MTR(\delta\omega_s) = 1 - Z_\text{lab} \tag{3.33}$$

describes the difference in the Z-spectrum between a system with and without exchanging pools, but it is not suitable to isolate R_ex from direct saturation ($R_{1\rho,w}$).

A very common method is the asymmetry analysis, where the difference to a reference scan without exchange on the opposite side of the Z-spectrum

$$Z_\text{ref} = Z(\Delta\omega = -\delta\omega_s) \tag{3.34}$$

with symmetrical axis at $\Delta\omega = 0\,\text{ppm}$ is formed:

$$MTR_{\text{asym}}(\delta\omega_s) = Z_{\text{ref}} - Z_{\text{lab}} = \frac{R_{1w} R_{\text{ex},s}^{\text{max}}}{R_{1\rho,w}(R_{1\rho,w} + R_{\text{ex},s}^{\text{max}})} \tag{3.35}$$

Assuming that the direct saturation is symmetric, $R_{1\rho,w}(\delta\omega_s) = R_{1\rho,w}(-\delta\omega_s)$, MTR_{asym} corresponds to a zero-order spillover correction. To improve the spillover correction from zero- to first-order correction, MTR_{asym} can be normalized based on the reference scan:

$$MTR_{\text{asym}}^{\text{norm}}(\delta\omega_s) = \frac{Z_{\text{ref}} - Z_{\text{lab}}}{Z_{\text{ref}}} = \frac{R_{\text{ex},s}^{\text{max}}}{R_{1\rho,w} + R_{\text{ex},s}^{\text{max}}}. \tag{3.36}$$

Another approach to analyze CEST effects of interest is the inverse metric MTR_{Rex} [7, 103]:

$$MTR_{Rex}(\delta\omega_s) = \frac{1}{Z_{\text{lab}}} - \frac{1}{Z_{\text{ref}}} = \frac{R_{\text{ex},s}^{\text{max}}}{R_{1w}} \tag{3.37}$$

which is completely separated from the influence of R_{2w}.

The techniques outlined in this chapter for assessing the Z-spectrum can also be used for the pulsed saturation scheme [102, 103]. While MTR_{Rex} is simply scaled with the duty cycle compared to cw saturation:

$$MTR_{Rex}^{\text{pulsed}} = \frac{DC \cdot \overline{R_{\text{ex},s}^{\text{max}}}}{R_{1w}}, \tag{3.38}$$

the analytical expression of $MTR_{\text{asym}}^{\text{pulsed}}$ becomes more complicated:

$$MTR_{asym}^{\text{pulsed}} = \frac{DC \cdot R_{1w} \cdot \overline{R_{\text{ex},s}^{\text{max}}}}{\left(DC \cdot \overline{R_{1\rho,w}} + R_{1w}\,(1 - DC)\right)\left(DC \cdot (\overline{R_{1\rho,w}} + \overline{R_{\text{ex},s}^{\text{max}}}) + R_{1w}\,(1 - DC)\right)}. \tag{3.39}$$

3.4.2 Multi-pool system

Examining in-vivo studies, many different pools including rNOE and ssMT interact and contribute to the Z-spectrum, as visualized in Figure 3.5. The analytical solution can be easily extended to describe a multi-pool system. Assuming that the back-exchange rate is very small and that there is no exchange among the exchangeable pools, the individual exchange-dependent relaxation terms $R_{\text{ex},i}$ add up linearly to the global relaxation rate in the rotating frame [104]:

$$R_{1\rho} = R_{1\rho,w} + \sum_i R_{\text{ex},i}. \tag{3.40}$$

Transferred to the steady-state solution Z^{ss} (see. Eq. 3.25), it follows that the individual effects in the Z-spectrum add reciprocally [71]:

$$\frac{1}{Z^{\text{ss}}} = \frac{1}{Z_w^{\text{ss}}} + \sum_i \frac{1}{Z_i^{\text{ss}}} \tag{3.41}$$

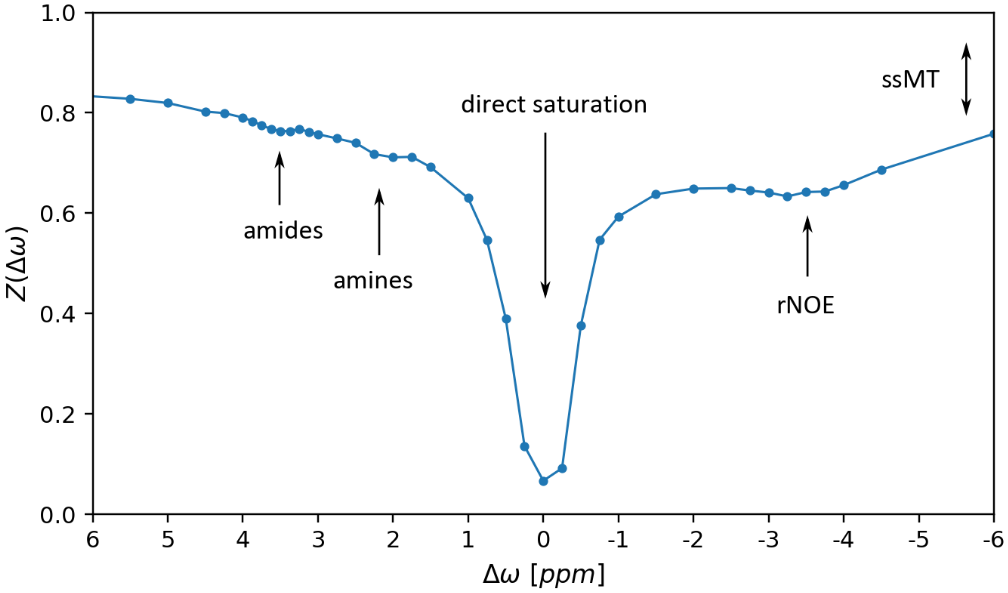

Figure 3.5: Exemplifying in-vivo Z-spectrum contains multiple CEST effects (e.g. amides and amines), direct water saturation and a contribution of aliphatic protons (rNOE). The very broad effect of semi solid MT shows up as a general reduction of the Z-spectrum.

Therefore, the on-resonant label scan introduced in Equation 3.32 changes to

$$Z_{\text{lab}} = \frac{R_{1w}}{R_{1\rho,w}(\delta\omega_s) + \sum_i R_{\text{ex},i}(\delta\omega_s)}. \tag{3.42}$$

As shown in Equations 3.20 and 3.27, the individual CEST effects as well as the direct water saturation can be approximated by Lorentzian-shaped functions. The Z-spectrum of a multi-pool system in steady-state can be approximated as:

$$Z^{\text{ss}} \approx 1 - \mathrm{L}_w - \sum_i \mathrm{L}_i, \tag{3.43}$$

where L_w is the Lorentzian-shaped function of the direct water saturation and L_i the Lorentzian-shaped functions of the individual exchangeable pools.

Given all the contributions to the Z-spectrum in the in-vivo measurements, the asymmetry analysis is not sufficient to isolate the CEST contrast of interest as there are contributions on both sides of the direct water saturation. The example in-vivo Z-spectrum in Figure 3.5 depicts the effects of amides and amines downfield of the direct saturation and the rNOE effect upfield.

An alternative approach is to define the reference scan as the sum of all other effects:

$$Z_{\text{ref}}(\delta\omega_s) = \frac{R_{1w}}{R_{1\rho,w}(\delta\omega_s) + \sum_{i,i\neq s} R_{\text{ex},i}(\delta\omega_s)}. \tag{3.44}$$

The contribution of the individual pools can e.g be determined by Lorentzian line fitting (see Eq. 3.43) [105].

The magnetization transfer ratio for the separation of the CEST effect of interest can now be calculated as a linear difference[94]:

$$MTR_{\text{LD}}(\delta\omega_s) = Z_{\text{ref}}(\delta\omega_s) - Z_{\text{lab}}(\delta\omega_s). \tag{3.45}$$

The same result as in the asymmetry analysis can be obtained, but here it is independent of the shape of the other pools.

3.4.3 Factors affecting the Z-spectrum

In order to obtain the maximum CEST effect, it is necessary to take a closer look at the dependencies of the Z-spectrum on various factors of the experiment. To simplify the consideration, this chapter is dedicated to the two-pool model. Figure 3.6 a) shows that the Z-spectrum converges the steady state with increasing saturation time t_{sat}. If the PTR (introduced in Eq. 3.5) is considered, it can be seen that the equilibrium occurs approximately at $t_{\text{sat}} \approx 3 \cdot T_1$, which corresponds to around 3 s in the example.

For a defined saturation amplitude B_1, an optimal exchange rate can be determined by examining the maximum value of $R_{\text{ex}}^{\text{max}}$ (see Eq. 3.22) with respect to k_{sw}:

$$\begin{aligned} \frac{\partial}{\partial k_{sw}} R_{\text{ex}}^{\text{max}} &= 0 && (3.46)\\ k_{sw,\text{opt}} &= \omega_1, && (3.47) \end{aligned}$$

which is also depicted in Figure3.6 b). In the case of cw-saturation and $B_1 = 1\,\mu$T, the optimum exchange rate is about $k_{sw,opt} = 267.5$ Hz.

A closer look at the FWHM equation of the direct water saturation (compare Eq. 3.28) clarifies that both a decrease of the transverse relaxation time of water T_{2w} and an increase of the longitudinal relaxation time T_{1w} lead to a broadening of the direct water saturation, which is depicted in Figure 3.6 c) and d). While changes in T_{2w} mainly influences the spillover effect, increased T_{1w} improves simultaneously the CEST effect. With a longer longitudinal relaxation time of the water pool T_{1w}, the magnetization remains long enough to reach the steady state of the CEST saturation.

The dependence of the CEST effect on the field strength of the main magnetic field B_0 is probably the most fundamental and important one, because the spectral resolution benefits significantly from higher field strengths [101], which can be clearly seen in Figure 3.7 a). The peak width (calculated in Hz) decreases with increasing B_0, whereas the peak position, depending on its chemical shift, always remains at the same position of the Z-spectrum (in ppm). This leads to improved spectral resolution, which becomes especially necessary for fast exchanging pools since the peak width increases with the

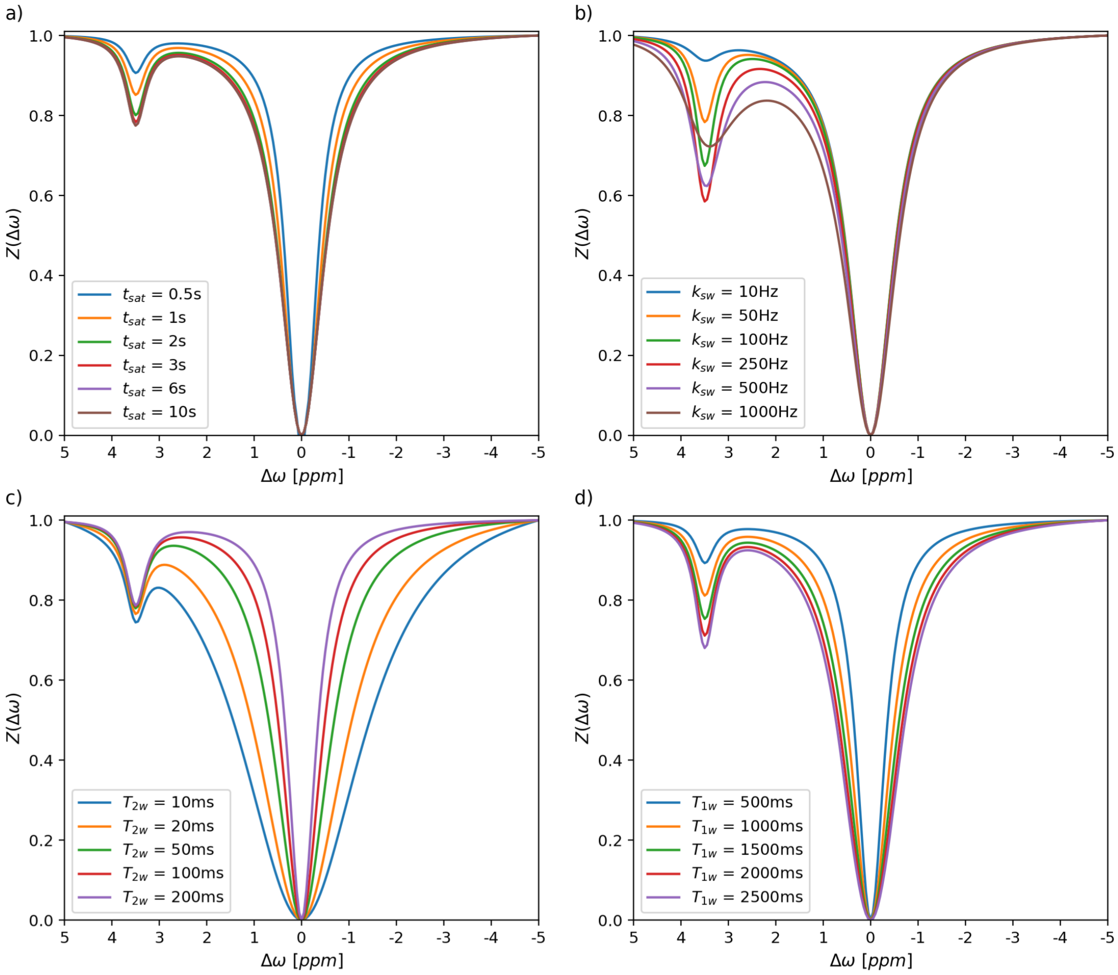

Figure 3.6: Simulated Z-spectra using cw-saturation with CEST effect at 3.5 ppm for different saturation times t_{sat} (a), different exchange rates k_{sw} (b), varying T_{2w} (c), and T_{1w} values (d). If not varied, JEMRIS simulation parameters were: $B_0 = 7\,\text{T}$, $B_1 = 1\,\mu\text{T}$, $t_{\text{sat}} = 3\,\text{s}$, $T_{2w} = 80\,\text{ms}$, $T_{1w} = 1220\,\text{ms}$,$T_{2s} = 15\,\text{ms}$, $T_{1s} = 1220\,\text{ms}$, $k_{sw} = 0.5\,\text{kHz}$ and $f_s = 0.5\,\%$.

exchange rate (see Eq. 3.21). Moreover, the relaxation rates are also dependent on the main magnetic field, which in turn influences the Z-spectrum as shown above. While the longitudinal relaxation rates decreases with B_0, the transverse relaxation rates increases, leading to a broadening of the peak widths. The field-dependence of the R_2 relaxation rate is usually negligible because the contribution of R_{2s} to the peak width (see Eq. 3.28) is very small compared to the contribution of k_{sw} [101].

The influence of the strength of the excitation field B_1 on the CEST experiment is particularly evident when the labeling efficiency α is considered. In the large shift limits, the labeling efficiency is given by [71]:

$$\alpha_{\text{LS}} = \frac{(\gamma B_1)^2}{(\gamma B_1)^2 + k_{sw}\,(k_{sw} + R_{2s})}, \tag{3.48}$$

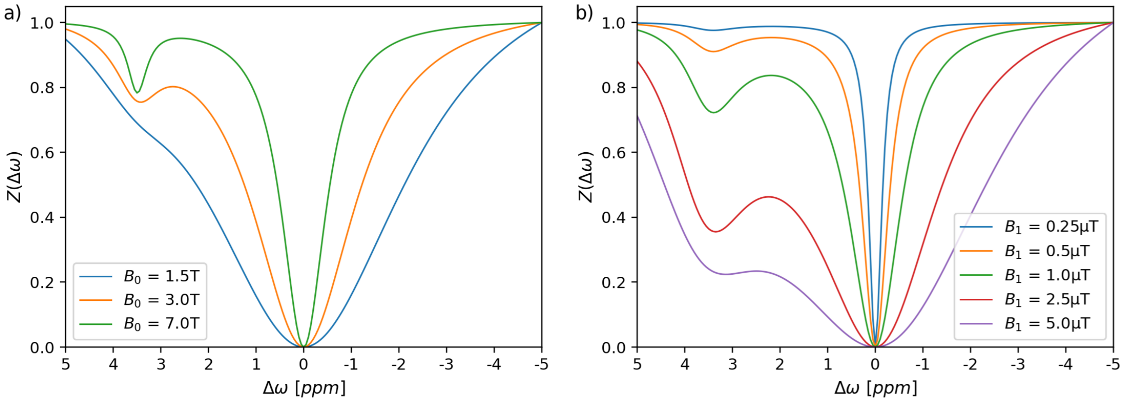

Figure 3.7: Simulated Z-spectra using cw-saturation with CEST effect at 3.5 ppm for different saturation amplitudes B_1 (a) and different field strength, B_0(b). If not varied, JEMRIS simulation parameters were: $B_0 = 7\,\mathrm{T}$, $B_1 = 1\,\mu\mathrm{T}$, $t_{\mathrm{sat}} = 5\,\mathrm{s}$, $T_{2w} = 80\,\mathrm{ms}$, $T_{1w} = 1220\,\mathrm{ms}$, $T_{2s} = 15\,\mathrm{ms}$,$T_{1s} = T_{1w}$, $k_{sw} = 0.5\,\mathrm{kHz}$ and $f_s = 0.5\,\%$.

which can be further simplified under the assumption that $R_{2s} \ll k_{sw}$:

$$\alpha = \frac{(\gamma B_1)^2}{(\gamma B_1)^2 + (k_{sw})^2}. \tag{3.49}$$

However, despite the fact that labeling efficiency clearly benefits from a higher B_1 field, both the peak width of the direct water saturation (see Eq. 3.28) and the width of the CEST peak (see Eq. 3.21) become broader with higher B_1, thereby the separation of the individual effects from each other becomes more difficult. Due to the inverse correlation of these two effects, the choice of an applicable B_1 is always a compromise between high labeling efficiency and narrow peak width, which is depicted in Figure 3.7 b). Beyond that, B_1 inhomogeneities, as they occur pronounced in UHF experiments, lead to spatial variances of the voxelwise Z-spectra, due to varying labeling efficiency and peak width, which immensely affect the quantification of the CEST effect.

3.4.4 CEST imaging in neurodegenerative diseases

CEST imaging allows to study molecular processes in the brain non-invasively and it has been used successfully in several diseases, such as brain tumors and stroke. Especially the field of neurodegenerative diseases (ND) may benefit from the developments of CEST imaging. NDs are a significant challenge for the aging society notably since clinical treatment is to a large extent limited to symptom management [106]. Classical MR imaging methods are successfully applied in the later stages of disease, but are of limited use in the early stages where biochemical changes predominate over structural changes.

Over the past decade, many research groups have investigated the potential of CEST for NDs, particularly for the most common forms, Alzheimer's (AD) and Parkinson's disease (PD). In the following, a brief explanation is provided of how the functional exchanging groups of the human brain and the related CEST effect can be associated with different pathological processes in neurodegenerative diseases. More detailed information can be found in the publications of [15, 106–109].

Amide proton transfer is a potential indicator of protein aggregates, which are associated with histopathological features in AD as amyloid plaques, made up of abnormally folded amyloid beta, and neurofibrillary tangles composed of hyperphosphorylated tau [107]. Abnormal protein load is related to increased amide CEST contrast and has also been observed in patients with mild cognitive impairment (MCI), a potential precursor of AD. Also, in PD, the increased APT is related to the increase in cytosolic proteins and peptides, such as the accumulation of misfolded α-synuclein. In contrast, reduced APT in the substantia nigra region could be related to selective loss of neurons. In addition, also decreased aliphatic rNOE in the substantia nigra was detected in early-stage PD as well as an age-related change in the amide pool [110].

An increased CEST signal which originates from the exchangeable protons of Myo-Inositol may be a marker of gliocell proliferation, which increases in early Alzheimer's disease [111]. The microglial proliferation leads to a neuroinflammatory response, which in turn is a potential factor in a range of neurodegenerative diseases. Also the CEST signal of glutamate seams to be sensitive to the activation of glial cells and is increased in early stages of neuroinflammation [108]. However, the major involvement of the primary excitatory neurotransmitter is synaptic transmission and it affects cognitive abilities, learning and memory. ^{1}H-MRS studies in the human brain showed a decrease in hippocampal glutamate concentration from healthy controls to patients with MCI to full-blown Alzheimer's disease [112]. Also in case of tauopathy, alterations in glutamate levels have been observed, due to the disrupted function of neurotransmitters caused by neurofibrillary tangles [113, 114].

Besides the endogenous contrast agents of the human brain, dynamic glucose-enhanced MRI experiments, where the glucose uptake is recorded by CEST imaging, could provide insides into neuropathological incidents of neurodegenerative diseases [108]. Glucose, the brain's main source of energy, and its consumption are associated with synaptic function, oxidative metabolism in neurons, and aerobic glycolysis in astrocytes. However, glucose must be injected intravenously for this purpose.

CHAPTER 4

Methods and materials

In this chapter, the technical equipment and methods for whole-brain CEST imaging are introduced. The focus is on sequence development, data processing and optimizing individual procedural steps.

4.1 MR imaging systems

The MRI experiments presented in this work were performed on the Siemens MAGNETOM 7 T whole-body scanner (Siemens Heathineers, Erlangen, Germany) at the German Center for Neurodegenerative Diseases (DZNE, Bonn, Germany), depicted in Figure 4.1. The MR system contains three orthogonal gradient coils, providing a maximum nominal gradient strength of 70 mT/m together with a maximal gradient slope rate of 200 mT/m. In addition to spatial encoding, the gradient system is employed for first-order B_0 shimming. Moreover, the scanner is equipped with additional shim-coils, which are employed for second-order shimming, and with four third-order field components.

Figure 4.1: Siemens MAGNETOM 7 T whole body MR tomograph of the German Center for Neurodegenerative Diseases (DZNE) in Bonn.

Two different head coils (Nova Medical, Wilmington, USA) were utilized for all measurements:

- a 32Rx/1Tx head coil with 32 receive channels and a single transmit coil (sTx)
- a 32Rx/8Tx head coil with 32 receive channels and eight transmit coils enabling parallel transmit (pTx)

The main development process was done using the sTx coil, while the pTx coil was only used for the last part of the project. Unless otherwise stated, measurements were performed with the sTx coil.

The C++ based framework Siemens IDEA (version B17 and, after an upgrade, version E12) was used for sequence development. The environment offers complete control over the pulse sequence design within subject and equipment protection limits through the independent definition of RF and gradient pulse sequences.

4.2 The CEST sequence

The development of a sequence to acquire high quality whole-brain CEST data was the main part of this work. The CEST sequence consists of two sections per volume acquisition:

1. a frequency-selective saturation module to prepare the magnetization transfer,
2. a centric-reordered segmented 3D-EPI readout to spatially encode the prepared signal.

Since all necessary image information per saturation frequency is acquired after a single saturation period, the sequence is called "snapshot 3D-EPI CEST" [41].

The schematic diagram of the final sequence, which is used with the single transmit coil (IDEA version E12), is depicted in Figure 4.2. More information on the sequence differences of earlier development versions with IDEA version B17 can be found in Appendix A.

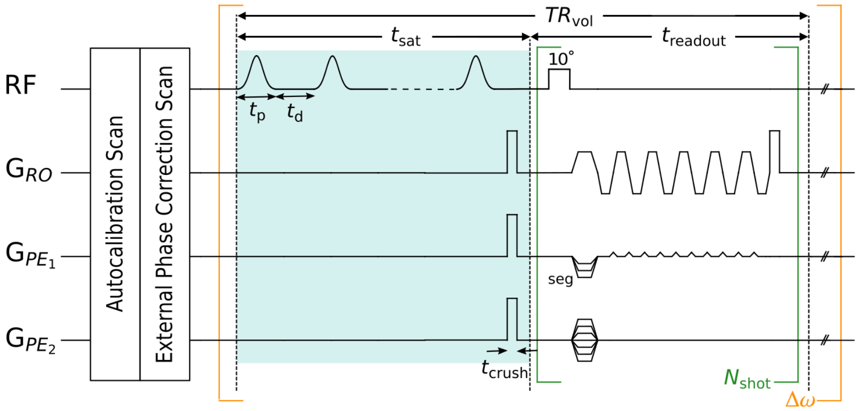

Figure 4.2: Schematic sequence diagram of the snapshot 3D-EPI CEST sequence. The shaded area represents CEST saturation, which is then followed by a centric-reordered 3D-EPI readout with single rectangular water-selective excitation. The segmented CAIPI scheme is shown on the second phase encoding axis. Prior to the irradiation offset loop ($\Delta\omega$), the GRAPPA autocalibration scan and the external 3-readout phase correction scan are acquired on a single occasion.

4.2.1 CEST saturation

The spectrally selective CEST saturation period (Fig. 4.2, blue shaded area) consists of a train of N Gaussian RF pulses of duration t_p and mean amplitude B_1. The time delay t_d after each Gaussian RF pulse is chosen equal to t_p to maintain a duty cycle $DC = 50\,\%$ (see Equation 3.6) to control SAR constraints. The last RF pulse is followed by crusher gradients (of a duration t_crush) in all three directions to dephase the residual magnetization in the xy-plane before the image readout is played out. The total saturation time t_sat is given by:

$$t_\mathrm{sat} = N \cdot t_\mathrm{p} + (N-1) \cdot t_\mathrm{d} + t_\mathrm{crush} \tag{4.1}$$

The center frequency of the RF pulses is shifted by $\Delta\omega$ from the ^{1}H resonance frequency. To obtain a full Z-spectrum, the frequency is varied for each repetition in a range from -60 to 60 ppm, based on previous publications [30, 37, 94, 115]. In order to individually adapt the sampling pattern to the expected CEST effects, a list of frequency offsets is loaded as a .txt file during each measurement preparation. To improve the quantification of the CEST effects of amides, amines and the rNOE, the sampling density is increased between -6 and 6 ppm.

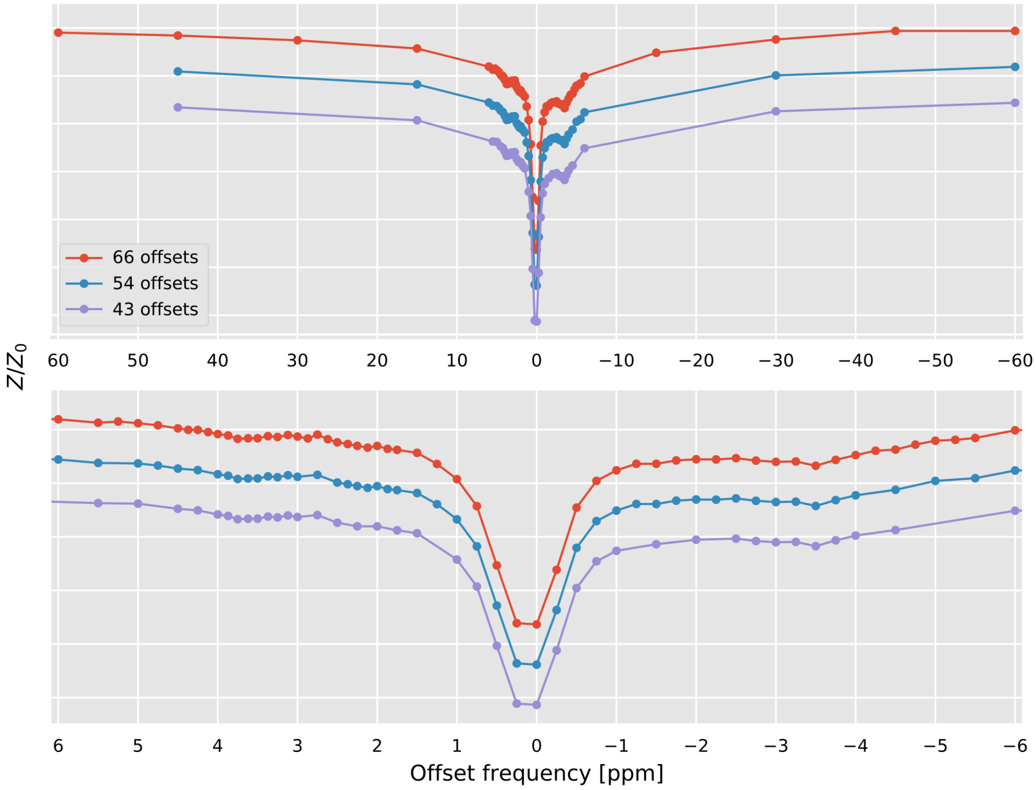

Figure 4.3: Single voxel Z-spectra with visualization of the 66, 54 and 43 offsets. The spectra with reduced number of measurement points are shifted by −15 % and −30 %, respectively, for better visualization. In the lower part of the figure the offset range is zoomed in to show the denser sampling of the amide, amine and rNOE peaks, with emphasis on the amide contrast.

To reduce the overall measurement time, that scales with the total number of frequency offsets, three different lists with non-uniformly distributed off-center frequencies (offset lists) were tested. For this purpose, a set of 66 saturation frequencies was acquired and the CEST maps were then processed using all 66 offsets or a reduced subset of 54 or 43 offsets. The primary focus was the amide contrast. Consequently, the sampling pattern around 3.5 ppm was not reduced, as illustrated in Figure 4.3. The complete offset lists are shown in Table 4.1.

$\Delta\omega$ [ppm]	-60	-45	-30	-15	-6	-5.5	-5.25	-5	-4.75	-4.5	-4.25
list 66	x	x	x	x	x	x	x	x	x	x	x
list 54	x		x		x	x		x		x	
list 43	x		x		x					x	
$\Delta\omega$ [ppm]	-4	-3.75	-3.5	-3.25	-3	-2.75	-2.5	-2.25	-2	-1.75	-1.5
list 66	x	x	x	x	x	x	x	x	x	x	x
list 54	x	x	x	x	x	x	x	x	x	x	x
list 43	x	x	x	x	x	x	x		x		x
$\Delta\omega$ [ppm]	-1.25	-1	-0.75	-0.5	-0.25	0	0.25	0.5	0.75	1	1.25
list 66	x	x	x	x	x	x	x	x	x	x	x
list 54	x	x	x	x	x	x	x	x	x	x	x
list 43		x	x	x	x	x	x	x	x	x	
$\Delta\omega$ [ppm]	1.5	1.75	1.875	2	2.135	2.25	2.375	2.5	2.625	2.75	2.875
list 66	x	x	x	x	x	x	x	x	x	x	x
list 54	x	x	x	x	x	x	x	x		x	
list 43	x	x		x		x		x		x	
$\Delta\omega$ [ppm]	3	3.125	3.25	3.375	3.5	3.625	3.75	3.875	4	4.125	4.25
list 66	x	x	x	x	x	x	x	x	x	x	x
list 54	x	x	x	x	x	x	x	x	x		x
list 43	x	x	x	x	x	x	x	x	x		x
$\Delta\omega$ [ppm]	4.375	4.5	4.75	5	5.25	5.5	6	15	30	45	60
list 66	x	x	x	x	x	x	x	x	x	x	x
list 54		x	x	x		x	x	x		x	
list 43		x		x		x		x		x	

Table 4.1: Full saturation offset list apart from the two M_0 measurements at $\Delta\omega = -300$ ppm (upper row). The frequencies that are included in the respective lists are marked with an "x". The 54 offset list mainly reduces the sampling pattern outside the ranges of amide, amine or rNOE peaks compared to the 66 offset list. In addition, frequencies greater than 6 ppm are no longer measured on either side of the water frequency, but are measured asymmetrically to each other. In the 43 offset list, the focus is mainly on the amide peak, so the sampling pattern is also reduced around the amine frequency and the broader rNOE peak.

For the normalization, which is essential to generate the Z-spectrum, a reference volume M_0 with far off-resonant center frequency $\Delta\omega = -300$ ppm is acquired. To avoid that e.g. patient movement during the M_0 scan impedes the complete image series, two M_0 images are additionally acquired at the beginning of each CEST series. In the absence of artifacts, these are averaged before being used for normalization. In order to obtain a fully relaxed image, a recovery period prior to the saturation pulse train was established at $t_{\mathrm{rec},M_0} = 6\,\mathrm{s}$, while it was reduced to $t_{\mathrm{rec}} = 0\,\mathrm{s}$ for all saturated volumes.

4.2.2 3D-EPI readout

To minimize the total measurement time of a whole-brain CEST experiment, the goal in the sequence design was to acquire the entire image data following a single saturation module, comparable to a previous approach [30]. In this context, the primary challenge was to reduce the duration of the readout train, while simultaneously maximizing the contrast information.

The 3D-EPI [35, 116] readout is time efficient due to the few excitation pulses required. Additionally, it benefits from the ability to accelerate the data acquisition in both phase encoding directions further reducing the loss of prepared saturation during the readout. Considering the steady-state equation (Eq. 2.30), the prepared saturation magnetization decays during the 3D-EPI readout train with:

$$M_z(n) = M_{\text{sat}} \cdot \left(\cos\alpha \cdot \mathrm{e}^{-TR/T_1}\right)^n \tag{4.2}$$

Here, M_{sat} is the prepared saturation magnetization and n is the number of excitations which corresponds to the number of acquired partitions for a segmentation factor of one. Figure 4.4 depicts the decay of the prepared saturation for the different brain tissues. After only 25 excitations, the prepared saturation is reduced to its half.

For the acquisition of the whole-brain volume in sagittal orientation, the FOV corresponds to a size of $208 \times 160 \times 208\,\text{mm}^3$, resulting in 80 partitions for an isotropic resolution of 2 mm. When all partitions are acquired, two thirds of them are obtained with less than half of the original prepared

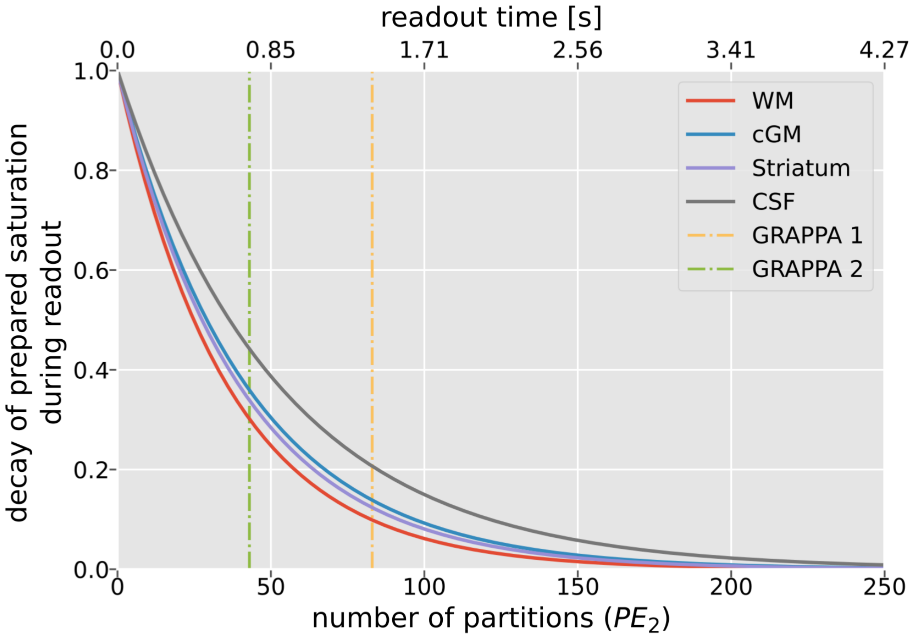

Figure 4.4: Simulated decay of the prepared saturation during readout for the different tissue types of the brain: WM, cortical GM (cGM), striatum and CSF. Additionally, the length of the EPI readout without acceleration in the second phase encoding direction (GRAPPA 1) and with an acceleration factor of two (GRAPPA 2) is depicted. Simulation parameters: $FA = 10°$, $TR = 17.07\,\text{ms}$, $T_1 = [1357, 2007, 1730, 4636]\,\text{ms}$ for WM, cGM, striatum and CSF, respectively (according to [117]).

saturation. Already an acceleration factor of two, reduces the number of these partitions to about one third and even the last ones are still measured with 30 % of the original prepared saturation. There are only three initial dummy excitations to extend the EPI readout, which are used to stabilize the phase (see Section 4.4.2).

The $R_1 \times R_2$ -fold undersampled k-space data (primary, PE_1, and secondary phase encoding, PE_2) combined with partial Fourier along the primary EPI phase encoding direction allows for minimal echo times TE and repetition times TR. Moreover, a high PE_1 acceleration factor and a high readout bandwidth serve to mitigate the impact of susceptibility-induced geometric distortion artifacts. To reconstruct the undersampled data, using a GRAPPA [47] implementation, the necessary autocalibration signal, containing 36×16 fully sampled calibration lines, is separately acquired by a fast low angle shot (FLASH) reference scan according to [118] only once at the beginning of the sequence (see Figure 4.2).

To counteract off-resonance artifacts (e.g. chemical shift, geometric distortions) and T_2^*-blurring, which come along with higher resolution, a segmented k-space blipped-controlled aliasing in parallel imaging (skipped CAIPI) [119] sampling scheme was used, further minimizing the geometry-dependent parallel imaging noise penalty (g-factor [120]). Figure 4.5 depicts the implemented trajectory, which schematic representation can be expressed as $3 \cdot 1_y \times 6_{z2}$. The trajectory implies a segmentation factor of $\Delta k_z = 3$ along the secondary phase encoding direction with a shift of $\Delta k_y = 1$ along the first phase encoding direction. However, since the z-blips are omitted between two consecutive excitations, the trajectory can also be described in a simplified form as $3 \times 2_{y1}$, which is also referred to as shot-selective CAIPI.

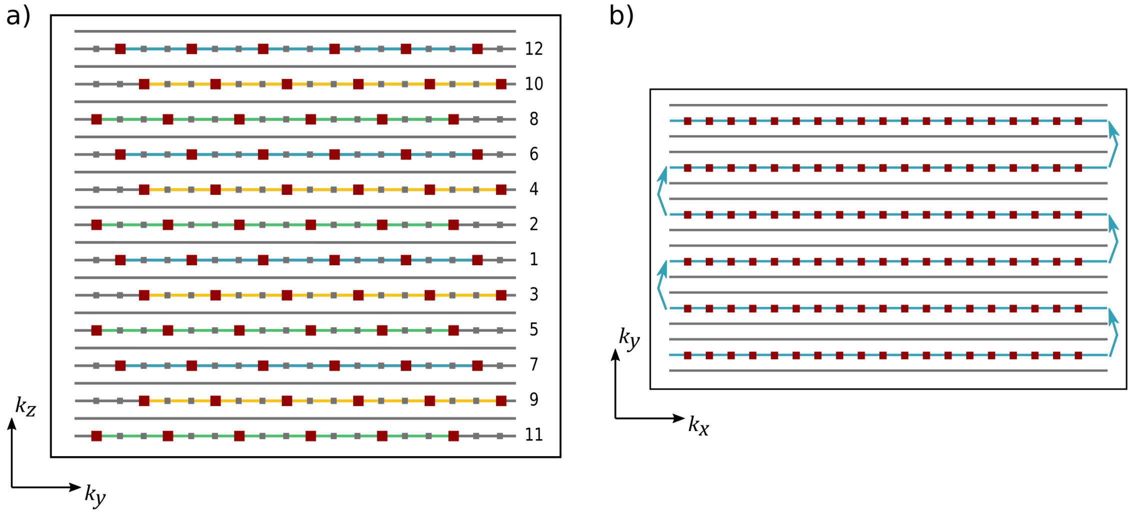

Figure 4.5: Schematic diagram of the k-space trajectory acquired with the shot-selective CAIPI pattern. a) The numbering denotes the shots and additionally illustrates the centric-reordered secondary-phase encoding direction. The shots with identical sampling are kept in the same color (blue, green or yellow) while skipped k-space data is shown in gray. b) In a single shot, all samples that match one secondary-phase encoding value are acquired. In the following shot, all samples of the next phase encoding value are measured with an offset of one. Acquired data is depicted with dark red dots, while the skipped samples are drawn in gray.

For further optimization of the contrast-to-noise ratio (CNR) in the image data, the acquisition of the partitions can also be performed centrically instead of linearly, which means that the dephasing gradient in the second phase encoding direction is played out with increasing amplitude but always opposite polarity to the previous partition. Centric-reordering yields the advantage that the central k-space planes, which store the contrast information of the image, are captured with the full prepared saturation.

Similar to the autocalibration scan, the phase correction scan, which consists of three EPI readouts, was implemented to be measured only once at the beginning of the sequence to counteract ghosting artifacts (compare Section 2.4.3). The external phase correction (ePC) methodology was employed to ensure that all volumes were corrected in a uniform manner, in contrast to internal phase correction (iPC), which may exhibit variability between acquisitions. Moreover, the use of an ePC scan shortens the minimum readout time.

To suppress fat chemical shift artifacts, a spatially non-selective single rectangular water-selective excitation (WE) pulse [121] was used, reducing the RF power and increasing the SNR efficiency in comparison to the conventional fat saturation approach typically employed in EPI. Here, the suppression of the fat signal is achieved by choosing the length of the rectangular pulse in such a way that the off-resonant lipid spins, which precess around the effective field B_{eff} (see Eq. 2.12), have only a longitudinal component at the end of the pulse and thus, do not contribute to the measured signal. In comparison to the equally effective binomial-11 water-selective excitation, the single rectangular RF pulse is less susceptible to B_0 inhomogeneities. A nominal flip angle of 10° was used close to the Ernst Angle (see Equation 2.31) of 9.07° for white matter with $T_1 = 1357\,\mathrm{ms}$ according to [117].

4.2.3 Adaptions for parallel transmit

A stable use of the pTx system was first ensured after the system upgrade of the 7 T MRI scanner to version E12. Therefore, the development of the necessary adaptations to incorporate parallel transmission into the sequence was integrated during a late stage of this thesis. All pTx pulses were calculated by Daniel Löwen as part of his doctoral thesis and were implemented by Yannik Völzke as part of the SCAFIELD project. More detailed information about the PUSHUP-CEST sequence development can be found in the recently submitted work of Völzke et al. [42].

For homogenization of the CEST saturation, the PUSH [122] (pulse design for saturation homogeneity) method, which was recently introduced for MT experiments, was transferred into the snapshot 3D-EPI CEST sequence [42]. Therefore, multiple subpulses with identical envelope function were used and weighted with different B_1 shims in order to homogenize the root-mean-square of the local B_1 amplitude, B_1^{rms}, during the saturation. Cosine-filtered Gaussian pulses were selected as the envelope function here. These B_1 shims are obtained by solving the minimization problem

$$w_{i,j} = \min\left(\left\|\sum_j \left|\rho_i(\vec{r})w_{i,j}\right| - B_1^{\mathrm{targ}}\right\|_2 + \lambda \left\|w\right\|_2\right). \tag{4.3}$$

where, $w_{i,j}$ is the complex amplitude of the j-th subpulse and the i-th coil, $\rho_i(\vec{r})$ is the complex B_1^+

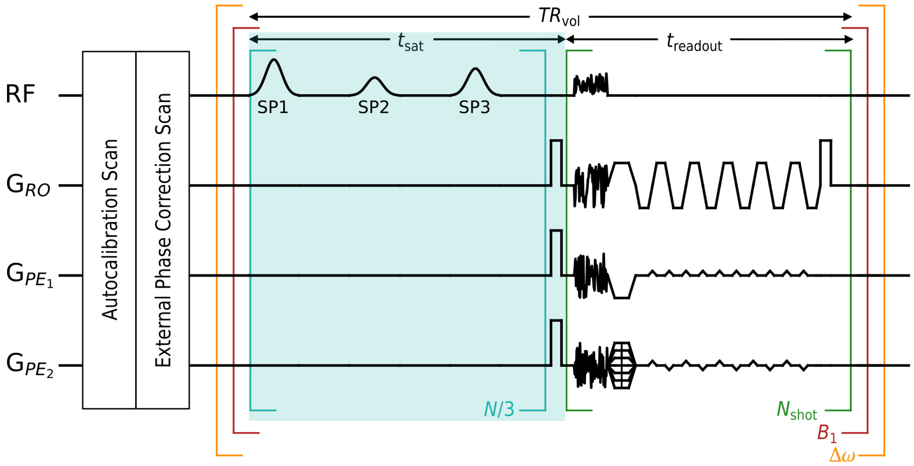

Figure 4.6: Schematic sequence diagram of the PUSHUP saturation module combined with the snapshot 3D-EPI readout. The saturation module contains three cosine-filtered Gaussian subpulses, which are played out $N/3$ times in an interleaved fashion. After the last saturation pulse, a crusher gradient disperses transversal magnetization. Afterwards, a CAIPIRINHA accelerated multi-shot 3D-EPI readout acquires a whole-brain image. Universal binomial-11 GRAPE are used for homogeneous water-selective excitation. The brackets indicate the repetition order. For each off-center frequency, all B_1 amplitudes are acquired in direct succession.

profile of the i-th coil and B_1^{targ} is the target B_1 amplitude. Additionally, a regularization parameter λ allows for a trade-off between homogeneity and SAR efficiency.

The minimization problem 4.3 can be solved for different region-of-interests (defined by masks). This allows to calculate different pulses for whole-brain and region-specific applications. In this work, three PUSH subpulses (SP) are implemented with respect to the whole-brain mask, which was extracted from MPRAGE [123] images using the brain extraction function of antspynet [124]. A schematic sequence diagram is depicted in Figure 4.6.

Since the iterative calculation of the optimal subject-specific pTx pulses during the measurement is time-consuming, the PUSH subpulses were calculated in advance as so called universal pulses (UP) [125]. This results in the name of the saturation module: PUSHUP [42]. The design of universal pulses is based on the assumption, that for the same type of experiments with a relatively small number of variables, the differences between subjects are moderate. Instead of solving the minimization problem in Eq. 4.3 for only one subject, it is now solved for multiple subjects simultaneously. The preceding database study was performed on ten young, healthy volunteers and includes in-vivo B_1 maps, acquired using AFI [126], B_0 maps and anatomical MPRAGE [123] images.

Moreover, the rectangular excitation pulse of the 3D-EPI sequence is changed to a universal binomial-11 GRAPE [127] pulse for homogeneous water-selecitve excitation and simultaneous fat suppression in the whole brain (see Fig. 4.6). The GRAPE pulse was calculated on the same database as the PUSHUP pulses but with the aim to homogenize the flip angle distribution instead of B_1^{rms}.

4.3 Image processing and artifact compensation

In order to obtain contrast maps from the acquired image series, several processing steps are necessary. Besides the CEST evaluation, it is also essential to align the different sequences and to compensate image artifacts in order to avoid resulting biases in the CEST contrasts.

4.3.1 Pre-processing

Before the final quantification of the CEST image series, all acquired MR images have to be registered to each other, i.e. adjusted in resolution and FOV. Using a distortion correction, susceptibility artifacts are removed from the CEST data to allow quantification of the CEST effect in all regions of the brain. For further analysis, the T_1 weighted MPRAGE image is segmented into its tissue types.

Image registration

CEST image series, structural images as well as the field maps are acquired with the same alignment but with varying FOV and resolution. For this purpose, linear registration by means of affine transformations is applied.

Image registration is a minimization problem in which the image transformation T^*, that minimizes the differences between the reference image Y and floating image X after its transformation, is desired [128]:

$$T^* = \arg \min_{T \in S_T} C\,(Y, T(X)) \tag{4.4}$$

where S_T is the space of allowable transformations, C is the cost function and $T(X)$ is the transformed floating image. For linear registration of 3D images, S_T is a set of all affine transformations consisting of the 12 parameters for the composite effects of translation, rotation, isotropic scaling, and shear.

Moreover, the image quality of the transformed image is determined by the type of interpolation.

Motion correction

In a CEST acquisition, a series of brain images are acquired. While the total time to acquire all the necessary images is several minutes, the time between individual volumes is only a few seconds. The voxel-by-voxel analysis assumes that voxels do not change spatially over time. However, under real conditions, especially when clinical patients are involved, there will always be some degree of subject movement, necessitating correction of these displacements.

Motion correction involves the image registration of multiple image volumes [128]. Since all images were acquired from the same subject and with the same imaging parameters, apart from the saturation frequency, the rigid body transformation space with its 6 parameters for translation and rotation is used. Assuming that there is very little movement between two successively acquired images, the result of one registration can be used as the initial assumption for the next registration.

The definition of a reference image, to which the whole image series will be aligned, is an important element of the image registration process. Zhang et al. [129] showed that one of the saturated images is much more suitable as reference than the unsaturated image, because the unsaturated contrast is significantly different to the remaining image series. The volume at the saturation frequency of

$\Delta\omega = 3.5$ ppm is chosen as reference image, since this provides the least motion artifacts for CEST evaluation of the amide contrast .

Distortion correction

Due to the EPI readout, the images suffer from susceptibility-induced geometric distortion artifacts, which need to be corrected. Besides the possibility to segment the data acquisition in the first phase encoding direction to reduce the distortions, the remaining artifacts can also be calculated out retrospectively [130]. Therefore, two separate images are needed with the same image parameters, except for opposing polarities of the phase-encoding blips, leading to distortions in opposing directions. Using these two images and the acquisition parameters, the susceptibility-induced off-resonance field is determined with which the sum-of-square difference of the two images is minimized after their unwrapping.

Assuming that the field induced by susceptibility is constant for the whole image series, the resulting field can be applied to correct all images. For this reason, motion correction is performed first.

Segmentation

To improve computational performance, it is useful to extract the brain and remove the non-brain tissue from the image of the entire head. For this purpose, a deformable model that adapts to the brain surface is used [131].

For the interpretation of the CEST contrast maps, a probabilistic segmentation of the brain into the three different tissue types is performed using the MPRAGE data. Exemplifying ROIs of gray matter (GM), white matter (WM) and cerebrospinal fluid (CSF) are shown in Figure 4.7. To do this, it is necessary to correct for spatial intensity variations caused by RF inhomogeneities (also known as bias field). The segmentation algorithm is based on a hidden Markov random field model and an attendant expectation-maximization algorithm [132].

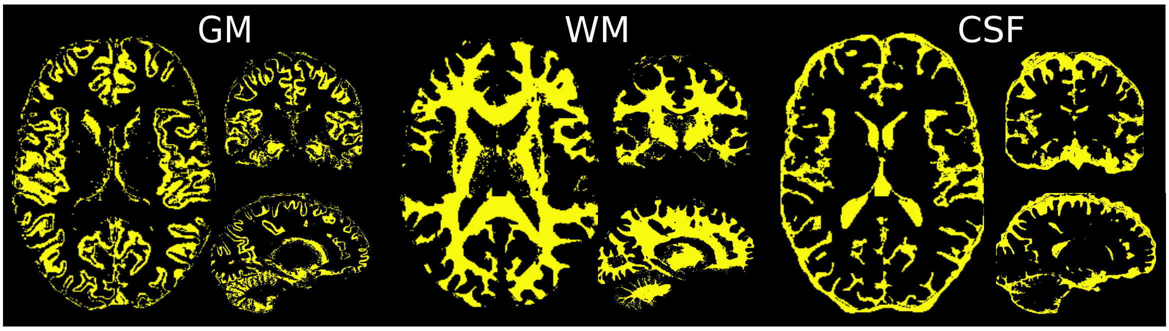

Figure 4.7: Exemplifying segmented ROIs for gray matter (GM), white matter (WM) and cerebrospinal fluid (CSF) of a healthy volunteer in axial, coronal and sagittal orientation. The subject-specific tissue segmentation is based on T_1-weighted MPRAGE images.

4.3.2 CEST quantification

To obtain quantitative maps of the isolated CEST contrasts from the acquired and pre-processed MR data, voxel-wise Z-spectra are generated at the first step. For this purpose, each presaturated volume is normalized with the unsaturated volume $M_{z,0}$ which is acquired first for each CEST sequence with $\Delta\omega = -300\,\text{ppm}$.

Since the different magnetization transfer effects overlap in the in-vivo Z-spectrum, it is necessary to isolate the individual CEST effects in order to make a quantitative statement. To achieve this, both the labeled Z-value (Z_{lab}), resonant to the desired effect, and the reference Z-value (Z_{ref}), which includes components of other effects like direct water saturation or ssMT, must be determined. Furthermore, it is necessary to compensate for noise and outliers in the acquired MR data set.

5-pool Lorentzian fit model

For stable extraction of Z_{lab} and Z_{ref}, a 5-pool Lorentzian model [37, 133] was voxel-wise fitted to each Z-spectrum using the Levenberg–Marquardt algorithm:

$$Z(\Delta\omega) = \frac{M_z(\Delta\omega)}{M_{z,0}} = Z_{\text{base}} - \sum_i L_i(\Delta\omega) \tag{4.5}$$

with

$$L_i(\Delta\omega) = A_i \frac{\Gamma_i^2/4}{\Gamma_i^2/4 + (\Delta\omega - \delta_i)^2}. \tag{4.6}$$

The five pools i represent direct water saturation, semisolid magnetization transfer, xchange-relayed NOE and the CEST effect of amides and amines. The individual Lorentzian function L_i depends on the frequency offset $\Delta\omega$ and is defined by amplitude A_i, chemical shift δ_i and full width at half maximum Γ_i. Z_{base} is a correction parameter to compensate for a systematic signal reduction due to imperfect recovery. An exemplifying fitted Z-spectrum of a single WM voxel from a healthy volunteer is shown in Figure 4.8.

To gain the label Z-value the entire fit is employed:

$$Z_{\text{lab}}(\Delta\omega) = Z_{\text{base}} - \sum_i^{n=5} L_i(\Delta\omega). \tag{4.7}$$

In contrast, the reference Z-value is obtained by excluding the Lorentzian pool of interest j:

$$Z_{\text{ref},j}(\Delta\omega) = Z_{\text{base}} - \sum_{i\neq j}^{n=5} L_i(\Delta\omega). \tag{4.8}$$

Start parameters and boundaries for the fitting routine are listed in Table 4.2.

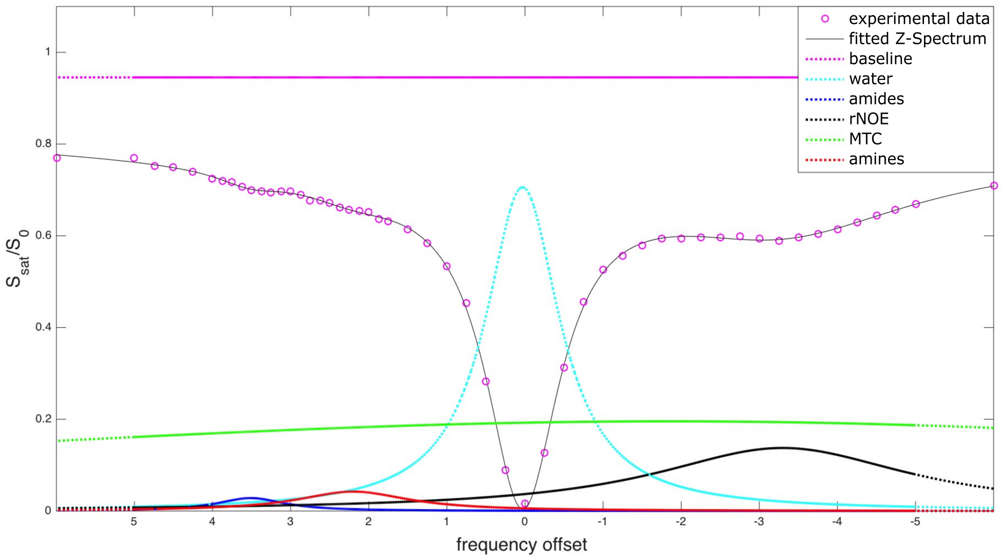

Figure 4.8: Exemplifying experimental data and fitted Z-spectrum of a single WM voxel after B_0 and B_1 correction (only the section between 6 and -6 ppm is shown). Additionally, the Lorentzians of the individual pools are shown at the bottom.

	Start	**Upper**	**Lower**
Z_{base}	1.000	1.0	0.50
A_{water}	0.900	1.0	0.02
Γ_{water}	1.400	10.0	0.30
δ_{water}	0.000	1.0	-1.00
A_{ssMT}	0.100	1.0	0.00
Γ_{ssMT}	25.000	100.0	10.00
δ_{ssMT}	-1.000	-1.0	-4.00
A_{rNOE}	0.020	0.4	0.00
Γ_{rNOE}	3.000	5.0	1.00
δ_{rNOE}	-3.500	-2.0	-4.50
A_{amides}	0.025	0.2	0.00
Γ_{amides}	0.500	3.0	0.40
δ_{amides}	3.500	4.0	3.00
A_{amines}	0.010	0.2	0.00
Γ_{amines}	1.500	3.0	1.00
δ_{amines}	2.200	2.5	1.00

Table 4.2: Fit parameters of the five-pool Lorentzian fit including starting points as well as upper and lower limits. While Z_{base} and amplitude values, A_i, are given in the relative range from 0 to 1, chemical shift, δ_i, and FWHM, Γ_i, of each pool are given in ppm.

CEST metric

With Z_{lab} and Z_{ref} different metrics to quantify the magnetization transfer ratio can be calculated to including different orders of spillover and ssMT correction. Two different metrics are used to obtain contrast maps, according to Section 3.4:

$$MTR_{\text{LD}}(\Delta\omega) = Z_{\text{ref}}(\Delta\omega) - Z_{\text{lab}}(\Delta\omega) \tag{4.9}$$

$$MTR_{Rex}(\Delta\omega) = \frac{1}{Z_{\text{lab}}(\Delta\omega)} - \frac{1}{Z_{\text{ref}}(\Delta\omega)} \tag{4.10}$$

B_0 correction

The increased B_0 inhomogeneities observed at high field strengths due to local susceptibility-induced field shifts lead to spectral shifts in the Z spectrum. These are particularly easy to detect in the direct saturation (DS) when its center frequency deviates from 0 ppm.

To guarantee an accurate evaluation of the CEST data it is therefore essential to correct the B_0 shifts. Using a B_0 map, which represents the shifts in ppm, the CEST data are linearly interpolated voxel by voxel onto a fine grid and shifted by the corresponding frequency deviation $\Delta\omega_{B0}$ [134].

The B_0 maps are obtained by a short dual-echo scan immediately before the CEST measurement. Alternatively, B_0 maps can also be obtained by using the voxel-wise center frequency of the DS.

B_1 correction

CEST effects are strongly dependent on the saturation amplitude B_1 [37, 71], as described in Section 3.4.3. Due to the high field strength of 7 T and the large FOV in whole-brain measurements, the CEST experiment is affected by stronger B_1 inhomogeneities. As a benchmark, deviations of 50 % are typical across the brain at 7 T.

To minimize the influence of B_1 inhomogeneities on the quantification of CEST effects, the interpolation approach of Windschuh et al. [37] was applied as a retrospective correction method. For this purpose, it is necessary to perform several CEST measurements with different B_1 amplitudes as well as to acquire a B_1 map to determine the CEST contrasts for a defined $B_{1,\text{out}}$.

Using the acquired relative B_1 map $rB_1(\vec{r})$, the actual saturation amplitude $B_1(\vec{r})$ in each voxel can be determined:

$$B_1(\vec{r}) = rB_1(\vec{r}) \cdot B_{1,\text{norm}} \tag{4.11}$$

where $B_{1,\text{norm}}$ is the nominal B_1 value specified in the protocol settings.

The B_1 correction is applied to the already B_0-corrected Z-spectra by voxel-wise spline interpolation. By adding an initial data point $Z(\Delta\omega, B_1 = 0\mu\text{T}) = 1$, the stability of the interpolation is increased [37]. After the so-called Z-B_1-correction, the CEST contrasts can be quantified by evaluating the corrected Z-spectrum, calculated for a chosen B_1-value $B_{1,\text{out}}$.

In addition to the Z-spectrum based B_1 correction, a contrast-based 1-point B_1 correction was performed for pTx data using a method recently introduced by Lipp et al. [135] for the B_1 correction of MT saturation maps. In this method, the calculated MTsat map is voxel-wise multiplied by a factor

$$F(C,\vec{r}) = \frac{1}{1 + (B_1^{\text{norm}}(\vec{r}) - 1)C}, \tag{4.12}$$

where $B_1^{\text{norm}}(\vec{r})$ is the local, normalized B_1^{rms} and C a constant factor that needs calibration. In this work, C was estimated for each CEST contrast individually. C was chosen such that it minimizes the root-mean-square difference between the 3-point B_1-corrected and the 1-point B_1-corrected maps. This was evaluated with PUSHUP whole-brain maps, were the lowest B_1^{rms} inhomogeneities are to be expected. The optimal C was found to be 1.44 for ssMT, -0.292 for rNOE and -0.108 for amides. Due to the much lower saturation homogeneity, this approach fails to effectively B_1-correct sTx CEST maps.

4.3.3 Post processing workflow

The entire data processing pipeline is illustrated in Figure 4.9. First, all CEST image series were registered to the 3.5 ppm image (amides) of the measurement with saturation amplitude nearest $B_{1,\text{out}}$ using FSL's [136–138] motion correction tool MCFLIRT [128]. For this purpose, the reference volume is extracted using one of the FSL utility functions FSLROI.

Subsequently, geometric distortion correction is applied to the motion corrected data using voxel shift maps. This distortion field is determined from two short EPI pre-scans with opposite first phase encoding directions (AP and PA) using the FSL tool TOPUP [130, 136]. In the next step, the CEST data is masked based on the distortion-corrected reference image using the brain extraction tool BET [131].

In preparation for the CEST evaluation, the acquired B_0 and B_1 maps are converted to relative field maps with the help of a python based Jupyter notebook [139], and registered to the reference image in order to match resolution and FOV using FSL's FLIRT [128, 140]. Since the field maps contain very few structural elements of the brain, only the information from the Nifty header is used for registration.

Using the frequency offsets identified by the relative B_0 maps, the Z-spectrum data are shifted and subsequently corrected for B_1 inhomogeneities using the approach of Windschuh et al. [37]) based on the relative B_1 map. Afterwards, the Lorentzian difference method is used to generate the peak-selective CEST maps. A custom MATLAB routine (MathWorks, Natick, USA) based on a publicly available toolbox (`https://www.cest-sources.org`) was used to process Z-spectra and CEST maps.

At last, MTR_{LD} maps are analyzed in white matter (WM) and gray matter (GM) regions identified from a 0.7 mm isotropic T_1-weighted scan using FSL's FAST interface [132]. For this purpose, the MTR_{LD} maps are registered to the T_1 weighted data using FLIRT [128, 140] based on the transformation determined from the reference image. Mean values and standard deviations, as well as histograms were calculated in python based Jupyter notebooks [139].

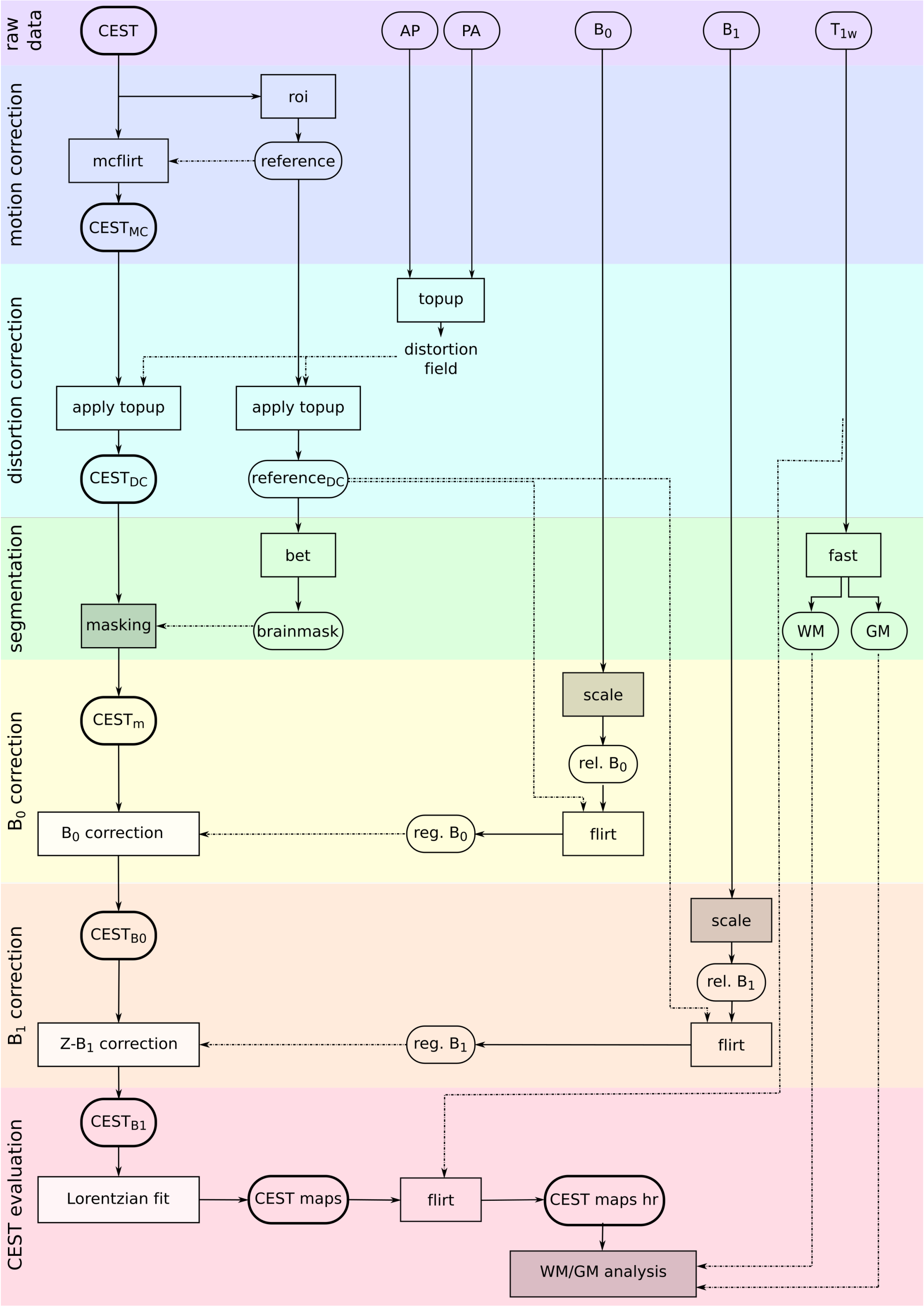

Figure 4.9: Complete processing workflow from acquired raw data to CEST maps. The different colors represent the different processing steps. Image data is framed by rounded outlines whereby CEST data is bold-framed. Algorithms are represented by rectangular frames, distinguishing between FSL (transparent), iPython (darkened) and Matlab (lightened). Auxiliary variables are unframed. Solid lines mark the images to be handled, while dotted lines denote the auxiliary structures of the respective process step.

4.4 Simulations and phantom experiments

Since the measurable CEST effect strongly depends on the used saturation scheme of the experiment, simulations and phantom measurements were deployed to determine the best parameters of the saturation pulse train. Moreover, phantom measurements were carried out to analyze the evolution of the signal magnitude and the global frequency offset during the whole-brain readout.

4.4.1 Bloch-McConnell simulations

CEST simulations were performed with the open-source MRI simulation framework JEMRIS (`www.jemris.org`) [95]. JEMRIS provides an MRI sequence development and simulation environment for the most general case of non-interacting classic spins. Numerical integration of the Bloch equations in the rotating frame is performed using time-varying stepwise ODE solvers in cylindrical coordinates. Extended by the Bloch-McConnell equations, which were introduced in Equation 3.8, JEMRIS allows to optimize the CEST saturation and thus maximize this effect [141, 142]. Appendix B contains examples for the verification of CEST simulations with JEMRIS. These examples are compared with other established simulations and with simple phantom experiments.

JEMRIS simulations were implemented to design a saturation module that maximizes amide contrast while minimizing unwanted side effects and artifacts. Therefore, all experiments were performed with a two pool model, containing water and amide protons. While for the water pool only the relaxation times have to be defined, the model for the exchangeable pool contains besides the chemical shift also the information about the exchange rate and concentration of the solute. The simulation parameters of the two-pool model are given in Table 4.3.

	water	**amides**
T_1	2000 ms	1000 ms
T_2	115 ms	33 ms
$\delta\omega$	0 ppm	3.5 ppm
k_s		0.03
f_s		0.001

Table 4.3: Simulation parameters of the two-pool model, containing a large water pool and a much smaller solute pool (amides). This two-pool model was used in all JEMRIS experiments.

The experiments were performed for $B_0 = 7\,\mathrm{T}$. The saturation module consists of N Gaussian shaped RF-pulses with varying RF duration t_p and duty cycle DC. The number of pulses is chosen in a way that the combination of different pulse lengths and duty cycles each matches a defined saturation time t_sat. Furthermore, the length of the pulse train is varied in a range of 1 to 12 s for six different pulse durations with a duty cycle of 50 % as well as for $t_\mathrm{p} = 30\,\mathrm{ms}$ combined with a varying duty cycle, see Table 4.4. Following the saturation module, the entire FID signal is immediately measured and no spatial encoding is simulated. The experiment is repeated for saturation frequencies $\Delta\omega$ ranging from -5 to 5 ppm with a 0.1 ppm interval. Example Z-spectra are presented in Figure 4.10.

Simulated CEST effects were analyzed by calculating the MTR_asym at $\Delta\omega = 3.5\,\mathrm{ppm}$ (see. Eq. 3.35). MTR_asym is evaluated in dependence of t_sat for different combinations of t_p and DC. Since the specific absorption rate is one of the limiting factors in in-vivo CEST measurements, the SAR contribution

B_0 [T]	7
B_1 [µT]	1
n_{spins}	2
$\Delta\omega$ [ppm]	-5 to 5
t_{sat} [s]	1 to 12
t_{p} [ms]	5, 15, 30, 45, 60, 90
DC [%]	25, 33.3, 50, 66.7, 75

Table 4.4: Simulation parameters of the JEMRIS experiments to investigate the CEST effect in dependency of the saturation time t_{sat} for varying pulse duration t_{p} and duty cycle DC.

due to these saturation moduls is estimated by:

$$\text{SAR} \propto \int B_1^2(t)\mathrm{d}t, \tag{4.13}$$

where $B_1(t)$ is the time dependent RF saturation amplitude, containing the full pulse train.

Because the flip angle changes with the varying length of the Gaussian RF pulse (see. Eq. 2.9), the dependence of the CEST effect on the pulse duration t_{p} and the flip angle FA is also investigated by means of MTR_{asym}. Here, the simulation was performed under the condition of $t_{\text{sat}} = 4$ s and $DC = 50$ % with t_{p} ranging from 5 to 100 ms for three different saturation amplitudes $B_1 = [0.5, 1.0, 1.5]$ µT.

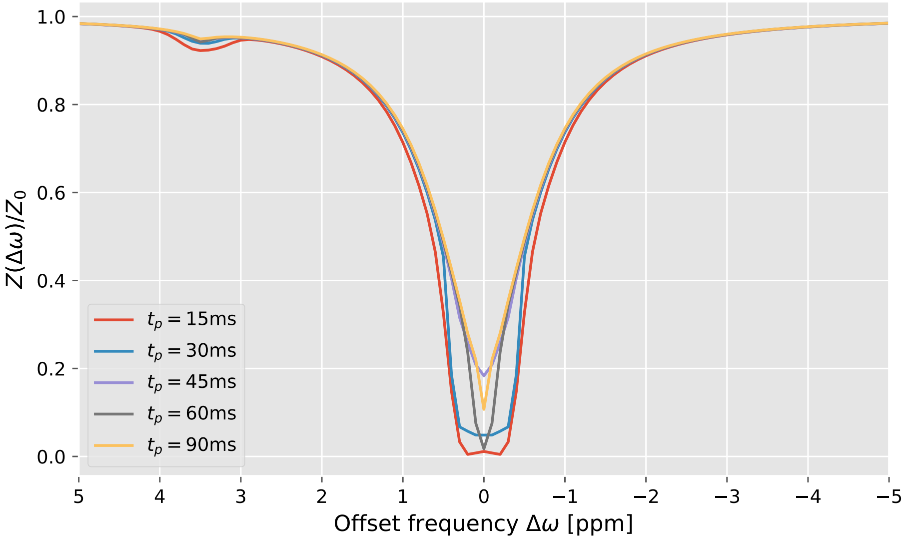

Figure 4.10: Example Z-spectra of the simulated CEST experiment of the two-pool model with a train of Gaussian shaped RF pulses. Simulation parameters: $t_{\text{sat}} = 6$ s, $DC = 50$ %, $t_{\text{p}} = [15, 30, 45, 60, 90]$ ms.

4.4.2 Phantom validation

Phantom experiments were executed to validate the simulation results under real conditions, including the 3D-EPI readout, but without the concomitant effects of the human brain. In addition, signal and frequency evolution during the 3D-EPI readout were investigated independent of the saturation module.

Design of the saturation pulse train

The CEST experiments were performed in two available, in-house made phantoms filled with aqueous solutions, one containing the two brain metabolites glutamate and GABA (ratio 2:1) and the other containing creatine (Cr) and GABA (ratio 2:1). The two phantoms were positioned within the head coil at the same time.

Following the simulations, 25 phantom experiments were performed with a saturation module of $t_{\mathrm{sat}} = 4\,\mathrm{s}$ containing Gaussian shaped RF-pulses with varying pulse duration t_{p} between 5 and 95 ms in steps of 5 ms, except for the range from 20 to 45 ms where the step width is reduced to 2.5 ms. The duty cycle was kept constant at $DC = 50\,\%$. After a M_0 measurement at -300 ppm, the sequence is repeated 101 times to acquire the Z-spectrum from -5 to 5 ppm with a spectral resolution of 0.1 ppm. Here, frequency offsets larger than 5 ppm were not sampled, since no ssMT effect is to be expected.

The mean Z-spectrum and the associated standard deviation was calculated of a 5×5 voxel ROI ($10 \times 10 \times 2\,\mathrm{mm}^3$) centered in the corresponding phantom. Beyond that, an evaluation of the mean MTR_{asym} and the related standard deviation within the ROI were performed.

Evolution of signal magnitude and frequency offset

Another phantom experiment was performed to analyze the evolution of the signal magnitude and the global frequency offset during a full 3D-EPI acquisition. Therefore, a spherical phantom (D165 yellow; Siemens AG, Munich, Germany), containing Polydimethylsiloxan oil, was used. Solely for this experiment internal phase correction scans were applied. The iPCs were acquired between each excitation pulse and the EPI-typical spatial encoding gradients, see Fig. 4.11.

Taking the sum of the iPC data after each excitation, the signal magnitude was first determined using RMS coil combination. The phase evolution between the initial and the third echoes of the iPC scan, with the same readout gradient polarity, was employed to calculate the global frequency offset relative to the reference frequency. For this purpose, the point-wise phase difference was determined between these echos following Fourier transform along the read dimension. The result was then averaged over all coils and readout points, with the corresponding magnitudes serving as weights. This provides the global phase difference $\Delta\phi$ between the two echoes, which is directly proportional to the global frequency offset Δf, according to

$$\Delta f = \frac{\Delta\phi}{4\pi \cdot \Delta t_{\mathrm{echo}}} \tag{4.14}$$

Here, the temporal spacing between echo 1 and 3 equals two times the EPI echo spacing, Δt_{echo}.

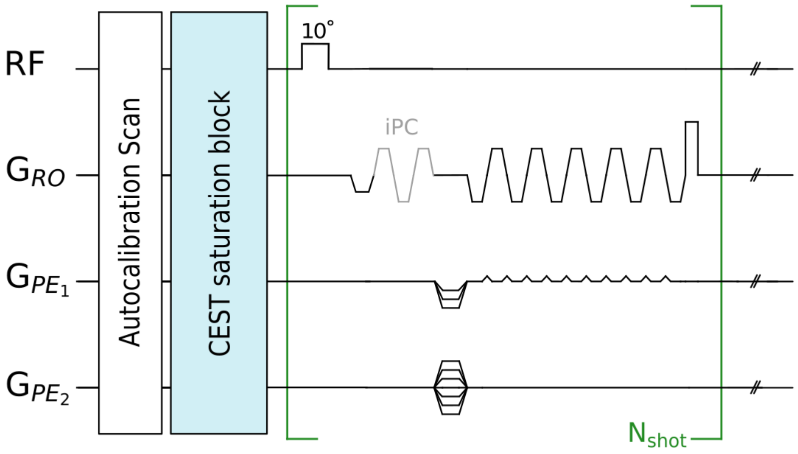

Figure 4.11: Schematic sequence diagram of the 3D-EPI including internal phase correction (iPC) scans. Each iPC scan is recorded subsequent to the excitation pulse and comprises three readout gradients, with the middle one having the opposite polarity.

4.5 In-vivo imaging

Human in-vivo data were acquired from young healthy volunteers (male and female in the age of 20 to 40 years). All examinations were in accordance with the guidelines set by the local ethics committee and after obtaining written informed consent from the subjects.

The imaging and saturation parameters were mainly the same for the in-vivo measurements. Sequence parameters of the final protocol are listed in Table 4.5. However, some adjustments were made during the sequence development process, in particular as a result of the IDEA upgrade from version B17 to E12. Deviations from the protocol can also be found in Appendix A.

Based on the simulation results, the saturation period was set to $t_{\mathrm{sat}} = 3.6\,\mathrm{s}$ and contains unless stated otherwise 120 Gaussian RF pulses ($t_{\mathrm{p}} = 15\,\mathrm{ms}$, $t_{\mathrm{d}} = 15\,\mathrm{ms}$, $DC = 50\,\%$) with a saturation amplitude of $B_{1\mathrm{mean,sat}} = 0.8\,\mu\mathrm{T}$. A minimal echo time of $TE = 6\,\mathrm{ms}$ was used with a bandwidth of 2290 Hz/Px, resulting in readout duration of $t_{\mathrm{readout}} = 734\,\mathrm{ms}$. The acquisition time per offset was $TR_{\mathrm{vol}} = t_{\mathrm{sat}} + t_{\mathrm{readout}} = 4.4\,\mathrm{s}$. With 43 saturation offsets, two M_0 scans, and including GRAPPA autocalibration as well as external phase correction scans, this resulted in a total acquisition time of $TA = 3:27\,\mathrm{min}$ for a whole-brain CEST spectrum.

While all measurements during sequence development were performed at an isotropic resolution of 2 mm, the final protocol had to be adapted to acquire whole-brain CEST data at an improved resolution with voxel size of $(1.61\,\mathrm{mm})^3$. For better comparability with the results of the PUSHUP-CEST approach using parallel transmit (see Section 4.2.3), the high-resolution data were acquired in circular polarized (CP) mode, also utilizing the pTx head coil.

parameter	**sTx**	**pTx**
isotropic resolution	2.0 mm	1.61 mm
FOV (AP, FH, RL)	$208 \times 160 \times 208$ mm^3	$207 \times 181 \times 216$ mm^3
total acquisition time (TA)	3:27 min	3:40 min
repetition time (TR)	4400 ms	4700 ms
echo time (TE)	6.0 ms	6.7 ms
EPI factor	26	24
echo spacing	0.56 ms	0.61 ms
acquisition bandwidth	2290 Hz/Px	1964 Hz/Px
acceleration factor	6 (3×2)	8 (4×2)
segmentation factor	3	1
partial Fourier	6/8	6/8
orientation	sagittal	sagittal
phase encoding direction	anterior - posterior	anterior - posterior
k-space ordering	centric out	centric out

Table 4.5: Final acquisition parameters of the snapshot 3D-EPI CEST sequence used for in-vivo measurements. Parameters differ for experiments utilizing the single transmit and the parallel transmit head coil.

4.5.1 Determination of imaging parameters

In-vivo experiments on healthy subjects were part of the verification of the 3D-EPI optimizations process. To review the efficiency of a water-selective excitation pulse, the snapshot 3D-EPI CEST sequence was acquired with and without water-selective excitation. Moreover, full Z-spectra were acquired with linear as well as with centric-reordered second phase encoding direction.

Based on the analysis of the global frequency evolution, three initial dummy excitations were implemented between the saturation period and the 3D-EPI readout (included in $t_{\text{readout}} = 734\,\text{ms}$). The effect of these dummies was investigated by means of the temporal signal-to-noise ratio (tSNR), which is a measure for the signal stability over time. For this purpose, 40 unsaturated images each with and without dummy excitations were acquired of the same subject. tSNR was calculated voxel-wise as temporal mean value divided by the temporal standard deviation [143]:

$$\text{tSNR}(\vec{r}) \propto \frac{\text{mean}(\vec{r})}{\text{standard deviation}(\vec{r})} \tag{4.15}$$

where, $\vec{r}$ denotes the location of voxel.

4.5.2 B_1 inhomogeneity counteracting

A major challenge of whole-brain CEST experiments is the strong B_1 variation within the large FOV, which is required to cover the complete brain tissue. In order to generate reliable contrast maps using the retrospective B_1 correction (see Section 4.3.2), several in-vivo experiments were performed to identify the best setup.

Global RF distribution

In a first step, B_1 mapping was performed on nine subjects to characterize the global RF distribution. B_1 mapping was accomplished using a volumetric single-shot DREAM[67] variant (3DREAM) [66], including the following sequence parameters: TR = 3334 ms, TE_1/TE_2 = 1.1/2.04 ms, FA_{nom} = 60°, $GRAPPA$ 2 × 2, voxel size = $(4\,\mathrm{mm})^3$, TA = 6.6 s. The resulting flip angle map represents the actual flip angle, which deviates from the nominal flip angle due to strong B_1 inhomogeneities at 7 T. In the context of this analysis, the flip angle maps were converted to reference voltage maps by:

$$U_{\mathrm{ref}}(\vec{r}) = \frac{FA(\vec{r})}{FA_{\mathrm{nom}}} \cdot U_{\mathrm{nom}}. \tag{4.16}$$

The reference voltage is defined by the system's vendor as the voltage required for full inversion with a 1 ms block pulse. FA is referred to the measured flip angle, FA_{nom} denotes the nominal sequence flip angle and U_{nom} is the reference voltage employed in the acquisition of the B_1 map.

Subsequently, a non-linear registration of the reference voltage maps to the 1 mm T_1-weighted MNI template was performed utilizing the AntsRegistration interface [144]. The non-linear transformation was determined from a non-saturated CEST volume (M_0) of the same session to which the reference voltage map was linearly registered using FLIRT [138] as an intermediate step. A joint histogram was calculated for the reference voltage across all subjects. Furthermore, a 1 mm maximum probability map (threshold 25) of FSL [136–138] was utilized to analyze the mean reference voltage separately for the different brain regions. The voxel-wise standard deviation between subjects was calculated in addition to the group reference voltage map.

Number of B_1 values

The number of necessary CEST data sets with different nominal B_1 was investigated for optimal B_1 inhomogeneity correction. To this end, the CEST sequence was repeated seven times within one session with a healthy subject. The nominal saturation amplitude of $B_{1,\mathrm{sat}} = 0.8\,\mu\mathrm{T}$, was scaled by adjusting the reference voltage for each Z-spectrum measurement, which also scales the flip angle of the single-rectangular water-selective excitation pulses. Based on the previously analyzed reference voltage distribution, the reference voltage was adapted in a range of 150 to 450 V with a 50 V increment without exceeding SAR limits.

Afterwards, the B_1 correction of the Z-spectrum data were performed based on the 3DREAM B_1 map applying different reference voltage combinations, listed in Table 4.6. The number of distinct reference voltages (B_1 sampling points) considered for the combinations is denoted as N_{B1}. Each reference voltage combination included the additional assumption of zero-crossing for all CEST effects at 0 V.

To evaluate the B_1 correction with a varying number of B_1 sampling points, MTR_{Rex} with $N_{B1} = 7$ was assumed as the ground truth. Therefore, the voxel-wise absolute error (AE) for each N_{B1} was calculated as well as the whole-brain median of the absolute error. In order to quantify the AE as a function of the actual B_1, the brain was divided into 40 regions of discrete B_1 bins. The median AE was calculated for each B_1 bin, with CSF regions excluded in both cases.

N_{B1}	**reference voltage, U_{ref} [V]**						
1				300			
2		200					450
3		200		300			450
4	150	200		300			450
7	150	200	250	300	350	400	450

Table 4.6: Corresponding reference voltages for the distinct B_1 sampling points N_{B1} utilized for the varying B_1 correction combinations in sTx experiments.

Dielectric bags

A common approach to compensate for the wavelength effect that causes B_1 variations is to use high permittivity materials (HPMs) near the region of interest. This method relies on a displacement current within the dielectric material that generates a secondary field according to the modified Ampere's law [145]. This passive RF shimming by means of HPMs with so-called dielectric bags has already been demonstrated in various neuroimaging applications at 7 T [146–150].

To investigate the viability of dielectric bags for whole-brain CEST experiments, the complete CEST experiment was performed with and without bags in one healthy subject. To this end, a set of three rectangular pouches of $18 \times 12 \times 0.8\,\text{cm}^3$ (Multiwave Technologies, Geneva, Switzerland), containing Calcium titanate $CaTiO_3$ as dielectric material (relative permittivity ε_r between 100 and 120 [146]) combined with Deuterium oxide D_2O, were placed between head and receive coil. Previous examinations (data not shown here) revealed the benefit of positioning one bag lengthwise under the head and two bags to the right and left of the head at ear level.

Based on the B_1-correction analysis, the CEST sequence was repeated three times with reference voltages of $U_{\text{ref}} = [200, 300, 425]$ V for both setups. The maximum reference voltage had to be reduced from 450 to 425 V compared to previous experiments, as the SAR contribution increased due to the integration of the dielectric bags.

Parallel transmit

Another approach that has become increasingly popular in the recent past is the use of parallel transmit due to the potential for homogenization of the transmit field.

To this end, the PUSHUP-CEST sequence was used for in-vivo experiments on five healthy volunteers utilizing the 32-channel receive, 8-channel transmit coil (Nova Medical, Wilmington). With identical EPI settings, listed in Table 4.5, two CEST experiments have been performed: one with CP saturation and the other using the whole-brain optimized saturation with three PUSHUP subpulses. In both cases, three B_1 amplitudes have been measured. The CP saturation is used with 50 %, 100 %, and 150 % of the target B_1^{rms} of 0.8 µT based on the results of previous examinations. Due to the smaller expected B_1^{rms} variation when PUSHUP saturation is used, the range was reduced to 80 %, 100 %, and 120 %. To avoid the immediate succession of high SAR saturation modules, each B_1 amplitude was used for one off-center frequency before repeating this for subsequent frequencies. The repetition order is also shown in Figure 4.6 of Section 4.2.3. It should be noted that in contrast to the sTx version of the sequence, only the saturation B_1 was scaled, but not the excitation pulses of the 3D-EPI readout as the universal 11-binominal GRAPE pulse is used in both setups. The reference voltage was set to $U_{\mathrm{ref}} = 335\,\mathrm{V}$, which corresponds to the mean B_1 of the CP distribution.

According to the experiments with single transmit 4.5.2, B_1 correction of the PUSHUP-CEST data was performed with four different combinations of B_1 sampling points:

- no B_1 correction
- $N_{B1} = 1$: only central B_1 amplitude (100%)
- $N_{B1} = 2$: only outer B_1 amplitudes (80% and 120%)
- $N_{B1} = 3$: all three B_1 amplitudes (80%, 100% and 120%)

Finally, the contrast maps were compared with those of CP saturation, corrected with 3 N_{B1} to identify the necessary number of B_1 sampling points in whole-brain CEST experiments using pTx pulses.

4.5.3 Evaluation of whole-brain CEST

To evaluate the performance of the developed snapshot 3D-EPI CEST sequence and the related processing pipeline to deliver high-quality whole-brain contrast maps, a number of in-vivo measurements were performed.

Based on the simulation and phantom experiment results, five different saturation schemes were measured within one session of a healthy volunteer. The number of Gaussian-shaped RF pulses N_{p} was varied to kept the total saturation time the same at $t_{\mathrm{sat}} = 3.6\,\mathrm{s}$. The saturation parameters are summarized in Table 4.7. In all cases, three different reference voltages of $U_{\mathrm{ref}} = [200, 300, 450]\,\mathrm{V}$ with nominal $B_{1,\mathrm{sat}} = 0.8\,\mu\mathrm{T}$ were used to acquire the CEST sequence, corresponding to the B_1-correction analysis.

N_{p}	t_{p} [ms]	t_{d} [ms]	DC [%]	t_{sat} [s]	$B_{1,\mathrm{sat}}$ [μT]
120	15	15	50	3.6	0.8
60	30	30	50	3.6	0.8
40	45	45	50	3.6	0.8
30	60	60	50	3.6	0.8
20	90	90	50	3.6	0.8

Table 4.7: CEST saturation parameters for the different saturation schemes.

Moreover, test-retest measurements were performed to review the reproducibility of the complete CEST pipeline. For this purpose, one healthy subject was measured on three different days with the same protocol, and for three other subjects the CEST sequences were measured twice within one session. In each case, three reference voltages were used for retrospective B_1 correction and separate B_0 and B_1 maps were acquired immediately before the CEST sequence block was played out. Besides the CEST maps and the mean values for WM and GM, the intra-subject coefficient of variation was determined in both cases.

Statistical evaluation of whole-brain CEST maps were performed on the datasets of 14 different subjects to compare the mean MTR_{LD} for MTC, rNOE and amides. The final saturation parameters are listed in Table 4.8. The CEST data of nine subjects were acquired with the 2 mm isotropic resolution protocol using the sTx coil. Eight of these measurements were carried out with the offset list containing 66 frequencies and one with the shortened offset list with 43 frequencies. The measurements of the five other subjects were carried out using the pTx coil and a resolution of 1.61 mm, each with PUSHUP saturation as well as in CP mode. For both variants, the offset list with 43 frequencies was used. To compare the final protocols of the sTx and pTx experiments, the 3-point B_1-corrected data for the sTx and CP data were used, while in the case of the pTx acquisition, the 2-point B_1-corrected data were used.

N_p	120
t_{p} [ms]	15
t_{d} [ms]	15
DC [%]	50
t_{sat} [s]	3.6
$B_{1,\mathrm{sat}}$ [µT]	0.8

Table 4.8: CEST saturation parameters for the CEST evaluation.

4.5.4 In-vivo examination protocol

Based on the results of all the optimization processes presented in this chapter, a protocol for high-resolution whole-brain CEST imaging has been implemented for routine use in neuroscientific and clinical studies. The protocol for a 2 mm isotropic sTx experiment is listed below.

- **Localizer scans**: A set of three-plane, low-resolution images with a large FOV are obtained first and used to identify the ROI for following sequences. (0:14 min)
- **Anatomical images**: A high-resolution 3D MPRAGE [123] sequence with 0.8 mm isotropic resolution is carried out. (3:30 min)
- **Shimming**: At least one automatic 3D shim and two manual 3D shims were performed to improve B_0 homogeneity in the volume of interest. The adjustment volume was set to cover only the brain and was adopted for the following measurements. (approx. 3-5 min)
- **AP/PA measurements**: To correct remaining distortions retrospectively, two short 3D-EPI scans without CEST saturation (one with reversed PE_1) were acquired with five repetitions each. (0:14 min)
- **Field mapping**: By integrating the dual-echo principle into the 3DREAM [66] sequence, both B_1 and B_0 maps are acquired simultaneously. (0:06 min)
- **CEST measurements**: The snapshot 3D-EPI CEST sequence is played out with three different reference voltages $U_{\mathrm{ref}} = [300, 450, 200]$ V. (3× 3:27 min)
- **Field mapping**: The 3DREAM [66] sequence is repeated to track possible field drifts. (0:06 min)

The total measurement, including positioning and shimming, takes approximately 20 min.

CHAPTER 5

Results

5.1 Optimization of the CEST saturation scheme

The design goal of the saturation scheme was to maximize the contrast of the amide protons and also to obtain good quality ssMT and rNOE contrasts, which are always included in the acquisition of the full Z-spectrum. The saturation scheme is determined by the total saturation time t_{sat} as well as the duration of the Gaussian-shaped RF pulses, t_{p} and the interpulse delay t_{d} or the duty cycle DC, respectively. To enable the application of whole-brain CEST experiments in clinical studies, the second goal was to keep the measurement time as short as possible without substantial loss of contrast.

5.1.1 Simulations

JEMRIS simulations of a two-pool model, including water and amides, were carried out to determine the necessary length of the saturation period t_{sat} to achieve a sufficient saturation effect. Figure 5.1 shows the development of the CEST effect, represented by $MTR_{\mathrm{asym}}(\Delta\omega = 3.5\mathrm{ppm})$, as a function of t_{sat}. Simulations were performed for six different pulse durations t_{p} with constant $DC = 50\,\%$ and five varying duty cycles at a fixed $t_{\mathrm{p}} = 30\mathrm{ms}$. For all simulated variations, approx. 95 % of the CEST effect is achieved after 6 seconds while around 60 % of the maximum contrast is already gained after 1.8 s. For $t_{\mathrm{sat}} \geq 9$ s, MTR_{asym} reaches 99 % of the CEST effect gained after 12 seconds.

Considering the SAR estimation (see Eq. 4.13) associated with the simulations from Figure 5.1, it becomes clear that the specific absorption rate increases linearly with the length of the saturation period (see Fig. 5.2). The contribution to the SAR is independent of the pulse duration if duty cycle and total saturation time are kept constant. In contrast, the SAR amount increases with increasing duty cycle due to the shortened interpulse delay.

Moreover, Figure 5.1 shows that the CEST effect increases with an increasing duty cycle and offers particular advantages in the range of 50 % and higher. A short pulse duration also leads to a notably increased CEST effect. The simulation of the CEST effect as a function of the pulse duration is shown in Figure 5.3 (left) for three different saturation amplitudes, fixed duty cycle of $DC = 50\,\%$ and total saturation time of $t_{\mathrm{sat}} = 4\mathrm{s}$. In general, the CEST effect decreases with increasing pulse duration t_{p},

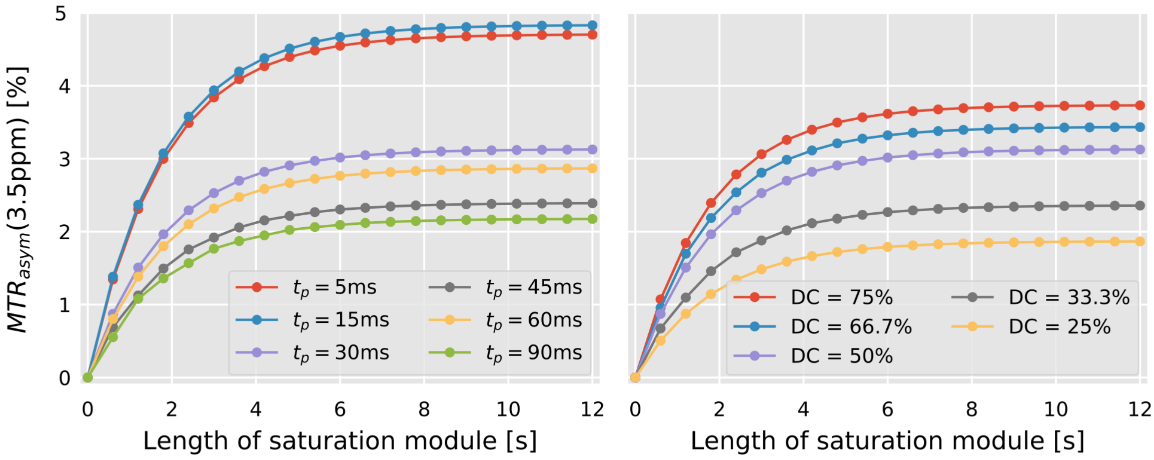

Figure 5.1: MTR_{asym} of simulated 2-pool model plotted against the length of the saturation module for a pulsed saturation scheme. Six exemplifying pulse durations with constant duty cycle $DC = 50\,\%$ are shown on the left, while five different duty cycles with constant pulse duration of $t_{\mathrm{p}} = 30\,\mathrm{ms}$ are shown on the right. For all variants, nearly maximum saturation is achieved after approximately 6 s. The larger the duty cycle, the higher the MTR_{asym}. There is no such clear correlation between MTR_{asym} and pulse duration.

but oscillates depending on the flip angle (see Fig. 5.3, right), which in turn is determined by pulse duration and saturation amplitude. The signal is maximum for odd multiples of π and minimum for even ones. Therefore, the oscillation frequency is higher with increasing saturation amplitude B_1.

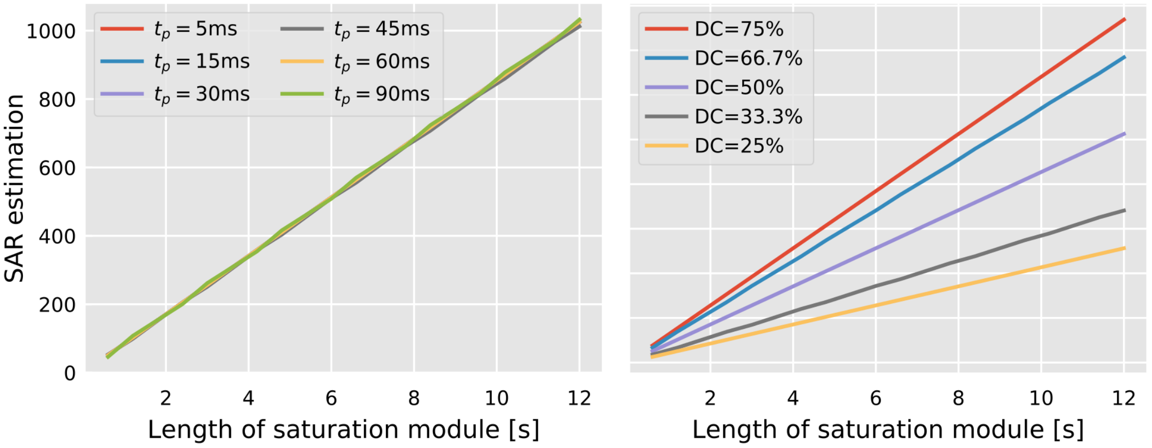

Figure 5.2: SAR estimation for the BMC-simulations shown in Fig. 5.1. SAR estimations are depicted as function of t_{sat} for varying pulse duration t_{p} and fixed $DC = 50\,\%$ (left) as well as for varying DC and fixed $t_{\mathrm{p}} = 30\mathrm{ms}$ (right). SAR increases linear with t_{sat} and decreases with decreasing DC. SAR is independent of t_{p} if DC and t_{sat} are kept constant.

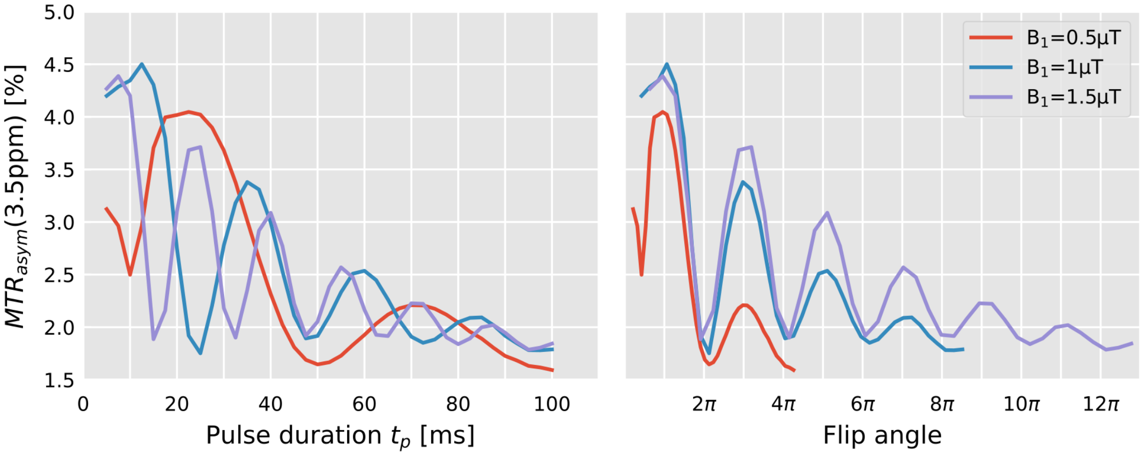

Figure 5.3: MTR_{asym} of simulated 2-pool model plotted against the duration of the Gaussian shaped saturation pulses (left) and against the flip angle of these pulses (right). The total saturation time t_{sat} is kept constant at 4 s. The signal oscillates depending on the flip angle. The signal becomes maximum at odd multiples of π. Besides the oscillation, a steady decrease of the signal with increasing pulse duration can be observed.

5.1.2 Phantom experiments

Phantom experiments were performed on two in-house made phantoms containing GABA combined with glutamate or creatine to proof the dependency of the CEST effect on pulse duration and flip angle. Figure 5.4 a depicts five exemplifying Z-spectra of a 5×5 voxel ROI within the glutamate containing phantom acquired with varying pulse duration $t_{\mathrm{p}} = [15, 20, 45, 60, 90]$ ms. Duty cycle and total saturation time were kept constant for all measurements at $DC = 50\,\%$ and $t_{\mathrm{sat}} = 4$ ms, respectively. Besides the mean Z-value, the standard deviation within the ROI is shown. All 25 mean Z-spectra of 5×5 voxel ROIs and the associated standard deviation within both phantoms are captured in Appendix C. For all Z-spectra, both the water peak at 0 ppm and the peak associated with glutamate around 3 ppm are clearly recognizable. The water peak becomes narrower with increasing pulse duration, but the maximum saturation also decreases by approx. 10 % when comparing the saturation pulse trains with $t_{\mathrm{p}} = 15$ ms and $t_{\mathrm{p}} = 90$ ms. The standard deviation within the ROI is low for all saturation schemes for saturation frequencies greater than ±1 ppm and decreases clearly in the area of direct water saturation with longer pulse duration, whereby the standard deviation remains in a similar range for the pulse duration larger than $t_{\mathrm{p}} = 30$ ms. Corresponding observations can also be made in the Z-spectra of the phantom with GABA and creatine (see Fig. C.1 and C.2).

A closer look at the glutamate peak in Figure 5.4 b) shows that the peak at a very short pulse duration of 15 ms is narrower compared to all others and the baseline of the Z-spectrum is higher. In general, the baseline seems to decrease slightly with increasing pulse length. While the peak minimum of the Z-spectrum acquired with a pulse length of 15 ms is exactly at 3 ppm, the saturation still seems to be maximum at 2.75 ppm for all longer pulse lengths. Furthermore, it can be observed that the standard deviation within the ROI is almost the same for the Z-Spectra acquired with a pulse duration of 30 ms and above (see Fig. 5.4 c)). In comparison, the standard deviation for pulse durations of 15 ms is slightly higher.

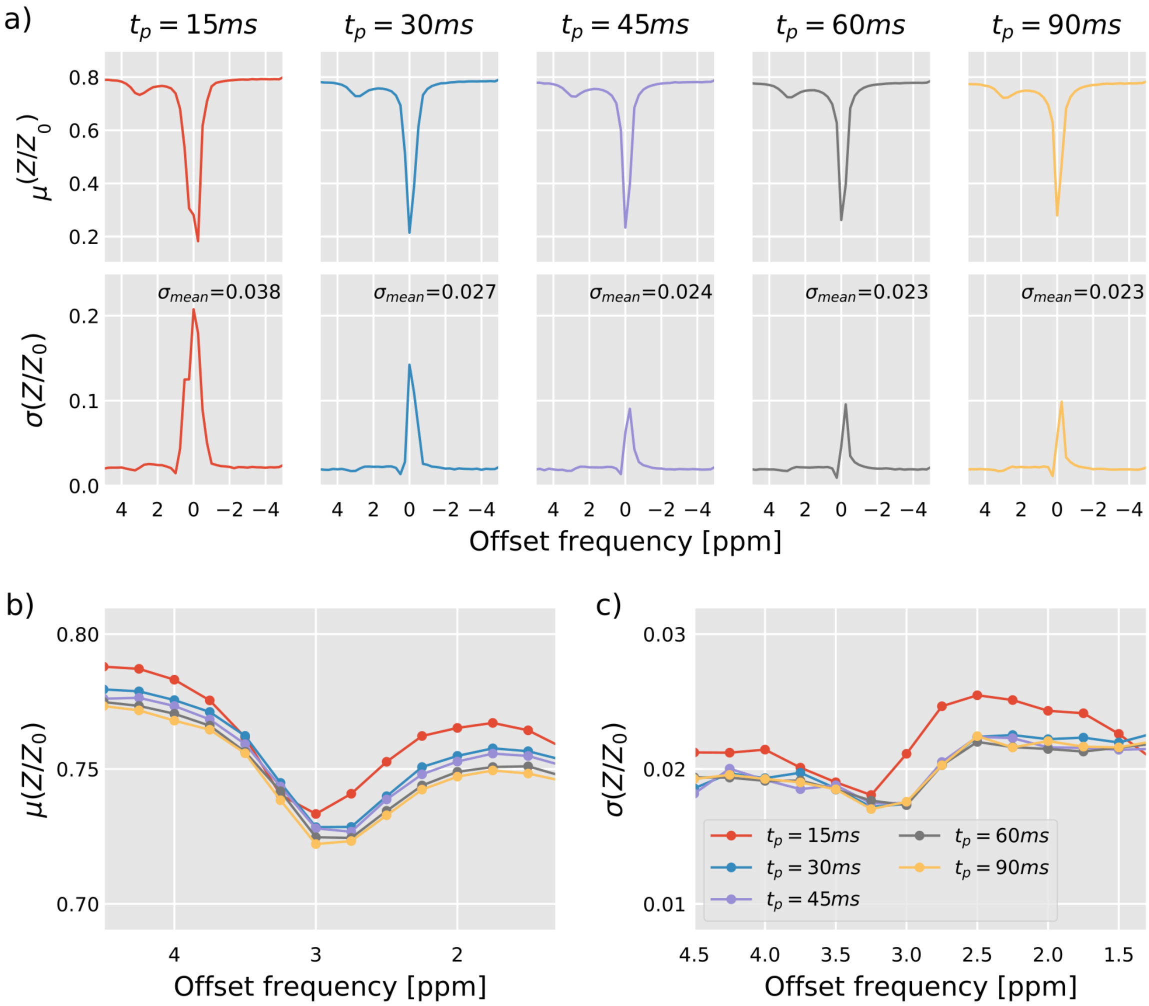

Figure 5.4: Mean Z-spectra of a phantom containing glutamate and GABA within a ROI of 5 × 5 voxel and the associated standard deviation within this ROI. Five exemplifying pulse durations, t_p=[15,30,45,60,90] ms, are shown in a frequency offset range of $\Delta\omega = [-5, 5]$ ppm (a) and in the zoomed frequency section around the CEST effect of glutamate, which is expected at 3.0 ppm (b, c). The standard deviation decreases with increasing pulse duration, notably around the water frequency. The CEST effect and its deviation within the ROI is very similar for pulse durations longer than 15 ms.

Figure 5.5 shows the MTR_asym analysis of the 5 × 5 voxel ROI selected within the Phantom containing GABA and glutamate. By plotting MTR_asym against the frequency offset (Fig. 5.5 a), it is evident that almost no difference can be seen between the acquisitions of longer pulse duration. Whereas, the analysis of MTR_asym of the data acquired with $t_\mathrm{p} = 15$ ms deviates both between 3 ppm and 4 ppm as well as in the area of direct water saturation (smaller than 1.5 ppm) shows clear differences with considerably higher standard deviations within the ROI. Similar observations can also be made in the MTR_asym analysis of the second phantom, which contains GABA and creatine, whose CEST effect is expected at 2 ppm (see Fig. C.3 and C.4).

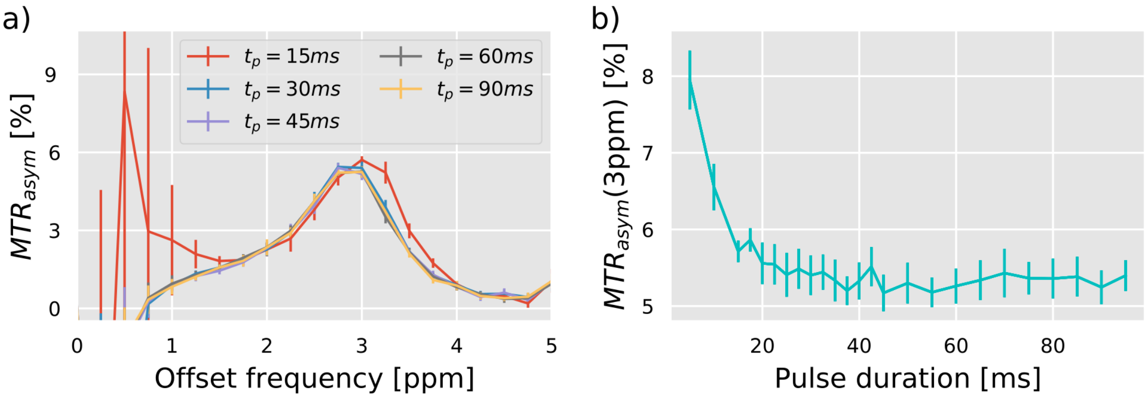

Figure 5.5: MTR_{asym} analysis of the phantom containing glutamate and GABA within a 5×5 voxel ROI. a) MTR_{asym} is shown as a function of the frequency offset $\Delta\omega$. b) MTR_{asym} of $\Delta\omega = 3$ ppm is plotted against the pulse duration t_{p}. The MTR_{asym} settles around 5.4 % with increasing pulse duration while the MTR_{asym} for saturation pulses shorter than 20 ms is higher than 5.7 %.

Considering the CEST effect, represented by $MTR_{\text{asym}}(\Delta\omega = 3\text{ppm})$, as a function of the pulse duration t_{p} in Figure 5.5 b), it turns out that after an initial steep drop in the low pulse duration range, the CEST effect levels off. The oscillations of the CEST effect expected according to the simulations (see Fig. 5.3) cannot be observed here, even if the CEST effect shows slight variations.

5.1.3 In-vivo experiments

Measurements were performed on two healthy young subjects to investigate the dependence of the CEST effect on the pulse duration on the one hand and to compare the contrast maps when the number of saturation offsets is reduced.

Saturation pulse train

Figure 5.6 a depicts five exemplifying white matter Z-spectra of a 5×5 voxel ROI within an axial slice acquired with varying pulse duration $t_{\text{p}} = [15, 20, 45, 60, 90]$ ms and constant duty cycle DC=50 %. The total saturation time was kept constant for all measurements at $t_{\text{sat}} = 3.6$ ms. Additionally, the standard deviation within the ROI is shown below. The water peak at 0 ppm becomes slightly sharper with increasing pulse duration and the peak maximum is a little reduced for $t_{\text{p}} = [30, 60, 90]$ ms. While the ssMT effect appears as a broad reduction of the complete spectrum, the rNOE peak can be clearly recognized in the negative frequency range for all measurements. The effects of amides and amines can only be detected as weak dips around 3.5 and 2 ppm. The standard deviation within the ROI increased slightly in the area of direct water saturation, without any substantial overall differences between the various pulse durations.

A closer look at the Z-spectrum in the amide resonance frequency range in Figure 5.6 b) shows that the CEST effect for amides is most clearly visible at the shortest pulse duration, $t_{\text{p}} = 15$ ms, appears similar for the three medium pulse lengths and is less pronounced for the longest pulse duration, $t_{\text{p}} = 90$ ms. In contrast, the standard deviation within the WM ROI, which is depicted in Figure 5.6 c), do not differ conspicuously between the various acquisitions, even if $\sigma(Z)$ appears marginal lower.

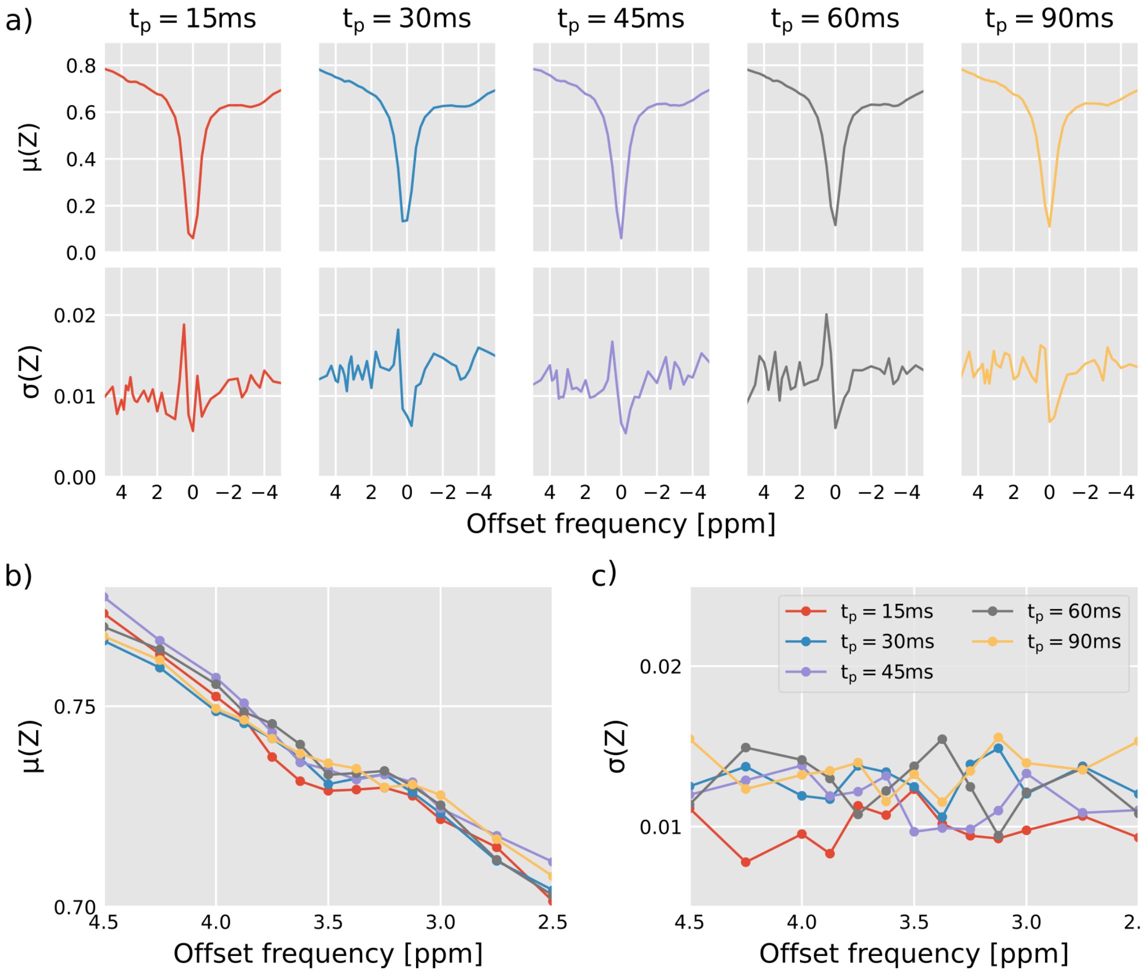

Figure 5.6: Mean Z-spectra of a healthy volunteer within a axial ROI of 5×5 voxel and the associated standard deviation within this ROI. The depicted Z-spectra are calculated within white matter from the motion corrected data set acquired with $U_{\mathrm{ref}} = 300\,\mathrm{V}$. The Z-spectra are shown for the five pulse durations t_{p}=[15,30,45,60,90] ms in a frequency offset range of $\Delta\omega = [-5, 5]$ ppm (a) and in the zoomed frequency section around the CEST effect of amides, which is expected at 3.5 ppm (b, c).

Figure 5.7 features the B_1-corrected CEST contrast maps for δ_{MTC}=-1 ppm, δ_{rNOE}=-3.5 ppm, δ_{amides}=3.5 ppm and δ_{amines}=2.2 ppm after the complete processing routine. The results of the five different saturation modules, containing 120×15 ms, 60×30 ms, 40×45 ms, 30×60 ms and 20×90 ms Gaussian shaped RF pulses, are presented row by row.

All MTC maps show a pronounced contrast between WM and GM, with GM having the lower values. There is no clear difference in the MTC maps between the different saturation modules. In contrast, the rNOE maps show a decrease in MTR_{LD} values with increasing pulse duration t_{p}. At the same time, the contrast between WM and GM improves, again with lower values for the voxels containing GM. When the amides are considered, the values of the MTR_{LD} maps is noticeably higher for a pulse duration of 15 ms than for the other modules, for which only a slight reduction of the values can be observed as the pulse duration increases. The difference between WM and GM is much smaller compared to MTC and no saturation module appears to provide a particular advantage. For both the contrast maps of amides and of amines, the MTR_{LD} in GM is generally higher than in WM. As in the case of MTC, the level of the amine maps does not deviate substantially between the different saturation modules. Likewise, no clear differences in the relatively low WM/GM contrast can be observed.

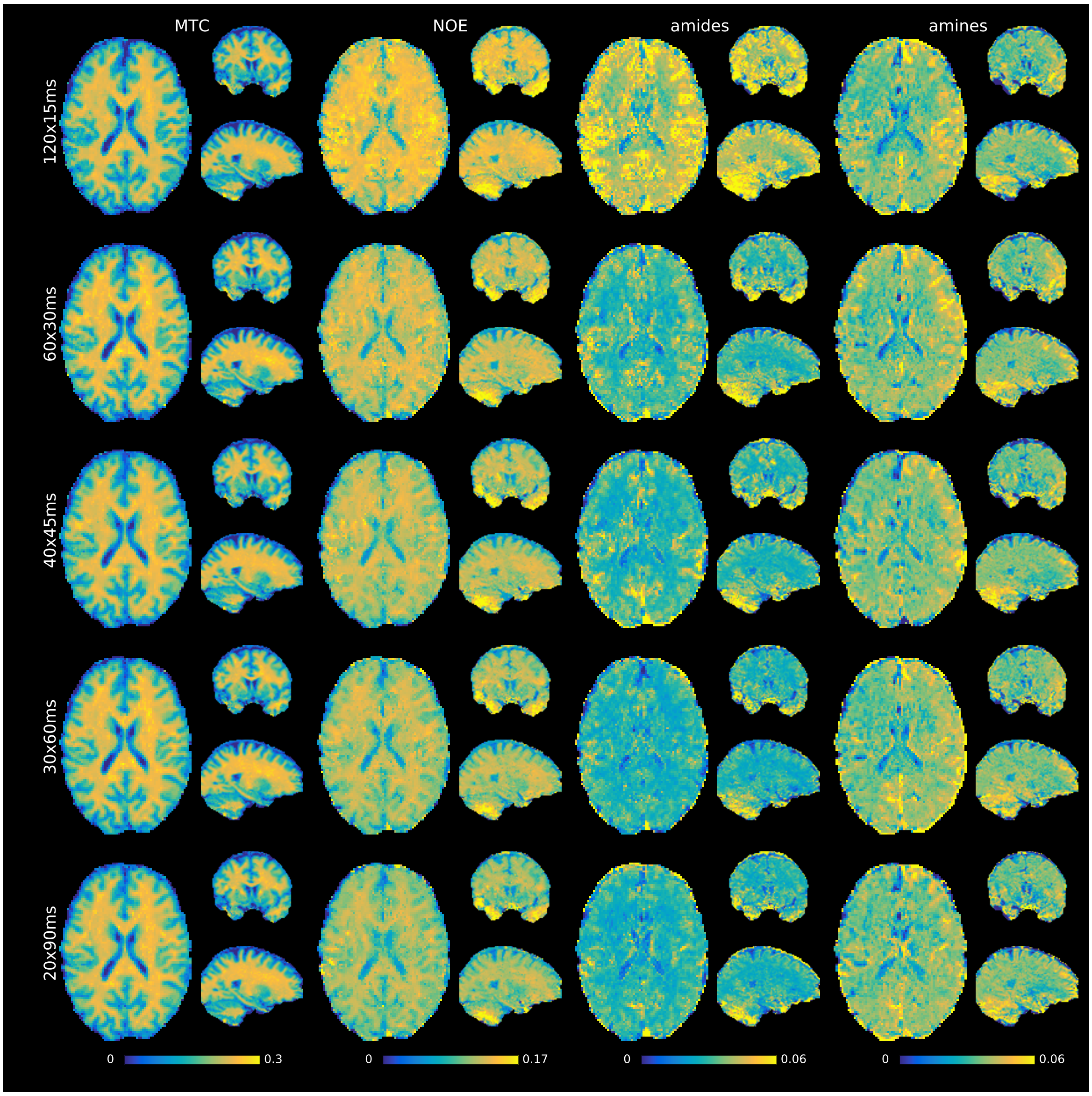

Figure 5.7: CEST contrast maps of a healthy subject for δ_{MTC}=-1 ppm, δ_{rNOE}=-3.5 ppm, δ_{amides}=3.5 ppm and δ_{amines}=2.2 ppm in axial, coronal and sagittal orientation (columns) and for five different saturation schemes with 120×15 ms, 60×30 ms, 40×45 ms, 30×60 ms and 20×90 ms Gaussian shaped RF pulses (rows). The total saturation time is $t_{\mathrm{sat}} = 3.6$ s in each case. The MTR_{LD} values of δ_{rNOE} and δ_{amides} reduces with increasing pulse duration while the values of δ_{MTC} and δ_{amines} is on the same level for all saturation schemes.

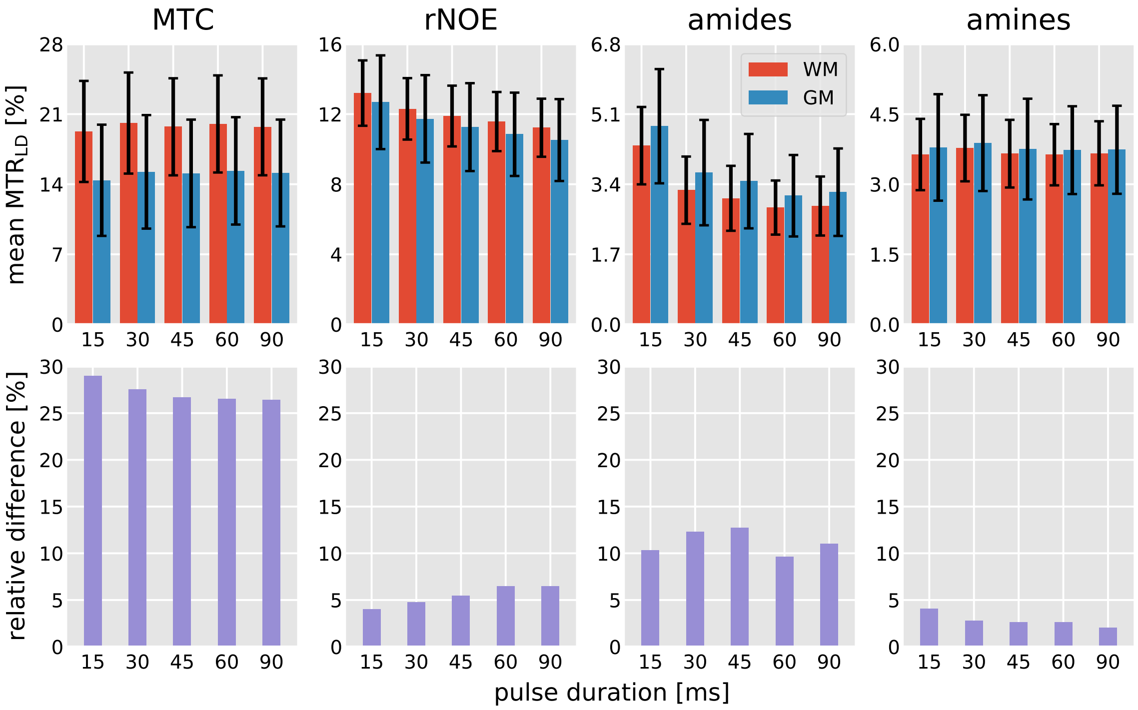

Figure 5.8: Mean and standard deviation of MTR_{LD}, which is presented in Fig. 5.7, in ROIs representing white and gray matter (see Fig. 4.7) as well as the corresponding relative difference between WM and GM given by: rel.diff $= 2 \cdot \left(|\, MTR_{\mathrm{LD}}^{\mathrm{WM}} - MTR_{\mathrm{LD}}^{\mathrm{GM}}\,|\right) / \left(MTR_{\mathrm{LD}}^{\mathrm{WM}} + MTR_{\mathrm{LD}}^{\mathrm{GM}}\right)$. The mean values of δ_{rNOE} and δ_{amides} reduced continuously with increasing pulse duration while die WM-GM contrast maximizes for δ_{amides} with the saturation scheme of 40×45 ms.

In Figure 5.8, the mean MTR_{LD} and the corresponding standard deviation values for whole-brain ROIs of GM and WM are shown for the contrast maps, which are presented in Figure 5.7. Additionally, the relative difference between WM and GM is shown in the bottom row. Table D.1 contains the values associated with Figure 5.8 and can be found in Appendix D. The mean values for WM and GM confirm the observations already made when visually examining the contrast maps in Figure 5.7. While the MTR_{LD} of MTC and amines is relatively constant, the WM/GM contrast decreases with increasing pulse duration for both contrasts. While the relative difference between WM and GM only decreases by a maximum of 9 % (from 28.98 % to 26.45 %) for the ssMT, the already conspicuously lower WM/GM contrast of the amines is reduced by 50 % (from 4.09 % to 2.04 %) for $t_{\mathrm{p}} = 90$ ms compared to $t_{\mathrm{p}} = 15$ ms. In the case of rNOE, the MTR_{LD} decreases from $t_{\mathrm{p}} = 15$ ms to $t_{\mathrm{p}} = 90$ ms by 15 % for WM and 17 % for GM, with the relative difference between WM and GM increasing by 60 % (from 4.04 % to 6.47 %). MTR_{LD} of amides is reduced by 34 % for WM and 33 % for GM when the pulse duration is increased from $t_{\mathrm{p}} = 15$ ms to $t_{\mathrm{p}} = 90$ ms. While the values decrease continuously with increasing pulse length, it is already reduced by 25 % for WM (23.5 % for GM) when the pulse duration is doubled to $t_{\mathrm{p}} = 30$ ms. The WM/GM contrast maximizes at a pulse duration of $t_{\mathrm{p}} = 45$ ms with 12.73 % and is minimal at $t_{\mathrm{p}} = 60$ ms with 9.64 %. For the shortest pulse duration of $t_{\mathrm{p}} = 15$ ms, the relative difference between WM and GM is 10.33 %.

Saturation offset scheme

With the aim of minimizing the measurement time of the CEST sequence, the frequency offset list was shortened from 66 frequencies to 54 and 43 varying frequencies by retrospectively reducing the complete data set. The acquisition of one saturated volume takes 4.4 s, so that the reduction from 66 to 54 frequency offsets corresponds to a time saving per B_1 amplitude of 52.8 s. Reducing the number of offsets even further to 43, results in a time saving of 92.4 s. This corresponds to a reduction of the total measurement time for a single reference voltage, which includes two M_0 scans as well as the autocalibration and the external phase correction scans, by 20.7 % and 32.8 % respectively.

Figure 5.9 depicts the CEST contrast maps for δ_{MTC}=-1 ppm, δ_{rNOE}=-3.5 ppm and δ_{amides}=3.5 ppm. The level of the MTR_{LD} maps of all contrasts is comparable for the three different offset lists. There is a minimal increase in the MTC values when reducing the saturation offsets, as well as a slight reduction in rNOE. No such general tendency can be seen in the amide maps. The differentiation between WM and GM also does not change considerably when the offset list is reduced.

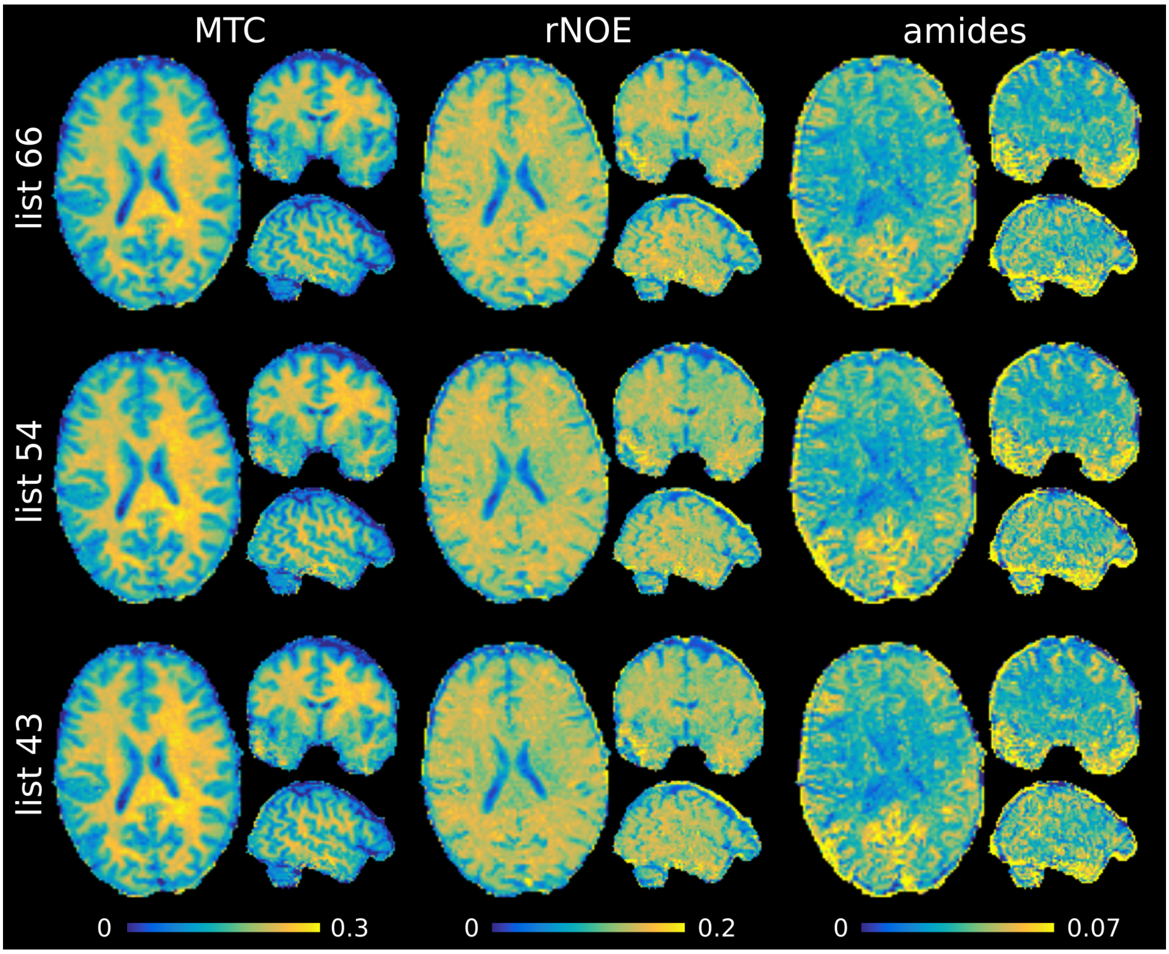

Figure 5.9: CEST contrast maps of a healthy subject for δ_{MTC}=-1 ppm, δ_{rNOE}=-3.5 ppm and δ_{amides}=3.5 ppm and δ_{amines}=2.2 ppm in axial, coronal and sagittal orientation and for three offset lists, containing 66, 54 and 43 saturation offsets. The quality of the CEST contrast maps is comparable for all offset schemes.

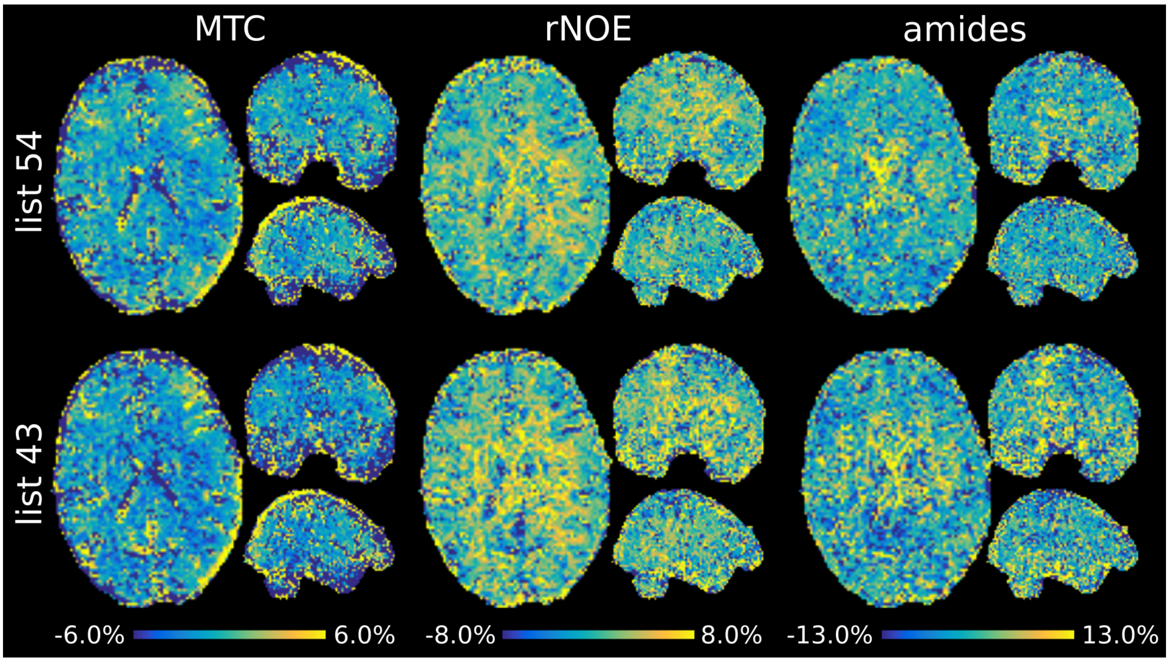

Figure 5.10: Relative difference maps for the contrasts shown in Fig. 5.9 in axial, coronal and sagittal orientation. The maps generated from raw data with 66 frequency offsets are compared to the maps derived from raw data with a reduced number of frequency offsets. The relative difference is smallest for the MTC contrast and highest for the amide contrasts. Except for CSF, there is no distinct brain structure visible in the difference maps.

When looking at the relative difference maps in Figure 5.10, it can be seen that the ssMT effect is the least influenced by the reduction of the offset list, whereas the CEST maps of the amides show the strongest deviations. The relative difference increases slightly for the more abbreviated offset list, list 43, compared to the middle list, list 54. While the relative difference for the ssMT contrast tends to be in the negative range, it is positive for the rNOE, which mirrors the observations in Figure 5.10. The reduction of frequency offsets also leads to a marginally negative trend in the relative difference for the amide maps, i.e. to an increase in the MTR_{LD} level. For all contrasts, CSF is the only brain structure that can also be identified in the relative difference maps.

5.2 Whole-brain CEST

Apart from the general optimization of the saturation scheme, the evaluation of the whole-brain CEST experiments focuses on two goals:

- The optimization of the 3D-EPI readout with regard to CEST imaging.
- The analysis of the B_1 dependency of whole-brain CEST at 7 T and the optimization of a B_1 correction method, if needed.

5.2.1 Optimization of the 3D-EPI readout for CEST imaging

With the aim of improving the contrast-to-noise ratio, an experiment was performed with one healthy subject to examine, on the one hand, if the CEST effect changes when the second phase-encoding PE_2 direction is acquired center out instead of the typical linear reordering, and on the other hand, to verify the effectiveness of the water-selective excitation pulse.

Figure 5.11 a-c depicts an axial slice at saturation frequency of $\Delta\omega = 0\,\text{ppm}$, where the signal strength is lowest due to direct water saturation. Using the same windowing, there is a substantially

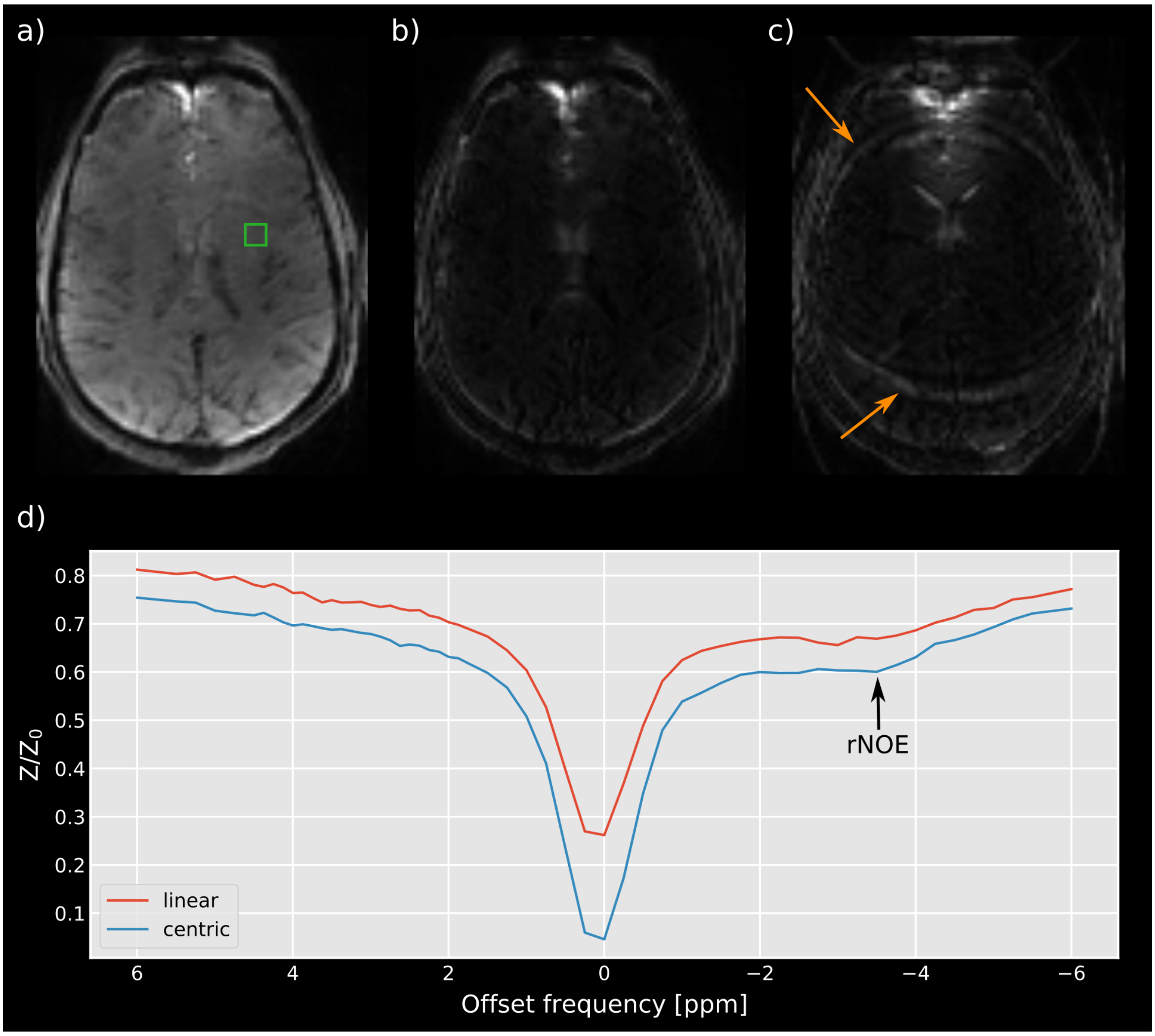

Figure 5.11: Axial example slice of the same saturation offset near the water frequency (nominal 0 ppm) acquired with linear (a) and centric PE_2 reordering (b). Additionally, the related in-vivo Z-spectra for a small region in WM (d) which is depicted by the green square in (a). The centric-reordered image shows maximum contrast of the direct water saturation, whereas longitudinal relaxation during linear readout reduces the effective saturation contrast. In the absence of water-selctive excitation, a fat chemical shift artifact is visible in first phase encoding direction (orange arrows in (c)). This artifact is not present in the images acquired with water-selective excitation, which are shown in (a) and (b).

higher signal intensity for the image acquired with linear second phase encoding (Fig. 5.11 a) compared to the images acquired with centric-reordering (Fig. 5.11 b-c). As the former mainly consists of non-saturated, recovered magnetization, this indicates an improved saturation contrast by the usage of centric-reordered second phase encoding direction. While the water-selective excitation pulse was played out in Figure 5.11 a and b, Figure 5.11 c was acquired without any fat suppression. In this case, chemical shift artifacts can be detected as light bands in the frontal and back region of the brain, which are indicated by the orange arrow. The chemical shift artifact appears along the first phase encoding direction, PE_1, induced by the fat component underneath the skin. However, the water-selective excitation successfully suppresses the fat chemical shift artifact for both centric and linear reordered second phase encoding direction.

A comparison of the Z-spectra presented in Figure 5.11 d clearly shows that the baseline of the entire Z-spectrum is lower with centric-reordered PE_2 than with linear PE_2. The highest difference of approx. 20 % occurs in the area of direct water saturation, with a deviation of approx. 5 to 10 % for the rest of the Z-spectrum. While the effects of amides and amines are not clearly visible in the mean Z-spectrum of the selected ROI, the rNOE peak is somewhat flatter in the linearly reordered second phase encoding direction compared to the center out acquisition.

Figure 5.12 a shows the evolution of the iPC signal magnitude and the drift of the frequency offset, which was measured within a phantom experiment. The signal magnitude approaches the steady-state relatively smoothly, with the signal dropping more rapidly within the first excitations. After 15 excitations, the signal magnitude has already reduced to half of its maximum and then decreases further by approx. 15 % up to the 40th excitation. In contrast, the frequency offset is fluctuating strongly for the first excitations, with maximum at the second excitation. Most of these initial fluctuations stabilize from the third excitation onwards, which is marked by the dashed line. The fourth to sixth excitations have a slightly lower frequency offset than the following excitations, whereby there is generally a very small global frequency drift of approximately 1 Hz from third to last excitation.

To examine the effects of frequency fluctuation on the quality of the CEST data, 40 unsaturated images were acquired within one healthy subject and the temporal signal-to-noise ratio was calculated. Figure 5.12 b shows the tSNR maps in orthogonal views for acquisitions including three initial dummy excitations ($N_D = 3$) and without dummy excitations ($N_D = 0$). No tissue structure is clearly recognizable within the tSNR maps and the tSNR is substantially lower in the lower caudal regions of the brain, including e.g. the cerebellum. The tSNR is increased by the usage of three dummy excitations compared to not using dummies. The tSNR improvement is more pronounced in the middle and upper regions of the brain compared to the lower regions. The whole-brain average tSNR improves by 18.6 % if three dummy excitations were used.

Whole-brain raw data

Figure 5.13 shows the raw data of a CEST data set, acquired with 2 mm isotropic resolution and at reference voltage of $U_{\text{ref}} = 300$ V, before it runs through the processing pipeline to obtain the CEST maps. The unsaturated image is presented in axial, sagittal and coronal view (Fig. 5.13 a). The signal intensity is slightly increased in the middle area of the head, while it is clearly reduced in the caudal area of the brain, such as the cerebellum. The arrows left of the axial slice indicate the phase encoding directions, PE_1 and PE_2. Only minimal distortion artifacts are visible near the skull bone in the

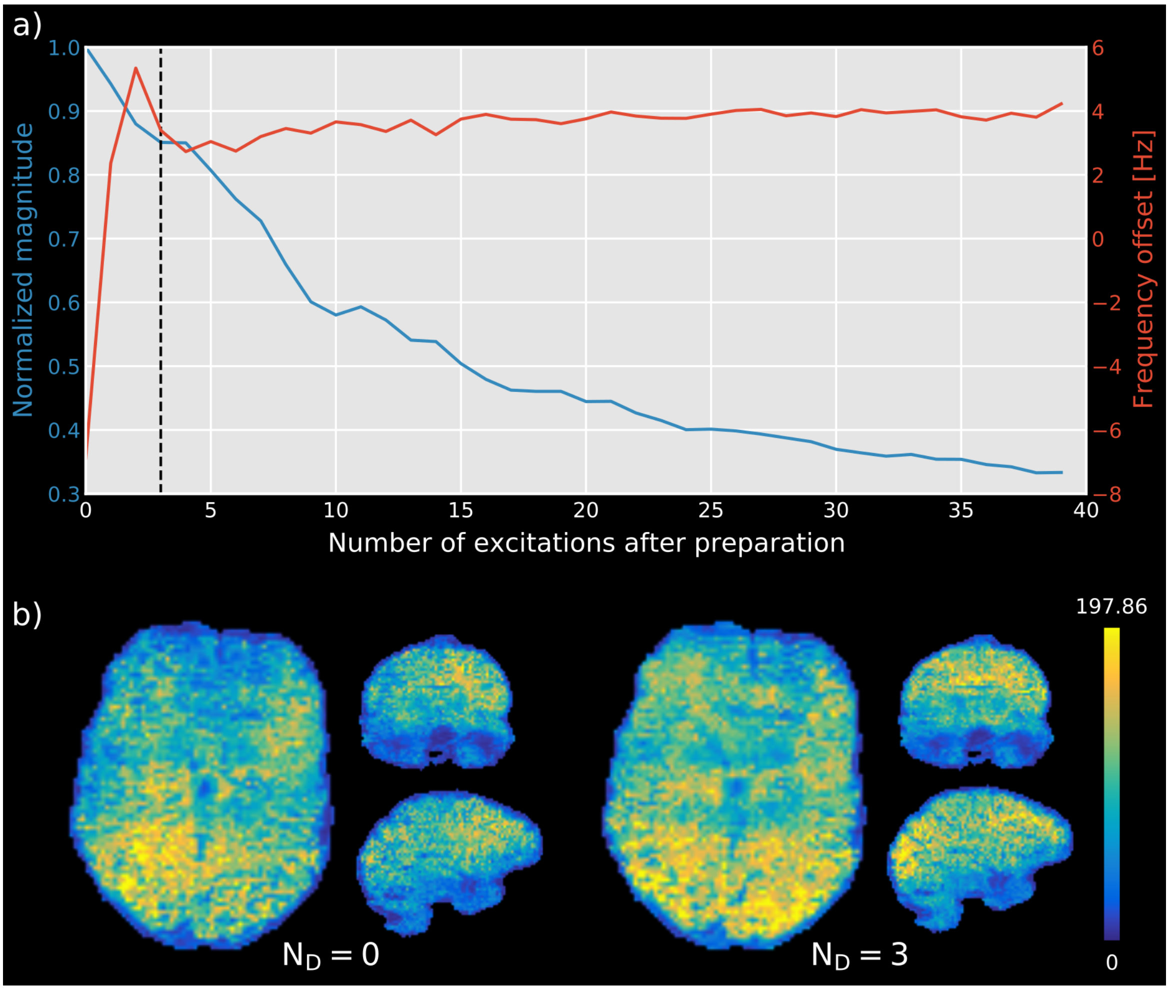

Figure 5.12: (a) Evolution of signal magnitude and global frequency offset during one 3D-EPI readout (phantom data). The global frequency offset in relation to the reference frequency (determined from the EPI phase correction scans) stabilizes after three excitations. The dashed line represents the fourth excitation, which corresponds to the position of the k-space center acquisition in case of three dummy excitations. b) Orthogonal views of the calculated tSNR maps for in-vivo data acquired without ($N_D = 0$) and with three dummy excitations ($N_D = 3$). The whole-brain average tSNR is observed to improve by 18.6 % through the dummy excitations.

extension of the first phase encoding direction, indicated by red arrows.

Figure 5.13 b depicts exemplifying axial slices of a selection of saturated images. The signal intensity is highest for saturation frequencies far away from the water frequency and drops substantially for frequencies smaller than ±1 ppm due to the direct water saturation. At a nominal saturation frequency of $\Delta\omega = 0$ ppm, the tissue signal is almost fully saturated and only the structure of CSF as well as the boundaries of brain and skin can be recognized very faintly. A bright CSF signal can be identified for all frequencies except $\Delta\omega = 0$ ppm, as well as a clear WM/GM contrast for frequencies larger than ±0.5 ppm. The closer the frequency offsets are to each other outside the influence of direct water saturation, the more difficult it is to recognize any optical differences between the images.

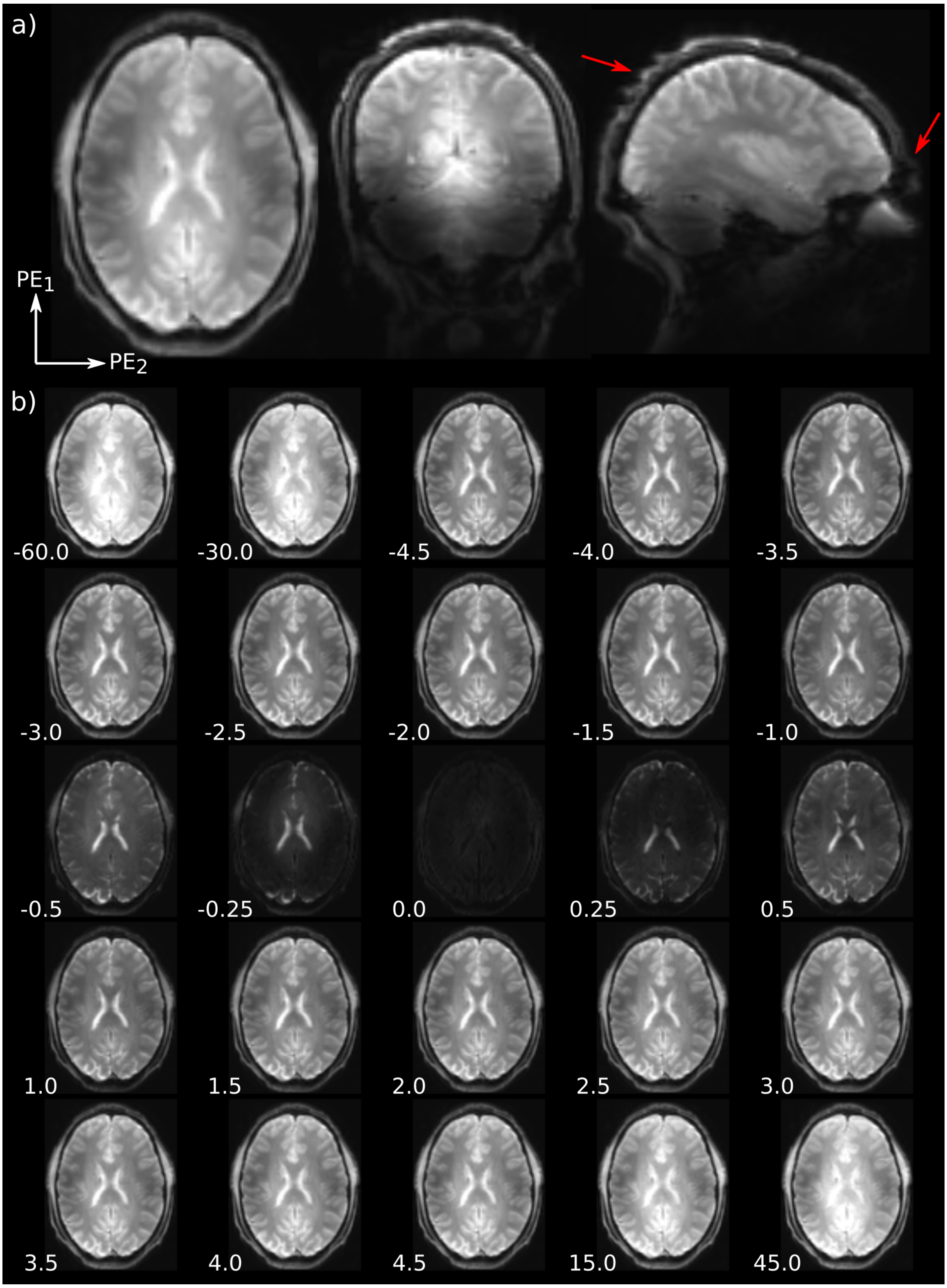

Figure 5.13: Raw magnitude images without any processing. a) Orthogonal example views of the unsaturated volume M_0. Phase encoding directions are indicated for the axial view. b) A selection of saturation offsets (given in ppm) is presented with differing contrasts. The tissue signal is nearly fully saturated at nominal 0 ppm.

5.2.2 Optimization of the B_1-correction for 7T experiments

In-vivo measurements were performed to analyze the B_1 distribution along the whole brain with the goal to find the best experimental setup for whole-brain CEST measurements with the methods introduced.

B_1 distribution (sTx)

Figure 5.14 a illustrates the local distribution of the voxel-wise group average required reference voltage ($N = 9$) using the single transmit coil. The reference voltage map is divided into discrete ranges between 150 V and 800 V with 50 V sections, apart from the high voltage range, which extends from 450 to 800 V, due to its lower expansion. The regions that require a low reference voltage are located in the central to upper area of the brain, whereas the high-voltage areas tend to be located in the lower area of the brain. Looking at the dependence of different brain areas shown in Figure 5.14 b, it becomes clear that the cerebellum and the temporal lobes in particular correspond to the area with the highest required reference voltages. Brain regions such as the frontal lobes or parietal lobes, on the other hand, can be assigned to regions of medium reference voltage. On the basis of the group average reference voltage map, a voltage of $U_{\text{ref}} = 300$ V was defined as 100 % for all in-vivo experiments.

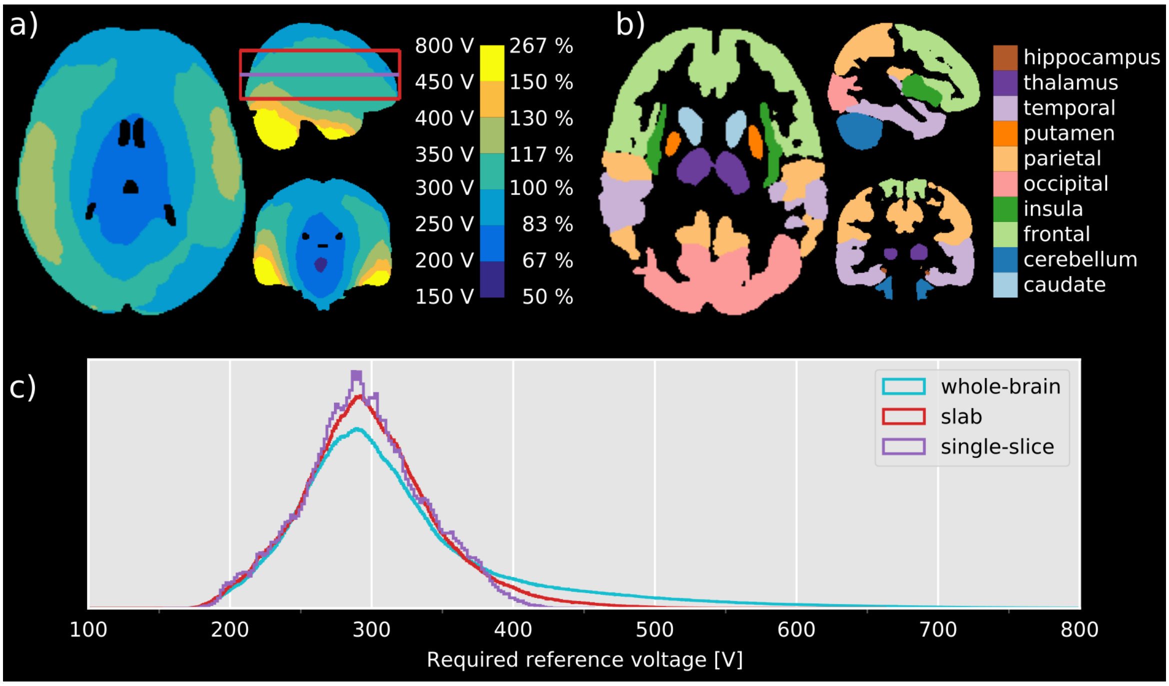

Figure 5.14: Required reference voltage analysis. a) Axial, coronal and sagittal views of the group mean reference voltage map ($N = 9$) in the MNI-domain. The axial slice (1 mm) is marked in purple in the sagittal view as well as a slab of 50 slices (red). ROIs of brain structures are shown in (b) for the same orthogonal views. Normalized single-slice and small volume histograms are presented in (c) alongside the histogram of the distribution of the reference voltages across the whole brain. As the volume increases, the high voltage tail of the distribution becomes longer. Based on this reference voltage distribution, the reference voltage of 300 V was defined as 100 %. Reference voltages beyond 450 V are related to the cerebellum and the temporal lobes.

Figure 5.14 c shows the probability histogram of the required reference voltage compared between ROIs of the whole brain, a central volume of 5 cm extension in head-feet direction and a single axial slice of 1mm thickness. While the minimum required reference voltage is around 170 V for all three ROIs, the maximum required reference voltage increases with the size of the ROI, especially for the whole-brain ROI. The maximum probability of the required reference voltage is the same for all ROIs at approx. 290 V.

Table 5.1 shows the mean average required reference voltage and the inter-subject variation for the different brain regions shown in Figure 5.14 b. The average required reference voltage for the cerebellum (415.42 V ± 101.35 V) and the temporal lobes (402.91 V ± 83.57 V), is up to 35 % higher compared to the average required voltage within the cerebrum (308.65 V ± 61.93 V). Similarly, the variance of the required reference voltages is considerably higher in these two brain areas than in the others. When comparing the reference voltages between the nine subjects, the highest variances are also found in the cerebellum (72.93 V ± 29.59 V) and the temporal lobes (44.57 V ± 18.96 V), although the cerebellum clearly differs from all regions within the cerebrum.

Region	**Group mean reference voltage**	**Inter-subject standard deviation**
Thalamus	217.40 V ± 11.06 V	15.92 V ± 2.92 V
Temporal Lobe	402.91 V ± 83.57 V	44.57 V ± 18.96 V
Putamen	271.50 V ± 11.39 V	23.95 V ± 4.29 V
Parietal Lobe	284.43 V ± 32.06 V	19.60 V ± 5.80 V
Occipital Lobe	317.00 V ± 39.01 V	35.57 V ± 15.93 V
Insula	312.07 V ± 16.14 V	27.33 V ± 6.94 V
Frontal Lobe	299.75 V ± 29.68 V	19.93 V ± 6.77 V
Cerebellum	415.42 V ± 101.35 V	72.93 V ± 29.59 V
Caudate	254.25 V ± 15.11 V	20.62 V ± 15.11 V
Cerebrum	308.65 V ± 61.93 V	26.57 V ± 14.82 V
Hippocampus	248.74 V ± 14.11 V	23.37 V ± 4.77 V

Table 5.1: Required reference voltage analysis per ROI. Column 2 provides the group mean reference voltage (see Fig. 5.14a) averaged per ROI ± standard deviation. Column 3 presents the inter-subject standard deviation of the reference voltage averaged per ROI ± standard deviation. A visual representation of the ROIs in column 1 is displayed in Fig. 5.14b. The cerebellum and the temporal lobes exhibit the highest mean reference voltages as well as the largest variation between subjects and within the regions.

Number of B_1 values (sTx)

In order to determine the number of CEST data sets to be acquired with different saturation amplitudes required for the retrospective B_1 correction and in order to specify the reference voltages that should be used, the CEST sequence was repeated in one healthy volunteer with seven different reference voltages ($U_{\text{ref}} = [150, 200, 250, 300, 350, 400, 450]$ V). Figure 5.15 illustrates the MTR_{Rex} maps for the MT contrast after B_0 correction and using varying B_1 correction including different combinations

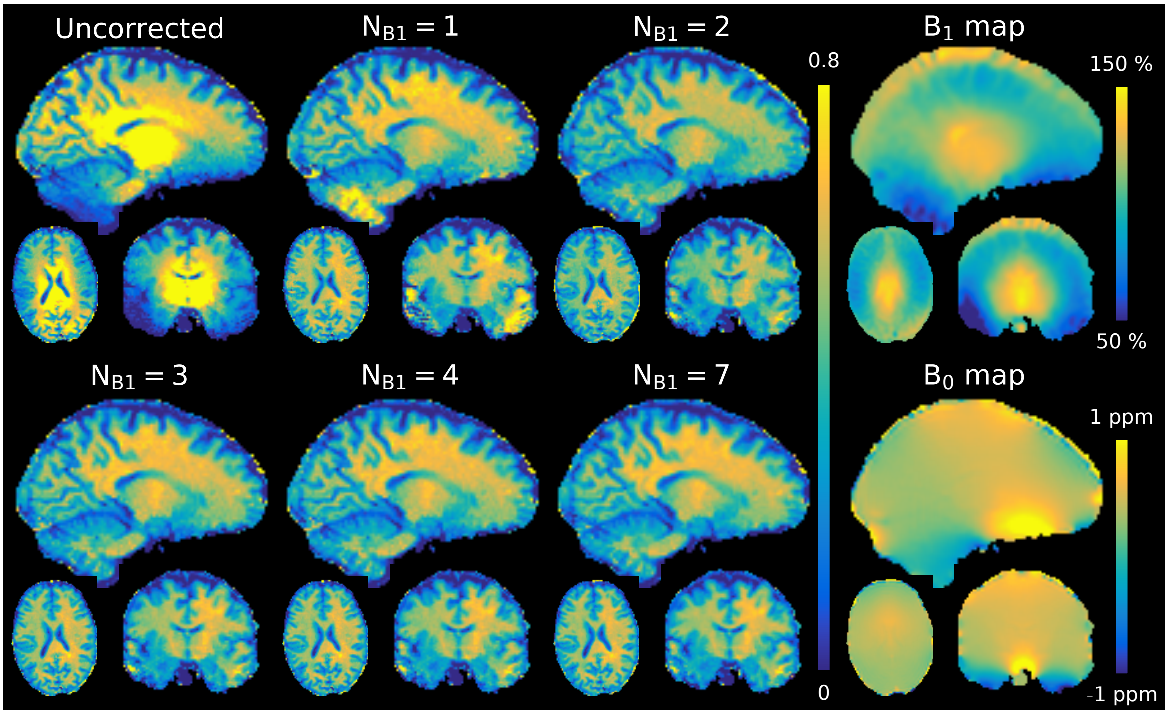

Figure 5.15: CEST maps for one healthy volunteer of the contrast parameter $MTR_{Rex}(\delta_{MTC})$ of representative sagittal, axial and coronal and views. B_1-uncorrected ($B_{1,\text{sat,nom}}$=0.8 µT) and Z-B_1-corrected ($B_{1,\text{sat}}$ =0.8 µT) maps generated with increasing number of reference voltages (B_1 sampling points, N_{B1}) are shown. Corresponding maps of measured B_0 and B_1 (scaled to the nominal B_1) are displayed on the right. The impact of B_1 inhomogeneity is observed to be reduced for all B_1-corrected maps, with increased image quality for higher numbers of B_1-values. The corrected data with $N_{B1} = 2$ differs in the WM/GM contrast and shows a global systematic offset compared to the other datasets.

of reference voltages, which are defined as B_1 sampling points, N_{B1}. Additionally, the related B_1 and B_0 maps are shown. The values of the B_1-uncorrected MTR_{Rex} map correlates considerably with the B_1 map. In areas of high B_1, the values increase, whereas MTR_{Rex} becomes minimal for areas of low B_1. Also the corrected map with $N_{B1} = 1$ shows an clear apparent bias by B_1, even if the relationship is mostly the opposite compared to the uncorrected map: In areas of low B_1, MTR_{Rex} is maximized and appears attenuated in regions of high B_1. The maps corrected with two or more B_1 sampling points are more homogeneous and no substantial correlation to B_1 can be observed. The WM/GM contrast of the corrected map with $N_{B1} = 2$ is less pronounced than that of the maps with a larger number of B_1 values. The difference between the corrected maps with $N_{B1} = [3, 4, 7]$ is only very small. In the regions of very low B_1, all uncorrected and corrected MTR_{Rex} maps exhibit elevated or diminished values, indicative of unsuccessful quantification. Considering the B_0 map, there is no correlation remaining after B_0 correction, neither for the uncorrected nor for the corrected MTR_{Rex} maps.

Figure 5.16 shows the whole-brain median absolute error of the B_1 corrected MTR_{Rex} of MTC, rNOE and amides with different numbers of B_1 sampling points N_{B1} compared to the maps corrected with $N_{B1} = 7$. Table D.2 contains the values associated with the first row of Figure 5.16 and can be

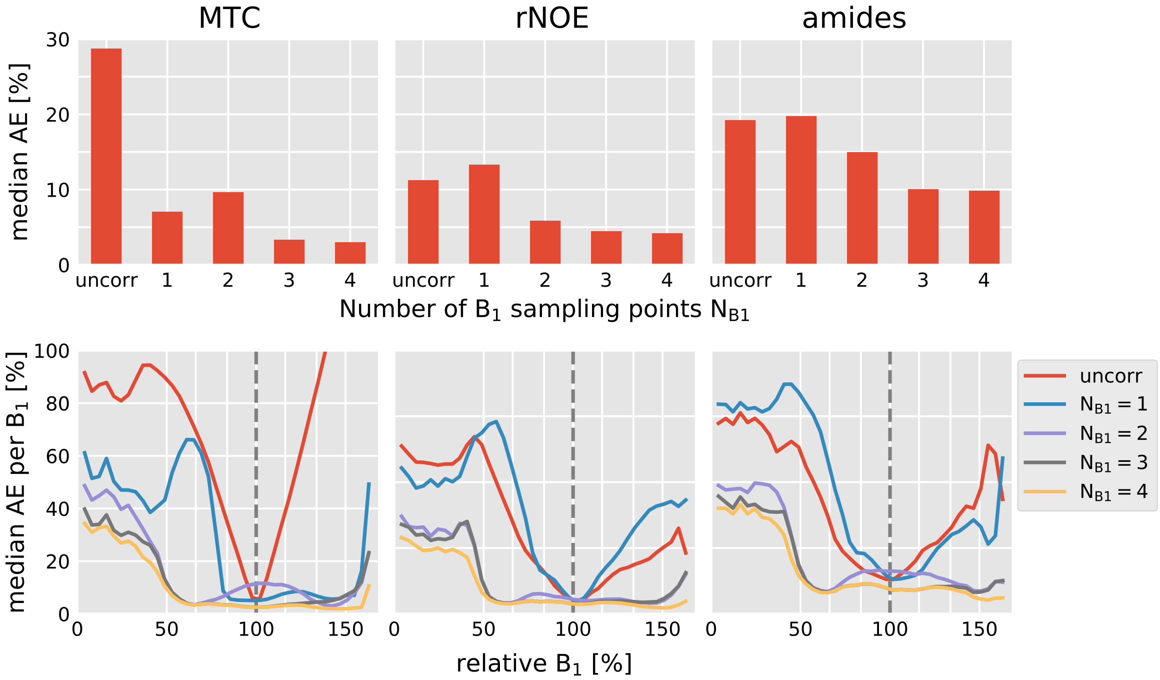

Figure 5.16: Whole-brain median absolute error (AE) of the B_1 correction with different numbers of B_1 sampling points N_{B1} under the assumption that $N_{B1} = 7$ corresponds to the ground truth (first row). The discrepancy between the corrections with $N_{B1} = 3$ and $N_{B1} = 4$ is minimal. However, for both cases, the median AE is clearly smaller than the correction with only 2 B_1 sampling points. The second row displays the median AE per B_1 which is plotted against the relative B_1. The dashed line indicates $rB_1 = 100\,\%$ which corresponds to the fitted $B_{1,\text{sat}} = 0.8\,\mu\text{T}$ and a reference voltage of 300 V. The median AE is highest for very small and very high rel. B_1 values and smallest in the range of $rB_1 = 100\,\%$.

found in Appendix D. While the median AE for the uncorrected MTC is by far the highest at 28.70 %, it is maximal for the 1-point correction in case of rNOE (13.32 %) and amides (19.78 %). The median AE increases for the MTC corrected with $N_{B1} = 2$ (9.6 %) compared to $N_{B1} = 1$ (7.1 %), whereas it is clearly reduced for amides and rNOE with 14.95 % and 5.84 %, respectively. The 4-point-correction has the lowest median AE for all three contrasts, but the median AE of the B_1 correction with $N_{B1} = 3$ is only 0.16 % to 0.32 % higher.

Furthermore, the second row of Figure 5.16 shows the median absolute error compared to the B_1 correction with $N_{B1} = 7$ as a function of the relative B_1. For all contrasts, the median AE is particularly high in areas where rel. B_1 is less than 65 %, as well as for regions where rel. B_1 is above 150 %. As the number of B_1 sampling points included in the B_1-correction increases, the median AE in the peripheral areas of rel. B_1 decreases. In the range of the fitted $B_{1,\text{sat}}$, which is defined as 100 %, the median AE is minimal for all contrasts, with the 2-point correction being the exception: In both the MTC and the amides, the median AE increases around 100 % ($U_\text{ref} = 300\,\text{V}$) for $N_{B1} = 2$ and then decreases again in the areas of the two integrated measurement points (($U_\text{ref} = [200, 450]\,\text{V}$). With the exception of the 1-point correction of the MTC, the median AE is always low if the rel. B_1 ranges between the B_1 sampling points included in the B_1-correction. The median AE of $N_{B1} = 3$ and $N_{B1} = 4$ differs only marginally if rel. B_1 is in the range of 50 % to 150 %. Generally, the median AE is slightly elevated in the central areas of rel. B_1 for the amide contrast compared to MTC and rNOE.

Dielectric bags

The CEST experiment was carried out twice on a young, healthy subject, with three dielectric bags positioned inside the head coil at both sides and under the head in the second run. Figure 5.17 shows the CEST maps for MTC, rNOE and amides after B_0 and B_1 correction in the standard setup (top row) and with the use of dielectric bags (middle row). In addition, the corresponding B_1 maps are shown. It is evident that in the case of the bags, the high B_1 region, located in the center of the brain, is slightly reduced, as well as that the low B_1 regions near temporal lobes and cerebellum are less pronounced. While the difference between the MTC maps is marginal, the WM/GM contrast for rNOE seems to be slightly improved by using the dielectric bags. Moreover, the very high values in the area of the temporal lobes (coronal view), which indicate insufficient quantification, are reduced with the usage of dielectric material. In the case of the amides, MTR_{LD} generally appears to be slightly higher in the experimental setup without dielectric bags. Even if the extremely high values in the temporal lobe area are somewhat reduced with dielectric bags, a clear area of very high values in the cerebellum can be recognized for both setups, indicating a failed quantification. These areas correlate very clearly

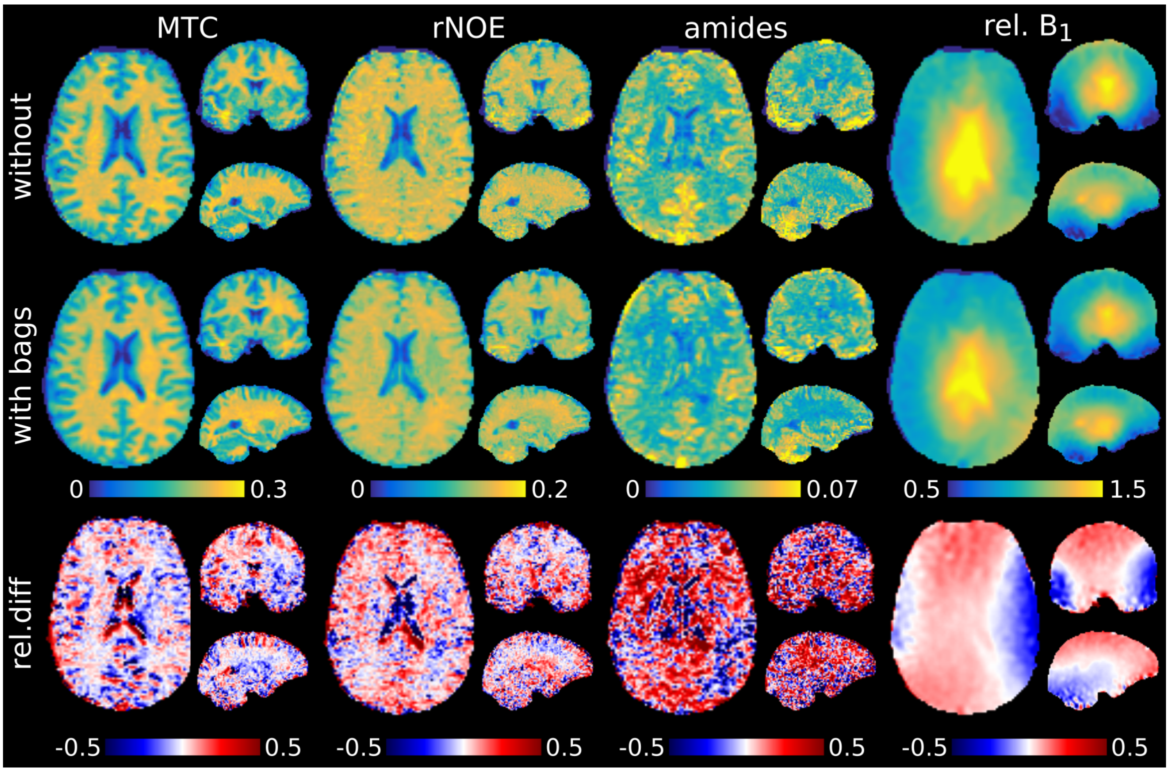

Figure 5.17: CEST contrast maps of a healthy subject for $\delta_{\mathrm{MTC}} = -1$ ppm, $\delta_{\mathrm{rNOE}} = -3.5$ ppm, and $\delta_{\mathrm{amides}} = 3.5$ ppm in axial, coronal and sagittal orientation as well as the associated relative B_1 maps: without the usage of dielectric material in the upper row and with dielectric bags in the middle row. The bottom row contains the relative difference maps between those shown above. While the CEST maps show no outstanding differences, the B_1 map with dielectric bags shows distinctly reduced areas of maximum and minimum relative B_1.

with the regions of minimum B_1.

The bottom row of Figure 5.17 shows the relative difference between the maps of the different setups. The highest differences in the MTC maps are observed in the proximity of CSF, whereas the difference in the area of WM is very small. The rNOE maps also differ only moderately in the area of WM, whereby the relative difference in the area of GM is higher over the whole-brain. However, a substantially greater difference can be observed in the amides, which is relatively uniform across the brain. In contrast to MTC and rNOE, no clear correlation to brain tissue can be identified. Similarly, there is no clear relation between the relative difference map of the amides and that of rel. B_1. The difference map of relative B_1 shows a clear divergence in the area of the temporal lobes and the cerebellum compared to the rest of the brain. These brain regions are nearest to the dielectric bags.

Table 5.2 compares the mean MTR_{LD} values within the ROIs of WM and GM for the contrasts of MT, rNOE and amides between the two experimental setups. The mean values for both tissue types and all contrasts are slightly reduced when dielectric bags are used, although the difference for the MTC is marginal.The variation within the ROIs of WM and GM is not very remarkable whether the electric bags are used or not. With the exception of $\mathrm{MTC_{WM}}$ and $\mathrm{rNOE_{WM}}$, however, the standard deviation within the ROI is slightly increased in the case of dielectric bags. The contrast between WM and GM is comparable, with a minimal increase in the relative difference for rNOE (13.16 % to 12.52 %) and a minimal reduction for MTC (35.32 % to 35.80 %) when dielectric bags are used.

		MTC	**rNOE**	**amides**
WM	**without**	20.25 % ± 4.66 %	14.25 % ± 4.74 %	3.90 % ± 2.26 %
	with bags	20.22 % ± 4.16 %	13.84 % ± 4.69 %	3.68 % ± 2.92 %
GM	**without**	14.10 % ± 2.27 %	12.57 % ± 1.10 %	4.83 % ± 1.19 %
	with bags	14.15 % ± 3.02 %	12.13 % ± 1.59 %	4.56 % ± 1.64 %
rel. diff.	**without**	35.80 %	12.52 %	21.30 %
	with bags	35.32 %	13.16 %	21.36 %

Table 5.2: Mean MTR_{LD} within ROIs of WM and GM for MTC, rNOE and amides as well as the relative difference between WM and GM given by $\text{rel.diff} = 2 \cdot \left(\mid MTR_{\mathrm{LD}}^{\mathrm{WM}} - MTR_{\mathrm{LD}}^{\mathrm{GM}} \mid \right) / \left(MTR_{\mathrm{LD}}^{\mathrm{WM}} + MTR_{\mathrm{LD}}^{\mathrm{GM}} \right)$, each for the experimental setup with and without dielectric bags. The mean values are slightly reduced for each contrast when dielectric bags are used, while the standard deviations within the ROIs are at a comparable level.

pTx experiments

As a further approach to homogenize CEST saturation and excitation, the CEST experiment was performed using the pTx coil. While measurements in CP mode are similar to the sTx experiments, the PUSHUP CEST sequence uses water-selective excitation pulses optimized for parallel transmit and pTx PUSHUP saturation pulses.

Figure 5.18 shows the relative B_1 distributions, normalized to the target B_1, for CP and PUSHUP saturation modules. The left plot depicts the distribution over the whole brain. The CP B_1 distribution is very broad and includes relative B_1 values from 0.25 to about 1.75. In addition to the maximum

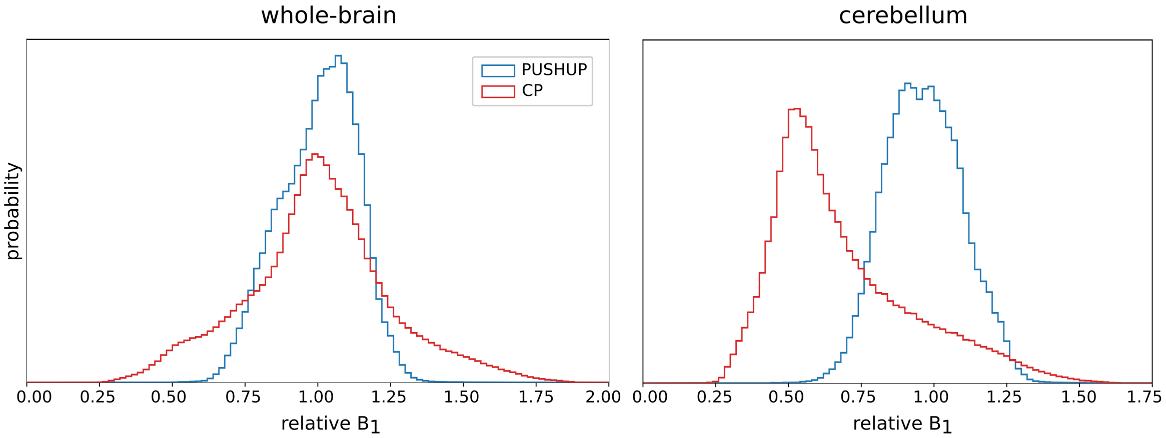

Figure 5.18: Group histograms of the relative B_1 distributions of the different saturation modules, merged over all subjects. The rel. B_1 distribution is normalized to the target $B_1 = 0.8\,\mu\mathrm{T}$. The B_1 distribution is evaluated in the whole brain (left) and additionally, only in the brain region of the cerebellum (right). In both cases, the B_1 distribution for the CP mode is clearly broader. In the cerebellum, the distribution is shifted to lower B_1 values.

probability around $rB_1 = 1$, a small local plateau can be seen in the area of $rB_1 = 0.5$. In comparison, the rel. B_1 distribution of the PUSHUP saturation is clearly narrower and the probability is mostly between $rB_1 = 0.75$ and $rB_1 = 1.25$. Its maximum is slightly shifted to a higher relative B_1.

Considering the distribution of relative B_1 only in the cerebellum in the right plot of Figure 5.18, the maximum probability for CP saturation shifts to $rB_1 = 0.5$. The probability of rB_1 being larger than 1 is much lower compared to the whole-brain distribution. Using the PUSHUP saturation, the rel. B_1 distribution within the cerebellum resembles the whole-brain distribution with a slightly widened maximum around $rB_1 = 1$.

With PUSHUP, no voxel is close to the point of divergence of the contrast-based 1-point B_1 correction of the ssMT amplitude. In contrast, when using CP saturation, both a few cerebral voxels and some voxels in the cerebellum would approach this value, which makes the use of a contrast-based 1-point correction difficult.

Moreover, the root-mean-square error of the normalized B_1 distribution of both saturation modules was calculated within the whole brain and also within the cerebellum only. With 12.9 % for whole-brain and 14.3 % for cerebellum, PUSHUP saturation leads to a more homogeneous saturation in both regions compared to the CP saturation, where the root-mean-square error is 22.3 % for whole-brain and even 39.7 % for cerebellum.

In-vivo CEST experiments were performed on five healthy volunteers, including three different B_1 amplitudes to determine the B_1 correction required for PUSHUP saturation.

Figure 5.19 depicts the CEST contrast maps for $\delta_{\mathrm{MTC}} = -1$ ppm and $\delta_{\mathrm{amides}} = -3.5$ ppm of one subject with different retrospective B_1 correction methods. In addition, the corresponding relative B_1 map is shown as well as the WM/GM segmentation mask. The B_1 distribution shows residual inhomogeneity mainly in the head-feet direction with a maximum area in the middle of the brain, best seen in the coronal and sagittal slices. The axial slice shows only small B_1 variations.

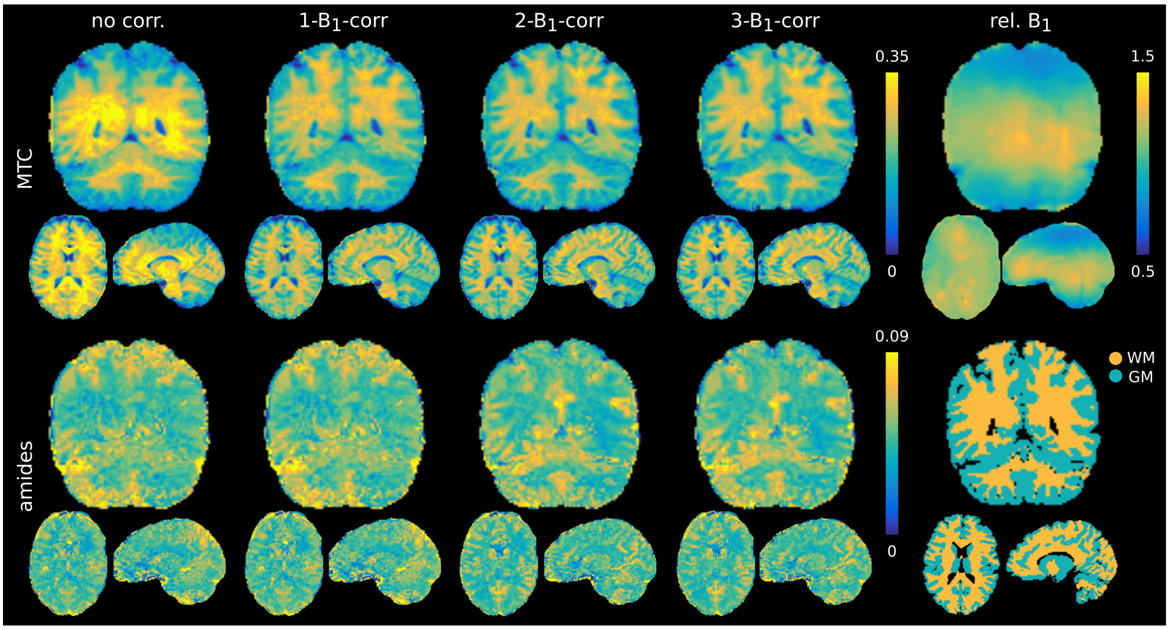

Figure 5.19: CEST contrast maps for one healthy volunteer acquired with the PUSHUP sequence for $\delta_{MTC} = -1$ ppm and $\delta_{\text{amides}} = 3.5$ ppm of representative axial, coronal and sagittal views. Uncorrected ($B_{1,\text{sat,nom}}$=0.8 µT) and contrast 1-B_1 corrected and Z-B_1-corrected ($B_{1,\text{sat}}$ =0.8 µT) maps derived with two and three B_1 sampling points (N_{B1}) are shown. Corresponding views of the relative B_1 map are displayed on the right. The impact of B_1 inhomogeneity is observed to be reduced for all B_1-corrected maps, with a slight increase in image quality for higher numbers of B_1 values.

The B_1 effects are most visible in the MTC images. Without B_1 correction, the intensity profile correlated with the B_1 map quite well. In the central regions of the brain, the measured signal is increased compared to the upper and lower parts, which correspond to areas with low B_1. With the contrast-based 1-point B_1-correction, this intensity profile can be compensated for, and the signal appears homogeneous through the whole brain. There are no major differences between 1-point, 2-point or 3-point B_1 correction in the MTC maps. All of these maps show a clear WM/GM contrast that is very well matched to the segmentation mask.

In the amide signal, the B_1 inhomogeneity is less obvious without B_1 correction and the signal already appears homogeneous. Due to the very low C in the 1-point B_1 correction in the amide amplitude, the 1-point corrected maps look almost identical. Using the 2-point correction, it appears that the WM/GM contrast is slightly sharper compared to the 1-point correction. In the low B_1 regions, the signal of the amides appears to be higher in the 1-point B_1 corrected maps than in those corrected with 2 B_1 sampling points. As with the MTC maps, there is no major difference within the amide maps between the 2-point and 3-point B_1 corrections, both resulting in a homogeneous signal across the brain.

Additionally, the group mean and standard deviation of the MTR_{LD} are shown in Figure 5.20 for both contrasts (upper row: MTC, lower row: amides) to compare the different B_1 correction methods. The single subject mean values are depicted as gray crosses and additionally listened in Table D.3 in Appendix D.

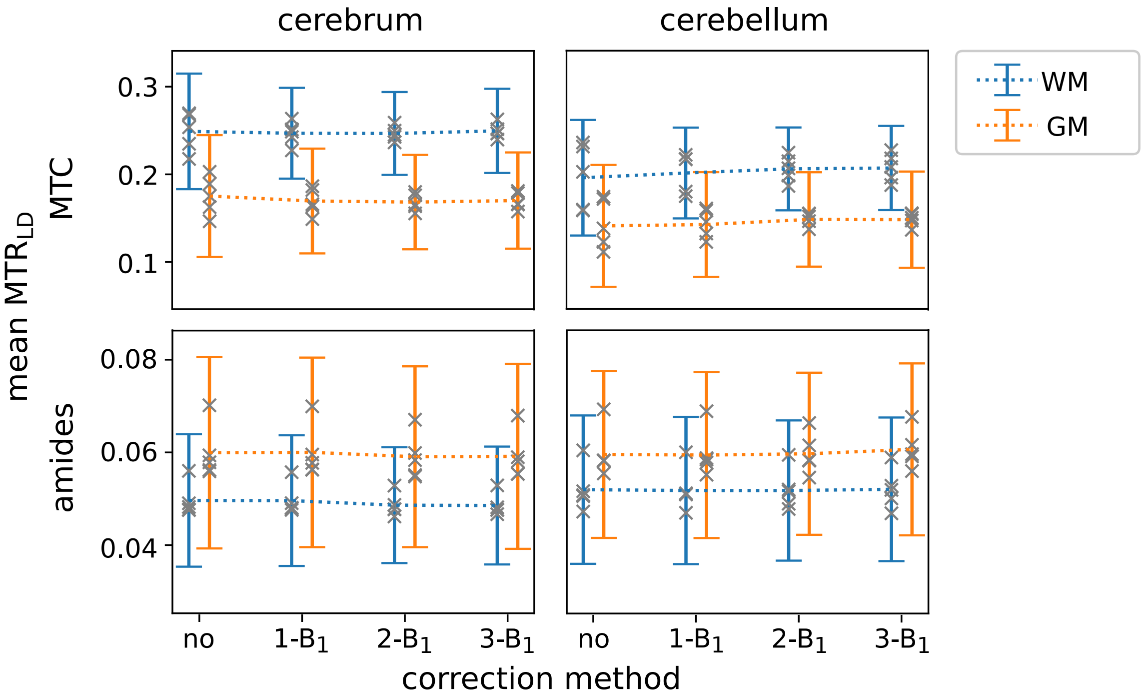

Figure 5.20: Group mean and standard deviation of MTR_{LD} for MTC (upper row) and amides (lower row) within the masks of white matter (blue) and gray matter (orange), calculated separately for cerebrum (left) and cerebellum (right) with varying number of N_{B1}. The gray crosses mark the single-subject mean values.

In the case of MTC, the group mean MTR_{LD} is 24.9 % ± 6.6 % in WM and 17.5 % ± 6.9 % in GM within the cerebrum without retrospective B_1-correction. While the mean amplitude is almost identical for all B_1-correction methods, the standard deviations drop for 1-point B_1-correction (24.9 % ± 5.0 %, 16.9 % ± 5.8 %) and drop further for 2-point B_1-correction (24.7 % ± 4.7 %, 16.8 % ± 5.4 %). Simultaneously, also the spread of single-subject mean values decrease. Within the cerebellum, the mean MTR_{LD} for MTC is 19.7 % ± 6.7 % in WM and 14.2 % ± 5.1 % in GM without B_1 correction, which is slightly less than in the cerebrum. Using 1-point B_1-correction, the mean amplitudes increase and the standard deviations decrease (20.6 % ± 5.8 %, 14.6 % ± 4.5 %). This trend continues for 2-point B_1-correction (20.7 % ± 5.9 %, 14.9 % ± 4.1 %).

The group mean MTR_{LD} of the amides is 6.0 % ± 2.1 % in GM and 5.0 % ± 2.0 % in WM of the cerebrum without B_1 correction and do not change substantially with B_1 correction. The sole variable that differs with the utilization of the 2-point or 3-point B_1 correction is the mean MTR_{LD} of the single subjects. In the cerebellum, the trend of the mean amide MTR_{LD} values exhibit a similar trend. 2-point B_1-correction leads to mean amide signal of 6.0 % ± 1.8 % in GM and 5.2 % ± 1.5 % in WM.

Figure 5.21 compares the CEST contrast maps (MTC, rNOE and amides) of the same subject acquired with PUSHUP saturation after 1-point B_1 correction (top row) and after 2-point B_1 correction (middle row) with the maps acquired in CP mode, corrected with 3 N_{B1} (bottom row), i.e. acquisition times increase approx. 1-, 2-, 3-fold from top to bottom. Additionally, the segmentation mask and the relative B_1 map for each saturation module is shown. The B_1 distribution of the PUSHUP saturation

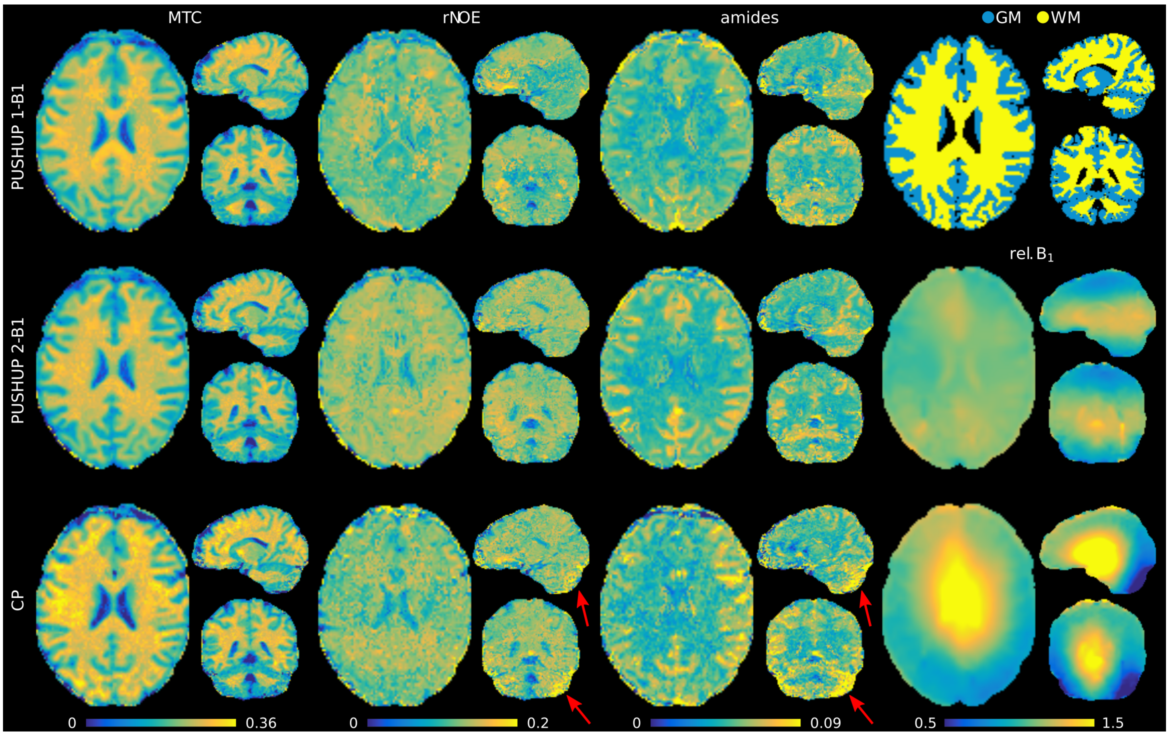

Figure 5.21: pTx MTR_{LD} maps of one healthy subject for $\delta_{MTC} = -1$ ppm, $\delta_{rNOE} = -3.5$ ppm and $\delta_{\mathrm{amides}} = 3.5$ ppm acquired with PUSHUP saturation (upper and central row) and with CP mode (lower row). While the CP maps are corrected with N_{B1}=3, PUSHUP maps after 1-point and after 2-point B_1 correction are shown. In the right column, the segmentation mask (upper row) and the relative B_1 maps are depicted. The red arrows indicate quantification artifacts in the CP maps that coincide with regions of low B_1^{rms}. In both the axial and sagittal planes, perturbations can be seen in all maps, indicating residual distortion artifacts.

differs substantially from that of the CP mode, not least due to the much smaller spread of B_1 values.

For every saturation module, very clear and homogeneous WM/GM contrasts can be seen in the MTC maps. However, increased MTC values in WM for CP saturation is visible.

In contrast, the rNOE contrast maps differ more clearly. Although the WM/GM contrast is not very pronounced in any of the variants, the contrast appears slightly sharper for 1-point PUSHUP, while the WM rNOE values are slightly higher in 2-point PUSHUP. In the region of the cerebellum, artificially high values are seen in the CP map (indicated by red arrows), overshadowing the contrast. This artifact is correlated with the regions in which the relative B_1 drops below 0.5.

The CP maps of the amide contrast, also show artificially high values within the region of low B_1. Outside these regions, a clear WM/GM contrast is visible. These artifacts do not occur in the PUSHUP maps and a homogeneous WM/GM contrast is visible throughout the whole brain, even if the GM amide values are slightly lower with 1-point B_1 correction.

In addition, all maps show slight residual distortion artifacts in the frontal region of the brain, best seen in the axial and sagittal views.

5.3 CEST quantification

To evaluate the performance of the developed 3D-EPI CEST sequence and the associated processing pipeline, test-retest measurements were performed. Moreover, the CEST maps and the whole-brain mean-MTR_{LD} values of 14 different subjects were analyzed.

5.3.1 Test-retest experiments

Figure 5.22 shows the CEST contrast maps of a subject who participated in the complete CEST experiment on three different days. The level of the MTR_{LD} for δ_{MTC}=-1 ppm, δ_{rNOE}=-3.5 ppm and δ_{amides}=3.5 ppm is comparable for all sessions, with slightly attenuated white matter values in the

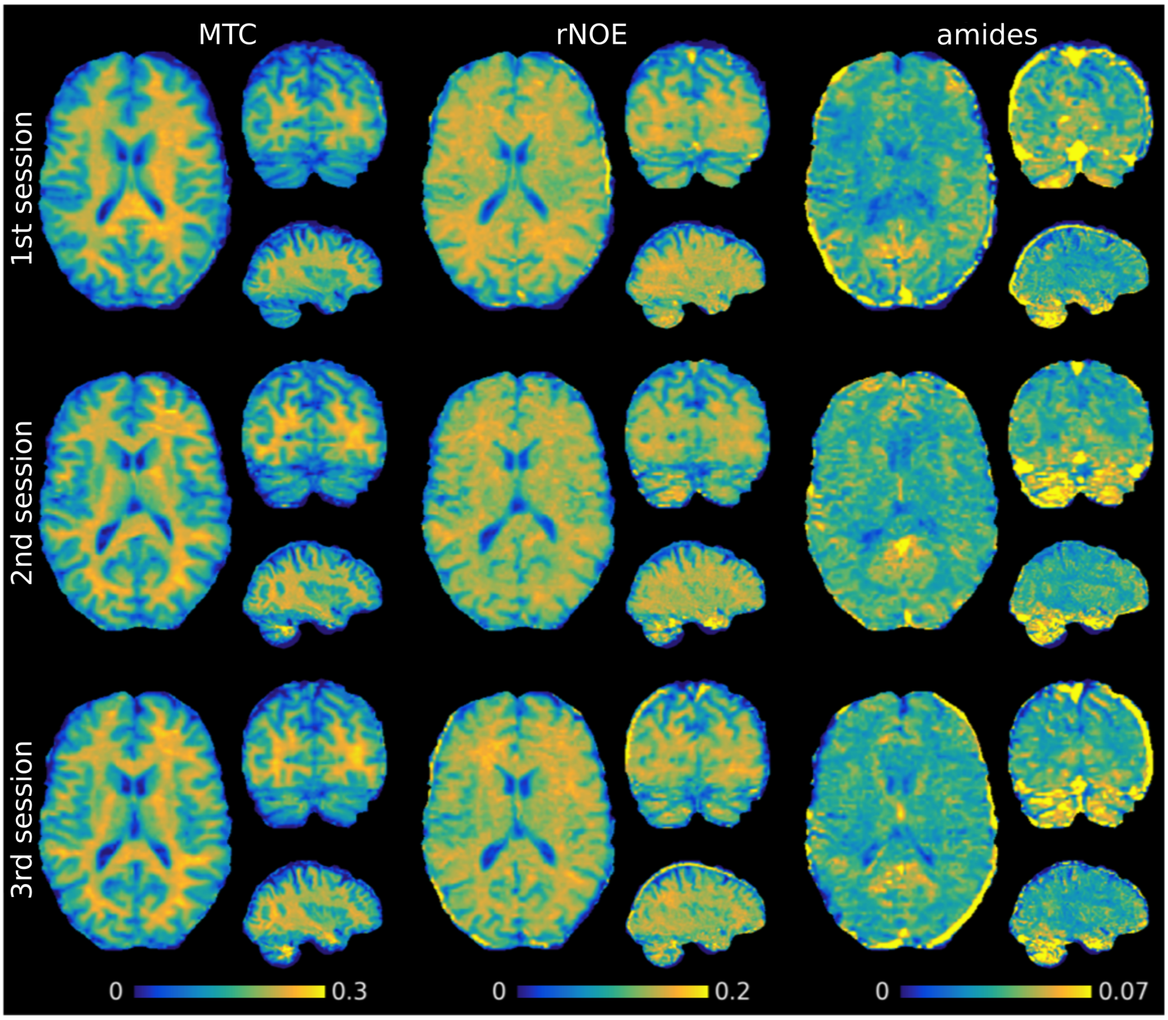

Figure 5.22: CEST contrast maps of one healthy subject for δ_{MTC}=-1 ppm, δ_{rNOE}=-3.5 ppm, δ_{amides}=3.5 ppm and δ_{amines}=2.2 ppm in axial, coronal and sagittal orientation (columns), measured with identical setting on three different days (rows). Even if there are small differences between the sessions, the CEST contrast maps are very similar overall. High value voxels in the maps suggest a lack of quantification.

maps of the first session. The differentiation between WM and GM also does not change substantially between sessions. In the amide maps, voxels with particularly high values are found in the area of the cerebellum as well as in the area of the CSF close to the skull bone, indicating insufficient quantification. These artifacts can also be found to a lesser extent in the sagittal views of the rNOE and MTC maps, with slight deviations between sessions.

The mean MTR_{LD} values within the ROIs of WM and GM are presented in Figure 5.23 (upper row) and additionally listed in Table D.4, which can be found in Appendix D. As can already be seen in Figure 5.22, the mean MTR_{LD} of MTC in WM (16.70 % ± 6.14%) is slightly lower in the first session than in the other two (18.27 % ± 5.70 % and 18.99 % ± 5.66 %). It can also be seen that the mean MTR_{LD} of rNOE in GM (11.81 % ± 3.61 %) is slightly higher in the first session (compared to 11.43 % ± 3.64 % and 11.46 % ± 3.54 %) whereas mean MTR_{LD} of rNOE in WM is lower in the first session (12.79 % ± 3.19 % to 13.02 % ± 3.01 % and 13.17 % ± 2.99 %). In contrast, the mean MTR_{LD} of the amides is quite constant, with only a small variance in GM for the first session (4.05 % ± 1.75 % to 4.17 % ± 1.67 % and 4.19 % ± 1.91 %). The standard deviation within the ROIs does not differ substantially between the sessions.

Moreover, the relative difference between WM and GM is depicted in the lower row of Figure 5.23. While the WM/GM contrast of the 2nd and 3rd session is on a comparable level, there is a clear discrepancy to the 1st session for all contrasts. In the case of the amides, the relative difference is 8.49 % for the first session and 11.14 % and 11.88 % for the other sessions.

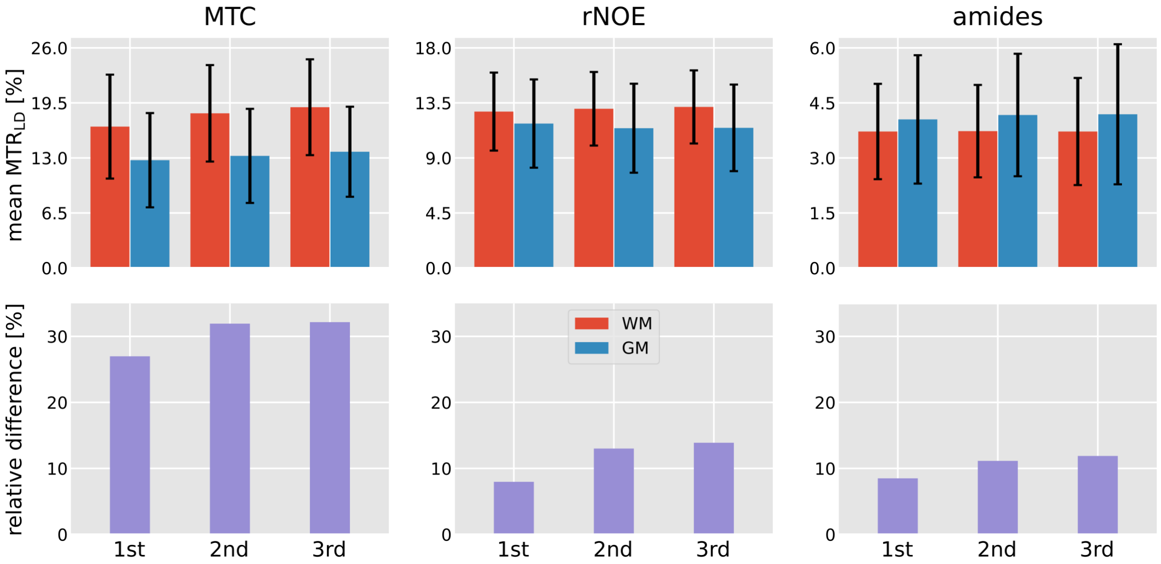

Figure 5.23: Mean and standard deviation of MTR_{LD}, which is depicted in Fig. 5.22, in ROIs representing white and gray matter (upper row). In addition, the relative difference between WM and GM given by rel.diff = $2 \cdot \left(| MTR_{\text{LD}}^{\text{WM}} - MTR_{\text{LD}}^{\text{GM}} | \right) / \left(MTR_{\text{LD}}^{\text{WM}} + MTR_{\text{LD}}^{\text{GM}} \right)$ is shown (lower row). While the MTR_{LD} of δ_{rNOE} is relatively constant over all measurements, it varies more clear for δ_{MTC} within WM and for δ_{amides} within GM. The WM/GM contrast also varies slightly between the sessions, although the same trend is evident for all three contrasts.

Table 5.3 contains the intra-subject coefficient of variation (CoV) between the individual sessions calculated separately for WM and GM. The CoV is largest for the MTC within WM (5.35 %) and smallest for amides within WM (0.13 %). While the CoV within GM is smaller than in WM for the MTC, it is larger within GM compared to WM for amides. In the case of the rNOE contrast, the CoV for WM and GM is at a comparable level.

	MTC	rNOE	amides
WM	5.32 %	1.20 %	0.13 %
GM	3.09 %	1.49 %	1.49 %

Table 5.3: Inter-session, intra-subject CoV of MTR_{LD}, which is depicted in Fig. 5.23 within ROIs of WM and GM. The highest CoVs can be found for MTC.

Another experimental setup involved test and retest measurements of the subjects within the same session. The MTR_{LD} maps for MTC, rNOE and amides of one out of the three volunteers are shown in Figure 5.24. No considerable difference can be observed between test and retest maps and likewise the distinguishability between WM and GM is similar. However, it is noticeable that the retest maps have a little blurred appearance, which also reduces the sharpness of the WM/GM contrast, especially for the maps of the amides. The occurrence of the high-value artifacts is comparable between the first and second measurement.

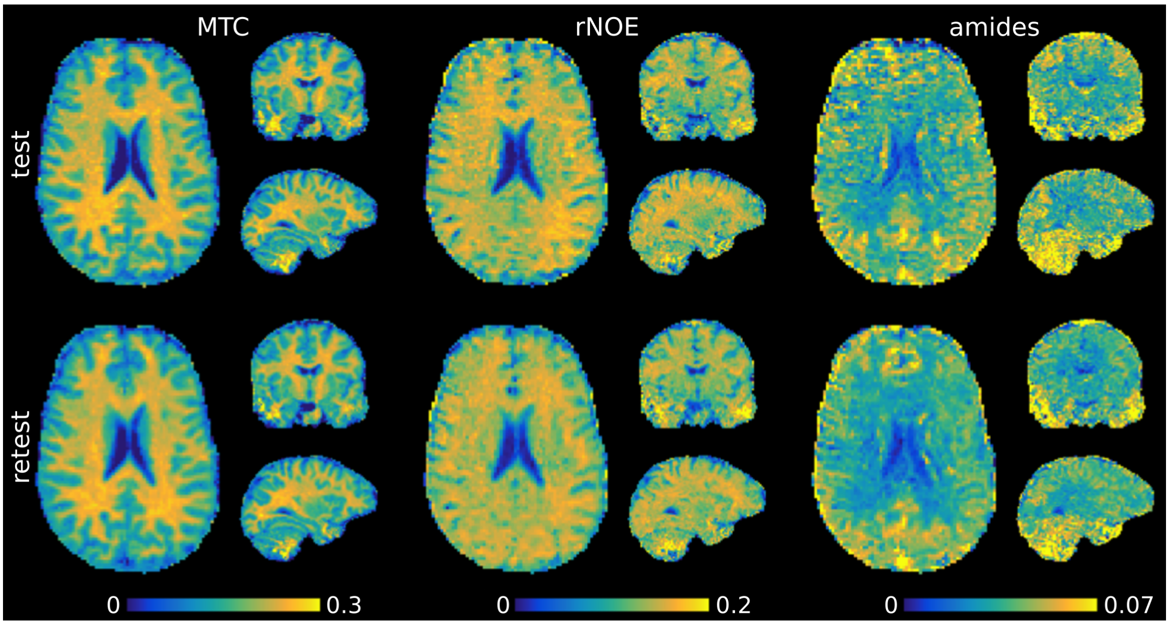

Figure 5.24: CEST contrast maps of one healty subject for δ_{MTC}=-1 ppm, δ_{rNOE}=-3.5 ppm and δ_{amides}=3.5 ppm in axial, coronal and sagittal orientation (columns). Test and retest measurements were acquired within the same session (rows). In general, the MTR_{LD} maps were well comparable. The retest maps, which were also registered on the reference image of the test data set, appear a little blurrier.

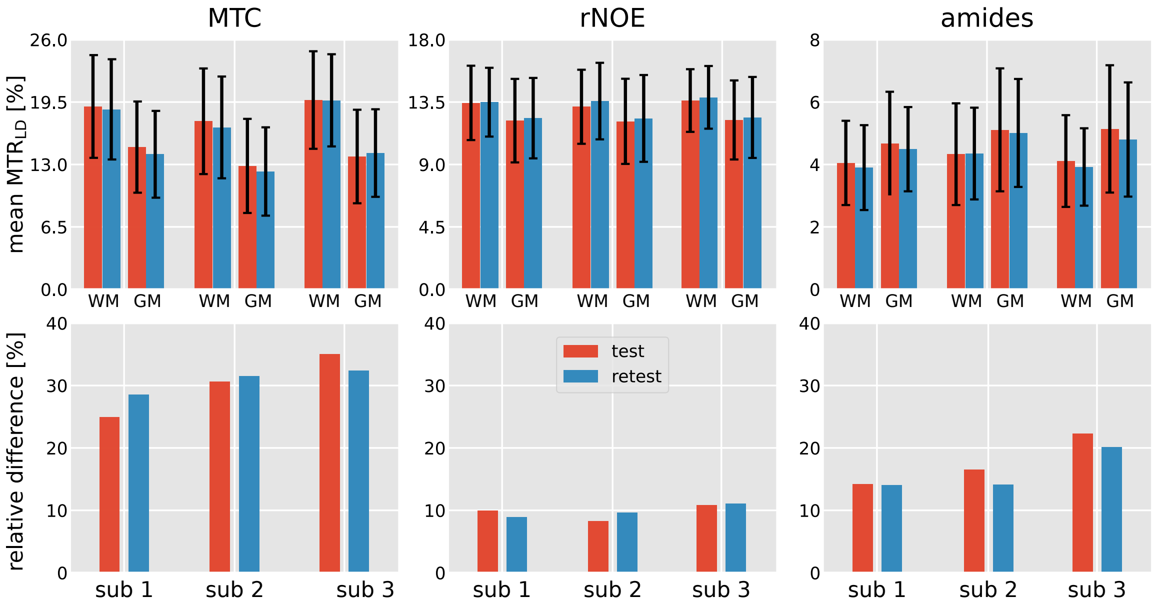

Figure 5.25: Mean and standard deviation of MTR_{LD} within WM and GM ROIs (upper row) of the test and retest measurements for all three subjects. The relative difference between WM and GM given by rel.diff $= 2 \cdot \left(|\, MTR_{\mathrm{LD}}^{\mathrm{WM}} - MTR_{\mathrm{LD}}^{\mathrm{GM}} \,|\right) / \left(MTR_{\mathrm{LD}}^{\mathrm{WM}} + MTR_{\mathrm{LD}}^{\mathrm{GM}}\right)$ is shown in the lower row. For all subjects small deviations can be recognized for each contrast, while the standard deviations do not differ substantially. The WM/GM contrast also varies between test and retest measurements, although there is no clear correlation of the contrasts.

Figure 5.25 compares the mean MTR_{LD} within WM and GM of all three subjects and a corresponding Table D.5 can be found in Appendix D. Although the mean MTR_{LD} values of test and retest measurements are relatively similar, there are differences for all contrasts. No trend can be seen that the different contrasts in WM and GM consistently deviate in the same direction. Nevertheless, the variance between the individual subjects is more pronounced than the variance within a subject. While MTC means differ only up to 0.75 % between test and retest measurements (GM 14.81 % ± 4.75 %, 14.06 % ± 4.52 %), they vary up to 3 % between subjects (WM 19.71 % ± 5.08 %, 16.86 % ± 5.30 %).

The second row of Figure 5.25 depicts the relative difference between WM and GM. Again, small differences can be observed between first and second measurement of the subjects. Both the differences between test and retest measurement (on average 0.89 %) as well as the variance between the different subjects is lowest for rNOE (0.84 % to 2.75 %). All measurements show that the relative difference for MTC is the highest (30.53 % ± 3.15 %) and for rNOE the lowest (9.80 % ± 0.98 %). In the case of the amides, the relative difference is much more variable between the subjects (up to 6 %) than it is between test and retest experiments (up to 2.4 %).

The intra-session, intra-subject CoV for all subjects is presented in Table 5.4, separately for WM and GM. Over all subjects, the CoV for MTC and amides is smaller in WM than in GM, whereby it is variable for rNOE. The smallest CoV can be found for MTC in WM (0.08 %) for the third subject and at the same time the highest CoV is calculated for amides in GM (3.42 %).

		MTC	rNOE	amides
sub 1	WM	0.79 %	0.19 %	1.89 %
	GM	2.60 %	0.73 %	1.97 %
sub 2	WM	1.86 %	1.53 %	0.23 %
	GM	2.31 %	0.86 %	0.99 %
sub 3	WM	0.08 %	0.84 %	2.37 %
	GM	1.28 %	0.73 %	3.42 %

Table 5.4: Intra-session, intra-subject CoVs of MTR_{LD}, which are depicted in Fig. 5.25 within ROIs of WM and GM. In the case of MTC and amides, the variance is larger in GM than in WM.

5.3.2 CEST contrast evaluation

To statistically evaluate the snapshot 3D-EPI CEST sequence, the measurement results of 14 test subjects were classified into three categories:

1. sTx experiments were performed on nine subjects, using an isotropic resolution of 2 mm. The experiments were carried out with both B17 and E12 version of the sequence and scanner software and were processed using the 3-point B_1 correction. While 66 frequencies were measured for eight subjects, the shortened list with 43 offsets could be used for the 9th subject.
2. Using the same saturation module in the CP mode with the pTx coil, five subjects were measured with an isotropic resolution of 1.61 mm and 43 offsets. As in the sTx experiments, 3-point B_1 correction was performed.
3. Within the same pTx session, these five subjects were measured with the PUSHUP saturation, also with the isotropic resolution of 1.61 mm and 43 offsets but with the 2-point B_1 correction.

Figure 5.26 shows the CEST contrast maps for MTC, rNOE and amides from two exemplifying subjects per experimental setup and the associated relative B_1 maps in representative axial, coronal and sagittal slices. The B_1 distribution in CP mode with its maximum in the central area of the brain and the minimum in the areas of the temporal lobes and the cerebellum resemble the B_1 maps of the sTx measurements. PUSHUP saturation, on the other hand, produces a narrower B_1 spread as well as a distinct distribution with a higher B_1 region in the central region of the head and a drop in the head-feet direction.

WM and GM are clearly distinguishable on all MTC maps. There is a discrepancy in MTC values of about 5 % between the 2 mm sTx and the 1.61 mm pTx maps. However, there is also a slight variation in the MTC values between the pTx experiments. While the pTx maps of the MTC have higher values, the values of the rNOE maps are somewhat lower compared to the sTx maps and the WM/GM contrast also seems to be slightly reduced. A clear WM/GM contrast can be seen in the sTx maps of the amides, the structural delineation is more pronounced in the pTx maps, which are acquired with increased resolution. The amide values are about 2 % lower with the sTx setup compared to the pTx acquisitions, similar to the MTC values. Artificially high values in the area of the cerebellum are seen on both sTx and pTx maps measured in CP mode, indicating inadequate quantification. In the case of the amide maps, the quantification artifacts completely overshadowing the contrast in the same brain regions. In this region, the relative B_1 is close to 0.5. These artifacts

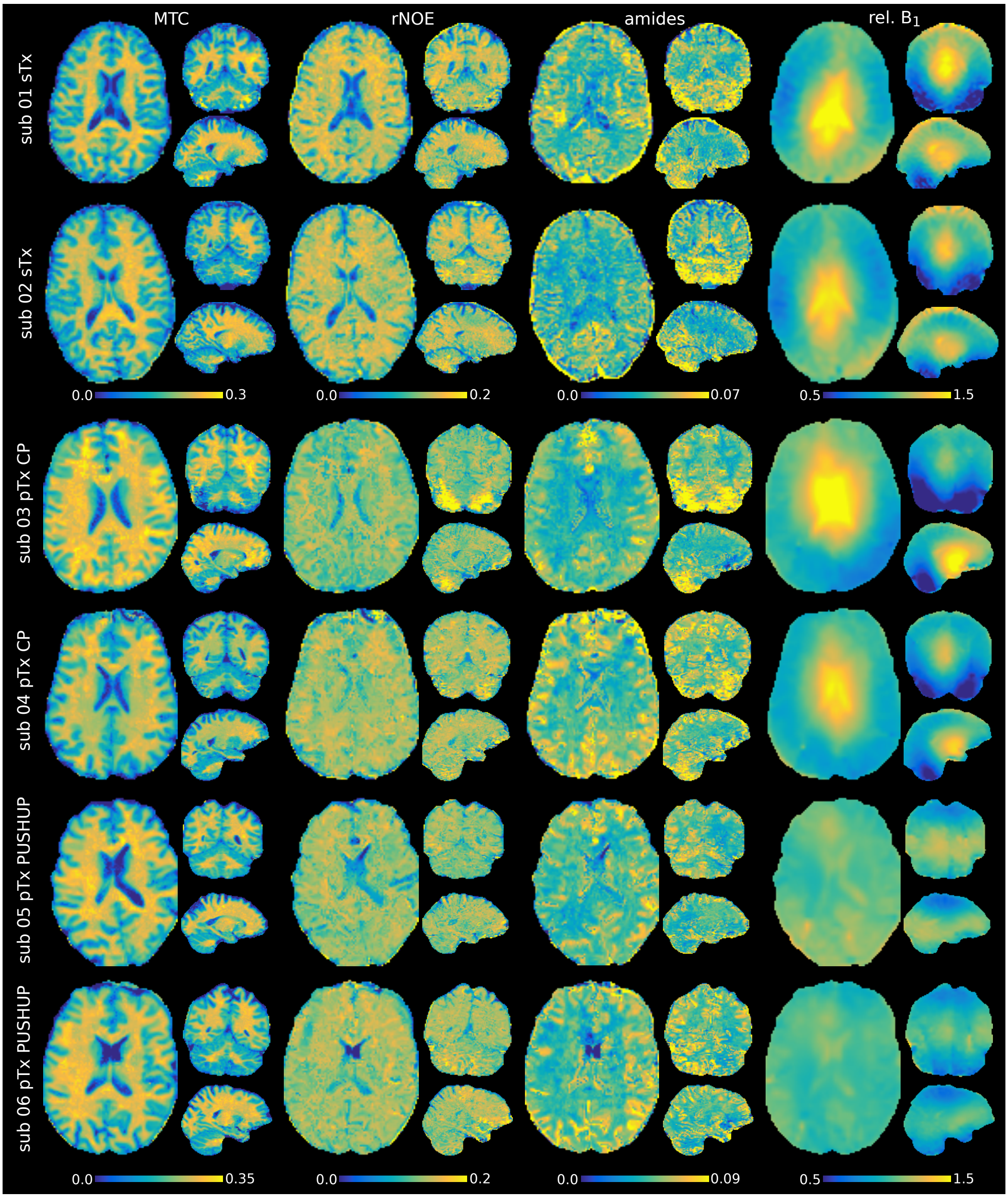

Figure 5.26: CEST contrast maps for $\delta_{\mathrm{MTC}} = -1$ ppm, $\delta_{\mathrm{rNOE}} = -3.5$ ppm and $\delta_{\mathrm{amides}} = 3.5$ ppm in axial, coronal and sagittal orientation (columns) and the corresponding relative B_1 maps. The maps of two subjects per measurement protocol are shown (rows): 2 mm sTx and 1.61 mm pTx with CP saturation using the 3-point B_1 correction and 1.61 mm pTx with PUSHUP saturation and 2-point B_1 correction. The amplitudes of the CEST contrast maps differ between sTx and pTx measurements. The PUSHUP experiments show a clear difference in the B_1 distribution and the PUSHUP maps are the only ones not affected by the quantification artifacts.

cannot be identified in maps acquired with PUSHUP saturation. Even in the cerebellum, all PUSHUP maps show artifact-free contrast.

Independently of the experimental setup, CSF can be identified most clearly in the MTC maps, somewhat less clearly in the rNOE maps and least clearly in the amide maps. At the same time, the WM/GM contrast is somewhat clearer in the amide maps than in the rNOE maps.

The mean MTR_{LD} within the WM and GM ROIs per subject is shown in Figure 5.27 (left and middle columns) and listed in Table D.6, which can be found in Appendix D. In addition, Table 5.5 summarizes the mean value of the group MTR_{LD} within WM and GM ROIs, separately for the three experimental settings. The third column of Figure 5.27 shows the relative difference between the mean MTR_{LD} of WM and GM for each subject. The associated Table D.7 can also be found in Appendix D.

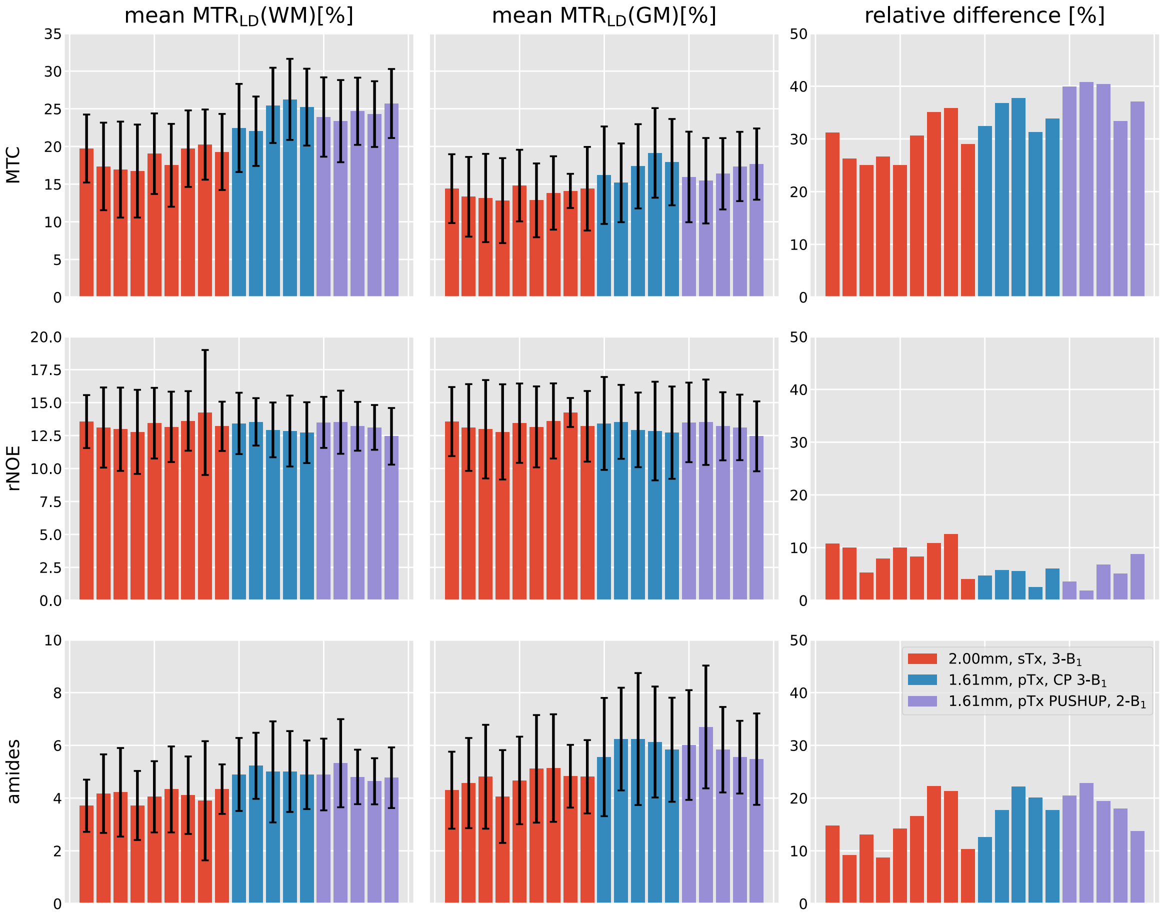

Figure 5.27: Mean and standard deviation of MTR_{LD} of MTC (upper row), rNOE (middle row) and amides (lower row) within WM (left column) and GM ROIs (middle column) and the relative difference given by rel.diff $= 2 \cdot \left(| MTR_{\mathrm{LD}}^{\mathrm{WM}} - MTR_{\mathrm{LD}}^{\mathrm{GM}} |\right) / \left(MTR_{\mathrm{LD}}^{\mathrm{WM}} + MTR_{\mathrm{LD}}^{\mathrm{GM}}\right)$ of the 14 subjects (19 experiments). The three different experimental setups are labeled by different colors: 2 mm sTx (red) and 1.61 mm pTx with CP saturation (blue) and 1.61 mm pTx with PUSHUP saturation (violet). There is a noticeable difference in the mean MTR_{LD} values between the sTx and pTx experiments.

In the case of MTC, the mean MTR_{LD} in WM varies by about 4 % from 16.74 % ± 6.17 % to 20.25 % ± 4.66 % in the sTx setup and by about 2 % from 12.81 % ± 5.54 % to 14.40 % ± 4.57 % in GM. In both tissues, the group mean MTR_{LD} is substantially higher in the pTx experiments: 24.28 % ± 1.71 % and 24.29 % ± 0.79 % in WM and 17.16 % ± 1.37 % and 16.56 % ± 0.83 % in GM. Although the group means of both pTx experiments are comparable, the variance within the ROIs and also between subjects decreases with the PUSHUP saturation. While the mean values show a clear discrepancy between sTx and pTx experiments, there is an overlap in the relative difference (i.e. contrast) between WM and GM, with the contrast being lowest using the sTx setting (24.99 % to 35.80 %) and highest using the PUSHUP saturation (33.38 % to 40.76 %).

The second row of Figure 5.27 shows the mean MTR_{LD} analysis for rNOE. In contrast to MTC, there is not much difference in the mean MTR_{LD} between the three experimental setups. The standard deviation within the WM ROI is slightly lower in the pTx experiments (up to 2.69 %) compared to the sTx experiments (up to 4.74 %). Nevertheless, it is striking that the WM/GM contrast is clearly smaller for both pTx experiments (4.90 % ± 1.29 % and 5.22 % ± 2.41 %) compared to the sTx measurements (8.85 % ± 2.60 %). This discrepancy is reflected in the means by a slightly higher group mean MTR_{LD} in WM (13.34% ± 0.41%) and a slightly lower group mean MTR_{LD} in GM (12.21% ± 0.27%) of the sTx trials. However, it should also be noted that the relative difference between the individual subjects has a very large variance of up to 10%.

Concerning the amides (bottom row of Figure 5.27), there is again a considerable increase of MTR_{LD} in both WM and GM from the sTx setup to the pTx setup. While the sTx group mean MTR_{LD} for WM is 4.06 % ± 0.22 %, it is 4.89 % ± 0.23 % for PUSHUP saturation and even higher for CP saturation (5.00 % ± 0.12 %). The same trend can be seen for GM. The variability between the subjects is lowest for the pTx setup in the CP mode. There is no substantial difference in the homogeneity within the ROI of WM and GM between the three experimental settings. The WM/GM contrast is substantially improved in the pTx experiments with a group mean relative difference of 18.07 % ± 3.18 % and 18.90 % ± 3.03 % compared to the sTx setting with a group mean relative difference of 14.48 % ± 4.63 % . The variance between subjects is also smaller for the pTx experiments, with a small advantage for the PUSHUP saturation.

	tissue	MTC [%]	rNOE [%]	amides [%]
sTx	WM	18.50 ± 1.28	13.34 ± 0.41	4.06 ± 0.22
	GM	13.74 ± 0.69	12.21 ± 0.27	5.70 ± 0.33
	rel.diff	29.41 ± 3.86	8.85 ± 2.60	14.48 ± 4.63
pTx CP	WM	24.28 ± 1.71	13.09 ± 0.33	5.00 ± 0.12
	GM	17.16 ± 1.37	12.46 ± 0.32	6.00 ± 0.27
	rel.diff	34.44 ± 2.48	4.90 ± 1.29	18.07 ± 3.18
pTx PUSHUP	WM	24.29 ± 0.79	13.15 ± 0.39	4.89 ± 0.23
	GM	16.56 ± 0.83	12.50 ± 0.65	5.92 ± 0.44
	rel.diff	38.31 ± 2.79	5.22 ± 2.41	18.90 ± 3.03

Table 5.5: Group mean MTR_{LD} values in ROIs of WM and GM, separately for the three different measurement protocols: 2 mm sTx and 1.61 mm pTx with CP saturation using the 3-point B_1 correction and 1.61 mm pTx with PUSHUP saturation and 2-point B_1 correction. All experiments were performed with 120 Gaussian-shaped RF pulses with t_{p} = 15 ms and DC = 50 %.

CHAPTER 6

Discussion

CEST imaging enables MR contrast to be modulated by the molecular milieu of the brain. The quantitative imaging of molecules and metabolites has already yielded numerous successes in the field of tumor imaging and can contribute to tumor staging, among other things. However, the use of CEST in neurodegeneration research is still in its infancy. In contrast to the clearly definable morphology of tumors, neurodegenerative changes are often diffuse and distributed throughout the brain, so that morphological changes usually do not become apparent until a very late stage of the disease. Clinical studies usually rely on large cohorts or long periods.

The challenges for a CEST sequence that can be used in clinical trials in neurodegenerative research are therefore to combine a high quality whole-brain FOV with a short acquisition time in order to include several imaging modalities in one experiment. In this work, a CEST experiment was implemented that is whole-brain capable using the time-efficient 3D-EPI readout combined with necessary field inhomogeneity correction methods. At the same time, it offers a high flexibility of the saturation module based on the snapshot concept.

6.1 Optimization of the CEST saturation scheme

Choice of the saturation parameters

Amide proton transfer is the most researched contrast in CEST imaging with a wide range of applications in cancer, stroke, Alzheimer's disease and more [151]. A train of Gaussian RF pulses was selected for the saturation module based on the publications of Zaiss et al. [30, 94, 115]. Simulations and phantom measurements were carried out to define the best experimental setup to maximize amide contrast under viable conditions. Three parameters were investigated:

First, the determination of the total saturation time t_{sat} involves a trade-off between the degree of saturation and the overall duration of the sequence, as the saturation is applied repeatedly for each frequency offset. According to JEMRIS simulations, the first two seconds of saturation had the most significant impact, achieving a high saturation level. However, a duration of approximately 6 s is recommended for a fully saturated effect. Simultaneously, the extended saturation time also results in an increased SAR contribution. As a compromise for time and SAR efficiency, the saturation time was set to 3.6 s, achieving nearly 85 % of maximum achievable contrast. In comparison, Zaiss et al. [30] proposed a total saturation time of 4.5 s, that would result in approximately 90 % of saturation (see Figure 5.1). However, the marginal benefit of stronger saturation would be accompanied by a 25 % increase in scan time, which in turn would be disadvantageous.

Secondly, the duty cycle (*DC*) was chosen with consideration of the saturation effect and SAR constraints, which can be a limiting factor in ultra-high field experiments. From the simulation results in Figure 5.1, it becomes clear that a *DC* higher than 50 % significantly increases the CEST contrast. However, because SAR is proportional to *DC*, a high duty cycle is problematic. To avoid exceeding the SAR limits, a *DC* of 50 % was chosen for the pulse train, in compliance with the publication of Zaiss et al. [30] which combined the saturation with a 3D spiral GRE readout at 9.4 T. Earlier publications of Zaiss et al. [94, 115] and Windschuh et al. [37] implemented a slightly higher *DC* of 60 %, using a single slice readout at 7 T.

Third, the simulations demonstrate a clear dependence of the CEST effect on both the pulse duration t_p and the flip angle. Despite the oscillations caused by the flip angle dependence (see Fig. 5.3), there is a tendency for the CEST effect of the amides to decrease with increasing pulse duration. Phantom experiments confirm this finding, but the effect tends to level off for a pulse duration longer than 20 ms. Contrary to the simulated results, the MTR_asym analysis does not show any oscillation that correlates with the flip angle. Looking at the direct water saturation, the peak width becomes narrower and the homogeneity of the saturation increases with prolonged pulse duration, although the saturation effect decreases.

Both the simulation results and the phantom measurements indicate that a short pulse duration is favorable for a higher CEST effect, although it should be long enough to generate a sufficiently narrow peak width. Zu et al. [99] have shown that the most efficient saturation with short pulses is achieved when the flip angle is equal to $FA = \gamma \cdot B_1 \cdot t_\mathrm{p} = 180\,^\circ$, as the magnetization of the solute pool is inverted during on-resonant irradiation at $\Delta\omega = \delta\omega_s$. With an average pulse amplitude of $B_1 = 0.8\,\mu\mathrm{T}$, the pulse duration of $t_\mathrm{p} = 15\,\mathrm{ms}$ satisfies this condition.

The in-vivo results (see. Fig. 5.7 and 5.8), obtained from the full processing pipeline, including B_1 correction, also clearly show that the values of the amides is substantial higher with $t_\mathrm{p} = 15\,\mathrm{ms}$ compared to a longer pulse duration, even if there is no distinct difference in the amine values. The amplitude of the rNOE contrast also decreases significantly with increasing pulse duration, while the MTC contrast is slightly lower at $t_\mathrm{p} = 15\,\mathrm{ms}$ compared to a longer pulse duration, yet the high quality of the MTC maps is not compromised. Therefore, the 3.6 s saturation module, which contains a train of 120 Gaussian RF pulses with $B_1 = 0.8\,\mu\mathrm{T}$, $t_\mathrm{p} = 15\,\mathrm{ms}$ and $DC = 50\,\%$, meets the SAR and time efficiency requirements while providing adequate amide contrast. The recent publication by Mennecke et al. [110] shows a similar saturation scheme, also containing 120 Gaussian-shaped RF pulses with a pulse duration of 15 ms, but with a shortened interpulse delay of $t_\mathrm{d} = 10\,\mathrm{ms}$, resulting in a slightly briefer total duration of $t_\mathrm{sat} = 3\,s$. With the complete independence of the saturation module and the readout train, realization of the shortened pulse train would generally be straightforward, presuming SAR limits for whole-brain imaging are not compromised.

Determination of frequency offsets

The optimization of the number of frequency offsets with which the Z-spectrum is sampled allows for significant reduction in the overall duration of the CEST experiment. The main challenge was to determine the minimum number of offsets needed for optimal sampling of the amide peak, while ensuring sufficient data for the 5-pool Lorentzian fit to separate the CEST effects from magnetization transfer and spillover effects [133].

Three different non-equidistantly offset lists of 66, 54 and 43 frequencies (see Table 4.1) were compared in the frequency range of ±60 ppm with denser sampling within ±5 ppm. Previous publications using Lorentzian peak-fitting algorithms have reported varying numbers of frequency offsets, with some using wider range of offsets, but all employing denser sampling within ±5 ppm [30, 31, 105].

In order to fit the very broad MTC peak, frequencies well outside the ±5 ppm range are required. While list 66 measures symmetrically around zero, the data points in the shortened lists are reduced and distributed asymmetrically. Apart from a slight increase in the MTC values, the quality of the MTC maps remains high, as evidenced by the fine GM structures. Moreover, the frequencies upfield of the Z-spectrum are more strongly attenuated due to the broader nature of the aliphatic rNOE peak compared to the CEST effects of amides and amines. Nevertheless, the rNOE peak is recorded in all variants with frequency increments of 0.25 to 0.5 ppm. The reduced sampling pattern in the range outside of −4 ppm may be the main reason for the small difference in the rNOE maps. While list 66 included a frequency increment of 0.125 ppm from 1.75 ppm to 4 ppm, the denser sampling is reduced from 2.5 ppm to 3 ppm for list 54 and further reduced in the frequency range of the amines for list 43, since the saturation was mainly optimized for amides. However, a frequency increment of 0.25 ppm was maintained to include the amine peak within the 5-pool Lorentzian fit. Although the deviation from the amide maps of list 66 is higher than for MTC and rNOE, the quality of the maps remains similar. Due to the spectral proximity of the peak maxima of amides and amines, as well as the higher peak width of the amines, the small changes in the amide maps can be explained by less densely sampled amine peaks and resulting uncertainties during the fit.

Furthermore, the frequency selective saturation is highly influenced by B_0 inhomogeneity due to local susceptibility-induced field shifts. Considering the whole-brain FOV, even after careful shimming, frequency variations can exceed 1 ppm in regions near the nasal cavity and ear canals. In contrast, variations appear to be smaller across other brain regions. To ensure the identification of CEST peaks in regions with higher B_0 inhomogeneity, the experiments included a long saturation offset list with a fine sampling pattern. In the end, a compromise between frequency increment and B_0 shift was chosen to reduce the offset list. The maps from all three frequency offset lists show good results after B_0 correction, without clear deviation due to B_0 inhomogeneities. This indicates not only that the frequency pattern is fine enough, but that the width of the peaks is also well captured to compensate for B_0 deviations.

With 43 offsets, the entire Z-spectrum can be measured in a time-efficient manner, which provides both a sufficiently dense sampling for the Lorentzian fit and robustness to small B_0 variations. The offset list recently published by Mennecke et al. [110] is somewhat longer with 54 offsets, but conforms quite well with 39 offsets in the range of ±5 ppm. Assuming sufficient time for the CEST measurement within the overall experiment, it might still be advantageous to add some offsets in the region of the amine peak.

6.2 Whole-brain imaging at 7T

In order to enable CEST imaging of the whole brain, a very fast readout with a moderate SAR contribution and a sufficient SNR for a high resolution is required. At the same time, the challenges of a whole-brain FOV at 7 T must be overcome. In addition to B_0 variations, the main challenge is severe B_1 inhomogeneity.

6.2.1 Adaptions of the 3D-EPI readout for CEST imaging

In this work, a fast and robust snapshot sequence based on a 3D-EPI readout was introduced to acquire 2 mm and 1.61 mm isotropic whole-brain CEST images at ultra high-fields. Since the introduction of the BOLD effect, EPI has become the benchmark sequence for acquiring functional MRI (fMRI) time series [35]. In particular, 3D-EPI sequences benefit not only from the high SNR efficiency due to the high ratio of signal acquisition time to the total acquisition time, but also from the ability to achieve high acceleration factors at high spatial resolutions without exceeding SAR or maximum RF power limits [35, 152]. Compared to the simultaneous multi slice (SMS-EPI) approach, which is also widely used, the 3D-EPI readout can provide an advantage in terms of tSNR [152] and additionally, provides a slice-independent CEST contrast. In particular, RF power deposition is reduced by small flip angle excitation and alternative fat suppression.

Through the introduction of water-selective excitation, the chemical shift artifact from fat could be efficiently suppressed. Compared to CHESS fat saturation [153], which is typically used in EPI experiments, potential MTC interaction was avoided and SAR was significantly reduced while SNR efficiency was increased [121]. In addition to the successful suppression of ghosting artifacts of lipid signals in the scalp, fat artifacts in the Z-spectrum were also minimized, which otherwise not only lead to pseudo-rNOE signal [154], but also impair the often used asymmetry analysis of the amides [155]. In the pTx experiments, the single-rectangular water-selective excitation pulse was replaced by the highly homogeneous water-selective binominal GRAPE excitation pulse [127], which suppressed the lipid signal effectively and beyond, lead to a homogeneous excitation through the whole brain. No fat artifacts are observed in the raw data of the PUSHUP CEST sequence, in the CEST contrast maps, or in the acquired MPRAGE images, which also use the binominal GRAPE excitation pulse [42].

The combination of 6-fold accelerated 3D-EPI readout with external phase correction scans and the acquisition of the ACS lines at the beginning of the sequence allows the acquisition of whole-brain images with 2 mm isotropic nominal resolution in $t_{\text{readout}} = 734$ ms. Increasing the acceleration to 8-fold, an improved resolution of 1.61 mm can be acquired within $t_{\text{readout}} = 1.1$ s. By centrally reordering the secondary phase encoding direction, the 3D-EPI readout achieves improved saturation contrast. By implementing initial dummy excitations to the 3D-EPI volume acquisition, systematic phase fluctuations along the secondary phase encoding direction can be avoided. The phase stabilization results in a tSNR increase of 18.6 %, even though a small amount of the initial magnetization is not used. Moreover, a high readout bandwidth, combined with parallel imaging, counteract susceptibility-induced geometric distortion artifacts, which can be a major problem with EPI. The remaining distortions are very small and accounted for by employing a commonly used EPI distortion correction technique based on a reversed phase encoding reference scan [130].

In addition to the CEST preparation, the EPI images are locally affected by B_0 inhomogeneities. This results in signal dropouts and geometric distortions in the aforementioned regions, which in turn leads to increased CEST quantification errors. Potential future improvements could include a third-order B_0 shim to reduce the field inhomogeneity or a 3D-EPI snapshot CEST readout, which would be additionally segmented along PE_1. In conjunction with parallel imaging, this would enable the utilization of even higher PE_1 bandwidth and shorter echo times than those employed in the present study, thereby further mitigating the impact of signal dropouts and distortions.

A GRE-based snapshot CEST approach with a volume coverage of $220 \times 160 \times 32\,\text{mm}^3$ at a resolution of $1.5 \times 1.5 \times 2\,\text{mm}^3$ was presented by Zaiss et al. [30]. The authors found that more than 5 % of the initial CEST contrast remains available at the end of the 2.5 s square-spiral readout. Since the GRE-based sequence is less affected by physiological noise and does not suffer from distortions along PE_1, it has the advantage of higher signal stability than the EPI approach. On the other hand, the speed and efficiency of the 3D-EPI readout allows, in the case of 2 mm isotropic resolution, a 6-fold increase in volume coverage in a third of the readout time with only a small fraction of the excitations. Thus, according to the calculations in [30] (see Equation 4.2), more than 30 % of the prepared CEST contrast is still available at the end of the 734 ms 3D-EPI readout. This is an indication that a longer 3D-EPI acquisition time may be a viable option for CEST contrast. Consequently, it is possible to implement a CEST protocol with an isotropic resolution of 1.61 mm in $t_{\text{readout}} = 1.1\,\text{s}$. Compared to the spiral GRE readout, the voxel volume can thus even be reduced by 7 % in about half the readout time, while maintaining whole-brain coverage. Another way to take full advantage of the remaining CEST contrast is to use additional segmentation along PE_1 or less parallel imaging acceleration. Furthermore, a higher flip angle would be possible to maximize SNR, although this would result in increased blurring along PE_2. In addition to the temporal advantage of the 3D-EPI readout, Mueller et al. [156] showed in their work that 3D-EPI has a significant tSNR advantage in direct comparison to the 3D-spiral GRE readout, which was also introduced as snapshot approach.

In comparison to the presented snapshot approach, steady-state CEST sequences [17, 31, 33], including one saturation pulse per excitation, are more vulnerable to motion artifacts since the acquisition time per volume is longer (10-18 s/volume) [17, 31, 33]. Another advantage of whole-brain snapshot acquisition is that motion across different CEST contrasts can be corrected for by retrospective motion correction. Despite only minor motion artifacts in the 3D-EPI raw data, retrospective motion correction between contrasts is mandatory for an accurate Z-spectrum analysis. Using the 3.5 ppm image as a reference for motion correction, no obvious motion artifacts were detected in the images. Similarly, for high-resolution CEST, the whole-brain acquisition in only 1.1 s over 45 repetitions did not reveal any apparent motion artifacts. Nevertheless, this would probably need to be reviewed for more motion-prone subject groups. Further, Khlebnikov et al. [32] showed that the pseudosteady-state pulsed 3D CEST acquisition scheme is more sensitive to the effects of slow-exchange CEST, such as rNOE and amide CEST, than the steady-state approach. The snapshot 3D-EPI CEST sequence corresponds to such a pseudo steady-state pulsed 3D CEST scheme with the long saturation block of 3.6 s. Nevertheless, due to the independence of saturation and imaging part, snapshot CEST is not limited to pseudo steady-state examinations. This approach provides great flexibility for CEST studies in clinical trials by allowing complete freedom in saturation design.

6.2.2 B_1 inhomogeneity

Global RF distribution

Strong spatial variations of the B_1 field due to wave propagation effects at ultra-high fields lead to an inhomogeneous excitation of the tissue and beyond directly influence the labeling efficiency for CEST saturation. This issue becomes especially evident when expanding the FOV from a single slice or a slab of a few centimeters to whole-brain coverage of approximately 15 to 20 cm (head-to-feet). Especially in the lower regions of the head, B_1 is particularly low, leading to insufficient signal and thus difficulties not only with CEST quantification, but also with processing steps such as brain extraction. Without pTx, this results in a very high reference voltage for scaling the saturation amplitude for the subsequent B_1 correction, which is restricted by the SAR limits.

The cerebellum and the temporal lobes represent two particularly challenging anatomical regions for quantification at 7 T. On the one hand, this is due to the requirement of sTx reference voltages higher than 450 V, and on the other hand, this is due to larger B_1 variations between the subjects. One potential hardware limitation is the relatively short transmit ring of the Rx/Tx coil along the z-direction. An extended head coil may be beneficial in improving head-feet coverage and thus the B_1 distribution in the lower regions of the brain.

Furthermore, the utilization of dielectric bags for passive B_1 shimming also offers the potential to improve the B_1 distribution in these regions. In a study by Haines et al. [146], an increase in signal intensity was observed in the temporal lobes, with values ranging from 70 to 140 %. As shown in Figure 5.17, the distribution of B_1 becomes slightly narrower when dielectric bags are used, resulting in decreased amount of B_1 in the center and improved B_1 in the lower part of the brain. However, there are still areas in the temporal lobes and particularly in the cerebellum where the relative B_1 is below 0.5, which correlates with quantification errors within the CEST maps. Besides, the application of the dielectric material inside the head coil can contribute to increased SAR [157, 158], resulting in a more severe limitation of the maximum reference voltage. During the experiment, U_{ref} had to be reduced from 450 to 425 V to comply the SAR restrictions, which can affect the subsequent B_1 correction. Although the passive shim effect of the dielectric bags in the cerebellum area is not sufficient, they provide improved quantification in the temporal lobes despite the reduced maximum U_{ref}. Before using the dielectric bags in clinical studies, it is important to note that the positioning of the bags is variable and that the patient's positioning in the head coil is also more uncomfortable. This could lead to increased restlessness and head movements, especially in a motion-prone patient group.

The most powerful approach to improve the B_1 distribution is the use of parallel transmit excitation [52, 53]. Compared to the very broad B_1 distribution with CP mode, the dispersion of B_1 values is significantly reduced using the PUSHUP saturation. Especially in the region of the cerebellum, the relative B_1 could be distinctly increased, which enables an adequate quantification of the amides even without retrospective B_1 correction. Further, the reduced B_1 spreading allows for smaller variations of the saturation amplitude to cover the whole-brain FOV for retrospective B_1 correction, which additionally results in the availability of SAR capacities.

The residual B_1 inhomogeneities are predominantly in head-feet extension. A primary reason for this spreading is the coil geometry, as all coil elements are arranged in a ring around the head-feet axis.

Consequently, the signal loss in this direction is the same because superposition cannot effectively compensate for it. 16 channel transmit coils using two rings [159] allow an optimization in this direction and may be able to significantly improve the homogeneity.

The PUSHUP saturation module results in a more uniform distribution of B_1 while maintaining similar SAR efficiency compared to the MIMOSA saturation of Liebert et al. [39]. Homogeneity can be further increased at the cost of increased SAR by reducing the regularization parameter during pulse calculation [42]. Equally, by increasing the regularization, the SAR requirements can be reduced at the trade-off of less homogeneous excitation. This strategy may be useful for UHF applications beyond 7 T, where SAR constraints are even more difficult to satisfy.

The calculation of universal pulses [125] for excitation and saturation enables a simple and fast execution of the CEST sequence during the measurement. The B_1 distribution is very consistent across all subjects, through the amplitude varies slightly from subject to subject. One way to minimize this issue is to use tailored pulses for each subject [38], which is time-consuming, less SAR-efficient and challenging to incorporate into a comprehensive study design. One potential alternative approach could involve calculating universal pulses on various subsets of the database, such as those based on head size, age, and gender, or by utilizing a more sophisticated clustering algorithm [160]. Yet, this requires further research and a much larger database than the one used here.

Restrospective B_1 correction

Without subsequent correction of the B_1 inhomogeneities, the CEST contrast shows a clear correlation to the B_1 pattern, even with the significantly narrower distribution of the pTx approach. To allow for an adequate quantification, it is recommended by Windschuh et al. [37] to include at least the B_1 sampling points that cover the highest and lowest B_1 values within the FOV. To account for a realistic range of B_1 values across the whole head, sTx reference voltages up to 450 V could be chosen without exceeding SAR limits. In part, this is attributable to the relatively low RF power deposition of the 3D-EPI readout. This represents a reasonable upper limit for CEST quantification at the 7 T system utilizing the 32/1 (Rx/Tx) channel head coil. Based on the global RF distribution analysis, it can be seen that 300 V is a reasonable average reference voltage for B_1 interpolation. Consequently, 150 V would be ideal as the minimum reference voltage to cover areas of high relative B_1. However, the comparison between 3-point and 4-point correction, which differ only in this sampling point, shows that 200 V is sufficient as a minimum reference voltage for the correction.

The results in Figures 5.15 and 5.16 indicate that acquiring three reference voltages with [200, 300, 450] V is a viable option for whole-brain CEST using the sTx coil. It is slightly more stable against stronger B_1 variations than the B_1-correction with $N_{B1} = 2$ (200 V, 450 V) for which a systematic CEST contrast difference was observed as well as a significant larger median absolute error compared to $N_{B1} = 7$. Due to the strong B_1 inhomogeneity in all spatial orientations at 7 T, it was shown that a B_1 correction with 2 sampling points is already necessary for single-slice experiments [37]. The introduction of further reference voltages to the interpolation did not result in a notable enhancement of the outcomes whereby the measuring time would be considerably longer. Zaiss et al. [30] presented a similar distribution of the three B_1 sampling points ([0.5, 0.8, 1.2] µT = [62.5, 100, 150] %) at 9.4 T although the FOV has a significantly smaller head-feet extent.

In the case of the pTx experiments, it was necessary to re-evaluate the B_1 correction. The B_1 distribution in CP mode corresponds to that of the sTx distribution, but the scatter of B_1 values is significantly smaller with PUSHUP saturation. As a result, the B_1 sampling points can be selected more narrowly, ([80, 100, 120] % instead of [66.67, 100, 150] %). Based on the results presented in Figure 5.19, it is evident that a subsequent B_1 correction is still required, even though PUSHUP provides a more homogeneous saturation. Without correction, the MTC maps show a clear correlation with the B_1 pattern. Although the amide maps are already significantly more homogeneous without B_1 correction than in CP mode, there is a slight correlation to the B_1 drop in the head-feet direction. The MTC is sufficiently compensated for the influence of B_1 with the adapted contrast-based 1-point B_1 correction [135]. However, a slight improvement can be observed in the case of the amides by using the 2-point B_1 correction. Quantification artifacts occur in the CP maps in areas of very low B_1, but both the 1-point and 2-point corrected PUSHUP maps are free of artifacts.

While three B_1 sampling points do not yield any improvement, a 2-point correction may result in a slightly more stable CEST quantification than the 1-point correction at the cost of twice the acquisition time. In particular, for motion-prone patient groups or in the context of extensive measurement protocols, a second measurement point may be neglected. Both correction methods agree with previous pTx publications. Mennecke et al. [110] used 2 B_1 sampling points in their 7 T study despite a smaller FOV and MIMOSA saturation. Liebert et al. [161] demonstrated that whole-brain CEST with MIMOSA saturation in combination with parallel transmit FOCUS excitation is viable with a 1-point correction as long as the B_1 variations are not too expensive. Either way, one or two B_1 sampling points correspond to substantially shorter scan time than three points that have to be used with CP mode saturation.

Recently, Hunger et al. [162] published the deepCEST method at 7 T, which is a promising alternative CEST quantification approach with implicit B_1 correction. The approach corrects the B_1 dependency using a neural feed-forward network with a single B_1 sampling point. The authors suggest that the algorithm has been successful due to the narrowed B_1 distribution by the MIMOSA saturation. This indicates that deepCEST may also be effective when used in combination with the PUSHUP saturation. To this end, it would be necessary to investigate how the deepCEST maps relate to the Lorentizian-fitted maps and whether deepCEST is able to neglect the small differences between the 1-point and 2-point corrected maps. Although there is no data yet on deepCEST processing for sTx data, the authors expect that this method may also lead to a reduction of B_1 sampling points and thus also of the total measurement time.

6.2.3 Imaging protocol

The 3D-EPI based CEST approach provides 2 mm isotropic CEST data of the whole brain, which is capable for 5-pool Lorentzian fitting, within a total acquisition time of 3:27 min per B_1 sampling point. Increasing the resolution to 1.61 mm isotropic voxel size combined with a higher acceleration factor (from 6 to 8), extends the total measurement time by only 13 s to 3:40 min. In the case of sTx experiments or pTx experiments in CP mode, the required acquisition of 2 additional B_1 sampling points to allow for B_1 correction still keeps the total scan time below 12 min. By taking full advantage of parallel transmission, the total measurement time is significantly reduced to less than 8 min or 4 min when 2- or 1-point correction is used, respectively.

However, in order to process the CEST data, additional measurements are required besides the 3D-EPI CEST sequence. Retrospective distortion correction [130] requires two non-saturated measurements with opposite phase encoding directions (AP and PA). These are acquired separately in the specified protocol with five image volumes each within 14 s. Although the measurement time is negligible over the duration of the entire experiment, it could be further reduced by minimizing the number of image volumes. It would also be conceivable to measure only one additional M_0 scan with reversed phase encoding direction to be used with the forward phase encoding M_0 scan of the CEST series, which would add less than five seconds of measurement time.

Through integration of the dual-echo principle into the 3DREAM sequence [66], fieldmapping of both B_1 and B_0 were captured together within 6 s. The well established B_0 correction method WASSR [134] acquires the pure direct water saturation typically from -1 to 1 ppm to calculate a water frequency reference. Although WASSR saturation can be combined with 3D-EPI readout to obtain the same resolution and thus a voxel-wise determination of B_0 variations, B_0 variations above 1 ppm, as they occur in whole-brain experiments, are not covered. On the other hand, the coverage of the WASABI [14] approach, which also determines B_1 at the same time, should be sufficient for whole-brain acquisitions with a frequency range of ± 1.5 ppm. However, both methods have the disadvantage of a significantly longer measurement time (in the order of a few minutes) due to the necessary repetitions to acquire the water Z-spectrum. Instead, 3DREAM acquires isotropic 4 mm field maps that have to be interpolated to compute the Z-spectrum, but the partial volume effect should be of secondary importance due to the mostly slowly changing field alterations. Moreover, the really short acquisition time enables to acquire field maps multiple times during the experiment in order to monitor the B_0 drift during the session. The field drift across seven CEST measurements (approx. 30 min) was relatively small (0.1 ppm, consistent with Windschuh et al. [163]) and could be disregarded since the smallest difference between two frequency offsets was 0.125 ppm. Nevertheless, it is advisable to include field mapping at least at the beginning and end of the CEST measurements to observe any field changes and to properly evaluate the CEST data.

The complete sTx CEST imaging protocol requires approximately 20 min, including three B_1 sampling points for B_1 correction, field mapping, shimming, and an anatomical scan for the WM/GM analysis. If the CEST measurements are integrated into a larger experiment, which typically includes anatomical sequences, approximately 15 min should be scheduled for the acquisition of the Z-spectra. In the case of pTx experiments, the measurement time is further reduced due to the lower number of B_1 sampling points.

6.3 CEST contrast maps

The 3D-EPI based CEST approach provides high quality CEST data of the whole brain with respect to speed and SAR requirements. A semi-automated processing pipeline was used to calculate the contrast maps of five different pools, incorporating correction methods for motion, distortion and field variations. The maps allow differentiation between WM, GM and CSF with a comparable profile of intensity over all subjects. The MTR_{LD} evaluation was classified within three groups due to variances in resolution and B_1 correction method.

The group means of rNOE vary relatively little between the three setups, but there is a distinction in the relative difference between WM and GM as the resolution increases from 2 mm to 1.61 mm. Consequently, the discrepancy may be attributed to reduced partial volume effect at 1.61 mm resolution.

The WM values from 12.44 to 14.25 % and the GM values from 11.40 to 13.26 % are in a comparable range to other 7 T works. Zaiss et al. [94] and Mennecke et al. [110] reported rNOE values of about 14 %, while Heo et al. [17] and Jones et al. [31] showed slightly smaller values between 6 and 8 %. While the first also used a pseudo-steady state approach, the second applied a steady-state approach, which may explain the differences to the results shown here. The WM/GM ratio, which range from 1.02 to 1.13, fall between the reported WM/GM ratios of 1.00 [110] and 1.34 [31].

The group means of MTC exhibited a notable increase in WM and GM, attributable to the reduction in voxel size. Consequently, it can be concluded that the partial volume effect of CSF is reduced in the 1.61 mm CEST maps compared to the 2 mm maps, leading to an increased MTR_{LD}. In their study, Zaiss et al. [94] reported an MTR_{LD} in WM of approximately 17 % at an in-plane resolution of $(1.56\,\mathrm{mm})^2$ and a slice thickness of 5 mm, resulting in an even larger voxel size. This value aligns with the mean value of the sTx group, which was found to be 18.50 %. The contrast between WM and GM also increases significantly as the resolution is increased, and this increase is further enhanced by the usage of the homogeneous PUSHUP saturation. Beyond, the variability between subjects using the PUSHUP saturation is less than in CP mode. The homogeneity of the MTC is also somewhat improved with PUSHUP when comparing the distribution per subject. The PUSHUP approach benefits from a more homogeneous excitation, fewer B_1 sampling points, and thus a shorter measurement duration and presumably less head movement.

The group mean values of the amides also demonstrate a clearly higher MTR_{LD} as well as a larger relative difference between WM and GM with increasing resolution. In contrast, the difference between CP mode and PUSHUP saturation is comparatively small. In the context of the sTx setup, the $MTR_{\mathrm{LD}} = 4.06\%$ for WM exhibits a high degree of concordance with the previously reported values of approx. 4 % by Heo et al. [17] and Zaiss et al. [94]. In contrast, Mennecke et al. [110] employed homogeneous MIMOSA saturation and an in-plane resolution of $1.8 \times 1.8\,\mathrm{mm}^2$ with 3 mm slice thickness, resulting in amide values of 5.1 and 6.3 % for WM and GM, respectively. With 4.89 to 5.00 % for WM and 5.92 to 6.00 % for GM, the group means of the PUSHUP approach are in the same range. Likewise, the WM/GM ratio in the range of 0.79 to 0.92 is in the similar range of 0.81 [110].

However, here both the rNOE and amide maps appear a bit noisy in parts. While the low WM/GM contrast in the rNOE maps may be a key factor, the amide peak is the smallest not only in intensity but also in peak width. Physiology-induced signal changes [164] are known to reduce temporal SNR, particularly in segmented 3D-EPI which may affect the quantification of amides. Hypothetically, it is conceivable to include physiological recordings (respiratory belt and plethysmograph) into the CEST processing. Analogous to the general linear model functional MRI analysis, it would be necessary to fit physiology-induced signal changes and contrast changes from dilute molecules simultaneously. This can be achieved by incorporating the modeled signal changes due to physiology (e.g. via RETROICOR [165]) into the Lorentzian fit. As a highly sophisticated alternative, one could obtain actual physiology-induced B_0 higher order field changes by an external field probe system, thereby reducing physiological noise during image reconstruction and correcting the actual CEST preparation frequency offset.

In addition to the spreading of MTR_{LD} across the 14 subjects and three experimental setups, there are also intra-subject variations. The CoV for the intra-session test-retest measurements is between 0.08 and 2.6 %. In addition to a small B_0 drift and coil heating during the measurements, the retest measurements in particular could be influenced by increased head movements due to the longer period of lying. Although the data are free of motion artifacts, even small displacements can lead to uncertainties in the distortion correction and slightly changed field corrections.

With a CoV of up to 5.32 %, the inter-session variations are more severe. A significant factor here is the positioning inaccuracy of the subject in the head coil. This may result in varying distortions or slight deviations in the field maps.

CEST imaging for neurodegeneration research

With regard to the widespread distribution of pathologies related to neurodegenerative diseases across the whole brain [15], an analysis of molecular mechanisms underlying chemical exchange is feasible for the majority of the brain. Due to the low B_1 values in the cerebellum and the temporal lobes in sTx experiments, the proposed sTx setup is suitable when only the cerebrum is investigated. The use of dielectric bags can lead to improved quantification in the temporal lobe area, but it should be considered that the dielectric bags lead to a higher SAR contribution as well as to a more uncomfortable positioning of the patient. Nevertheless, CEST of the cerebrum may prove to be a valuable tool for the investigation and detection of neurodegeneration. For instance, it is possible to quantify CEST effects localized in the hippocampus to investigate early Alzheimer's diseases [15].

The PUSHUP saturation overcomes B_1-related limitations and not only allows CEST quantification of the whole brain including the cerebellum, but also saves measurement time compared to the sTx setup. This may be of potential interest in studies of spinocerebellar ataxia, where MR spectroscopy has revealed metabolic changes in the brainstem and cerebellum [166]. However, a limiting factor of the PUSHUP approach is the requirement for a 7 T scanner with parallel transmission capability.

The 3D-EPI based snapshot CEST approach enables the cross-sectional or longitudinal investigation of chemical exchange in neurodegeneration throughout the brain. The time saved by the abbreviated readout can be allocated to extend the CEST saturation, extending the offset list, or averaging an optimized offset list for the metabolite of interest. The snapshot approach offers complete freedom in the design of the saturation block due to the independence of CEST saturation and signal acquisition. For instance, it may be feasible to design a very fast rNOE protocol (1 - 2 min), utilizing a limited number of offsets around the rNOE peak. Chen et al. [167] demonstrated that the rNOE effect was diminished in AD mice, which they attributed to the presence of aggregated proteins. In addition to the wide distribution of pathology throughout the brain, the diffuse morphology requires the comparison of patient groups with controls. Besides the changes in the brain caused by neurodegenerative diseases, there are numerous other factors to consider. Recently, Mennecke et al. [110] showed that the CEST effect is age-dependent. The snapshot 3D-EPI CEST approach is well suited for large and multi-modality studies, including those performed at 3 T [156], due to its manageable time effort and high degree of flexibility.

CHAPTER 7

Conclusion

The MRI signal contains information not only about distinct tissue compositions, but also about the immediate magnetic, chemical and physical interactions of the spin system. Some of this information is exploited by CEST imaging, offering insights into biochemistry with unprecedented resolution. Especially in the field of neurodegenerative disease research, deeper knowledge of the molecular milieu of the brain can facilitate a more comprehensive understanding of disease pathogenesis. The introduction of the first clinical 7 T scanners has led to an increase in the usefulness of this methodology, as CEST imaging benefits significantly from higher field strength. The aim of this thesis was to develop a robust and rapid method for whole-brain CEST imaging at 7 T, suitable for integration into study protocols of neurodegenerative disease research.

The primary challenge was to identify a rapid and efficient saturation scheme, that optimizes the CEST contrast, depending on the protein concentration. A pulse train comprising Gaussian-shaped RF pulses was optimized for the amide contrast, with a secondary consideration of the rNOE contrast. In order to obtain a purer contrast than that achievable through a simple asymmetry analysis, a frequency offset pattern was designed with the intention of measuring a complete Z-spectrum. This enables the application of a 5-pool Lorentzian fitting procedure for the purpose of quantification. It has been demonstrated that a sufficiently robust CEST effect can be achieved with a total saturation duration of $t_{\mathrm{sat}} = 3.6\,\mathrm{s}$. The use of $120 \times 15\,\mathrm{ms}$ pulses and a DC of 50 % allows the maximization of amide contrast while maintaining SAR within the prescribed limits. By reducing the number of frequency offsets to 43, the measurement time was significantly reduced, while maintaining a stable CEST contrast.

The acquisition of a whole-brain FOV necessitates a rapid readout with a high acquisition duty cycle to minimize the attenuation of the prepared signal during the readout and, furthermore, to minimize the duration of the volume acquisition. By employing a snapshot approach with centric-reordered 3D-EPI readout, the full coverage of the whole brain can be achieved following a single saturation block. While an isotropic resolution of 2 mm can be achieved within 734 ms, an isotropic resolution of 1.61 mm can be achieved within 1.1 s without exceeding the signal attenuation limits. For this purpose, ePC scans and ACS at the beginning of the sequence were implemented in combination with high acceleration factors ($R = 6$ or $R = 8$). By achieving an acquisition time per offset of less than 5 s, the intra-volume motion artifacts are significantly reduced. Furthermore, the FOV coverage allows for retrospective motion correction between volumes. A combination of dummy excitations and a binomial water-selective excitation pulse has been demonstrated to yield improved tSNR and the efficient suppression of fat artifacts. The use of small flip angles and relatively long repetition times in the 3D-EPI approach results in very small contribution to the SAR.

In a third step, correction methods for the increased field inhomogeneities at ultra-high field were investigated. The correction of susceptibility-induced B_0 variations was found to be highly effective, even in regions with deviations up to 1 ppm. This was achieved through a combination of dense sampling of the full width of the CEST peaks and subsequent shift of the frequencies during Z-spectrum calculation utilizing the B_0 field map. In addition, due to the substantial B_1 deviations, which reached up to 50 % of the nominal B_1 in whole-brain coverage, it was necessary to assess the efficacy of different B_1 correction methods. The acquisition of three B_1 sampling points, with scaling that covers the B_1 range within the SAR limits, allows for the correction of a significant part of the B_1 variations. In the area of the cerebellum and the temporal lobes, retrospective correction is insufficient due to inadequate B_1. While passive shimming via dielectric bags can enhance the B_1 contribution in the temporal lobes slightly, CEST measurements beyond the cerebrum are only viable with pTx. For this purpose, the snapshot 3D-EPI sequence was adapted for parallel excitation. The PUSHUP approach achieves good homogenization of the B_1 field and successful CEST quantification was achieved in the whole brain, including the cerebellum. However, subsequent correction methods, including one to two B_1 sampling points, are still necessary to minimize the influence of residual B_1 deviations.

The developed methods were integrated in a sophisticated imaging protocol for the examination of healthy volunteers. The evaluation of 14 in-vivo experiments showed that although the quality of individual CEST contrast maps is high, quantitative differences can be detected. These are partially caused by different parameters such as resolution and B_1 correction method. Nevertheless, test-retest measurements have demonstrated that the reproducibility of the results is challenging due to the multitude of variables that must be considered during quantification. Despite the inherent difficulty in conducting a direct comparison between individual patients, whole-brain CEST should be well-suited for cohort studies involving a large number of participants. This is underscored by the moderate time demand and high flexibility of the snapshot 3D-EPI CEST approach, making it a good candidate for large multimodality studies.

Bibliography

[1] Felix Bloch, *Nuclear Induction*, Physical Review **70** (1946) 460 (cit. on pp. 1, 5, 6).

[2] E. M. Purcell, H. C. Torrey and R.V . Pund, *Resonance Absorption by Nuclear Magnetic Moments in a Solid*, Phys. Rev **69** (1946) 37 (cit. on pp. 1, 5).

[3] P.C. Lauterbur, *Image Formation by Induced Local Interactions: Examples Employing Nuclear Magnetic Resonance*, Nature **242** (1973) 190 (cit. on pp. 1, 8).

[4] Sture Forsén and Ragnar A. Huffman, *Study of moderately rapid chemical exchange reactions by means of nuclear magnetic double resonance*, The Journal of Chemical Physics **39** (1963) 2892 (cit. on pp. 1, 22).

[5] KM M Ward, AH H Aletras and RS S Balaban, *A new class of contrast agents for MRI based on proton chemical exchange dependent saturation transfer (CEST)*, Journal of Magnetic Resonance **143** (2000) 79 (cit. on pp. 1, 22).

[6] Jinyuan Zhou et al., *Practical data acquisition method for human brain tumor amide proton transfer (APT) imaging*, Magnetic Resonance in Medicine **60** (2008) 842 (cit. on p. 2).

[7] Moritz Zaiss and Peter Bachert, *Exchange-dependent relaxation in the rotating frame for slow and intermediate exchange - modeling off-resonant spin-lock and chemical exchange saturation transfer*, NMR in Biomedicine **26** (2013) 507 (cit. on pp. 2, 28, 31).

[8] Feliks Kogan et al., *Method for high-resolution imaging of creatine in vivo using chemical exchange saturation transfer*, Magnetic Resonance in Medicine **71** (2014) 164 (cit. on p. 2).

[9] Kejia Cai et al., *Magnetic resonance imaging of glutamate.*, Nature medicine **18** (2012) 302 (cit. on pp. 2, 26).

[10] Kannie W Y Chan et al., *Natural D-Glucose as a biodegradable MRI contrast agent for detecting cancer*, Magnetic Resonance in Medicine **68** (2012) 1764 (cit. on p. 2).

[11] Simon Walker-Samuel et al., *In vivo imaging of glucose uptake and metabolism in tumors*, Nature Medicine **19** (2013) 1067 (cit. on p. 2).

[12] Xiang Xu et al., *Dynamic Glucose Enhanced (DGE) MRI for Combined Imaging of Blood Brain Barrier Break Down and Increased Blood Volume in Brain Cancer*, Magnetic Resonance in Medicine **74** (2015) 1556 (cit. on p. 2).

[13] Xiang Xu et al., *Dynamic Glucose-Enhanced (DGE) MRI: Translation to Human Scanning and First Results in Glioma Patients*, Tomography **1** (2015) 105 (cit. on p. 2).

[14] Patrick Schuenke et al., *Adiabatically prepared spin-lock approach for T1ρ-based dynamic glucose enhanced MRI at ultrahigh fields*, Magnetic Resonance in Medicine **78** (2017) 215 (cit. on pp. 2, 101).

[15] Johannes Brettschneider et al., *Spreading of pathology in neurodegenerative diseases: a focus on human studies*, Nature Reviews Neuroscience **16** (2015) 109, ISSN: 1471-003X (cit. on pp. 2, 36, 103).

[16] Daniel Paech and Lisa Loi, "Chemical Exchange Saturation Transfer (CEST) Imaging", *Functional Neuroradiology*, ed. by S.H. Faro and F.B. Mohamed, Springer International Publishing, 2023 293 (cit. on p. 2).

[17] Hye Young Heo et al., *Whole-brain amide proton transfer (APT) and nuclear overhauser enhancement (NOE) imaging in glioma patients using low-power steady-state pulsed chemical exchange saturation transfer (CEST) imaging at 7T*, Journal of Magnetic Resonance Imaging **44** (2016) 41 (cit. on pp. 2, 3, 97, 102).

[18] Jinyuan Zhou et al., *Amide Proton Transfer (APT) Contrast for Imaging of Brain Tumors*, Magnetic Resonance in Medicine **50** (2003) 1120 (cit. on pp. 2, 25, 26).

[19] Zhibo Wen et al., *MR Imaging of High-Grade Brain Tumors Using Endogenous Protein and Peptide-Based Contrast*, NeuroImage **51** (2010) 616 (cit. on p. 2).

[20] Daniel Paech et al., *Assessing the predictability of IDH mutation and MGMT methylation status in glioma patients using relaxation-compensated multipool CEST MRI at 7.0 T*, Neuro-Oncology **20** (2018) 1661 (cit. on p. 2).

[21] Yan Bai et al., *Noninvasive amide proton transfer magnetic resonance imaging in evaluating the grading and cellularity of gliomas*, Oncotarget **8** (2017) 5834 (cit. on p. 2).

[22] Anna Tietze et al., *Assessment of ischemic penumbra in patients with hyperacute stroke using amide proton transfer (APT) chemical exchange saturation transfer (CEST) MRI*, NMR in Biomedicine **27** (2014) 163 (cit. on p. 2).

[23] Guisen Lin et al., *APT weighted MRI as an effective imaging protocol to predict clinical outcome after acute ischemic stroke*, Frontiers in Neurology **9** (2018) 1 (cit. on p. 2).

[24] Guodong Song et al., *Evolution of cerebral ischemia assessed by amide proton transfer-weighted MRI*, Frontiers in Neurology **8** (2017) (cit. on p. 2).

[25] J. A. Wells et al., *In vivo imaging of tau pathology using multi-parametric quantitative MRI*, NeuroImage **111** (2015) 369 (cit. on p. 2).

[26] Rui Wang et al., *Amide proton transfer magnetic resonance imaging of alzheimer's disease at 3.0 Tesla: A preliminary study*, Chinese Medical Journal **128** (2015) 615 (cit. on p. 2).

[27] He Zhu et al., *Fast 3D Chemical Exchange Saturation Transfer (CEST) Imaging of the Human Brain*, Magnetic Resonance in Medicine **64** (2010) 638 (cit. on p. 2).

[28] Benjamin Schmitt et al., *Optimization of pulse train presaturation for CEST imaging in clinical scanners*, Magnetic Resonance in Medicine **65** (2011) 1620 (cit. on p. 2).

[29] Adrienne N. Dula et al., *Development of chemical exchange saturation transfer at 7T*, Magnetic Resonance in Medicine **66** (2011) 831 (cit. on p. 2).

[30] Moritz Zaiss, Philipp Ehses and Klaus Scheffler, *Snapshot-CEST: Optimizing spiral-centric-reordered gradient echo acquisition for fast and robust 3D CEST MRI at 9.4 T*, NMR in Biomedicine **31** (2018) (cit. on pp. 2, 3, 39, 41, 93–95, 97, 99).

[31] Craig K. Jones et al., *In vivo three-dimensional whole-brain pulsed steady-state chemical exchange saturation transfer at 7 T*, Magnetic Resonance in Medicine **67** (2012) 1579 (cit. on pp. 2, 3, 95, 97, 102).

[32] Vitaliy Khlebnikov et al., *Comparison of pulsed three-dimensional CEST acquisition schemes at 7 tesla: steady state versus pseudosteady state*, Magnetic Resonance in Medicine **77** (2017) 2280 (cit. on pp. 2, 3, 97).

[33] Nuno Andre da Silva et al., *FET PET and chemical exchange saturation transfer MRI in brain tumors - A hybrid MR/PET study*, NuklearMedizin **45** (2018) 1031 (cit. on pp. 2, 3, 97).

[34] Glyn Johnson, Youssef Zain Wadghiri and Daniel H Turnbull, *2D multislice and 3D MRI sequences are often equally sensitive*, Magnetic Resonance in Medicine **41** (1999) 824 (cit. on p. 2).

[35] B. A. Poser et al., *Three dimensional echo-planar imaging at 7 Tesla*, NeuroImage **51** (2010) 261 (cit. on pp. 2, 15, 41, 96).

[36] Mark E. Ladd et al., *Pros and cons of ultra-high-field MRI/MRS for human application*, Progress in Nuclear Magnetic Resonance Spectroscopy **109** (2018) 1 (cit. on p. 2).

[37] Johannes Windschuh et al., *Correction of B1-inhomogeneities for relaxation-compensated CEST imaging at 7T*, NMR in Biomedicine **28** (2015) 529 (cit. on pp. 3, 39, 47, 49, 50, 94, 99).

[38] Desmond H.Y. Tse et al., *B1+ inhomogeneity mitigation in CEST using parallel transmission*, Magnetic Resonance in Medicine **78** (2017) 2216 (cit. on pp. 3, 99).

[39] Andrzej Liebert et al., *Multiple interleaved mode saturation (MIMOSA) for B 1+ inhomogeneity mitigation in chemical exchange saturation transfer*, Magnetic Resonance in Medicine **82** (2019) 693 (cit. on pp. 3, 99).

[40] Thaddée Delebarre et al., *Efficient optimization of chemical exchange saturation transfer MRI at 7 T using universal pulses and virtual observation points*, Magnetic Resonance in Medicine (2023) (cit. on p. 3).

[41] Suzan Akbey et al., *Whole-brain snapshot CEST imaging at 7 T using 3D-EPI*, Magnetic Resonance in Medicine **82** (2019) 1741 (cit. on pp. 4, 38).

[42] Yannik Völzke et al., *PUSHUP-CEST: Calibration-free whole-brain ultra-high field CEST imaging using universal parallel transmission*, Magnetic Resonance in Medicine **under review** (2024) (cit. on pp. 4, 43, 44, 96, 99).

[43] E Mark Haacke et al., *Magnetic Resonance Imaging - Physical Principles and Sequence Design*, 1999 (cit. on p. 5).

[44] Z.-P. Liang and P. Lauterbur, *Principles of Magnetic Resonance Imaging: A Signal Processing Perspective*, 1999 (cit. on p. 5).

[45] Matt A. Bernstein, Kevin F. King and Xiaohong Joe Zhou, *Handbook of MRI Pulse Sequences*, 2004 (cit. on p. 10).

[46] Jolanda Schwarz, *Advanced Image Reconstruction Methods for Ultra-High Field MRI*, PhD thesis, 2020 (cit. on p. 12).

[47] Mark A. Griswold et al., *Generalized Autocalibrating Partially Parallel Acquisitions (GRAPPA)*, Magnetic Resonance in Medicine **47** (2002) 1202 (cit. on pp. 12, 42).

[48] Felix A. Breuer et al., *Controlled aliasing in volumetric parallel imaging (2D CAIPIRINHA)*, Magnetic Resonance in Medicine **55** (2006) 549 (cit. on p. 12).

[49] J. T. Vaughan et al., *7T vs. 4T: RF power, homogeneity, and signal-to-noise comparison in head images*, Magnetic Resonance in Medicine **46** (2001) 24 (cit. on p. 12).

[50] Andrew G. Webb and Christopher M. Collins, *Parallel transmit and receive technology in high-field magnetic resonance neuroimaging*, International Journal of Imaging Systems and Technology **20** (2010) 2 (cit. on p. 12).

[51] Francesco Padormo et al., *Parallel transmission for ultrahigh-field imaging*, NMR in Biomedicine **29** (2016) 1145 (cit. on p. 12).

[52] Yudong Zhu, *Parallel Excitation with an Array of Transmit Coils*, Magnetic Resonance in Medicine **51** (2004) 775 (cit. on pp. 12, 98).

[53] Ulrich Katscher and Peter Börnert, *Parallel RF transmission in MRI*, NMR in Biomedicine **19** (2006) 393 (cit. on pp. 12, 98).

[54] William Grissom et al., *Spatial domain method for the design of RF pulses in multicoil parallel excitation*, Magnetic Resonance in Medicine **56** (2006) 620 (cit. on p. 13).

[55] Kawin Setsompop et al., *Magnitude least squares optimization for parallel radio frequency excitation design demonstrated at 7 tesla with eight channels*, Magnetic Resonance in Medicine **59** (2008) 908 (cit. on p. 13).

[56] Suwit Saekho et al., *Small tip angle three-dimensional tailored radiofrequency slab-select pulse for reduced B1 inhomogeneity at 3 T*, Magnetic Resonance in Medicine **53** (2005) 479 (cit. on p. 13).

[57] M. A. Cloos et al., *KT-points: Short three-dimensional tailored RF pulses for flip-angle homogenization over an extended volume*, Magnetic Resonance in Medicine **67** (2012) 72 (cit. on p. 13).

[58] P. Mansfield, *Multi-planar image formation using NMR spin echoes*, Journal of Physics C: Solid State Physics **10** (1977) (cit. on p. 13).

[59] B. Chapman et al., *Real-time movie imaging from a single cardiac cycle by NMR*, Magnetic resonance in medicine **5** (1987) 246 (cit. on p. 13).

[60] Allen W Song, Eric C Wong and James S Hyde, *Echo-Volume Imaging*, Magnetic Resonance in Medicine **32** (1994) 668 (cit. on p. 15).

[61] P. Mansfield, R. Coxon and J. Hykin, *Echo-volumar imaging (EVI) of the brain at 3.0 T: first normal volunteer and functional imaging results*, J Comput Assist Tomogr. **19** (1995) 847 (cit. on p. 15).

[62] H. Bruder et al., *Image reconstruction for echo planar imaging with nonequidistant kspace sampling*, Magnetic Resonance in Medicine **23** (1992) 311 (cit. on p. 16).

[63] Erika Schneider and Gary Glover, *Rapid in Vivo Proton Shimming ERIKA*, Magnetic Resonance in Medicine **18** (1991) 335 (cit. on p. 17).

[64] Peter Jezzard and Robert S. Balaban, *Correction for geometric distortion in echo planar images from B0 field variations*, Magnetic Resonance in Medicine **34** (1995) 65 (cit. on p. 17).

[65] Mark Jenkinson, *Fast, automated, N-dimensional phase-unwrapping algorithm*, Magnetic Resonance in Medicine **49** (2003) 193 (cit. on p. 17).

[66] Philipp Ehses et al., *Whole-brain B1-mapping using three-dimensional DREAM*, Magnetic Resonance in Medicine **82** (2019) 924 (cit. on pp. 17, 18, 57, 60, 101).

[67] Kay Nehrke and Peter Börnert, *DREAM-a novel approach for robust, ultrafast, multislice B1 mapping*, Magnetic Resonance in Medicine **68** (2012) 1517 (cit. on pp. 17, 18, 57).

[68] Jinyuan Zhou and Peter C.M.van Zijl, *Chemical exchange saturation transfer imaging and spectroscopy*, 2006 (cit. on pp. 19, 20).

[69] Peter C M Van Zijl and Nirbhay N. Yadav, *Chemical Exchange Saturation Transfer (CEST): What is in a Name and What Isn't?*, Magnetic Resonance in Medicine **65** (2011) 927 (cit. on pp. 19, 21, 22).

[70] Elena Vinogradov, A. Dean Sherry and Robert E. Lenkinski, *CEST: From basic principles to applications, challenges and opportunities*, Journal of Magnetic Resonance **229** (2013) 155, URL: `http://dx.doi.org/10.1016/j.jmr.2012.11.024` (cit. on p. 19).

[71] Moritz Zaiss and Peter Bachert, *Chemical exchange saturation transfer (CEST) and MR Z-spectroscopy in vivo: A review of theoretical approaches and methods*, 2013 (cit. on pp. 19, 23, 25–31, 34, 49).

[72] Peter C.M. Van Zijl and Akansha Ashvani Sehgal, *Proton chemical exchange saturation transfer (CEST) MRS and MRI*, eMagRes **5** (2016) 1307 (cit. on pp. 19, 20).

[73] Peter C.M. van Zijl et al., *Magnetization Transfer Contrast and Chemical Exchange Saturation Transfer MRI. Features and analysis of the field-dependent saturation spectrum*, NeuroImage **168** (2018) 222 (cit. on pp. 19, 20, 25, 26).

[74] Johannes Windschuh, *Isolation of Unbiased Chemical Exchange Saturation Transfer Effects at 7 T and Application to Brain Tumors*, PhD thesis, 2016 (cit. on p. 19).

[75] Ferdinand Zimmermann, *Relaxation-Compensated Amide Chemical Exchange Saturation Transfer MRI of the Human Breast*, PhD thesis, 2019 (cit. on p. 19).

[76] Oscar Millet et al., *The static magnetic field dependence of chemical exchange linebroadening defines the NMR chemical shift time scale*, Journal of the American Chemical Society **122** (2000) 2867 (cit. on p. 20).

[77] Steffen Goerke, Moritz Zaiss and Peter Bachert, *Characterization of creatine guanidinium proton exchange by water-exchange (WEX) spectroscopy for absolute-pH CEST imaging in vitro*, NMR in Biomedicine **27** (2014) 507 (cit. on p. 20).

[78] Yawen Bai et al., *Primary structure effects on peptide group hydrogen exchange*, Proteins: Structure, Function, and Bioinformatics **17** (1993) 75 (cit. on p. 20).

[79] Huaping Mo and Thomas C. Pochapsky, *Intermolecular interactions characterized by nuclear Overhauser effects*, Progress in Nuclear Magnetic Resonance Spectroscopy **30** (1997) 1 (cit. on p. 20).

[80] Ionel Solomon, *Relaxation processes in a system of two spins*, Physical Review **99** (1955) 559 (cit. on p. 20).

[81] R. M. Henkelman, G. J. Stanisz and S. J. Graham, *Magnetization transfer in MRI: A review*, NMR in Biomedicine **14** (2001) 57 (cit. on p. 21).

[82] Steven D. Wolff and Robert S. Balaban, *Magnetization transfer contrast (MTC) and tissue water proton relaxation in vivo*, Magnetic Resonance in Medicine **10** (1989) 135 (cit. on p. 21).

[83] N. Goffeney et al., *Sensitive NMR detection of cationic-polymer-based gene delivery systems using saturation transfer via proton exchange [18]*, Journal of the American Chemical Society **123** (2001) 8628 (cit. on p. 23).

[84] Jinyuan Zhou et al., *Quantitative Description of Proton Exchange Processes between Water and Endogenous and Exogenous Agents for WEX, CEST, and APT Experiments*, Magnetic Resonance in Medicine **51** (2004) 945 (cit. on p. 23).

[85] Feliks Kogan, Hari Hariharan and Ravinder Reddy, *Chemical Exchange Saturation Transfer (CEST) Imaging: Description of Technique and Potential Clinical Applications*, Current Radiology Reports **1** (2013) 102, ISSN: 21674825 (cit. on p. 25).

[86] Jiadi Xu et al., *Variable Delay Multi-Pulse Train for Fast Chemical Exchange Saturation Transfer and Relayed-Nuclear Overhauser Enhancement MRI*, Magnetic Resonance in Medicine **71** (2014) 1798 (cit. on pp. 25, 26).

[87] Tao Jin et al., *Spin-locking versus chemical exchange saturation transfer MRI for investigating chemical exchange process between water and labile metabolite protons*, Magnetic Resonance in Medicine **65** (2011) 1448 (cit. on pp. 25, 26).

[88] Mohammad Haris et al., *In vivo Mapping of Brain Myo-Inositol*, NeuroImage **54** (2011) 2079 (cit. on p. 26).

[89] Tao Jin et al., *MR imaging of the amide-proton transfer effect and the pH-insensitive nuclear overhauser effect at 9.4 T*, Magnetic Resonance in Medicine **69** (2013) 760 (cit. on p. 26).

[90] Guanshu Liu et al., *Nuts and bolts of chemical exchange saturation transfer MRI*, NMR in Biomedicine **26** (2013) 810 (cit. on p. 26).

[91] Edvards Liepinsh and Gottfried Otting,
Proton exchange rates from amino acid side chains - Implications for image contrast,
Magnetic Resonance in Medicine **35** (1996) 30 (cit. on p. 26).

[92] Joshua I. Friedman et al., *Transfer Rate Edited Experiment for the Selective Detection of Chemical Exchange via Saturaion Transfer (TRE-CEST)*, 2015 (cit. on p. 26).

[93] Harden M. McConnell, *Reaction Rates by Nuclear Magnetic Resonance*,
The Journal of Chemical Physics **28** (1958) 430 (cit. on p. 26).

[94] Moritz Zaiss et al., *A combined analytical solution for Chemical Exchange Saturation Transfer and semi-solid Magnetization Transfer*, **28** (2015) 217
(cit. on pp. 27, 33, 39, 93, 94, 102).

[95] Tony Stöcker et al., *High-performance computing MRI simulations*,
Magnetic Resonance in Medicine **64** (2010) 186 (cit. on pp. 27, 52).

[96] Fang Liu et al.,
Fast Realistic MRI Simulations Based on Generalized Multi-Pool Exchange Tissue Model,
IEEE Transactions on Medical Imaging **36** (2017) 527 (cit. on p. 27).

[97] Donald E Woessner et al., *Numerical Solution of the Bloch Equations Provides Insights Into the Optimum Design of PARACEST Agents for MRI*, **799** (2005) 790 (cit. on p. 27).

[98] Phillip Zhe Sun et al.,
Simulation and Optimization of Pulsed Radio Frequency Irradiation Scheme for Chemical Exchange Saturation Transfer (CEST) MRI - Demonstration of pH-Weighted Pulsed-Amide Proton CEST MRI in an Animal Model of Acute Cerebral Ischemia,
Magnetic Resonance in Medicine **66** (2011) 1042 (cit. on pp. 27, 29).

[99] Zhongliang Zu et al.,
Optimizing Pulsed-Chemical Exchange Saturation Transfer Imaging sequences,
Magnetic Resonance in Medicine **66** (2011) 1100 (cit. on pp. 27, 29, 94).

[100] Oleg Trott and Arthur G. Palmer, *R 1ρ relaxation outside of the fast-exchange limit*,
Journal of Magnetic Resonance **154** (2002) 157 (cit. on p. 28).

[101] Moritz Zaiss et al., *Theory of chemical exchange saturation transfer MRI in the context of different magnetic fields*, NMR in Biomedicine **35** (2022) 1 (cit. on pp. 29, 33, 34).

[102] Jan-eric Meissner et al., *Quantitative pulsed CEST-MRI using Ω -plots*, (2015) 1196
(cit. on pp. 30, 31).

[103] Moritz Zaiss et al., *Inverse Z-spectrum analysis for spillover-, MT-, and T1-corrected steady-state pulsed CEST-MRI - application to pH-weighted MRI of acute stroke*,
NMR in Biomedicine **27** (2014) 240 (cit. on p. 31).

[104] Oleg Trott and Arthur G. Palmer, *Theoretical study of R 1 q rotating-frame and R 2 free-precession relaxation in the presence of n -site chemical exchange*, **170** (2004) 104
(cit. on p. 31).

[105] Kimberly L Desmond, Firas Moosvi and Greg J Stanisz, *Mapping of Amide , Amine , and Aliphatic Peaks in the CEST Spectra of Murine Xenografts at 7 T*,
Magnetic Resonance in Medicine **71** (2014) 1841 (cit. on pp. 33, 95).

[106] Peiyu Huang and Minming Zhang, *Magnetic Resonance Imaging Studies of Neurodegenerative Disease: From Methods to Translational Research*, Neuroscience Bulletin **39** (2023) 99 (cit. on pp. 35, 36).

[107] Chunmei Li et al., *Amide proton transfer imaging of Alzheimer's disease and Parkinson's disease*, Magnetic Resonance Letters **3** (2023) 22 (cit. on p. 36).

[108] Anna Orzyłowska and Wendy Oakden, *Saturation Transfer MRI for Detection of Metabolic and Microstructural Impairments Underlying Neurodegeneration in Alzheimer ' s Disease*, Brain Science **12** (2022) (cit. on p. 36).

[109] John Q. Trojanowski and Harald Hempel, *Neurodegenerative disease biomarkers: Guideposts for disease prevention through early diagnosis and intervention John*, Prog Neurobiol. **95** (2011) 491 (cit. on p. 36).

[110] Angelika Mennecke et al., *7 tricks for 7 T CEST : Improving the reproducibility of multipool evaluation provides insights into the effects of age and the early stages of Parkinson ' s disease*, (2023) 1 (cit. on pp. 36, 94, 95, 100, 102, 103).

[111] Mohammed Haris et al., *MICEST: A potential tool for non-invasive detection of molecular changes in Alzheimer's disease*, Journal of neuroscience methods **212** (2013) 87 (cit. on p. 36).

[112] Mohammad Haris et al., *Imaging of glutamate neurotransmitter alterations in Alzheimer's disease*, NMR in Biomedicine **26** (2013) 386 (cit. on p. 36).

[113] Rachelle Crescenzi et al., *In vivo measurement of glutamate loss is associated with synapse loss in a mouse model of tauopathy*, NeuroImage **101** (2014) 185 (cit. on p. 36).

[114] Rachelle Crescenzi et al., *Longitudinal imaging reveals subhippocampal dynamics in glutamate levels associated with histopathologic events in a mouse model of tauopathy and healthy mice*, Hippocampus **27** (2017) 285 (cit. on p. 36).

[115] Moritz Zaiss et al., *Downfield-NOE-suppressed amide-CEST-MRI at 7 Tesla provides a unique contrast in human glioblastoma*, Magnetic Resonance in Medicine **77** (2017) 196 (cit. on pp. 39, 93, 94).

[116] Rüdiger Stirnberg et al., *Rapid whole-brain resting-state fMRI at 3 Tesla: Efficiency-optimized three-dimensional EPI versus repetition time-matched simultaneous-multi-slice EPI*, NeuroImage **163** (2017) 81 (cit. on p. 41).

[117] V N Ikonomidou et al., *T 1 measurements at 7T with application to tissue specific imaging*, Proc. Intl. Soc. Mag. Reson. Med. **14** (2006) 920 (cit. on pp. 41, 43).

[118] D. Ivanov et al., *Robust ACS acquisition for 3D echo planar imaging*, In Proc Intl Soc Mag Reson Med **23** (2015) 2059 (cit. on p. 42).

[119] Rüdiger Stirnberg and Tony Stöcker, *Segmented K-space blipped-controlled aliasing in parallel imaging for high spatiotemporal resolution EPI*, Magnetic Resonance in Medicine **85** (2021) 1540 (cit. on p. 42).

[120] K P Pruessmann et al., *SENSE: sensitivity encoding for fast MRI.*, Magnetic resonance in medicine : official journal of the Society of Magnetic Resonance in Medicine / Society of Magnetic Resonance in Medicine **42** (1999) 952 (cit. on p. 42).

[121] Rüdiger Stirnberg et al., *Rapid fat suppression for three-dimensional echo planar imaging with minimized specific absorption rate*, Magnetic Resonance in Medicine **76** (2016) 1517 (cit. on pp. 43, 96).

[122] David Leitão et al., *Parallel transmit pulse design for saturation homogeneity (PUSH) for magnetization transfer imaging at 7T*, Magnetic Resonance in Medicine **88** (2022) 180 (cit. on p. 43).

[123] John P. 3rd Mugler and James R. Brookeman, *Threedimensional magnetizationprepared rapid gradientecho imaging (3D MP RAGE)*, Magnetic Resonance in Medicine **15** (1990) 152 (cit. on pp. 44, 60).

[124] Nicholas J. Tustison et al., *The ANTsX ecosystem for quantitative biological and medical imaging*, Scientific Reports **11** (2021) 9068 (cit. on p. 44).

[125] Vincent Gras et al., *Universal pulses: A new concept for calibration-free parallel transmission*, Magnetic Resonance in Medicine **77** (2017) 635 (cit. on pp. 44, 99).

[126] Vasily L. Yarnykh, *Actual flip-angle imaging in the pulsed steady state: A method for rapid three-dimensional mapping of the transmitted radiofrequency field*, Magnetic Resonance in Medicine **57** (2007) 192 (cit. on p. 44).

[127] L. Van Damme et al., *Universal nonselective excitation and refocusing pulses with improved robustness to off-resonance for Magnetic Resonance Imaging at 7 Tesla with parallel transmission*, Magnetic Resonance in Medicine **85** (2021) 678 (cit. on pp. 44, 96).

[128] Mark Jenkinson et al., *Improved optimization for the robust and accurate linear registration and motion correction of brain images*, NeuroImage **17** (2002) 825 (cit. on pp. 45, 50).

[129] Yi Zhang et al., *Selecting the reference image for registration of CEST series*, Journal of Magnetic Resonance Imaging **43** (2016) 756 (cit. on p. 45).

[130] Jesper L R Andersson, Stefan Skare and John Ashburner, *How to correct susceptibility distortions in spin-echo echo-planar images: application to diffusion tensor imaging*, NeuroImage **20** (2003) 870 (cit. on pp. 46, 50, 97, 100).

[131] Stephen M Smith, *Fast Robust Automated Brain Extraction*, Human Brain Mapping **17** (2002) 143 (cit. on pp. 46, 50).

[132] Yongyue Zhang, Michael Brady and Stephen Smith, *Segmentation of Brain MR Images Through a Hidden Markov Random Field Model and the Expectation-Maximization Algorithm*, IEEE Transactions on Medical Imaging **20** (2001) 45 (cit. on pp. 46, 50).

[133] Moritz Zaiss, Benjamin Schmitt and Peter Bachert, *Quantitative separation of CEST effect from magnetization transfer and spillover effects by Lorentzian-line-fit analysis of z-spectra*, Journal of Magnetic Resonance **211** (2011) 149 (cit. on pp. 47, 95).

[134] Mina Kim et al., *Water saturation shift referencing (WASSR) for chemical exchange saturation transfer (CEST) experiments*, Magnetic Resonance in Medicine **61** (2009) 1441 (cit. on pp. 49, 101).

[135] Ilona Lipp et al., *B1+-correction of magnetization transfer saturation maps optimized for 7T postmortem MRI of the brain*, Magnetic Resonance in Medicine **89** (2023) 1385 (cit. on pp. 49, 100).

[136] Stephen M. Smith et al., *Advances in functional and structural MR image analysis and implementation as FSL*, NeuroImage **23** (2004) 208 (cit. on pp. 50, 57).

[137] Mark W. Woolrich et al., *Bayesian analysis of neuroimaging data in FSL.*, NeuroImage **45** (2009) 173 (cit. on pp. 50, 57).

[138] Mark Jenkinson et al., *FSL*, NeuroImage **62** (2012) 782 (cit. on pp. 50, 57).

[139] Thomas Kluyver et al., *Jupyter Notebooks - a publishing format for reproducible computational workflows*, Positioning and Power in Academic Publishing: Players, Agents and Agendas - Proceedings of the 20th International Conference on Electronic Publishing, ELPUB 2016 (2016) 87 (cit. on p. 50).

[140] Mark Jenkinson and Stephen Smith, *A global optimisation method for robust affine registration of brain images*, Medical Image Analysis **5** (2001) 143 (cit. on p. 50).

[141] Miriam Rabea Kubach et al., *Demonstrating the Influence of Magnetisation Transfer on Putative T1 Relaxation Times: a Simulation Study*, Proc **18** (2010) 2948 (cit. on p. 52).

[142] Suzan Akbey and Tony Stöcker, “CEST Simulations with JEMRIS.”, *ESMRMB*, 2020 L01.99 (cit. on pp. 52, 121).

[143] W Van Der Zwaag et al., *Temporal SNR Characteristics in Segmented 3D-EPI at 7T*, **352** (2012) 344 (cit. on p. 56).

[144] Nicholas J. Tustison et al., *Logical circularity in voxel-based analysis: Normalization strategy may induce statistical bias*, Human Brain Mapping **35** (2014) 745 (cit. on p. 57).

[145] Qing X. Yang et al., *Manipulation of image intensity distribution at 7.0 T: Passive RF shimming and focusing with dielectric materials*, Journal of Magnetic Resonance Imaging **24** (2006) 197 (cit. on p. 58).

[146] K. Haines, N. B. Smith and A. G. Webb, *New high dielectric constant materials for tailoring the B1+distribution at high magnetic fields*, Journal of Magnetic Resonance **203** (2010) 323 (cit. on pp. 58, 98).

[147] Wouter M. Teeuwisse, Wyger M. Brink and Andrew G. Webb, *Quantitative assessment of the effects of high-permittivity pads in 7 Tesla MRI of the brain*, Magnetic Resonance in Medicine **67** (2012) 1285 (cit. on p. 58).

[148] Kieran R. O’Brien et al., *Dielectric Pads and Low-B1+ Adiabatic Pulses: Complementary Techniques to Optimize Structural T1w Whole-Brain MP2RAGE Scans at 7 Tesla*, Journal of Magnetic Resonance Imaging **40** (2014) 804 (cit. on p. 58).

[149] Manushka V. Vaidya et al., *Improved detection of fMRI activation in the cerebellum at 7T with dielectric pads extending the imaging region of a commercial head coil*, Journal of Magnetic Resonance Imaging **48** (2018) 431 (cit. on p. 58).

[150] Paul S. Jacobs et al., *Repeatability of B1+ inhomogeneity correction of volumetric (3D) glutamate CEST via High-permittivity dielectric padding at 7T*, Magnetic Resonance in Medicine **88** (2022) 2475 (cit. on p. 58).

[151] Jinyuan Zhou et al., *APT-Weighted MRI: Techniques, Current Neuro Applications, and Challenging Issues*, Journal of Magnetic Resonance Imaging **50** (2019) 347 (cit. on p. 93).

[152] Rüdiger Stirnberg et al., *Rapid whole-brain resting-state fMRI at 3 Tesla: Efficiency-optimized three-dimensional EPI versus repetition time-matched simultaneous-multi-slice EPI*, NeuroImage **163** (2017) 81 (cit. on p. 96).

[153] A. Haase et al., *1H NMR chemical shift selective (CHESS) imaging*, Physics in Medicine and Biology **30** (1985) 341 (cit. on p. 96).

[154] Jianhua Lu et al., *Observation of true and pseudo NOE signals using CEST-MRI and CEST-MRS sequences with and without lipid suppression*, Magnetic Resonance in Medicine **73** (2015) 1615 (cit. on p. 96).

[155] Phillip Zhe Sun et al., *Suppression of lipid artifacts in amide proton transfer imaging*, Magnetic Resonance in Medicine **54** (2005) 222 (cit. on p. 96).

[156] Sebastian Mueller et al., *Whole brain snapshot CEST at 3T using 3D-EPI : Aiming for speed , volume , and homogeneity*, (2020) 1 (cit. on pp. 97, 103).

[157] Andreas K. Bitz et al., *RF safety evaluation of different configurations of high-permittivity pads used to improve imaging of the cerebellum at 7 Tesla*, Proceedings of the 23rd Annual Meeting of ISMRM, Milan, Italy **918** (2014) 4892 (cit. on p. 98).

[158] Thomas M Fiedler, Mark E Ladd and Andreas K Bitz, *Local SAR elevations in the human head induced by high-permittivity pads at 7 Tesla*, Proc. Intl. Soc. Mag. Reson. Med **23** (2015) 291903 (cit. on p. 98).

[159] Markus W. May et al., *A patient-friendly 16-channel transmit/64-channel receive coil array for combined head–neck MRI at 7 Tesla*, Magnetic Resonance in Medicine **88** (2022) 1419 (cit. on p. 99).

[160] Raphaël Tomi-Tricot et al., *SmartPulse, a machine learning approach for calibration-free dynamic RF shimming: Preliminary study in a clinical environment*, Magnetic Resonance in Medicine **82** (2019) 2016 (cit. on p. 99).

[161] Andrzej Liebert et al., *Whole-brain quantitative CEST MRI at 7T using parallel transmission methods and B1+ correction*, Magnetic Resonance in Medicine **86** (2021) 346 (cit. on p. 100).

[162] Leonie Hunger et al., *DeepCEST 7 T: Fast and homogeneous mapping of 7 T CEST MRI parameters and their uncertainty quantification*, Magnetic Resonance in Medicine **89** (2023) 1543 (cit. on p. 100).

[163] Johannes Windschuh et al., *Assessment of frequency drift on CEST MRI and dynamic correction: application to gagCEST at 7 T*, Magnetic Resonance in Medicine **81** (2019) 573 (cit. on p. 101).

[164] W. Van Der Zwaag et al., *Temporal SNR characteristics in segmented 3D-EPI at 7T*, Magnetic Resonance in Medicine **67** (2012) 344 (cit. on p. 102).

[165] Gary H. Glover, Tie Qiang Li and David Ress, *Image-based method for retrospective correction of physiological motion effects in fMRI: RETROICOR*, Magnetic Resonance in Medicine **44** (2000) 162 (cit. on p. 102).

[166] Janna Krahe et al., *Neurochemical profiles in hereditary ataxias: A meta-analysis of Magnetic Resonance Spectroscopy studies*, Neuroscience & Biobehavioral Reviews **108** (2020) 854 (cit. on p. 103).

[167] Lin Chen et al., *Protein aggregation linked to Alzheimer's disease revealed by saturation transfer MRI*, NeuroImage **188** (2019) 380 (cit. on p. 103).

APPENDIX A

Sequence development

The first version of the snapshot 3D-EPI CEST sequence was developed using IDEA version B17. It was developed before the upgrade to IDEA Version E12 was available for the 7T MRI scanner.

Figure A.1 shows the schematic diagram of the earlier sequence version. While the saturation module is the same, there are two key differences in the readout part:

1. Water-selective excitation was performed using a spatially non-selective binomial-11 water-selective excitation pulse, as the rectangular water-selective excitation pulse was not available in the B17 version.
2. GRAPPA parallel imaging with 3×2 - fold undersampling was employed to speed up the readout, as CAIPIRINHA was only available in IDEA version E12.

This results in slightly different readout parameters: BW=2246 Hz/pixel, TE = 5.9 ms, TR_{vol} = 4330 ms, echo spacing = 0.6, segmentation = 1.

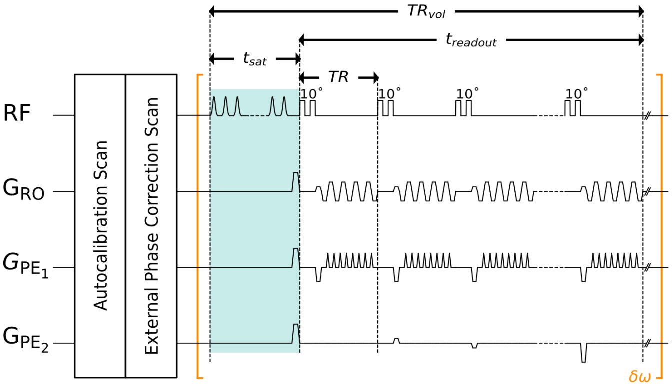

Figure A.1: Schematic diagram of the develop-version of the snapshot 3D-EPI CEST sequence, which is utilized with the older IDEA version B17.

APPENDIX B

JEMRIS simulation verification

The CEST simulations with JEMRIS were verified with the analytical solution and the simulation based on a matrix solution provided by `www.cest-sources.org`. In addition, simple phantom experiments were performed to verify the JEMRIS results. The results were presented at the ESMRMB 2020 [142].

Using JEMRIS, the z-magnetization directly after the saturation block was simulated. First, a two-pool experiment with a continuous wave saturation was simulated and compared to the analytical and the matrix approach. The simulation parameters are shown in Table B.1.

sample	$\delta\omega$	fraction	exchange rate [Hz]	T_1 / T_2 [ms]
water	0.00			2000 / 115
glutamate	3.00	0.002	1000	1000 / 10

Table B.1: Simulation parameters for the two-pool sample to compare the BMC simulations of JEMRIS, matrix and analytical approach.

Figure B.1 shows Z-spectra and MTR_{asym} analysis of the two-pool continuous wave simulation. As expected, the results of the three approaches are in excellent agreement. Small deviations to the

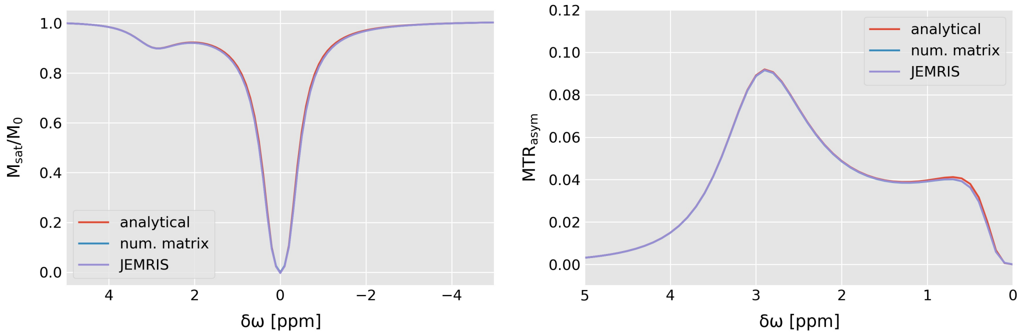

Figure B.1: Simulated Z-Spectra and $MTR_{\mathrm{asym}}(3\,\mathrm{ppm})$ by JEMRIS, cest-sources and the analytical solution.

analytical solution for both numerical approaches can be attributed to time discretization and limited floating-point precision. JEMRIS uses an adaptive step-size integrator for the solution of the BMC equation, which is typically less efficient than an optimized implementation of the matrix approach, but it provides greater flexibility for the simulation of arbitrary sequences.

Second, three different protocols with pulsed saturation trains were used. Phantom data were acquired at a 7T Siemens scanner with a 32-channel Nova head coil applying the 3D-EPI CEST sequence with 2mm isotropic resolution. Experiments were performed on an available, in-house made phantom, containing two brain metabolites Glutamate and GABA(ratio 2:1). As there is a broad discrepancy in reported CEST parameters, simulation parameters were manually adjusted to match the phantom data. Simulation parameters are given in Table B.2.

sample	$\delta\omega$	fraction	exchange rate [Hz]	T_1 / T_2 [ms]
water	0.00			2000 115
glutamate	3.00	0.002	1000	1000 / 10
GABA	2.75	0.001	2000	1000 / 10

no. pulses	t_p [ms]	B_1^{sat} [μT]	t_{sat} [s]	DC
10	100	1	2	50
20	50	1	2	50
40	25	1	2	50

Table B.2: Simulation parameters for multi pool samples and the saturation modules to compare the BMC simulation of JEMRIS with the phantom experiments.

Figure B.2 shows the Z-spectra of measured phantom data and related BMC simulations using different saturation modules. A short pulse duration results in strong side lobes of the frequency response, which generates wiggles in the Z-spectrum. This is consistent in measured and simulated data. In order to accurately simulate CEST effects, the exact parameters are needed. These parameters can potentially be extracted by iterative adapting the simulation parameters in a reference experiment.

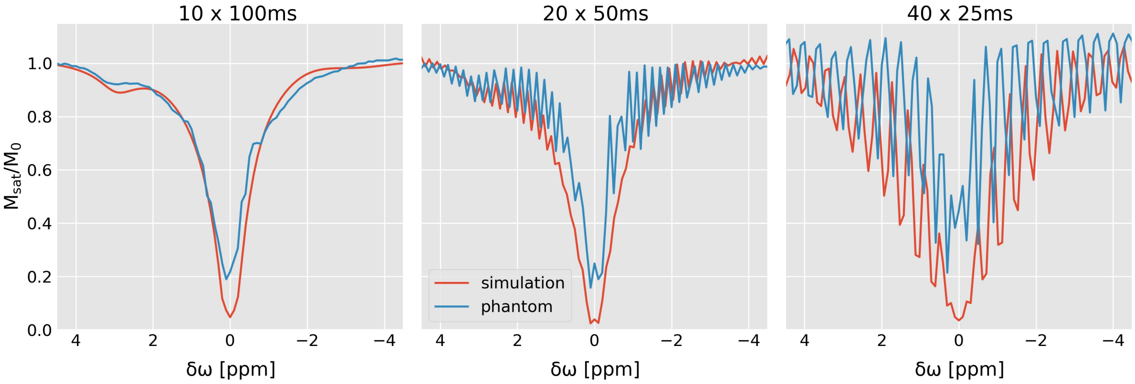

Figure B.2: Z-spectra simulated with JEMRIS and corresponding Z-Spectra of a ROI within the in-house made phantom.

APPENDIX C

Phantom measurements

Phantom experiments were performed on two in-house made phantoms containing GABA combined with glutamate or creatine to proof the dependency of the CEST effect on pulse duration and flip angle. The parameters of the saturation module are shown in Table C.1

B_1 [μT]	1
$\Delta\omega$ [ppm]	-5 to 5
t_{sat} [s]	4
DC [%]	50
t_p [ms]	5, 10, 15, 20, 22.5, 25, 27.5, 30, 32.5, 35, 37.5, 40, 42.5, 45, 50, 55, 60, 65, 70, 75, 80, 90, 95

Table C.1: Parameters of the saturation module used for phantom experiments.

Figure C.1 depicts the Z-spectra of a 5×5 voxel ROI within the glutamate containing phantom (red) and a 5×5 voxel ROI within the creatine containing phantom (blue). Figure C.2 shows the corresponding standard deviations within the 5×5 voxel ROI.

Moreover, the mean MTR_{asym} of the two 5×5 voxel ROIs within the phantoms containing glutamate and GABA (red) as well as creatine and GABA (blue) is shown in Figure C.3, while the depending standard deviation is depicted in Figure C.4.

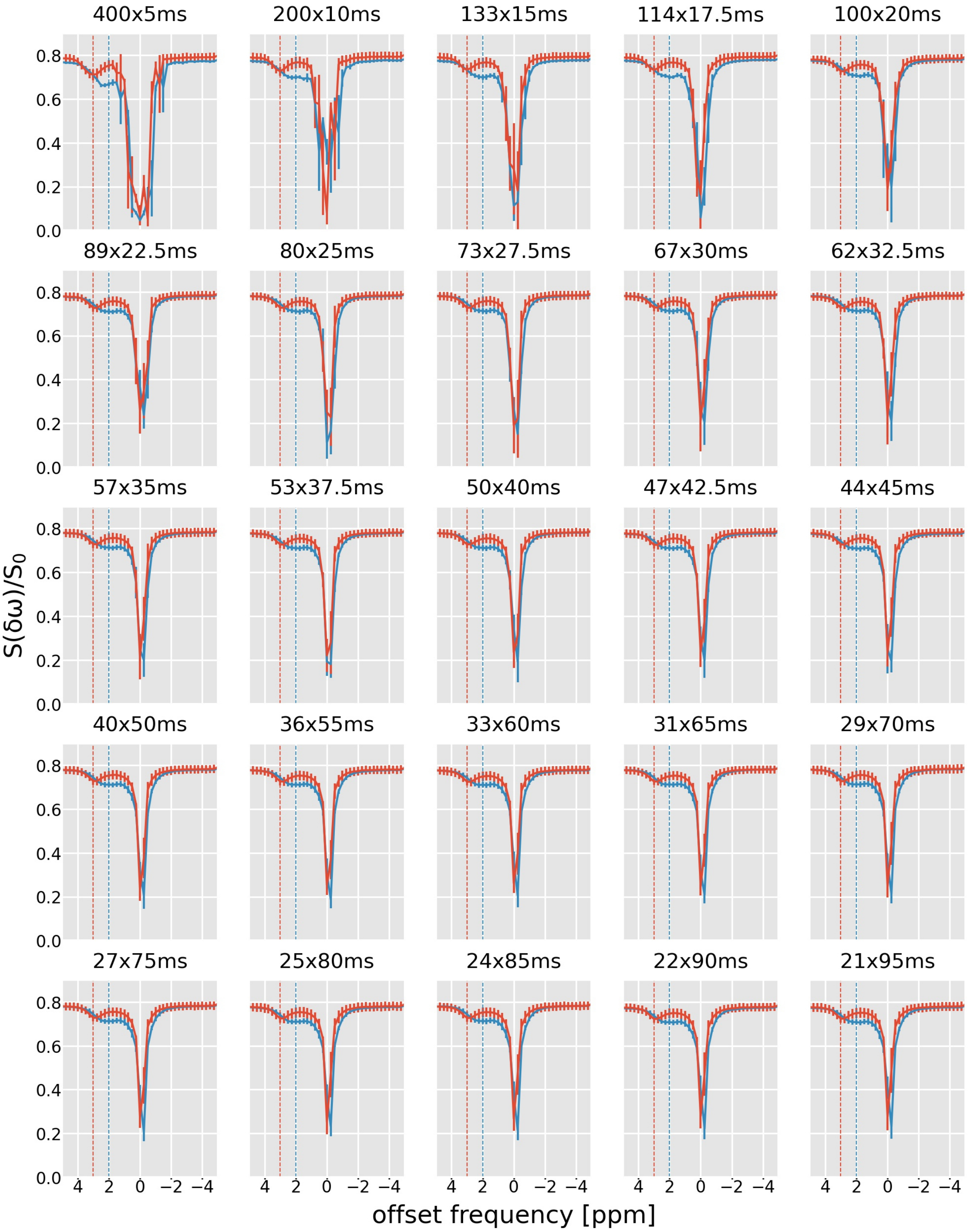

Figure C.1: Mean Z-spectrum of a 5x5 voxel ROI of the phantom containing glutamate and GABA (red) and the phantom containing creatine and GABA(blue).

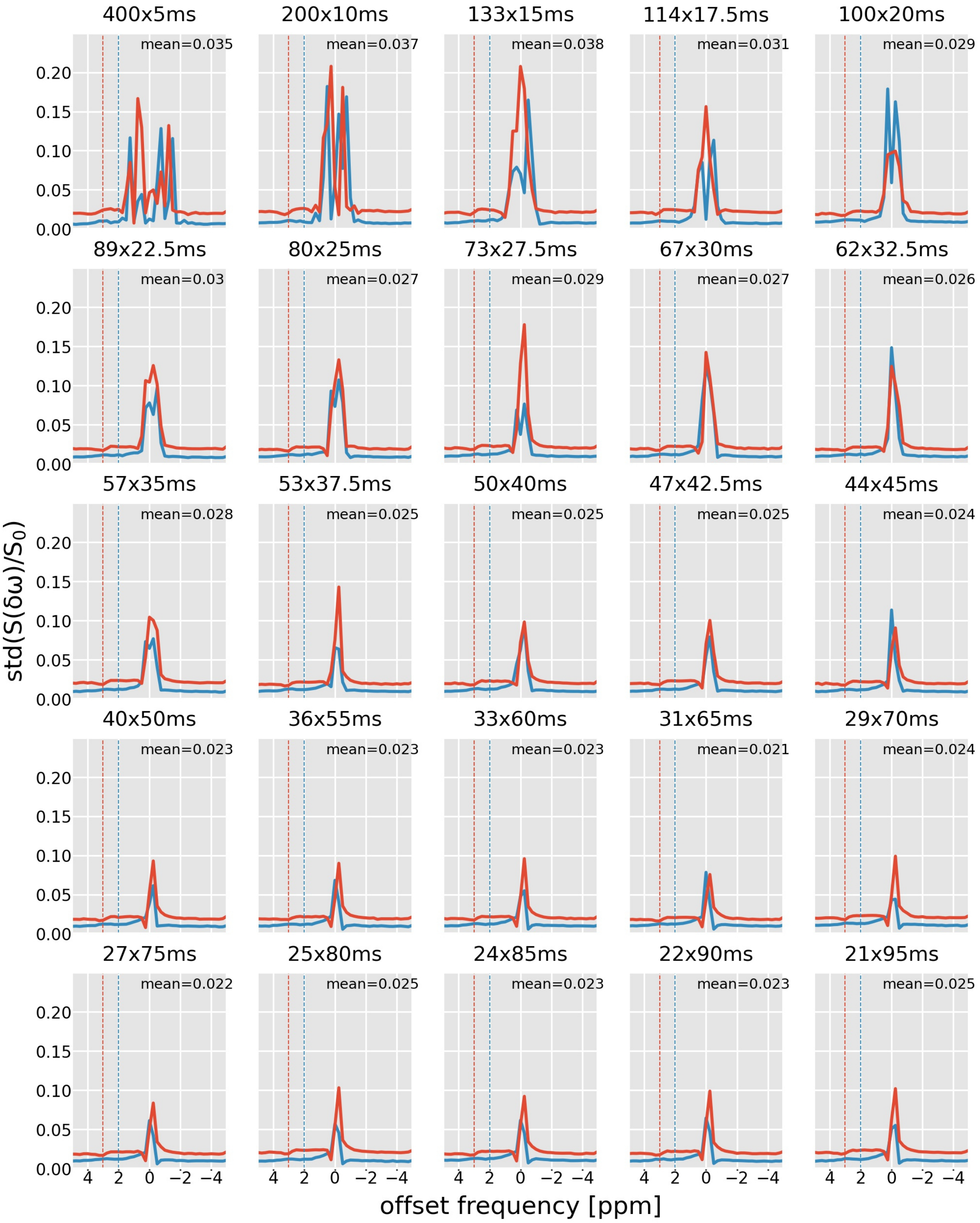

Figure C.2: The associated standard deviation for C.1.

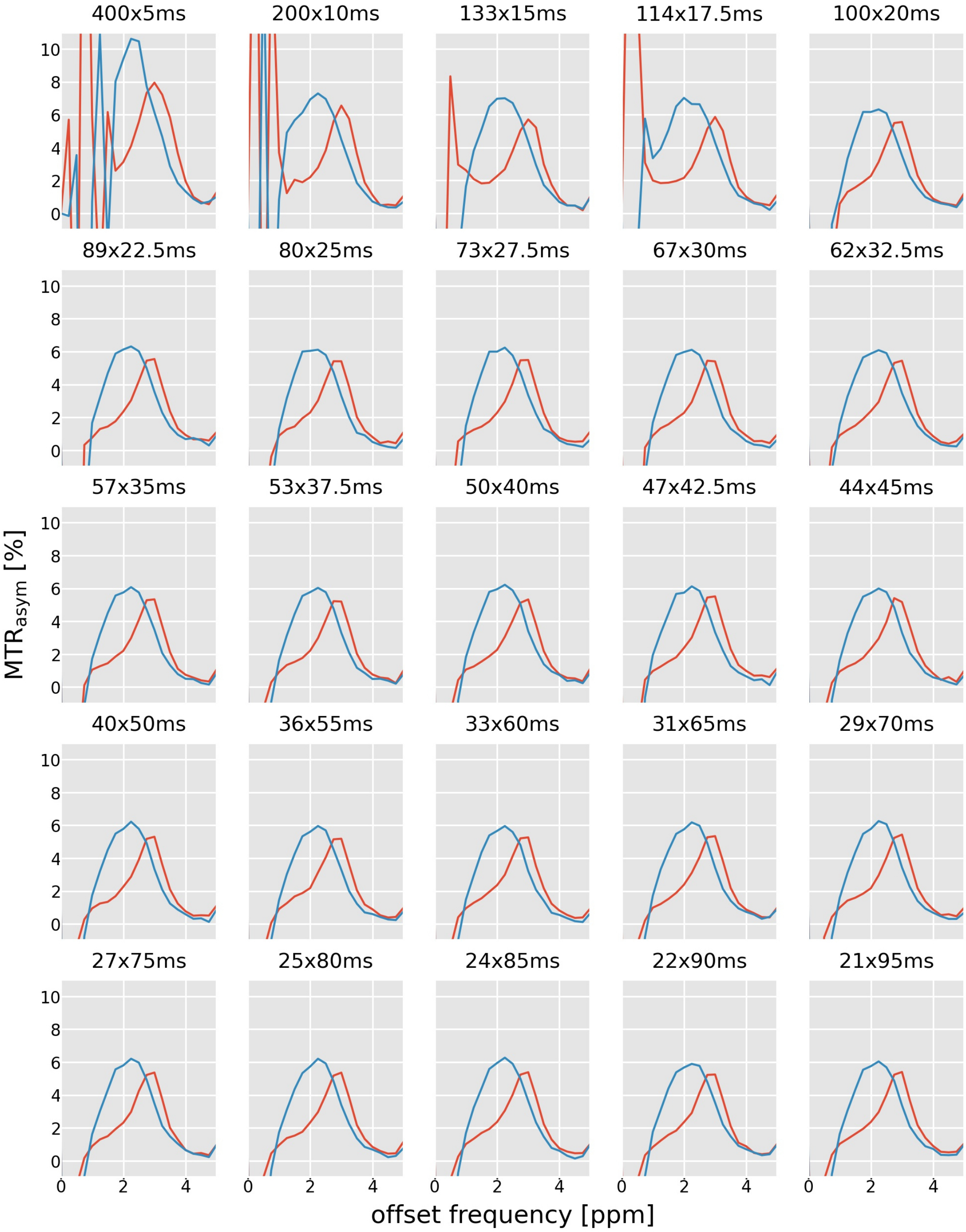

Figure C.3: Mean MTR_{asym} analysis of a 5x5 voxel ROI of the glutamate phantom (red) and the phantom containing creatine and GABA(blue).

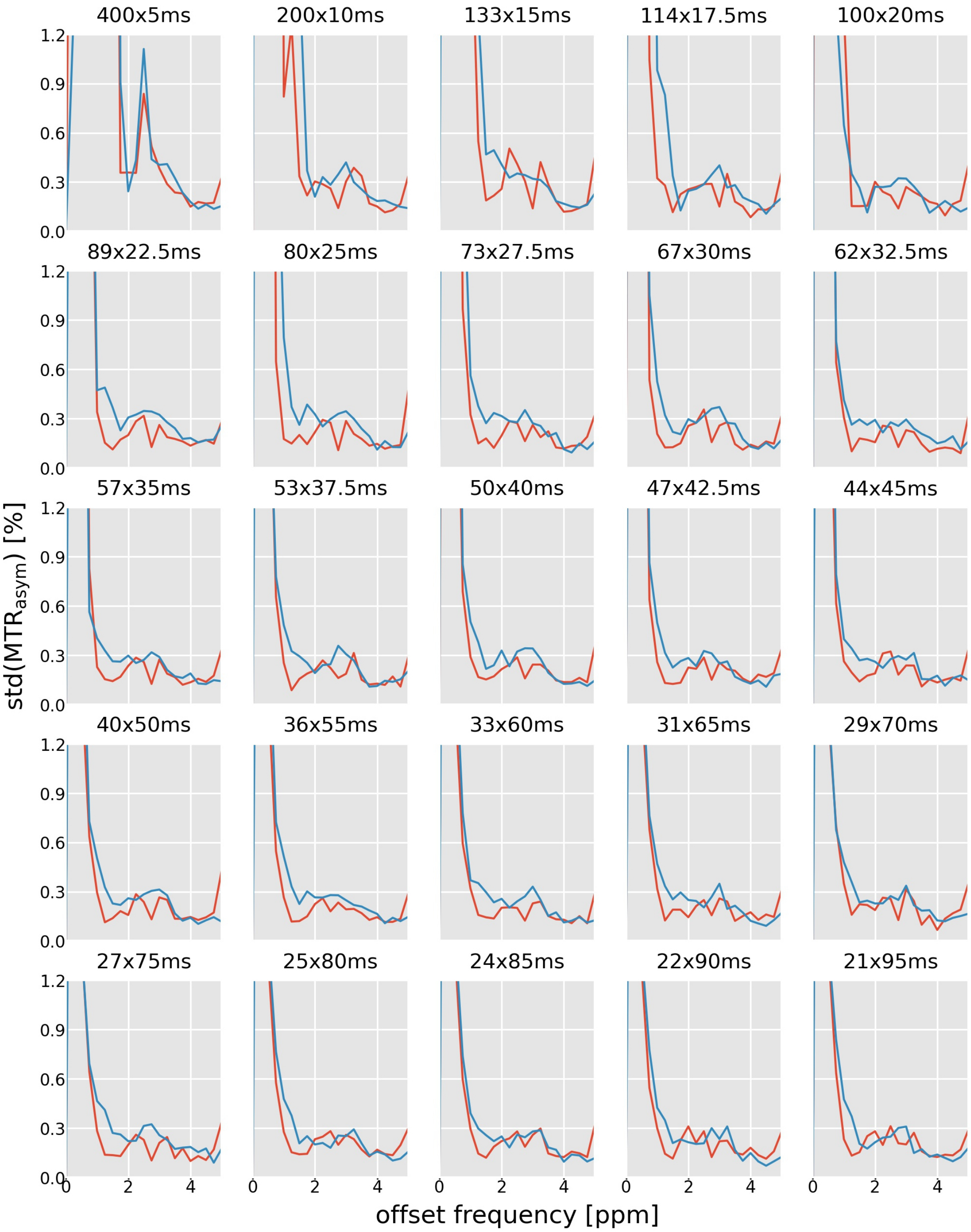

Figure C.4: The associated standard deviation for C.3.

APPENDIX D

In-vivo measurements

saturation scheme	tissue	MTC [%]	rNOE [%]	amides [%]	amines [%]
120 × 15 ms	WM	19.27 ± 5.05	13.2 ± 1.87	4.34 ± 0.94	3.64 ± 0.76
	GM	14.39 ± 5.55	12.68 ± 2.68	4.81 ± 1.39	3.79 ± 1.14
	rel. diff.	28.98	4.04	10.33	4.09
30 × 65 ms	WM	20.11 ± 5.05	12.3 ± 1.75	3.25 ± 0.82	3.77 ± 0.71
	GM	15.24 ± 5.67	11.73 ± 2.5	3.68 ± 1.28	3.88 ± 1.03
	rel. diff.	27.57	4.75	12.3	2.77
40 × 45 ms	WM	19.73 ± 4.85	11.89 ± 1.73	3.06 ± 0.79	3.65 ± 0.72
	GM	15.08 ± 5.37	11.26 ± 2.51	3.47 ± 1.14	3.75 ± 1.08
	rel. diff.	26.72	5.46	12.73	2.65
30 × 60 ms	WM	20.02 ± 4.85	11.58 ± 1.69	2.83 ± 0.66	3.63 ± 0.66
	GM	15.33±5.36	10.85 ± 2.38	3.12 ± 0.99	3.73 ± 0.94
	rel. diff.	26.52	6.49	9.64	2.66
20 × 90 ms	WM	19.73 ± 4.84	11.22 ± 1.66	2.87 ± 0.72	3.66 ± 0.69
	GM	15.12±5.33	10.52 ± 2.34	3.21 ± 1.06	3.74 ± 0.94
	rel. diff.	26.45	6.47	11.03	2.04

Table D.1: Mean MTR_{LD} and the associated standard deviation within WM and GM ROIs for MTC, rNOE, amides and amines, which are associated with Figure 5.8.

N_{B1}	MTC [%]	rNOE [%]	amides [%]
0	28.70	11.27	19.22
1	7.07	13.32	19.78
2	9.64	5.84	14.95
3	3.32	4.48	10.03
4	3.00	4.17	9.87

Table D.2: Median Absolute Error (AE) of the B_1 corrected MTR_{Rex} of MTC, rNOE and amides with different numbers of B1 sampling points N_{B1} compared to the maps corrected with $N_{B1} = 7$, corresponding to Figure 5.16.

		WM	GM	cWM	cGM
MTC [%]	none	24.9 ± 6.6	17.5 ± 6.9	19.7 ± 6.7	14.2 ± 5.1
	1-point	24.9 ± 5.0	16.9 ± 5.8	20.6 ± 6.4	14.6 ± 4.5
	2-point	24.7 ± 4.7	16.8 ± 5.4	20.7 ± 5.9	14.9 ± 4.1
	3-point	25.0 ± 4.8	17.0 ± 5.5	20.8 ± 6.2	14.9 ± 4.3
amides[%]	none	5.0 ± 1.4	6.0 ± 2.1	5.2 ± 1.6	6.0 ± 1.8
	1-point	5.0 ± 1.4	6.0 ± 2.0	5.2 ± 1.6	6.0 ± 1.8
	2-point	4.9 ± 1.2	5.9 ± 2.0	5.2 ± 1.5	6.0 ± 1.8
	3-point	4.9 ± 1.3	5.9 ± 2.0	5.2 ± 1.6	6.1 ± 1.9

Table D.3: Mean MTR_{LD} and the associated standard deviation within WM and GM ROIs within the cerebrum and within the cerebellum (cWM, cGM) for MTC and amides. MTR_{LD} was calculated for each subject measured with the PUSHUP saturation and for the different B_1 correction methods, associated with Figure 5.20.

tissue	session	MTC [%]	rNOE [%]	amides [%]
WM	1st	16.70 ± 6.14	12.79 ± 3.19	3.72±1.30
	2nd	18.27 ± 5.70	13.02 ± 3.01	3.73±1.26
	3rd	18.99 ± 5.66	13.17 ± 2.99	3.72±1.46
GM	1st	12.73 ± 5.57	11.81 ± 3.61	4.05 ± 1.75
	2nd	13.24 ± 5.56	11.43 ± 3.64	4.17 ± 1.67
	3rd	13.73 ± 5.32	11.46 ± 3.54	4.19 ± 1.91
rel. diff	1st	26.98	7.97	8.49
	2nd	31.93	13.01	11.14
	3rd	31.15	13.89	11.88

Table D.4: Mean MTR_{LD} and the associated standard deviation within WM and GM ROIs for MTC, rNOE, amides for a single subject, measured at three different days, associated with Figure 5.23.

subject	tissue	session	MTC [%]	rNOE [%]	amides [%]
1st	WM	test	19.04 ± 5.35	13.44 ± 2.68	4.05 ± 1.35
		retest	18.74 ± 5.22	13.49 ± 2.48	3.90 ± 1.36
	GM	test	14.81 ± 4.75	12.16 ± 3.01	4.67 ± 1.66
		retest	14.06 ± 4.52	12.34 ± 2.90	4.49 ± 1.35
	rel. diff	test	24.99	10.00	14.22
		retest	28.54	8.90	14.06
2nd	WM	test	17.50 ± 5.50	13.16 ± 2.67	4.33 ± 1.63
		retest	16.86 ± 5.30	13.57 ± 2.76	4.35 ± 1.24
	GM	test	12.85 ± 4.90	12.11 ± 3.07	5.11 ± 2.04
		retest	12.27 ± 4.60	12.32 ± 3.13	5.01 ± 1.83
	rel. diff	test	30.64	8.31	16.53
		retest	31.51	9.66	14.10
3rd	WM	test	19.71 ± 5.08	13.61 ± 2.26	4.11 ± 1,47
		retest	19.68 ± 4.80	13.84 ± 2.26	3.92 ± 1.24
	GM	test	13.83 ± 4.87	12.21 ± 2.85	5.14 ± 2.04
		retest	14.19 ± 4.56	12.39 ± 2.92	4.8 ± 1.83
	rel. diff	test	35.06	10.84	22.27
		retest	32.42	11.06	20.18

Table D.5: Mean MTR_{LD} and the associated standard deviation within WM and GM ROIs for MTC, rNOE, amides for test and retest measurements of three subjects, acquired within one session each, associated with Figure 5.25.

tissue	sequence	subject	MTC [%]	rNOE [%]	amides [%]
WM	sTx	sTx 01	19.73 ± 4.51	13.56 ± 2.01	3.71 ± 0.99
		sTx 02	17.35 ± 5.81	13.11 ± 3.04	4.17 ± 1.49
		sTx 03	16.93 ± 6.37	12.98 ± 3.16	4.22 ± 1.68
		sTx 04	16.74 ± 6.17	12.78 ± 3.19	3.72 ± 1.31
		sTx 05	19.04 ± 5.35	13.44 ± 2.68	4.05 ± 1.35
		sTx 06	17.50 ± 5.50	13.16 ± 2.67	4.33 ± 1.63
		sTx 07	19.71 ± 5.08	13.61 ± 2.26	4.11 ± 1,47
		sTx 08	20.25 ± 4.66	14.25 ± 4.74	3.90 ± 2.26
		sTx 09	19.27 ± 5.05	13.20 ± 1.87	4.34 ± 0.94
	CP	pTx 01	22.46 ± 5.85	13.42 ± 2.33	4.90 ± 1.38
		pTx 02	22.02 ± 4.61	13.54 ± 1.80	5.22 ± 1.25
		pTx 03	25.45 ± 5.00	12.93 ± 2.08	4.99 ± 1.92
		pTx 04	26.25 ± 5.38	12.84 ± 2.69	5.01 ± 1.53
		pTx 05	25.22 ± 5.10	12.72 ± 2.31	4.88 ± 1.30
	PUSHUP	pTx 01	23.91 ± 5.27	13.50 ± 1.94	4.90 ± 1.36
		pTx 02	23.36 ± 5.45	13.51 ± 2.39	5.32 ± 1.67
		pTx 03	24.67 ± 4.46	13.20 ± 1.85	4.80 ± 1.03
		pTx 04	24.30 ± 4.37	13.12 ± 1.70	4.64 ± 0.87
		pTx 05	25.70 ± 4.58	12.44 ± 2.15	4.77 ± 1.15
GM	sTx	sTx 01	14.40 ± 4.57	12.18 ± 2.62	4.30 ± 1.46
		sTx 02	13.32 ± 5.29	11.86 ± 3.29	4.57 ± 1.71
		sTx 03	13.16 ± 5.86	12.31 ± 3.73	4.81 ± 1.97
		sTx 04	12.81 ± 5.64	11.81 ± 3.61	4.06 ± 1.76
		sTx 05	14.81 ± 4.75	12.16 ± 3.01	4.67 ± 1.66
		sTx 06	12.85 ± 4.90	12.11 ± 3.07	5.11 ± 2.04
		sTx 07	13.83 ± 4.87	12.21 ± 2.85	5.14 ± 2.04
		sTx 08	14.10 ± 2.27	12.57 ± 1.10	4.83 ± 1.19
		sTx 09	14.39 ± 5.55	12.68 ± 2.68	4.81 ± 1.39
	CP	pTx 01	16.19 ± 6.47	12.80 ± 3.52	5.56 ± 2.24
		pTx 02	15.18 ± 5.23	12.78 ± 2.81	6.24 ± 1.95
		pTx 03	17.37 ± 5.59	12.23 ± 2.83	6.24 ± 2.50
		pTx 04	19.14 ± 5.95	12.53 ± 3.74	6.13 ± 2.10
		pTx 05	17.92 ± 5.73	11.98 ± 3.50	5.83 ± 1.97
	PUSHUP	pTx 01	15.95 ± 6.01	13.02 ± 3.02	6.01 ± 2.08
		pTx 02	15.45 ± 5.67	13.26 ± 3.24	6.70 ± 2.33
		pTx 03	16.38 ± 4.73	12.33 ± 2.58	5.84 ± 1.62
		pTx 04	17.34 ± 4.60	12.47 ± 2.49	5.55 ± 1.38
		pTx 05	17.66 ± 4.73	11.40 ± 2.65	5.48 ± 1.73

Table D.6: Mean MTR_{LD} and the associated standard deviation within WM and GM ROIs for MTC, rNOE, amides of the 14 subjects, acquired with the three different experimental setups, associated with first and second row of Figure 5.27

tissue	sequence	subject	MTC [%]	rNOE [%]	amides [%]
rel.diff.	sTx	sTx 01	31.21	10.74	14.89
		sTx 02	26.24	10.06	9.20
		sTx 03	25.06	5.33	13.26
		sTx 04	26.61	7.91	8.53
		sTx 05	24.99	10.00	14.22
		sTx 06	30.64	8.31	16.53
		sTx 07	35.06	10.84	22.27
		sTx 08	35.80	12.52	21.30
		sTx 09	28.98	4.04	10.33
	CP	pTx 01	32.45	4.71	12.64
		pTx 02	36.81	5.78	17.70
		pTx 03	37.78	5.58	22.16
		pTx 04	31.32	2.47	20.11
		pTx 05	33.85	5.98	17.73
	PUSHUP	pTx 01	39.91	3.58	20.50
		pTx 02	40.76	1.85	22.88
		pTx 03	40.43	6.82	19.41
		pTx 04	33.38	5.10	17.95
		pTx 05	37.08	8.77	13.76

Table D.7: Relative difference of MTR_{LD} of WM and GM ROIs, depicted in Table D.6 and associated with the bottom row of Figure 5.27.

List of Figures

List of Tables

List of Abbreviations

ACS Auto Calibration Signal

AD Alzheimer’s Disease

AE Absolute Error

AP Anterior-Posterior

APT Amide Proton Transfer

BMC Bloch-McConnell

CAIPIRINHA Controlled Aliasing In Parallel Imaging Results In Higher Acceleration

CE Chemical Exchange

CEST Chemical Exchange Saturation Transfer

cGM cortical Gray Matter

CNR Contrast To Noise Ratio

CoV Coefficient Of Variation

CP Circularly Polarized

Cr Creatine

CSF Cerebrospinal Fluid

CT Computed Tomography

cw Continuos Wave

DC Duty Cycle

DREAM Dual Refocusing Echo Acquisition Mode

DS Direct Saturation

ePC External Phase Correction

EPI Echo Planar Imaging

ETL Echo Train Length

EVI Echo Volume Imaging

FA Flip Angle

FID Free Induction Decay

FLASH Fast Low Angle Shot

fMRI Functional Magnetic Resonance Imaging

FOV Field Of View

FWHM Full Width At Half Maximum

GABA Gamma-Aminobutyric Acid

Glu Glutamate

GM Gray Matter

GRAPPA GeneRalized Autocalibrating Partially Parallel Acquisitions

GRASE GRadient And Spin Echo

GRE Gradient Echo

HPM High Permittivity Materials

iPC Internal Phase Correction

LS Large Shift

MCI Mild Cognitive Impairment

mIns Myo Inositiol

MR Magnetic Resonance

MRI Magnetic Resonance Imaging

MRS Magnetic Resonance Spectroscopy

MT Magnetization Transfer

MTC Magnetization Transfer Contrast

MTR Magnetization Transfer Ratio

ND Neurodegenerative Disease

NMR Nuclear Magnetic Resonance

NOE Nuclear Overhauser Effect

ODE Ordinary Differential Equation

PA Posterior-Anterior

PC Phase Correction

PD Parkinson’s Disease

PE Phase Encoding

PET Positron Emission Tomography

ppm Parts Per Million

PTR Proton Transfer Ratio

pTx Parallel Transmit

PUSH Pulse Design For Saturation Homogeneity

RF Radio Frequency

rNOE Exchange-Relayed Nuclear Overhauser Effect

ROI Region Of Interest

SAR Specific Absoption Rate

SE Spin Echo

SNR Signal to Noise Ratio

SP SubPulse

ssMT Semi Solid Magnetization Transfer

STA Small Tip Angle

STE Stimulated Echo

sTx Single Transmit

TE Echo Time

TR Repetition Time

TSE Turbo Spin Echo

tSNR Temporal Signal to Noise Ratio

UHF Ultra High Field

UP Universal Pulses

WE Water Excitation

WM White Matter

Acknowledgements

I would like to take this opportunity to thank all those who have supported me along the way.

- Tony Stöcker for the opportunity to join the DZNE and for his continuous guidance and support. His open door was always appreciated.
- Tony Stöcker and Klaus Desch for their supervision and the necessary push to finish the writing.
- Rüdiger Stirnberg for allowing me to use his well-rounded 3D-EPI sequence which was great base for developing the snapshopt CEST sequence. Sequence development would not have been possible without this head start and his patience in answering all the questions that came up along the way.
- Philipp Ehses for introducing me to sequence development, for his patience in answering all my questions, and for thinking through all CEST-specific problems I encountered along the way.
- Moritz Zaiss for the great support and for teaching me all the CEST basics and patiently answering all my questions, for the fantastic week in Tübingen and last but not least for the CEST evaluation software and the basis of the CEST saturation module. The collaboration between our sites has always been very fruitful and full of joy.
- Yannik Völzke and Daniel Löwen for pTx pulse calculation and for the implementation of the PUSHUP sequence.
- My PhD student and office mates: Jolanda, Yannik, Alex, Markus, Martin, Marten and Difei. For all the brainstorming, the shared suffering, the many hours of laughter and conversation, the shared celebrations, and the always amicable support.
- Yannik Völzke, Philipp Ehses, Rüdiger Stirnberg and Jana-Tamara Engels for proof-reading.
- The whole AG-Stöcker group for creating such a great working environment and so many memorable moments.
- The KAS for the scholarship and for three years of interesting seminars and events.
- My very best colleagues at Strahlentherapie BRS, for always having my back and supporting me over the last three years.
- My family and friends for their love, unconditional support and tremendous understanding, especially over the past year.
- Jan, for always being my safe haven.